Synthesis and Luminescence Studies of Ir(III) Complexes and Iridium/Lanthanide Dyads

Ahmet Cankut

The University of Sheffield

Department of Chemistry

A thesis submitted to the University of Sheffield in partial fulfilment of the requirements for the degree of Doctor of Philosophy

June 2015

Abstract

This thesis is concerned with the preparation and photophysical studies of various Ir(III) complexes and Ir(III)/Ln(III) dyads.

Chapter 1 provides an introduction to the background of d-metal and f-metal luminescence and their use in biological applications. The emphasis is on the use of Ir(III) chromophores based on phenylpyridine ligands to stimulate emission from Ln(III) ions *via* an energy-transfer mechanism (the 'antenna effect'). Examples of these Ir(III)/Ln(III) dyads from literature are given.

Chapter 2 describes the preparation of the complexes $[Ir(fppy)_2L^{pytz}]$ and $[Ir(fppy)_2L^{pic}]$ and looks at their photophysical properties when titrated with $[Ln(hfac)_3]$ (Ln = Eu, Tb and Gd). The studies showed that the complexes were able to sensitise luminescence from Eu(III) and partially from Tb(III) through a combination of PEnT and PET mechanisms.

Chapter 3 describes the preparation of $[Ir(fppy)_2L^{pytz}]$ and $[Ir(fppy)_2L^{tol}].(PF_6)$ and the change of their luminescence properties during pH titrations. The two water soluble complexes $[Ir(ppy\text{-}PEG)_2L^{pytz}]$ and $[Ir(ppy\text{-}PEG)_2L^{tol}]$, based on the architecture of the first two complexes, were prepared. Their photophysical properties during pH titrations are reported. Preliminary cell imaging data for the latter two complexes showed they can undergo two-photon excitation at 780 nm and staining within the cytoplasm of MCF7 cells.

Chapter 4 describes the preparation of $[Ir(fppy)_2Lnap^{pic}]$ and $[Ir(fppy)_2L^2]$; where in both cases a naphthalene unit is used as a bridging ligand. Their photophysical properties after the addition on Ln(III) (Ln = Eu, Tb and Gd) are reported and showed naphthalene acts as a 'stepping stone' resulting in a two-step energy-transfer process from Ir(III) → ^{3}nap → Ln(III) resulting in quenching of Ir(III)-based luminescence. The preparation of $[Ir(fppy)_2L^3]$ which contains a phenyl spacer unit is reported. Addition of Eu(III) showed good balance between Ir(III) and sensitised Eu(III) emission.

Chapter 5 gives the experimental procedures and characterisation data for all the ligands and complexes reported in this thesis.

Declaration

Except where specific references have been made to other sources, the work within this thesis is the original work of the author. It has not been submitted, in whole or in part, for any other degree.

Ahmet Cankut

June 2015

This thesis is dedicated in loving memory to my brave friend James Edward Cardy.

12/06/1984 – 09/01/2014

Acknowledgements

Firstly I would like to thank my supervisor Mike Ward for giving me the opportunity to do my PhD. His enthusiasm for research, support and guidance has really helped me over the past few years. The man is a genius. He’s also a good laugh when he has had a few drinks.

I would also like to thank all the members of the Ward group, past and present. I’d like to especially thank Dan who taught me a lot when I started my PhD and Liz for her extensive knowledge on photophysics and for her contribution on the cell imaging work she carried out for some of my complexes. Thanks to my partner in crime Martina (aka Weiner) with whom I had constant laughs with, especially on our USA tour. A huge thank you to all the other members, Alex (aka A-Shell), Andy (thank you for the X-ray crystallography help), the legendary Ash, Atanu, Benji, Beth, Chris, Jerry, Methers, Shida, Suad, Will (also thanks for the X-ray crystallography help) and Zainab. Working (and drinking) with you guys has been amazing! You are all a fantastic bunch of people and I feel very fortunate to have had the opportunity to work alongside you. It has also been a blast sharing the office and lab with the Brammar group, Craig, Elliot, Inigo, Jamie, Jason, Ramide, Rebecca and Tom. I wish everyone the best of luck in the future.

I would also like to thank all the technicians in the department; Simon and Sharon for mass spec; Jenny and Mel for elemental analysis; Rob for help with HPLC; Pete and Nick from stores and Sue and Brain for NMR assistance.

A massive thanks to my second family, aka ‘the Nuffield Gym Fam/The Crew’; Debs and Ang (one of the nicest and most generous couples I know), Aimeé, Megan, Debbie, Jules, Mike, Sue and Divya. I love you guys. Training/eating/drinking and gossiping with you guys has been the best. You’ve kept me sane. I’m going to miss you all so much. Keep cake club alive for me and make sure no one takes my bike in spin or my spot in pump!

Thanks to all my close friends for providing endless laughs, support and company; Chris, Amanda (who is such an amazing person), Elf, Ashlie, Mike (aka Mika Wukka), ZBG (thanks for all the shopping trips Gal!), Leila, Hannah, Rachel, Laura, Georgia, Gemma and Izie.

Finally I would like to thank my family, particularly mum and dad for their support. Their enthusiasm for education was the inspiration for me to become an educated individual and without their help, pursuing higher education would not have been possible. I'd also like to thank my grandmother, Nilufer, whom I see as a second mother. I feel blessed to have such a generous, altruistic and kind person in my life. She is such an inspiration to me. I love you all very much.

Publications

[1] D. Sykes, **A. J. Cankut**, N. M. Ali, A. Stephenson, S. J. P. Spall, S. C. Parker, J. A. Weinstein and M. D. Ward, *Dalton Trans.,* 2014, **46**, 6414.

List of Abbreviations

acac	Acetylacetone
AIBN	Azobisisobutyronitrile
Ala	Alanine
BATH	4,7-diphenyl-1,10-phenanthroline (electron-transport layer of an OLED)
BET	Back energy transfer
BOC	*tert*-Butyloxycarbonyl
bpy	2,2'-bipyridine
CCD	Charge-coupled device
cd	Candela
CHO	Chinese hamster ovarian cell
cm	Centimetre
δ	Chemical shift
dfppy	Difluorophenylpyridine
DMAA	*N,N*-Dimethylallyamine
DME	Dimethoxyethane
DMEM	Dulbecco's modified Eagle's medium
DMF	Dimethylformamide
DMSO	Dimethyl sulfoxide
ES-MS	Electrospray Mass Spectrometry
ET	Energy-transfer
EtOH	Ethanol
g	Gram
h	Hours
HDF	Human dermal fibroblasts (skin cell)
HeLa	Henrietta Lacks (cancer cell)
HEPES	(4-(2-hydroxyethyl)-1-piperazineethanesulfonic acid) (Zwitterionic chemical buffer agent)
hfac	Hexafluoroacetylacetonate
HOMO	Highest occupied molecular orbital

HPLC	High Performance Liquid Chromatography
ILCT	Intra-ligand charge transfer
ISC	Intersystem crossing
ITO	Indium tin oxide
K	Kelvin
LC	Ligand-centred
LEC	Light-emitting electrochemical cell
LF	Ligand field
LLCT	Ligand-to-ligand charge transfer
LMCT	Ligand-to-metal charge transfer
Ln	Lanthanide
LUMO	Lowest unoccupied molecular orbital
Lys	Lysine
M	Molar
mA	Milliampere
MCF7	Human breast cancer cell
MeOD	Deuterated methanol
MeOH	Methanol
mg	Milligram
MHz	Megahertz
mL	Millilitre
μL	Microlitre
MLCT	Metal-to-ligand charge transfer
μM	Micrometre
mmol	Millimole
mol	Mole
μW	Microwatts
N-BS	*N*-Bromosuccinimide
NBS	Natal bovine serum
NIH 3T3	Fibroblast cells
NIR	Near infrared
nm	Nanometre
NMR	Nuclear Magnetic Resonance
OLED	Organic light-emitting diode

PBS	Phosphate buffer solution
PEG	Poly(ethylene glycol)
PET	Photoinduced electron-transfer
PEnT	Photoinduced energy-transfer
Ppm	Parts per million
ppy	Phenylpyridine
sh	Shoulder
Tert	Tertiary
THF	Tetrahydrofuran
TFA	Trifluoroacetic acid
TNF-α:	Tumor necrosis factor-α (pro-inflammatory cytokine)
TPD	*N,N'*-bis(3-methylphenyl)-*N,N'*-diphenylbenzidine (hole-transporting layer of an OLED)
UV-vis	Ultraviolet-visible
V	Volt

Table of Contents

Chapter 1: Introduction

Chapter 2: Photoinduced Enery-Transfer and Electron-Transfer

Chapter 3: Water Soluble Complexes for Cell Imaging

Chapter 4: Effect of Spacer Groups on d → f Energy-Transfer

Chapter 5: Experimental

Appendix: X-ray Crystallography Data

1

Introduction

1.1 Luminescence of Transition Metal Complexes

Over the past few decades an exciting new field has emerged and is developing fairly rapidly in chemistry; the study and application of the photochemistry and photophysics of transition metal complexes. This thesis looks at the concept of photophysics in d-block metal complexes, its applications, and will focus on the synthesis, characterisation and photophysical studies of iridium complexes.

A good example of a well-studied complex is $[Ru(bpy)_3]^{2+}$ where bpy is a 2,2'-bipyridyl ligand (**Fig. 1.01**). This photoactive complex is luminescent at room temperature and is widely used as a standard for quantum yield calculations.[1-3]

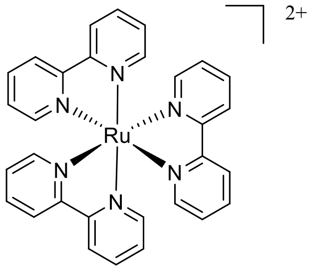

Figure 1.01. Structure of the complex $[Ru(bpy)_3]^{2+}$.

The metal centre has a 2+ charge and therefore has a low-spin d^6 configuration with a D_3 symmetric environment. This complex exhibits a Ru (d) → bpy (π^*) metal-to-ligand charge-transfer (MLCT) process as its lowest excited state, attributed to the strong π-accepting bpy ligands.[4]

Luminescence follows the absorption of a photon when a substance is photoexcited, which leads to an electron being promoted to a higher-energy excited state from its ground state. Upon relaxation back to the ground state, photons can be emitted instead of the energy being dissipated as heat. When discussing luminescence, there are two distinct types: fluorescence and phosphorescence. Fluorescence involves the spontaneous emission of light during a transition - usually from the lowest vibration level of the excited singlet state (S_1) to the ground state (S_0) of a system - shown in the simplified Jablonski diagram below (**Fig. 1.02**). This transition is a spin-allowed process obeying the selection rule $\Delta S = 0$.

The use of heavy-metal atoms such as Ru allows spin-orbit coupling to occur as a result of the high spin-orbit coupling constant ζ of these metals. This allows intersystem crossing (ISC) to occur resulting in population of the T_1 triplet state from the S_1 state. From there a radiative transition from T_1 to S_0 can occur and this type of spin-forbidden luminescence process is known as phosphorescence. In quantum mechanical terms this process is "forbidden" ($\Delta S \neq 0$) and is not usually observed in organic molecules. The forbidden nature leads to characteristically long luminescence decay lifetimes, e.g. the ^{3}MLCT state lifetime of $[Ru(bpy)_3]^{2+}$ is around 500 ns,[3] compared to 1-10 ns[5] for fluorescence from organic molecules.

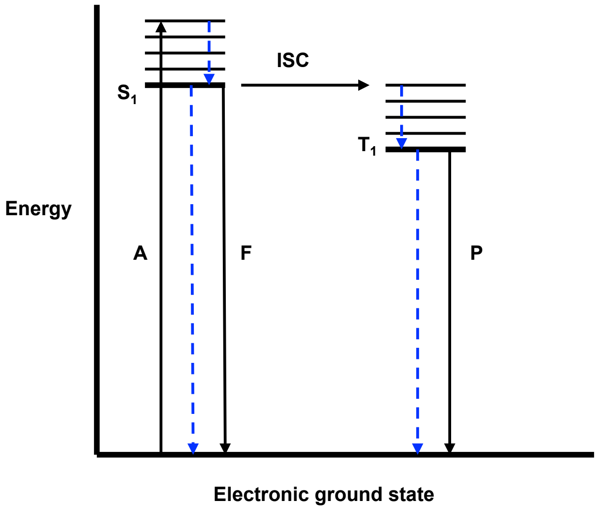

Figure 1.02. Jablonski energy diagram illustrating the transitions between electronic states of a molecule for the quantum mechanical processes of fluorescence and phosphorescence.[6] A = absorbance, F = fluorescence, P = phosphorescence, ISC = intersystem crossing, ET = energy-transfer, S = Singlet state, T = triplet state. Blue dashed lines represent non-radiative decay processes.

As well as having luminescence, the ability of $[Ru(bpy)_3]^{2+}$ to undergo a photo-induced electron transfer (PET) process from its excited state led to an interesting development of a model for photosystem II (PSII) in green plants, where PSII contains the photosensitiser - P_{680}. This consists of two chlorophyll dimers which rapidly photo-oxidise upon absorption of light, resulting in an electron transfer process through a chain of acceptors, and P_{680} is then regenerated by electron transfer from a tetramanganese cluster (**Fig. 1.03**). Using complexes based on $[Ru(bpy)_3]^{2+}$, Åkermark *et al.* developed dinuclear Ru-Mn complexes that mimic the behaviour observed for P_{680} (shown in **Fig. 1.03**).[7] Here the binuclear complex underwent a PET process upon photoexcitation in the presence of the electron acceptor methylviologen (MV^{2+}), where electron transfer from the excited state of Ru(II) occurred forming Ru(III) and $MV^{+\bullet}$, then an intermolecular electron transfer from coordinated Mn(II) to the photogenerated Ru(II) occurred with a first-order rate constant of 1.85 x 10^5 s^{-1}, regenerating Ru(II).

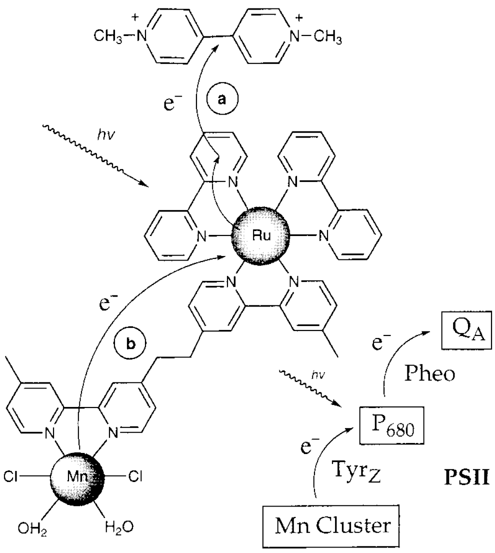

Figure 1.03. Ru-Mn complex undergoing PET process upon photoexcitation (mimicking the natural process shown on the right).[7]

Another d^6 MLCT system that has attracted attention is the rhenium (I) tricarbonyl bipyridine chromophore $[Re(CO)_3(bpy)X]$ (where X = anionic ligand) (**Fig. 1.04**) first used by Wrighton[8] and developed further by Meyer[9] for the rich photophysical properties of the MLCT excited state, and for the electrocatalytic reduction of carbon dioxide.[10]

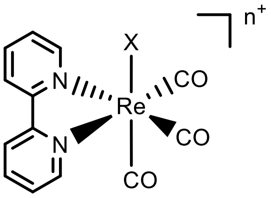

Figure 1.04. Structure of $Re(CO)_3(bpy)X$ (where X= anion such as Cl).

Various Re-diimine complexes have been synthesised and studied[11a,b] $[Re(CO)_3(N^\wedge N)((C\equiv C)_nR)]$ (n = 1,2,3; R = alkyl or aryl). These alkynylrhenium (I) complexes show intense long-lived orange-red luminescence upon photoexcitation at λ= 350 nm, originating from the ^{3}MLCT [dπ(Re) → π*(N^N)] excited state which includes some mixing of [π(C≡C) → π*(N^N)] ligand-to-ligand charge transfer (LLCT) character. More electron-donating alkynyl ligands result in lower energy MLCT emission bands, consistent with the σ- and π-donating ability of the alkynyl moieties. Further studies have shown the emission energies can be tuned by altering the type of alkynyl ligands used.[12,13]

Re(I) complexes have shown a great potential as cellular imaging agents due to their biocompatibility. An example of this was recently published by the Coogan group where tricarbonyl-rhenium metal complexes functionalised with amino acid ester derivatives were used (**Fig. 1.05**).[14]

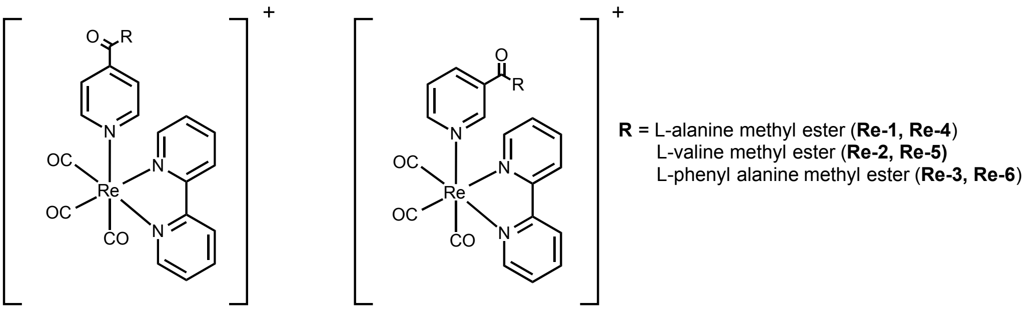

R = L-alanine methyl ester (**Re-1, Re-4**)
L-valine methyl ester (**Re-2, Re-5)**
L-phenyl alanine methyl ester (**Re-3, Re-6**)

Re(1-3) **Re(4-6)**

Figure 1.05. Chemical structure of the Re(I) complexes.

In this example, the Re(I) complexes are conjugated with simple amino acid derivatives in order to determine their effect on cellular uptake, localisation patterns and toxicity.

The amino acid derivatives were functionalised in either the *meta* or *para* position of the pyridyl groups. The pyridyl groups were functionalised instead of the diimine unit, as not to affect the emissive properties of the complexes, because generally phosphorescence is observed from the ^{3}MLCT [$d\pi(Re) \rightarrow \pi^*(diimine)$] transition in these types of complexes. All the complexes showed emission at ~ 540 nm, in degassed CH_2Cl_2 at 298 K.

The complexes were incubated in MCF-7 cells and both the *para* (**Fig. 1.06**) and *meta* (**Fig. 1.07**) derivatives showed good uptake into these cells.

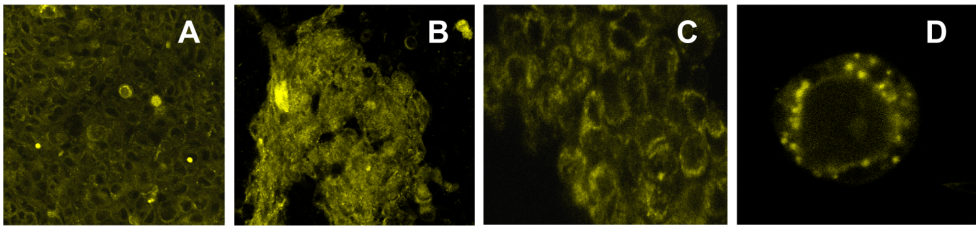

Figure 1.06. Cell images with complexes **Re-1** – **Re-3** showing clustering (A-C respectively) and localisation with complex **Re-2** (D).[14]

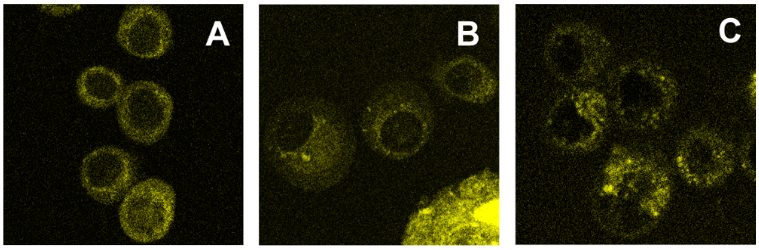

Figure 1.07. Cell images with complexes **Re-4** – **Re-6** showing localisation (A-C respectively).[14]

Clear differences on the effect of the cells were observed between the *para* and *meta*-substituted complexes. Clustering of dead and dying cells were observed in the cases

of the *para*-substituted analogues (**Re-1 – Re-3**), which had damaging effects on most of the cells. Despite some mitochondrial staining being observed (**Fig. 1.06** D), the samples showed considerable photobleaching and it was concluded that these complexes have limited use as imaging agents.
In contrast to this, cells incubated with the *meta*-substituted analogues remained healthy with no clustering, phototoxicity or photobleaching being reported.

While the exact mechanism of the toxicity in the *para* series remains unclear, it was likely that the complexes were interacting with unidentified biological components in the cell. One hypothesis on the difference in behaviour between the *para* and *meta*-substituted complexes was explained by the ease in which a intramolecular electron-transfer process could occur from the excited state of the Re(I) centre to the amino acid derivate in the *para*-substituted complexes compared to the *meta* derivatives. The result is the formation of amino acid radicals, which could then interact with endogenous donors within the cell.

This research shows how transition metal complexes can have suitable biocompatibility for use as cell-imaging agents and how the position of the coordinated ligands can have profound variation in cellular behaviour.

Another transition metal whose luminescence properties have been exploited for imaging applications is Pt(II). This metal differs from the previous examples in that it is a d^8 metal ion and therefore preferentially adopts a 4-coordinate square planar geometry. An example of a Pt(II) system that has been employed in cell imaging is that based on N^C^N-coordinated 1,3-di(2-pyridyl)benzene (dpyb), first prepared in 1960[15] and whose photophysical properties were reported in 2003.[16] In 2008 Botchway *et al*. reported a class of these complexes (**Fig. 1.08**) as dyes for steady-state and time-resolved emission imaging microscopy of live cells.[17]

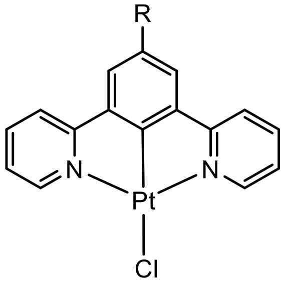

Figure 1.08. Structure of the [PtL^{n}Cl] complexes (where *n*= 1-4, = H, -C(O)CH$_3$, -CH$_3$ and –C$_6$H$_4$N(CH$_4$)$_2$, respectively).

These class of compounds were reported to have high d-d energy states relative to the emissive excited states due to the rigidity and strong ligand field associated with the tridentate cyclometallated ligand. This has the effect of removing potentially deactivating d-d pathways and resulted in an intense luminescence in degassed CH$_2$Cl$_2$ at room temperature (Φ= 0.6-0.7) with long emission lifetimes of 7 μs and 0.5 μs in degassed and aerated CH$_2$Cl$_2$ respectively. Highly structured emission profiles were observed which was attributed to a $^3\pi$-π* intraligand excited state mixed with some MLCT character. [PtL^{1}Cl] was used in time-resolved imaging of cells using a time-gated CCD camera. This resulted in the cells being visualised by the long-lived emission from the Pt(II) complex, which would have otherwise not been possible due to background fluorescence from the fluorescein emission swamping the image immediately after the laser excitation pulse (**Fig. 1.09**).

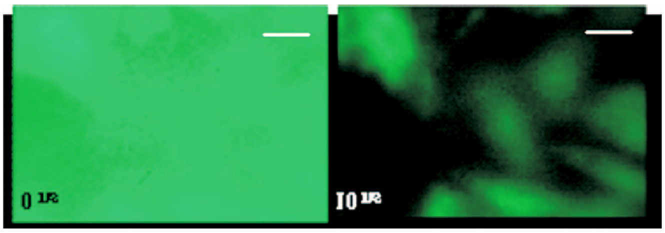

Figure 1.09. Time-gated cellular imaging: live CHO cells preincubated with [PtL^1Cl], imaged in the presence of solution of fluorescein in 1M NaOH. The left image was taken at 0 ns and right image at 10 ns delays after the 355 nm laser pulse. Taken from Ref. 17.

These experiments show exciting potential cell-imaging applications of [PtL^1Cl] whose long emission lifetimes allow images to be obtained without interference from background autofluorescence.

1.2 Iridium Complexes

Iridium (III) organometallic complexes based on phenylpyridine ligands have been of particular interest in phosphorescent devices, particularly as emitters in light-emitting electrochemical cells (LECs)[18,19], photocatalysis[20] and biological imaging.[21] These compounds have shown to be very versatile phosphorescent emitters[22] when compared to Pt(II) species as they feature less triplet-triplet annihilation and shorter lifetimes at higher currents in LECs; as a result higher quantum yields are achieved.[18] Interest in Ir(III) complexes is a result of their versatility as emitters due to the fact their colour of emission can be tuned across the visible spectrum.[23] Their colour tunability is a result of strong spin-orbit coupling leading to mixed singlet and triplet MLCT states as well as ligand-centred (LC) states[24] (**Fig. 1.10**) and sensitivity of luminescence to ligand substituents.

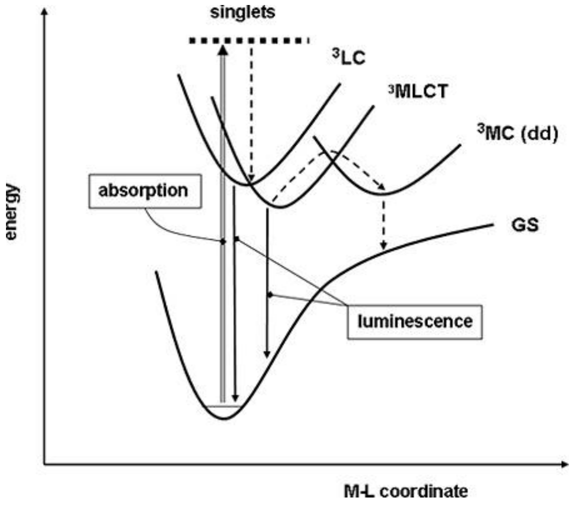

Figure 1.10. Electronic transitions of Pt(II) complexes involving MC, MLCT and LC excited states; the MC states are not emissive.[25]

Moreover, some predictions can be made regarding the design and properties of the ligands as the luminescence properties of Ir(III) complexes are related to the sigma-donating and electron-accepting abilities of these ligands.[24] A common green-emitting phosphor is $Ir(ppy)_3$ (ppy = 2-phenylpyridine) (**Fig. 1.11**) and it is believed that the emissive state comes from the highest occupied molecular orbital (HOMO) localised on iridium d and phenyl π orbitals, with the lowest unoccupied molecular orbital (LUMO) on the π* orbitals of the pyridine ring.[26,27]

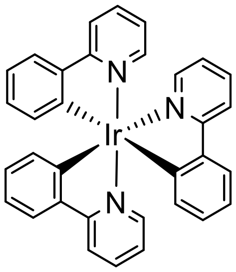

Figure 1.11. Structure of the green-emitting phosphor *mer*-Ir(ppy)$_3$.

The ppy ligand has been extensively used in phosphorescent Ir complexes. The deprotonated ppy ligand forms a strong σ-donating interaction with the metal centre which is essential for emission.[28] As Ir is commonly found in the +3 oxidation state, this anionic ligand serves to reduce the overall charge of the complex making it easier to solubilise in organic solvents, as well as satisfying the coordination sphere around Ir(III). The cyclometallating ligand also increases electron density on the metal centre, which helps to facilitate both ^{1}MLCT and ^{3}MLCT transitions. As mentioned earlier, the colour of the emission can be tuned and one way to do this is by adding electron withdrawing F atoms to the 2- and 4- positions on the phenyl group of ppy. The HOMO is thereby stabilised resulting in an increase in the HOMO-LUMO gap, resulting in a blue shift in emission.

These compounds can be readily prepared from the μ-dichloro bridged precursor dimer $[Ir(C^{\wedge}N)_2\text{-}\mu\text{-}Cl]_2$ (**Scheme 1.01**), which in turn can be readily prepared from the reaction of $IrCl_3.xH_2O$ and the relevant 2-phenylpyridine ligand.[29] The labile nature of the bridging chlorides means that another bidentate ligand can be added onto the metal centre quite easily to give $[Ir(ppy)_2L]^{n+}$, where n is the formal charge on the ligand, L.

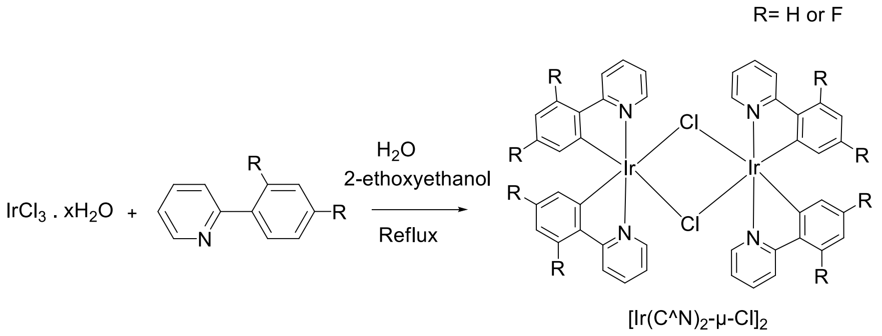

Scheme 1.01. Synthesis of the intermediates tetrakis(2-phenylpyridine-*C*^{2},*N'*)(*μ*-dichloro)diiridium and tetrakis[2-(2,4-difluorophenyl)-pyridine-*C*^{2},*N'*](*μ*-dichloro)diiridium for $[Ir(ppy)_2L]^+$ or $[Ir(fppy)_2L]^+$ complexes.

1.2.1 Tuning the Emission Colour of Iridium Complexes

A common ancillary ligand used in these $[Ir(ppy)_2L]^+$ systems is the 2,2'-bipyridine family. These $[Ir(ppy)_2(N^\wedge N)]^+$ complexes show remarkable photoluminescence quantum yields. A good example of tuning emission was reported by Huang *et al.* in 2006 with their concept of tuneable emission via the expansion of the π-conjugated system of the chelating ligand, based on 1-phenylisoquinoline iridium (III) complexes $[Ir(piq)_2(N^\wedge N)]\cdot PF_6$ containing N^N ligands with different conjugation lengths (**Fig. 1.12**).[30]

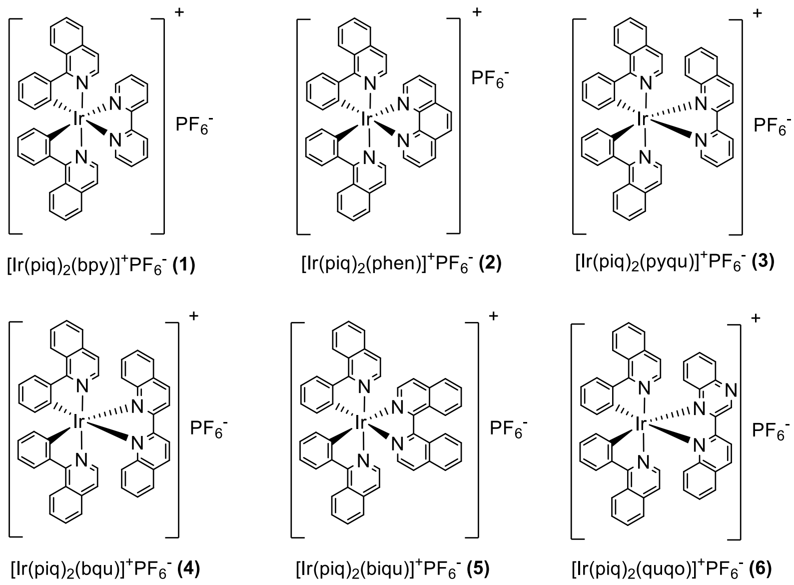

Figure 1.12. Chemical structures of the piq-based cationic iridium (III) complex [Ir(piq)$_2$(N^N)]$^+$PF$_6^-$ containing different N^N ligands reported by Huang *et al.*

The group showed that the emission wavelengths of the complexes could be tuned over a wide range from 586 to 732 nm (**Fig. 1.13**) for complexes **1**-**6**. The λ_{max} for emission of complexes **1**-**6** in CH_2Cl_2 at room temperature were 586 nm, 589 nm, 637 nm, 659 nm, 695 nm and 732 nm respectively. A red-shift in luminescence was observed in complexes with greater conjugated lengths as a result of elongation of the overall π conjugation, decreasing the energy levels of the LUMOs.

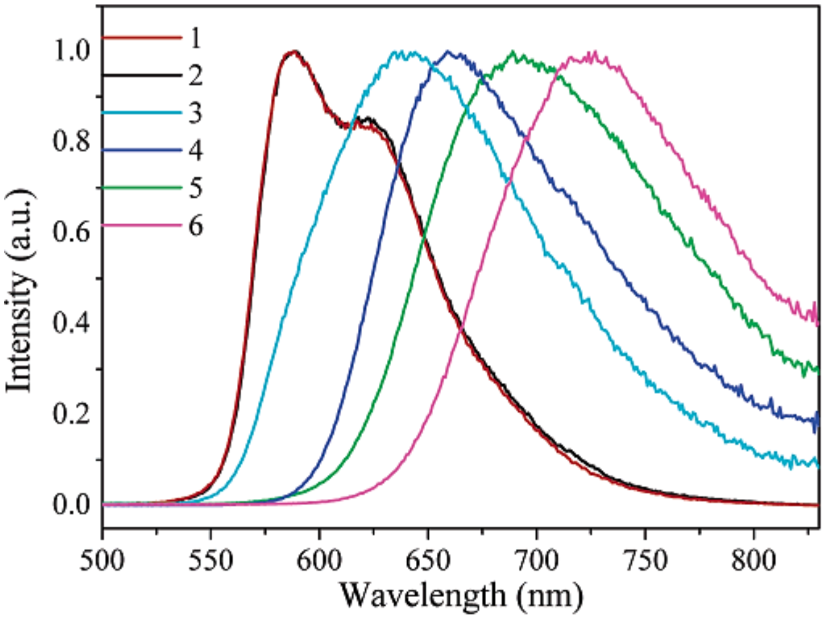

Figure 1.13. Room-temperature photoluminescence spectra of **1**-**6** in CH_2Cl_2 showing tuning of emission colour by varying the ancillary ligand of the Ir(III) complex.[30]

It was reported that for complexes **1**-**2**, the contribution of the excited state includes triplet ligand-centred (^{3}LC) ($\pi_{C^\wedge N} \rightarrow \pi^*_{C^\wedge N}$), ^{3}MLCT (dπ (Ir) → π* (diimine)) and ^{3}LLCT [$\pi_{C^\wedge N} \rightarrow \pi^*_{N^\wedge N}$]. The energy levels of the HOMO for each of the complexes were similar, however their LUMO energy levels varied which resulted in different energies for the ^{3}MLCT (dπ(Ir) → π* (diimine) transitions. As a result of the less-conjugated extent of the diimine ligands (bpy and phen), **1** and **2** had higher ^{3}MLCT energy levels which increased contributions from the ^{3}LC($\pi_{C^\wedge N} \rightarrow \pi^*_{C^\wedge N}$) state. In contrast, complexes **3**-**6** had low-energy ^{3}MLCT states and the contributions from ^{3}LC ($\pi_{C^\wedge N} \rightarrow \pi^*_{C^\wedge N}$) were small due to increased conjugation lengths of the diimine ligands (pyqu, bqu, biqu and quqo). As a result it was shown that changing the diimine ligands greatly affected the photoluminescence properties of these complexes.

1.2.2 Luminescent Iridium Complexes in Biological Applications

In 2008 Huang *et al*. also reported the use of cationic Ir(III) complexes for phosphorescence staining in the cytoplasm of living cells.[31] The complexes [Ir(dypy)$_2$(bpy)].PF$_6$ (**7**) and [Ir(dfppy)$_2$(quqo)].PF$_6$ (**8**) (**Fig. 1.14**) were shown to be useful phosphorescent dyes that exclusively stained the cytoplasm of living cells with bright green and red emission respectively.

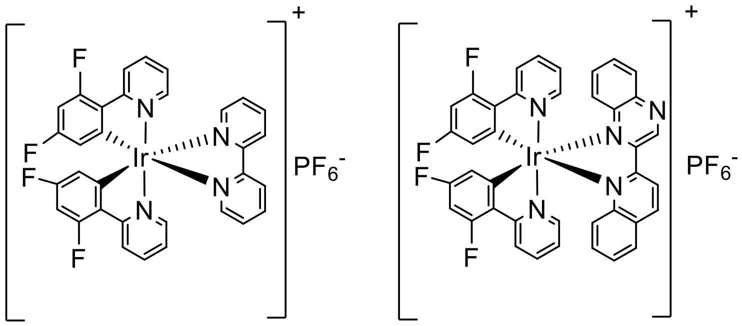

$[Ir(dfpy)_2(bpy)]^+PF_6^-$ **(7)** $[Ir(dfpy)_2(quqo)]^+PF_6^-$ **(8)**

Figure 1.14. Chemical structures of iridium (III) complexes **7** and **8**.

Complexes (**7**) and (**8**) showed maximum emission wavelengths at 530 nm and 643 nm respectively. Intracellular luminescence was observed after incubation into HeLa cells with 20 μM in DMSO/PBS (pH 7, 1 : 49, v/v) for 10 mins at 25°C with the maximum emission wavelengths blue shifting to 512 nm and 617 nm for compounds (**7**) and (**8**) respectively. Large intensity differences ($I_2/I_3 > 10$) between the cytoplasm and nucleus were revealed, which indicated preferential staining of the cytoplasm with the two complexes (**Fig. 1.15**).

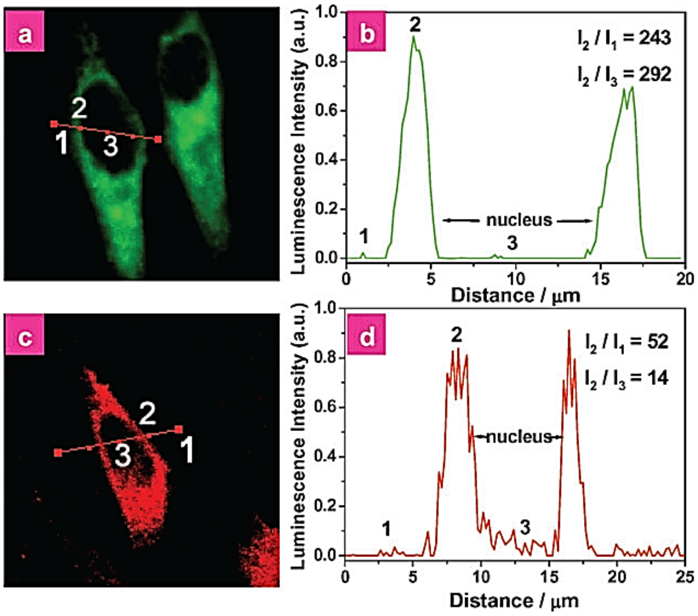

Figure 1.15. Confocal luminescence images and luminescence intensity profile (across the lines shown in (a) and (c) of HeLa cells incubated with 20 μM **7** or **8** in DMSO/PBS (pH 7, 1 : 49, v/v) for 10 min at 25°C. The signal-to-noise ratios (I_2/I_1) and cytoplasm-to-nucleus ratios (I_2/I_3) are shown in the right column (excitation at 405 nm).[31]

The two complexes showed low cytotoxicity as well as cell membrane permeability making them promising candidates for the design of specific phosphorescence bioimaging agents and were the first examples of the use of Ir(III) complexes as cell-permeable dyes for luminescence staining in the cytoplasm of living cells.

Other interesting Ir-based complexes for biological imaging designed by Lo *et al*. in 2006 were a series of cyclometallated iridium (III) dipyridoquinoxaline and dipyridophenazine complexes $[Ir(ppy)_2(N^\wedge N)]^+$, (N^N = dpq, dpqa, dppz, dppn) (**Fig. 1.16)** as luminescence intercalators for DNA.[32] The binding of the complexes to double-stranded calf thymus DNA and synthetic double-stranded oligonucleotides poly(dA).poly(dT) and poly(dG).poly(dC) were reported. The dppz and dppn complexes showed comparable binding affinities to calf thymus DNA (binding constants K= 2.0 x 10^4 M^{-1} and 7.8 x 10^4 M^{-1} respectively).

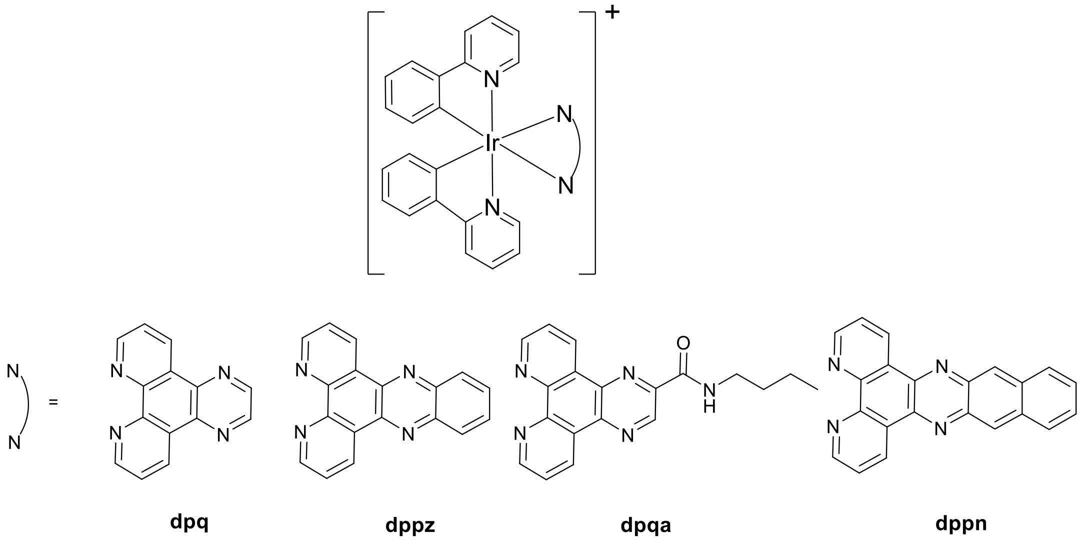

Figure 1.16. $[Ir(ppy)_2(N^\wedge N)]^+$, (N^N = dpq, dpqa, dppz, dppn) complexes used by Lo *et al*. as luminescent intercalators for DNA binding.

All complexes displayed emission enhancement in the presence of double-stranded calf thymus DNA. The emission intensity of the dpq complex at 591 nm was enhanced 33-fold, and new emission bands were observed at 602 nm and 606 nm for the dpqa and dppz complexes, respectively. These changes were ascribed to the intercalation of the complexes into the base pairs of the double-stranded DNA molecules which resulted in an increase in rigidity and hydrophobicity of the local surroundings of the complexes and the protection of the N^N ligands from interacting with H_2O molecules. Similar results were observed for the emission titrations with the synthetic double-stranded oligonucleotides, making these complexes potential candidates for DNA probes.

Ir(III) complexes do not need to have complicated architectures to be used as imaging agents. A nice example of a relatively simple Ir(III) complex (**Fig. 1.17**) was reported by Li for the imaging of nuclei in living cells.[33]

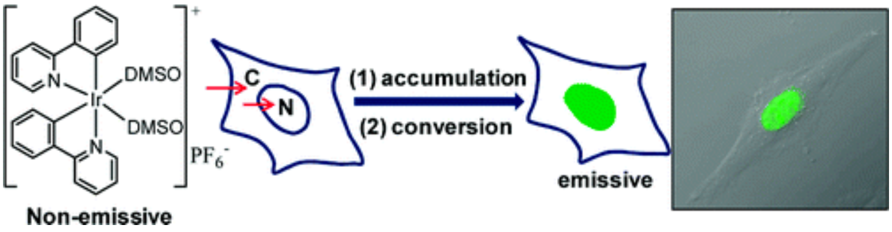

Figure 1.17. Chemical structure and mechanism of action of the Ir(III) complex, $[Ir(ppy)_2(DMSO)_2].PF_6$.[33]

The study showed that $[Ir(ppy)_2(DMSO)_2].PF_6$ is readily uptaken into live cells (**Fig. 1.18**) and accumulate rapidly (~ 6 min) into the nucleus of cells. The luminescence of the complex is enhanced ~ 200 fold due to reaction with histidine and histidine-containing proteins which displace the DMSO ligands.

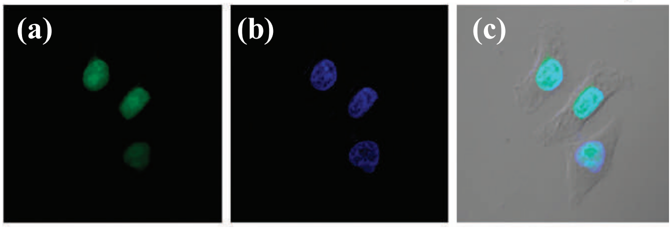

Figure 1.18. Confocal images of living HeLa cells incubated with (a) $[Ir(ppy)_2(DMSO)_2].PF_6$, (b) Hoechst 3328 (nuclear dye) and (c) overlay of the two images.[33]

Further work on similar non-emissive Ir(III) complexes as cellular reaction-based luminescence probes by the Li group were reported in 2013.[34]

The cell imaging properties of Ir(III) complexes can be exploited further and used as targeted sensors for specific ions in cells. One such application of this was reported by Wang and co-workers where an Ir(III) complex was used as a chemodosimeter that displayed high selectivity and sensitivity for Hg^{2+} ions.[35]

The complex on its own displayed weak phosphorescence in aqueous media, however phosphorescence was enhanced in the presence of Hg^{2+} ions due to the thiourea moiety of the complex undergoing intramolecular cyclic guanylation (**Fig. 1.19**).

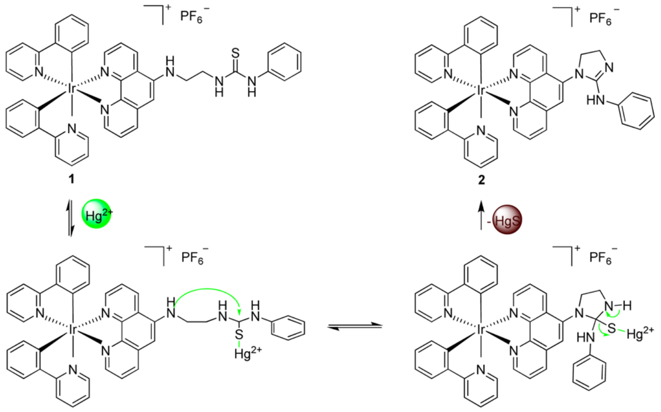

Figure 1.19. Proposed mechanism of cyclic guanylation of the thiourea moiety in the presence of Hg^{2+}. Taken from reference 35.

The study showed that the complex showed selective binding only to Hg^{2+} but none of the other metal ions commonly found in biological systems (Na^+, K^+, Mg^{2+}, Fe^{2+} etc.). This occurred over a wide pH range (pH = 4-10).

Confocal microscopy luminescence images of living cells in the presence and absence of Hg^{2+} showed that the complex retains its Hg^{2+} sensitivity within cells and had good cell permeation (**Fig. 1.20**) making it a good candidate as a chemodosimeter.

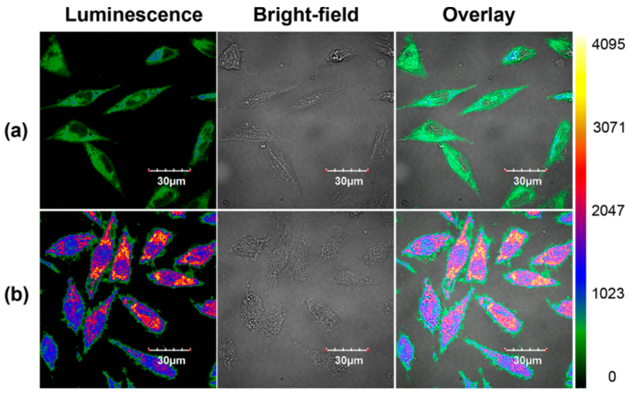

Figure 1.20. Confocal images of human hepatoma cells: (a) incubated with the Ir(III) complex; (b) further incubated with Hg^{2+} ions. Colour bar indicates intensity value. Taken from reference 35.

Stepping away from the imaging properties of Ir(III) complexes, a study in 2012 by Leung *et al*. reported the potential use of an Ir(III) complex as an anti-inflammatory drug.[36] The pro-inflammatory cytokine tumour necrosis factor-α (TNF-α) plays a key role in immunity and inflammation[37] and the dysregulation of TNF-α signalling has been associated with autoinflammatory diseases such as rheumatoid arthritis and Crohn's disease.[38] Synthetic therapeutic agents have been developed that directly bind to TNF-α directly, inhibiting the binding TNF receptor[39] however a disadvantage of these agents is that they cause weakening of the immune defences to infections.

The TNF-α complex consists of a trimer of identical subunits, with a hydrophobic binding site. Leung *et al.* used molecular modelling to investigate how the Λ- and Δ-forms of the Ir(III) complex $[Ir(ppy)_2(biq)]PF_6$ (**Fig. 1.21**) interacted with this site.

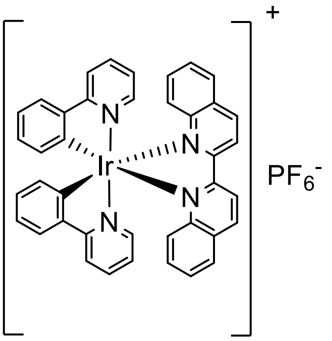

Figure 1.21. Chemical formula of $[Ir(ppy)_2(biq)]PF_6$ (**9**). Only the Λ enantiomer is shown.

The study showed that both the Λ- and -Δ forms of **9** occupy the binding pocket of the TNF-α dimer, thereby preventing the third TNF-α complex from forming the active trimer complex (**Fig. 1.22**).

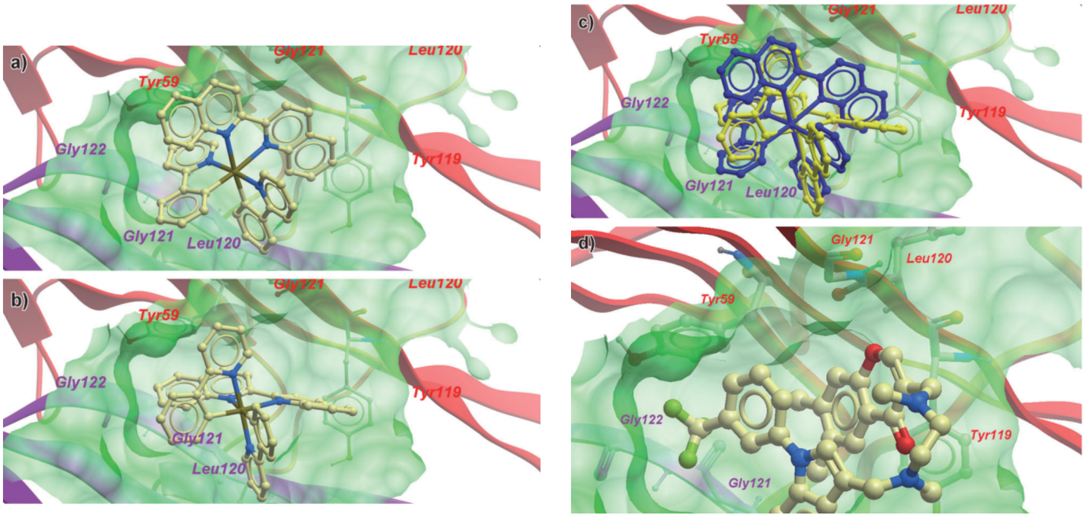

Figure 1.22. Low-energy binding conformations of a) Δ-**9**, b) Λ-**9**, c) superimposed Δ-**9** (blue) and Λ-**9** (yellow) and d) SPD304 bound to TNF-α dimer generated by virtual ligand docking. The two subunits of the TNF-α dimer are depicted in ribbon form and are coloured purple (A subunit) and red (B subunit). The binding pocket of the TNF-α dimer is a translucent green surface. The small molecules are depicted as ball-and-stick models, shown as: C yellow, Ir dark green, O red, N blue and F green. Taken from Ref. 36.

In vitro studies showed $[Ir(ppy)_2(biq)]PF_6$ disrupted the TNF-α-TNF receptor interaction with comparable potency to known organic molecule inhibitors of TNF-α. Structure-activity relationship (SAR) analysis revealed that the inhibition of TNF-α activity is dependent on the shape complementarity between the metal complex and the protein binding pocket rather than unspecific hydrophobic effects.

1.2.3 Other Applications of Luminescent Iridium Compelxes

Other than biological applications, Ir(III) complexes have been shown to be useful for applications in organic light-emitting diodes (OLEDs)[40,41] which have potential applications in flat-panel displays and lighting devices. One of the main requirements for OLEDs doped with phosphorescent emitters is that they should exhibit very high phosphorescence quantum efficiencies,[42] making Ir-based complexes an attractive option. For these devices, cyclometallating aromatic ligands have shown to be useful when assembling such luminescent compounds[43,44] for the following reasons: (i) aromatic cyclometallates tend to form stronger bonds with transition metal elements compared with other organic ligands; (ii) the d-d energy gap is large and therefore less radiationless quenching occurs due to the suppressed population of the higher lying, d-d excited state when there is stronger metal-ligand bonding; (iii) the occurrence of ligand-centred π-π* electronic transitions close to the MLCT state allows tuning of the emission wavelength (as discussed earlier). Blue phosphorescent devices can be produced by adding F groups at the *ortho* and *para* positions in the 2-pyridyl group giving the C^N chelate 2,4-difluorophenylpyridine (as mentioned earlier): the electron-withdrawing nature of the F groups results in a reduced stabilisation of the pyridyl π* orbital, consequently producing a π-π* gap that is substantially higher in energy than that of the parent ppy ligand.[45] The requirement for blue light emitters is essential for OLEDs to succeed in larger markets.[46]

The Ir(III) complex FIrpic (bis(4,6-difluorophenylpyridinato-*N*,C^2)picolinato iridium (III)) has a well-known blue phosphorescence[47] and a study published in 2009 by Lee *et al*. reported the complex [Ir(dfpypy)$_3$] (where dfpypy is a fluorine substituted 2,3'-bipyridine) (**Fig. 1.23**) that had an emission higher in energy than FIrpic.[48] [Ir(dfpypy)$_3$] showed an emission maximum of 438 nm with an additional intense peak at 463 nm in CH_2Cl_2 at room temperature. This shows a significant blue shift compared to FIrpic (**Fig. 1.24**).

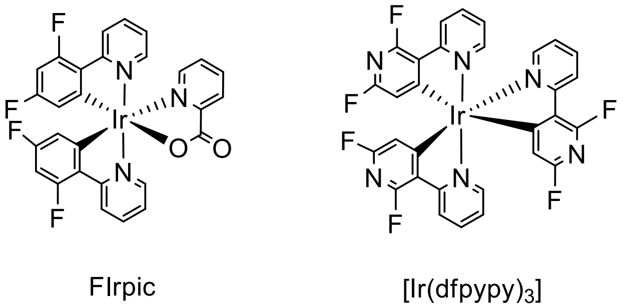

Figure 1.23. Chemical structures of the blue phosphorescent complexes FIrpic and [Ir(dfpypy)$_3$].

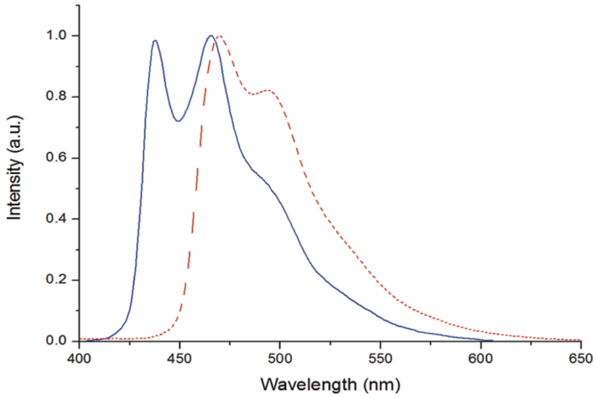

Figure 1.24. Normalised emission spectra of [Ir(dfpypy)$_3$] (blue) and FIrpic (red) in CH_2Cl_2 at room temperature.[48]

The blue emission band observed at room temperature for [Ir(dfpypy)$_3$] was attributed to the $^3\pi$-π* excited state with a contribution from the MLCT transition.[49] Moreover the complex also exhibited a remarkably high quantum yield of 77% in degassed CH_2Cl_2 at room temperature. This can be attributed to the improvement of the molecular rigidity (compared to FIrpic) which improves the luminescence quantum yield.[50] The blue nature of emission and high quantum yield of the complex makes it a promising compound for use in OLEDs.

Another example of a series of highly phosphorescent Ir complexes was reported by Grätzel *et al.* in 2003 for their potential application in OLED devices.[51] The complexes TBA[Ir(ppy)$_2$(CN)$_2$] (**10**), TBA[Ir(ppy)$_2$(NCS)$_2$] (**11**) and TBA[Ir(ppy)$_2$(NCO)$_2$] (**12**) (TBA = tetrabutylammonium cation) were developed and their photoluminescence properties were reported.

The emission spectra at 298 K in argon-degassed CH_2Cl_2 showed emission maxima at 470 nm, 506 nm and 538 nm for complexes **10**, **11** and **12** respectively, with longer lifetimes (0.8 µs - 3.4 µs) when compared to air-equilibrated CH_2Cl_2 solutions (70 ns - 90 ns) indicating emission from a triplet excited state.

A schematic representation of HOMO and LUMO orbitals of the complexes is shown in **Fig. 1.25**.

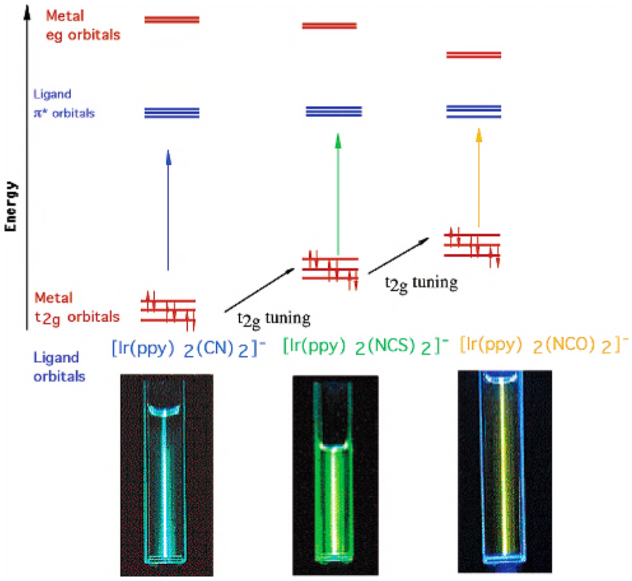

Figure 1.25. Schematic drawing of HOMO and LUMO orbitals for complexes **10-12** and their photoluminescence properties, obtained by exciting at 415.4 nm using a krypton laser.[51]

Blue, green and yellow emission was observed for complexes **10**, **11** and **12** respectively. Ligands such as CN^- increase the energy gap between the LUMO of the ppy ligand and the metal t_{2g} orbitals resulting in a blue shift of the lowest MLCT absorption and emission maxima. Moreover the high field strength of cyanide ligands inhibits nonradiative pathways by increasing the LUMO of the ppy ligand and empty metal e_g orbitals, and as a result 97% quantum yields in solution at room temperature were observed.

Another type of OLED is the light-emitting electrochemical cell (LEC), which makes use of ionic charges to facilitate electronic charge injection from the electrodes into the organic molecular semiconductor eliminating the need for a multi-layered structure for charge injection and transport required in OLEDs.[52] This is a promising alternative to OLEDs, especially for large-area lighting applications.[53]

In 2006 Grätzel *et al.* synthesised the novel green-blue phosphorescent cationic complex, [Ir (2-phenylpyridine)$_2$(4,4'-(dimethylamino)-2,2'-bipyridine)]PF_6 (**Fig.**

1.26) that exhibited photoluminescence quantum yields of 80 ± 10% with an excited-state lifetime of 2.2 μs in a CH_2Cl_2 solution at 298 K.[54]

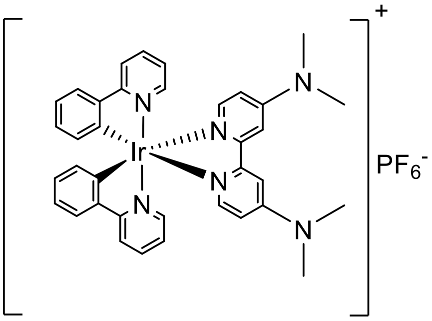

Figure 1.26. Chemical structure of [Ir bis(2-phenylpyridine)(4,4’-(dimethylamino)-2,2’-bipyridine)]PF_6.

The complex was used in the fabrication of single-layer light-emitting electrochemical cells. The LEC device emitted green-blue light at a bias as low as 2.5 V. The high quantum yields were attributed to the close-lying π-π* and MLCT states associated with 2-phenylpyridine and 4,4’-(dimethylamino)-2,2’-bipyridine which enhanced excited-state decay through radiative pathways.

1.3 Luminescence of Lanthanide Complexes

1.3.1 Overview of f-block Systems

There has been a long-standing interest in lanthanide luminescence due to the vast applications attributed to the unique photophysical properties of these elements. Lanthanides have shown particular use in applications such as luminescent sensors in immunoassays.[55,56] The development of this technology resulted in a variety of applications in biology, biotechnology and medicine including analyte sensing,[57] tissue and cell imaging[58] and monitoring drug delivery.[59] Growing technology outside of biology has also involved the use of lanthanides, from Er-doped optical fibres for telecommunications[59] to lanthanide-doped OLEDs[60] emitting in the NIR[61] or in the visible regions.[62] A pioneering innovation of lanthanide luminescence was the discovery of the highly emissive Y_2O_3 : Eu(III) material,[63] used as the phosphors for cathode-ray tubes and fluorescent lamps, which are still heavily used today.[64] Even the first red phosphor that enabled the development of the colour television screens can be attributed to europium-doped yttrium vanadate.[65]

Lanthanides generally exist as trivalent cations with an electronic configuration of $[Xe]4f^n$ where $n = 0\text{-}14$ and it is the transitions of the f-electrons that result in their interesting photophysical properties. These configurations are responsible for an opulent number of electronic levels, characterised by three quantum numbers, S, L and J within the Russell-Saunders coupling scheme, which can be used to describe the energy levels of the ions. The partial energy level diagrams are given in **Fig. 1.27**.

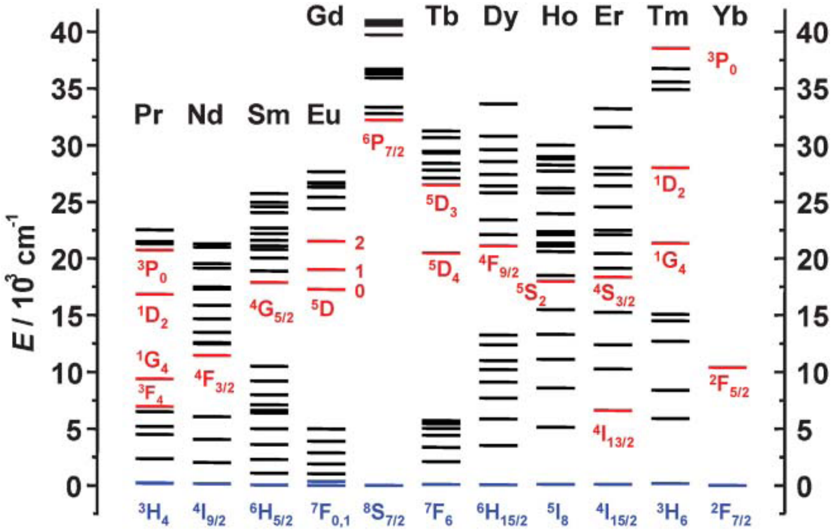

Figure 1.27. Partial energy level diagram for the lanthanide(III) aqua ions[66,67]. The main luminescent levels are shown in red while the fundamental levels are shown in blue.[67]

The majority of Ln(III) transitions occur from levels within the 4f subshell, however the f → f promotions are Laporte forbidden as well as being forbidden by electric dipole selection rules. Moreover the 4f orbitals are radially contracted to the extent that the filled 5s and 5p orbitals largely shield 4f electrons from their chemical environments resulting in very low molar absorption coefficients (typically < 3 M^{-1} cm^{-1}) making direct photoexcitation of lanthanide ions difficult. As a result of their small interaction with their surroundings, f → f transition energies in Ln(III) compounds are well defined and lead to sharp bands in their electronic absorption spectra and line-like bands in the emission spectra (**Fig. 1.28**).[68] The forbidden nature of the transitions also results in long radiative lifetimes up to the millisecond timescale. The excited state levels of Ln(III) ions are usually populated as a result of energy transfer from an attached organic receptor capable of absorbing energy and partially transferring some of this energy (antenna effect) from the triplet level of the receptor to the excited level of the Ln(III) ion.[69] The excited level of the Ln(III) ion can be further deactivated either radiatively with the emission of light, or non-radiatively by energy degradation to the vibrations of surrounding molecular groups.

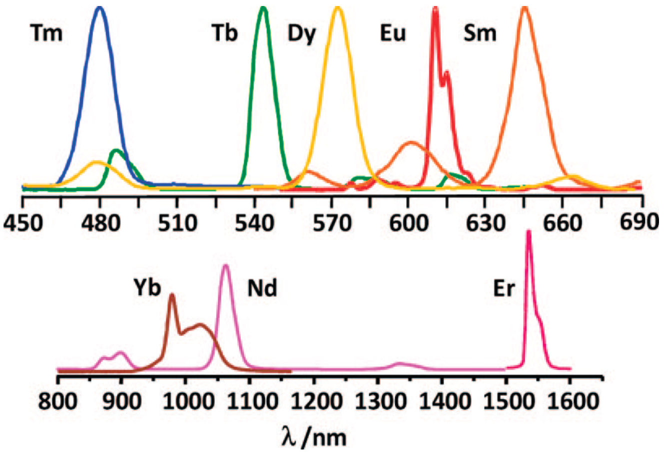

Figure 1.28. Luminescence spectra of some lanthanide tris(β-diketonates).[69]

1.3.2 Lighting Lanthanide Ions *via* Energy-Transfer

In 1942 Weissman discovered the antenna effect, where Ln(III) excited states can be populated by energy-transfer from excited states of the bound ligands.[70] This phenomenon can be illustrated by a Jablonski diagram (**Fig. 1.29**).

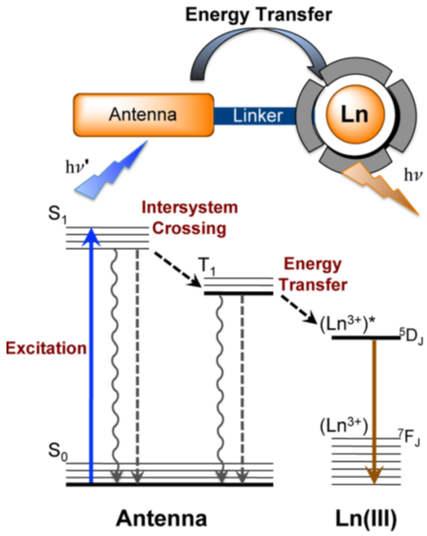

Figure 1.29. Diagram showing the processes involved in sensitising a lanthanide complex. S = singlet state, T = triplet state. Back energy-transfer processes are not shown.[71]

A classic example of a system using the antenna effect was demonstrated by Lehn and co-workers in 1987, when Eu(III) and Tb(III) ions were incorporated into cryptates (**Fig. 1.30**).[72]

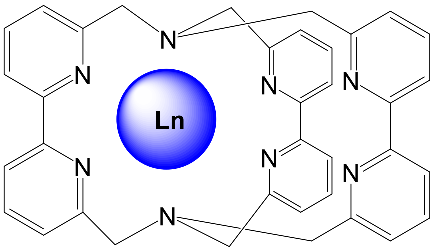

Ln = Eu^{3+}, Tb^{3+}

Figure 1.30. Structure of the cryptates incorporating Ln(III) ions reported by Lehn and co-workers.

The intramolecular energy-transfer from π-π* excited states of the ligands to the excited levels of Eu(III) and Tb(III) resulted in sensitised luminescence (with lifetimes of 1-2 ms) from the Ln units. As a result of these long lifetimes, the Eu(III) cryptate complex has been commercially developed by CisBio for use as Homogeneous Time Resolved Fluorescence (HTRF) assays in biology.

Other examples of exploiting the antenna effect have been reported by the Raymond group where lanthanide complexes based on 2-hydroxyisophthalamide chelating units were reported (**Fig. 1.31**).[73]

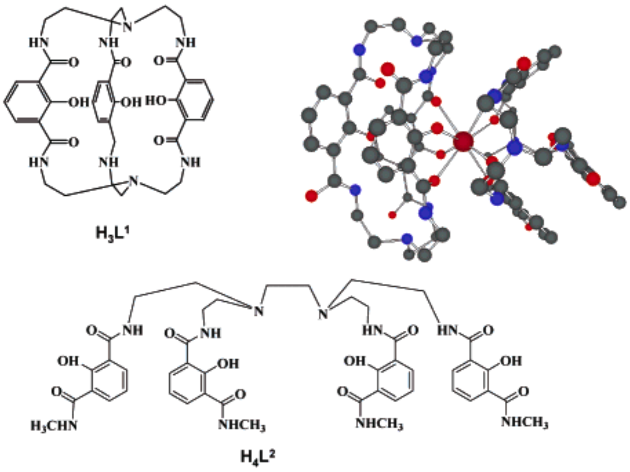

Figure 1.31. (Left) The ligand structures and (upper right) the single crystal X-ray structure of $[Eu(H_2\mathbf{L}^1)_2]^+$.[73]

Luminescence was observed from several Ln(III) ligands due to ligand-to-lanthanide energy transfer (**Fig. 1.32**).

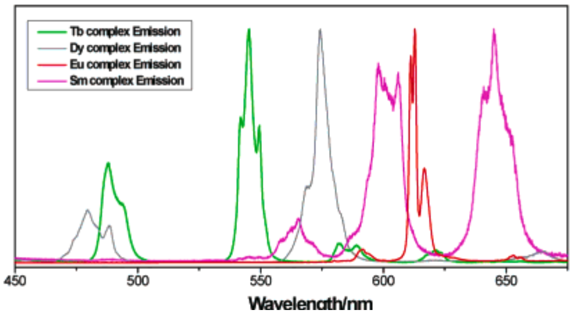

Figure 1.32. Normalised emission spectra of $[Ln(H_2\mathbf{L}^1)_2]^+$ where Ln = Sm, Eu, Tb and Dy. $\lambda_{ex} = 350$ nm.[73]

The complexes displayed high quantum yields (Φ ~ 0.6). These high quantum yields, combined with their high solubility and stability in water at physiological pH, make them ideal candidates for use in bioanalytical applications.

The process of energy-transfer to lanthanides is quite intricate and several mechanisms may be involved. Specifically it is likely that a combination of both Dexter and Förster mechanisms are involved.[74,75,76] Förster energy-transfer occurs by a long-range mechanism based on Columbic interactions and occurs through space without requiring any electronic coupling between donor and acceptor. The rate of this is proportional to r^{-6} (where r is the separation distance between the donor and acceptor units). This mechanism is shown to be efficient when the radiative transitions corresponding to the deactivation and the excitation of the two partners both have high oscillator strength.[77] Singlet-singlet energy-transfer between donor and acceptor is shown in **Fig. 1.33**.

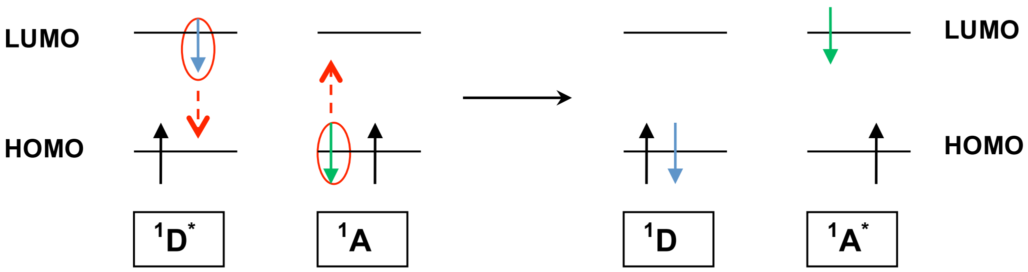

Figure 1.33. Schematic representation of Förster mechanism for singlet-singlet energy-transfer between a donor and acceptor. $^1D^*$ = excited singlet level of the donor, ^1D = singlet donor level, $^1A^*$ = excited singlet level of the acceptor, ^1A = singlet acceptor level.

The short-range Dexter energy-transfer has a rate that is proportional to e^{-r} and requires orbital overlap between donor and acceptor. The exchange mechanism can be enhanced by the superexchange mechanism when there is overlap between the orbitals of the donor and acceptor. Triplet-triplet Dexter energy-transfer between a donor and acceptor is shown in **Fig. 1.34** and requires physical exchange of two electrons which is why orbital overlap between donor and acceptor is required.

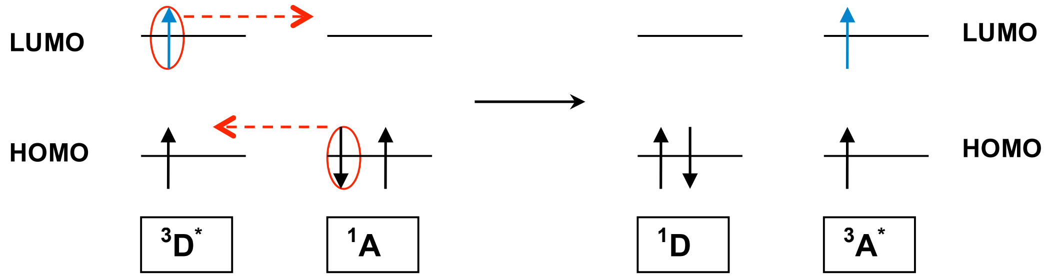

Figure 1.34. Schematic representation of Dexter mechanism of triplet-triplet energy transfer between a donor and acceptor. $^3D^*$ = excited triplet level of the donor, ^1D = singlet donor level, $^3A^*$ = excited triplet level of the acceptor, ^1A = singlet acceptor level.

Prediction of the mechanism and efficiency of the energy-transfer involved is not obvious as it is specific to the type of donor, lanthanide ion acceptor, the ligands used and the inter-chromophore distance. The efficiency relates to the spectroscopic overlap between the absorption of the energy of the donor and the emission of the f-f level of the accepting lanthanide.[78] When considering Förster energy-transfer, there is poor spectroscopic donor/acceptor overlap as the f-f transitions are so weak, resulting in very low-intensity bands in the absorption spectra. However, when considering Dexter energy-transfer, overlap is good as it is necessary to normalise the f-f transitions, so their low intensity no longer matters. Thus when considering efficiencies in terms of orbital overlap, Dexter energy-transfer can show higher efficiency than Förster energy-transfer.

However, Förster energy-transfer is more efficient at longer distances than Dexter mechanism, as efficiency of Dexter mechanism decays exponentially with an increase in inter-chromophore distance; hence Förster energy-transfer shows better efficiency at longer distances, as r^{-6} decays more slowly than e^{-r}.

In addition, other types of excited states can funnel energy to the Ln(III) ions: singlet $^1S^*$, triplet $^3T^*$, ILCT, LMCT, ^{3}MLCT, 4f-5d and sometimes 4f states from other lanthanide ions.[74] These energy donor levels always need to be of higher energy than the emissive level of the Ln(III) acceptors otherwise back energy-transfer occurs resulting in low quantum yields and short, temperature dependent lifetimes. For Eu(III) and Tb(III) a minimum donor/acceptor energy difference at room temperature to prevent back energy-transfer (BET) is around 2000 cm^{-1}. Efficient ISC takes place when the energy difference between the singlet and triplet states is around 5000 cm^{-1} therefore ligand designers follow the following rules:[74] ΔE ($^1S^*$-$^3T^*$) ≈ 5000 cm^{-1} and ΔE ($^3T^*$-Ln* emissive level) around 2500 – 3000 cm^{-1}.

As well as mastering electronic excitation of lanthanide ions, competing non-radiative deactivation of the excited states has to be minimised: such deactivation routes can include vibrational processes and photoinduced electron transfer.[79]

Deactivation of excited states through molecular vibrations should be considered in the design process. One well known process is the nonradiative vibrational energy-transfer process to O-H oscillators of coordinated H_2O molecules both in the inner and outer coordination sphere. This process has the effect of reducing the quantum yield (Φ_{Ln}) of the Ln(III) emission. Although this leads to loss of luminescence, one advantage arises from this process, and this is assessing the number of water molecules (q) that are in the inner coordination sphere of the Ln(III) ion. This is achieved by assuming that O-D oscillators do not contribute to the deactivation and that all other deactivation processes are the same in H_2O and D_2O. The value of q can therefore be quantified by **Equation 1.01** (the Horrocks' equation) by measuring the emission lifetimes in both H_2O and D_2O:[80,81]

$$q = A \cdot (k_{H2O} - k_{D2O} - B) - C$$

Equation 1.01. A, B, and C are known Ln-dependent parameters. The corrective factor B accounts for the presence of other deactivating vibrations such as N-H or C-H oscillators.

A good way to minimise vibration-induced deactivation processes is to design a coordination environment, free from high-energy vibrations and protecting the Ln(III) ion from solvent interaction by steric crowding. This environment would also contribute to reduce collision-induced deactivation in solution.[67] An example of this was shown by Pikramenou *et al.* in 2007 where the use of fully fluorinated imidodiphosphinate shells was implemented for the visible- and NIR-emitting lanthanides. Very high luminescence lifetimes in deuterated acetonitrile were observed in the case of (Nd, Er and Yb), due to the absence of C-H and O-H vibrations that would normally quench lanthanide emission.[82]

The complexes were formed by combining the lanthanides with three *N*-{*P*,*P*-di-(pentafluorophinoyl)}-*P*,*P*-dipentafluorophenylphosphinimic acid (HF_{20}tpip) ligands (**Scheme. 1.02**).

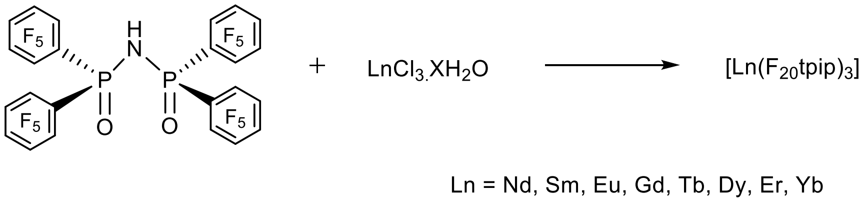

Scheme 1.02. Addition of HF_{20}tpip with Ln(III) to form $[Ln(F_{20}(tpip)_3]$.

1.3.3 Exploiting Lanthanide Luminescence for Biological Applications

The long luminescence lifetimes, high quantum yields, sharp line-like emission features and large Stokes shifts for luminescence of lanthanide complexes can be advantageous for their uses in biological applications, especially as imaging agents.

There have been applications of lanthanide complexes as fluorescence resonance energy transfer (FRET) donors for the study of extracellular processes and use as cell imaging agents.[83]

In 2006, Parker *et al*. reported on the behaviour of a cyclen based Eu(III) complex $[EuL]^{3+}$ (**Fig. 1.35**) that selectively stained cell nucleoli.[84]

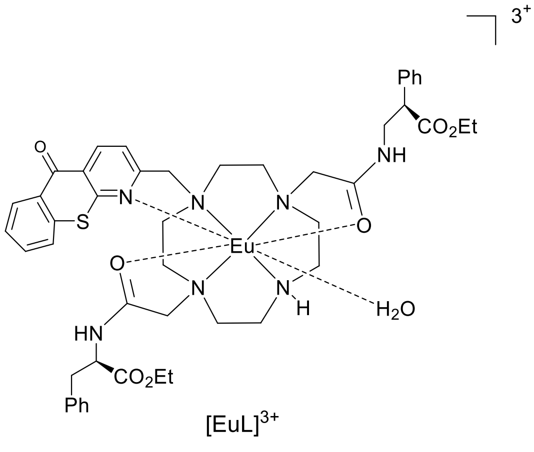

Figure 1.35. Chemical structure of $[EuL]^{3+}$ reported by Parker *et al.* as a nucleolar stain.

The complex $[EuL]^{3+}$ was shown to permeate into NIH 3T3, HeLa and HDF cells. Red luminescence images of cells were achieved at concentrations from 100 μM, where over 90% of the cells were considered healthy after a 24 h period, which was evident by the observation of the nucleolus over this period of time.

Colocalisation with SYTO RNA-Select dye confirmed the location of $[EuL]^{3+}$ in the cells (**Fig. 1.36**).

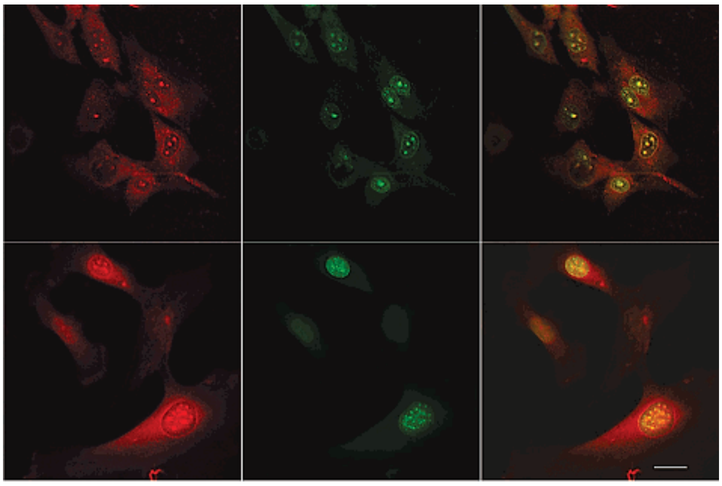

Figure 1.36. Colocalisation of $[EuL]^{3+}$ and SYTO RNA-Select dye: upper row, images by live cell loading $[EuL]^{3+}$ and SYTO dye; lower row, images by fixed cell loading; left column, Eu(III) luminescence; middle column, SYTO dye fluorescence; right column, merged image.[84]

More recently, the Parker group reported emissive europium complexes for live cell imaging.[85] All complexes reported were structurally related and were based on a triazacyclononane core containing three pyridyl-methylphosphinate groups. An example of one of these complexes, which bears ancillary glucamide groups, is given in **Fig. 1.37**.

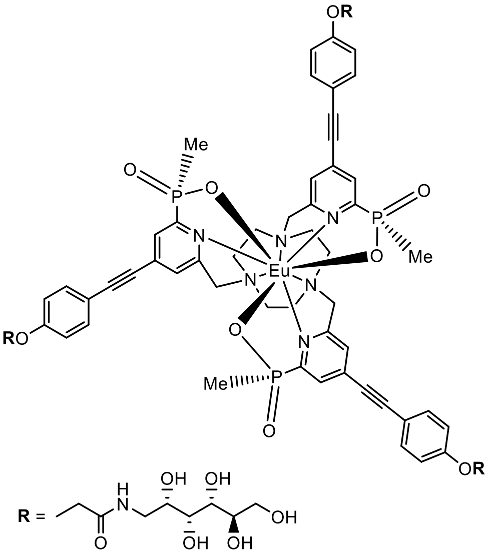

Figure 1.37. Structure of $[Eu.L^2]$ reported by the Parker group.

The cellular behaviour of [Eu.L^2] showed rapid intake into CHO and NIH-3T3 cells (**Fig. 1.38**). Co-localisation studies showed that the complex localised in the mitochondria of cells.

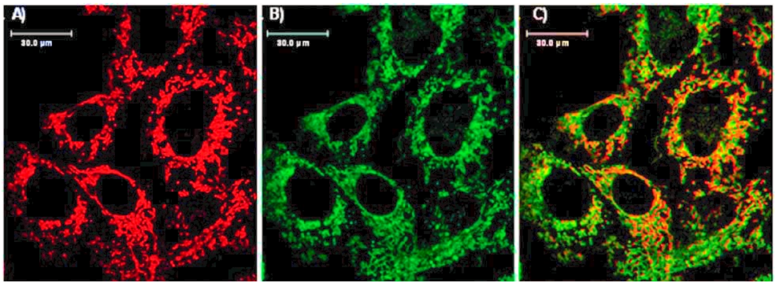

Figure 1.38. Laser scanning confocal microscopy images of: (a) [Eu.L^2] in NIH-3T3 cells (λ_{ex} = 355 nm, λ_{em} = 605-720 nm); (b) MitoTracker Green; (c) overlay of the two images. Taken from reference 85.

The study showed that by modifying the R groups of the complexes, different organelles within the cell could be targeted, thus allowing selective staining. The intense and long-lived luminescent mature of Eu allows improvements to current fluorescent organic dyes.

Another example for the use of lanthanides as luminescent biological probes was reported by Pierre and co-workers where a [Tb•L] complex (**Fig. 1.39**) was used for time-gated detection of adenosine triphosphate (ATP), adenosine diphosphate (ADP) and adenosine monophosphate (AMP).[86]

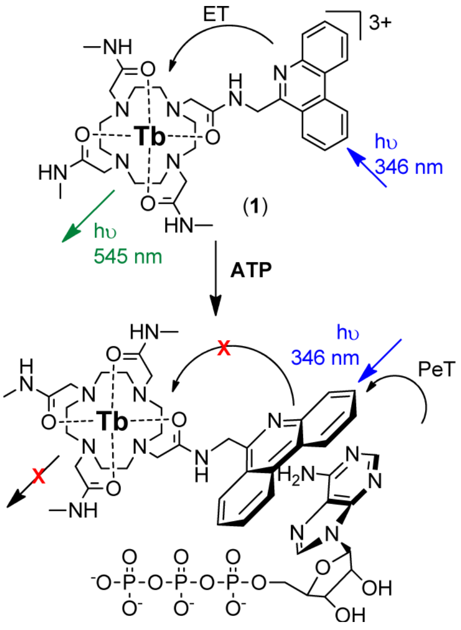

Figure 1.39. Chemical structure of the [Tb•L] complex and mode of action for sensing ATP. PeT = photoinduced electron-transfer. Taken from reference 86.

Understanding enzymatic reactions involving ATP hydrolysis such as kinases are important in the field of cancer therapy as it helps develop kinase inhibitors.[87,88]
[Tb•L] displayed strong luminescence in the absence of adenosine nucleotides (ATP, ADP and AMP) at concentrations within the cellular range. In the presence of the nucleotides, stacking occurs on the phenanthridine unit, resulting in PET quenching of the luminescence. Moreover the probe showed different binding affinity to ATP, ADP and AMP in buffered media allowing them to be readily distinguished by studying their Stern-Volmer relationships, where a higher Stern-Volmer constant was observed when there was a greater negative charge on the nucleotide. The work is ongoing and the group are currently investigating the application of [Tb•L] in high-throughput screening and kinetic studies of inhibition of kinases.

A novel use of a Eu(III) complex for imaging of damaged bones was reported by Gunnlaugsson *et al*. in 2009.[89] Microcracks in bones can appear with lengths of around 25-300 μm as a result of stress or repetitive loading and lead to medical conditions such as osteoporosis.[90] Imaging of damaged bone can be troublesome so the development of contrast agents capable of penetrating the bone matrix could help understand the complex morphology.[91] Gunnlaugsson *et al*. developed the complex

Eu.Na (**Fig. 1.40**) that contained a naphthalene antenna capable of sensitising the Eu(III) $^5D_0$ excited state and three iminodiacetate moieties capable of binding to Ca(II) sites within the hydroxyapatite lattice of the bone.

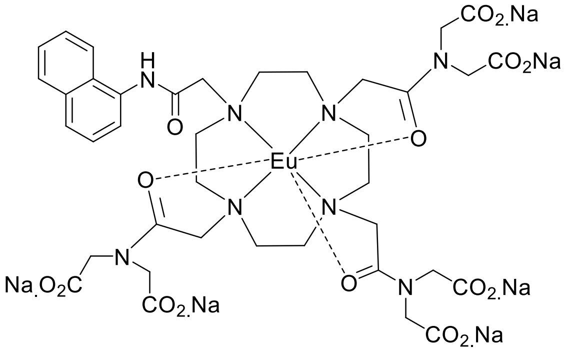

Eu.Na

Figure 1.40. Chemical structure of the complex Eu.Na.

For the imaging of bone cracks, bovine tibia specimens were polished and then scratched to expose fresh Ca(II) sites which were then treated with the Eu.Na complex in aqueous solution (1 x 10^{-3} M) for a period of 0 to 24 h. Steady-state fluorescence showed Eu(III) emission from the scratched areas were more intense than that of the undamaged surface and the sample was then imaged using confocal fluorescence laser-scanning microscopy (**Fig. 1.41**).

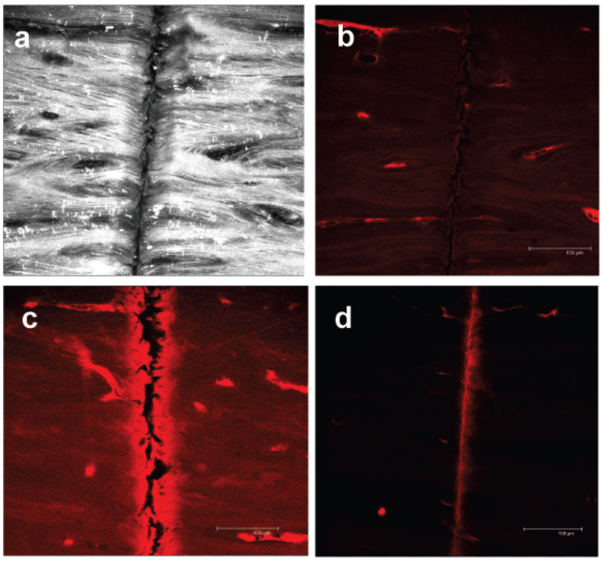

Figure 1.41. Confocal laser-scanning microscopy images of bone sample immersed in a 1 x 10^{-3} M solution of Eu.Na (pH 7.4, 20 mM HEPES, 135 mM KCl): (a) Reflected light image: 0 h, (b) Control, (c) 4 h, (d) 24 h. Bar = 150 μm.[89]

Results showed that emission contrast between healthy bone and scratched bone was clearer with increasing Eu.Na exposure time. It was shown that the complex selectively binds to the bone through chelation from the iminodiacetate moieties to the Ca(II) sites within the cracks making these types of compounds potential applicants as bone imaging agents.

1.3.4 Other Applications of Lanthanides

Like Ir(III) systems, lanthanides too can be used in OLEDs due to their photophysical properties described earlier, which leads to improved colour saturation and higher efficiency of the OLED.[92,93]

Lanthanide luminescence is highly monochromatic (as a result of the sharp emission bands), resulting in better colour saturation than when organic molecules are used as the emissive material. Spin statistics state that the efficiency of OLEDs based on fluorescent emitters are limited to 25% as the triplet states (75% probability of being generated) are not fluorescent. However when lanthanide complexes are used as the luminescent components, this limitation disappears as the excitation energy from the ligand can be transferred from either an excited singlet or triplet to the Ln ion. One of the first demonstrations of a lanthanide-based OLED was by Kido *et al.* in 1990 where green electroluminescence of the ternary complex $Tb(acac)_3(phen)$ was observed.[94] The OLED had a basic structure composed of ITO/TPD/$Tb(acac)_3(phen)$/Al and had brightness of 7 cd m^{-2} at a current density of 0.4 mA cm^{-2}. This work was a stepping-stone for the synthesis of new lanthanide-containing compounds with improved characteristics and optimisation of OLED architectures.[92,93,95]

Recently there has been growing interest in near-infrared (NIR) luminescence from lanthanide ions due to potential applications in optical communications[96], bioimaging[97] and sensors.[98] Lanthanides that exhibit narrow-line emission in the NIR range ([Ln(III)] = Pr, Nd, Ho, Er, Tm, Yb) are of special interest. In 2011, Katkova *et al.* developed NIR OLEDs based on NIR electroluminescent complexes $Ln_2(OON)_6$ of Pr, Nd, Ho, Er, Tm, and Yb with N,O-chelating ligands (where OON = 2-(2-benzoxyazol-2-yl)phenolate) and $Ln_2(SON)_6$ (where SON = 2-(2-benzothiazol-2-yl)phenolate).[99] The solid-state electronic absorption and electroluminescence spectra showed long-wavelength 4f-4f transitions making these complexes suitable as NIR-emitting materials in OLED devices. The best results were achieved using Nd(III) and Yb(III) complexes.

Another recent study of Ln(III) systems in NIR OLEDs was reported by Bian *et al.* where Nd(III), Er(III) and Yb(III) complexes were designed and synthesised based on a tridentate monoanionic N,N,O-ligand 6-(pyridine-2-yl)-1,5-naphthyridin-4-ol (PND).[100] Photophysical studies of the complexes and ligand revealed that PND had a suitable energy level to sensitise the NIR emitting lanthanide ions. $Yb(PND)_3$ had its highest photoluminescence quantum yield (0.9%) in a mixture of acetonitrile and methanol solution (10 : 1 v/v, 10^{-4} M). The compounds displayed high decomposition (T_d) and glass transition (T_g) temperature up to 420 and 265°C, respectively. This implies a great advantage of constructing the electronic devices via vacuum deposition method. NIR OLEDs were constructed with maximum NIR irradiance and maximum external quantum efficiency of 25 μW cm^{-2} and 0.019% for Nd(III), 0.46 μW cm^{-2} and 0.004% for Er(III) and 86 μW cm^{-2} and 0.14% for Yb(III), respectively.

1.4 Sensitisation of Lanthanide Luminescence *via* d → f Energy-Transfer

Recently there has been much attention for the use of d-block chromophores as antenna groups to generate luminescence from Ln(III) centres *via* d → f energy-transfer.[101] The basic architecture of these systems is shown in **Fig. 1.42** below.

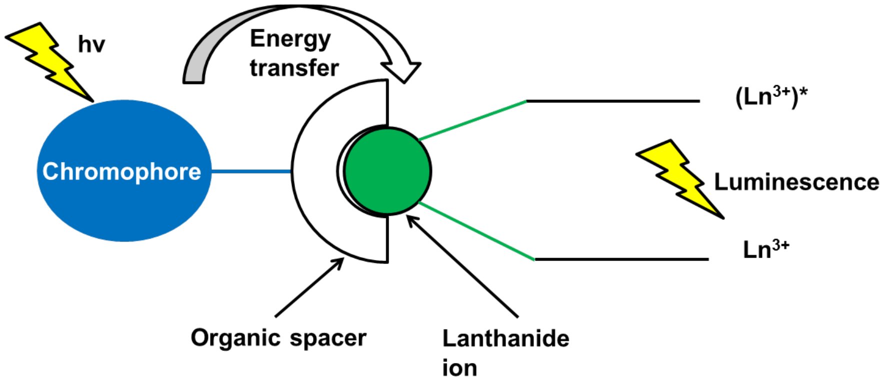

Figure 1.42. The basic architecture for photosensitising Ln(III) systems *via* d → f energy transfer.

Excitation of the Ln(III) ion can be achieved by connecting a d-block chromophore to an organic ligand, which is then connected to a lanthanide ion. This organic ligand binds both metals and also facilitates energy transfer from the d-metal to the lanthanide centre upon photoexcitation under UV light by providing a 'conducting' pathway. This d → f energy transfer depends on how effective the d-metal chromophore is as an energy-donor to the Ln(III) ion. These conditions are; (i) The ^{3}MLCT state of the donor must lie at least 2000 cm^{-1} above the f-f energy accepting level, or thermally-activated back energy-transfer will occur resulting in loss of luminescence;[102] (ii) the emission spectrum of the metal complex used as the donor must have a good overlap with the absorption spectrum of the f-block acceptor unit to ensure quick transfer of the excitation energy to the Ln(III) ion; and (iii) there needs to be a long-lived excited-state lifetime of the donor, because although d → f energy transfer may be fast, it may be that only an insignificant amount of the excited energy is transferred if other non-radiative decay pathways in the donor are competitive.[103]

Research by Faulkner and co-workers demonstrated Re-Ln hybrid complexes containing triazole-bridged systems.[104] Their structures are given in **Fig. 1.43** below.

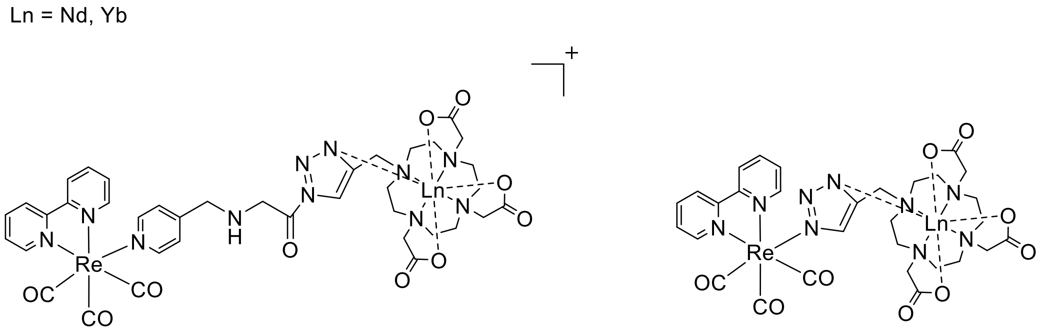

[ReL^1.Ln]

[ReL^2.Ln]

Figure 1.43. Re-Ln complexes bridged by triazole ligands.

The Re(I)-diimine chromophore acts as an effective sensitiser of Nd and Yb NIR emission. The triazole-bridged unit facilitates energy-transfer from the Re-chromophore to the lanthanides, where there was also a weak affinity of the N atom of the triazole to the Ln centre.

This study highlighted the significance of the donor/acceptor spectral overlap in the role of energy-transfer. Although sensitisation of both Nd and Yb was achieved, in the case of the [ReL^2.Yb] complex, a short-lived emission band was observed which was attributed to the Re ^{3}MLCT emission, whereas for [ReL^2.Nd] this band was not observed. This suggests sensitisation of Nd is more efficient than Yb, suggesting there is better spectral overlap of the Re unit with the high-energy excited states in the Nd f-f manifolds.

Another example of a Ln sensitiser using a d-block chromophore was demonstrated by Rajagopal and co-workers.[105] In this study a ruthenium complex based on a 1,3-bis(1,10-phenanthroline-[5,6-d]-imidazol-2-yl)benzene architecture (**Fig. 1.44**) was synthesised and used as a sensitiser of NIR emission from Nd, Yb and Er.

Ln = Nd, Yb, Er

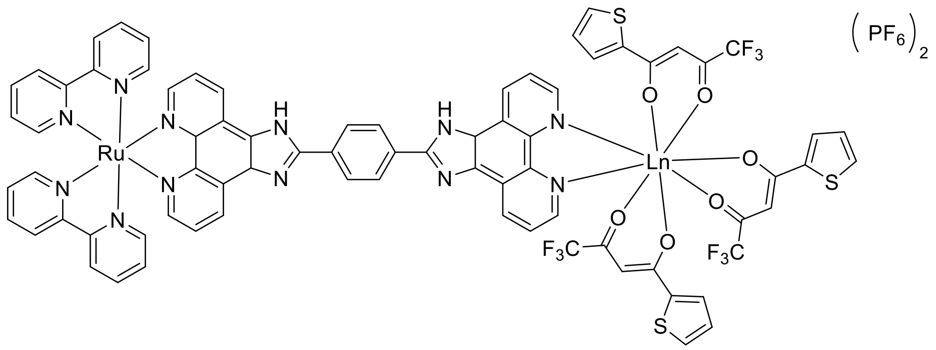

[RuL.Ln]

Figure 1.44. Structure of the NIR sensitiser [RuL.Ln].

The free [RuL] complex was titrated with Ln(tta)$_3$ (tta = thenoyl(trifluoro)acetone) (Ln = Nd, Yb, Er) in CH_3CN. Luminescence measurements showed that the Ru^{II}-based luminescence is partially quenched in the presence of [Ln(tta)$_3$] and quenching of the emission is greater with an increase in concentration of the lanthanide complexes. Observation of NIR emission confirmed that Ru acts as a sensitiser for Ln luminescence by energy-transfer from the ^{3}MLCT state to the emissive excited states of the Ln ions.

The energy-transfer in this case is facilitated by the conjugated bridging ligand and a short metal-metal distance, making both Dexter and Förster energy-transfer feasible.

When looking at the mechanism in which d → f energy-transfer occurs, it is not always predictable. Research from Ward *et al.* has shown that d → f ET can occur *via* both Dexter and Förster mechanisms in Os(II) → Nd(III) systems.[103] Here, an osmium complex (**Fig. 1.45**) was synthesised and Nd(NO$_3$)$_3$ hydrate was bound to the pendant macrocyclic site.

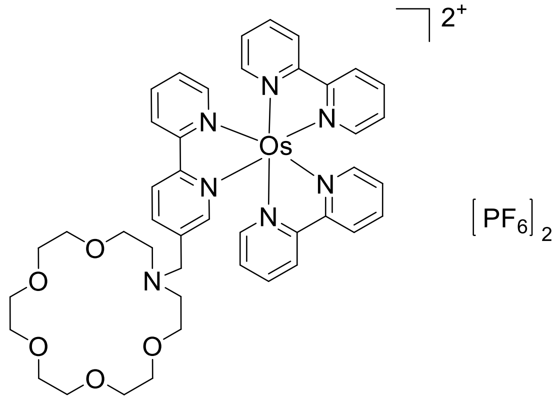

Figure 1.45. Osmium (II) complex used to study the photophysical properties of d □ f energy-transfer with $Nd(NO_3)_3$.

$Nd(NO_3)_3$ was bound to the aza-crown macrocycle of the complex in **Fig. 1.45** and the mechanisms of the energy-transfer were studied. It was reported that a combination of Dexter and Förster mechanisms were involved as the inter-chromophore distance was significantly higher than the Förster critical transfer distance, therefore requiring additional contribution from Dexter energy-transfer, achieved by weak electronic coupling through the saturated linkage.

The mechanism and efficiency of energy-transfer involved is specific to the type of d-metal donor, lanthanide ion acceptor, the ligands used and the inter-chromophore distance. The efficiency relates to the spectroscopic overlap between the absorption of the energy donor d-metal and the emission of the f-f level of the accepting lanthanide. When considering Förster energy-transfer, efficiency is related to donor-to-acceptor separation distance and is given in **Equation 1.02**:

$$E = \frac{1}{1 + (\frac{r}{R_0})^6}$$

Equation 1.02. E = efficiency of the energy-transfer, r = donor-to-acceptor separation distance and R_0 = distance at which the efficiency of energy transfer is 50%.

There is poor spectroscopic overlap as the f-f transitions are so weak, resulting in very weak f-f absorption bands. However, when considering Dexter energy-transfer, overlap is good as it is necessary to normalise the f-f transitions, resulting in large bands in the spectra. The rate constant is given in **Equation 1.03**:

$$k_{dexter} = K\,J\,\exp\left(\frac{-2R_{DA}}{L}\right)$$

Equation 1.03. J = spectral overlap integral, R_{DA} = distance between donor and acceptor, L = sum of the van der Waals radius and K is related to orbital interactions.

Thus when considering efficiencies in terms of orbital overlap, Dexter energy-transfer has a big advantage compared to Förster energy-transfer. However, as mentioned earlier, Förster energy-transfer shows better efficiency at longer distances, as r^{-6} decays more slowly than e^{-r}.

Interesting findings again published from Ward *et al.* highlighted the unpredictability of the type of ET mechanism involved. Here they studied ET of a Ru(II) → Nd(III) system,[106] shown in **Fig. 1.46**.

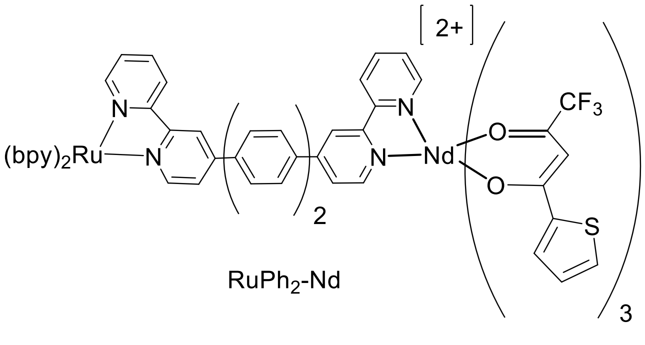

Figure 1.46. Ruthenium (II) complex used to study the photophysical properties of d→ f energy transfer with Nd(III) thenyl-trifluoroacetone.

The complex shown has a donor-acceptor distance of 20 Å. It would therefore be expected that Dexter energy-transfer is very unlikely to occur, hence crediting energy transfer to the Förster mechanism. However, results showed that the energy-transfer occurred by the Dexter mechanism, which was made possible by the presence of the long conjugated bridge, which permitted electronic coupling despite the large distance.

This research shows that the energy-transfer mechanisms involved for d → f systems are not yet fully understood to the extent that they can be easily predicted. However the presence of a conjugated spacer ligand between the d-metal donor and Ln(III) acceptor maximises efficiency of Dexter energy transfer due to good orbital overlap, even if the inter-chromophore distance is large. As the mechanism of energy-transfer is a complicated process, it is highly probable that the energy-transfer mechanisms involved for the Ir(III)-Ln complexes discussed later in this report, will be a combination of Dexter/Förster processes and/or a redox-based mechanism, in which the first step is photoinduced electron-transfer from the excited state of the d-block unit to the Ln(III), easily reducing it to Ln(II) or to the coordinated ligand to give a radical anion.

Iridium chromophores demonstrate many desirable properties as energy donors to lanthanide ions compared with traditional organic chromophores, such as: (i) their ability to be tuned synthetically to emit across the range of the visible spectrum (as discussed earlier); (ii) their long-lived excited states arising from ^{3}MLCT transitions, increasing the probability of energy transfer; (iii) their strong chemical stability during photoexcitation and kinetic inertness and (iv) their luminescence which results in the ability to monitor energy transfer to the Ln(III) $4f^n$ manifolds.[101,107]

Generating luminescence from lanthanides that emit in the visible region requires a chromophore whose excited state itself has a high energy. For example, Eu(III) has an emissive excited state at $^5D_0 \approx 17{,}300$ cm^{-1}, so the energy of the donor must lie at least 2000 cm^{-1} higher than this to prevent back energy transfer (as discussed earlier).

The type of bridging ligand used to coordinate to the d-block chromophore can have an effect on this, as they influence the triplet energy levels of the chromophore, and can also provide intermediate excited states of their own, thus affecting the energy-transfer process. This affect was reported by Huang and co-workers where a series of Ir(III)/Eu(III) dyads were prepared and their luminescence properties were investigated.[108] The complexes were based on a series of N^N, O^O-bridging ligands (**Fig. 1.47**).

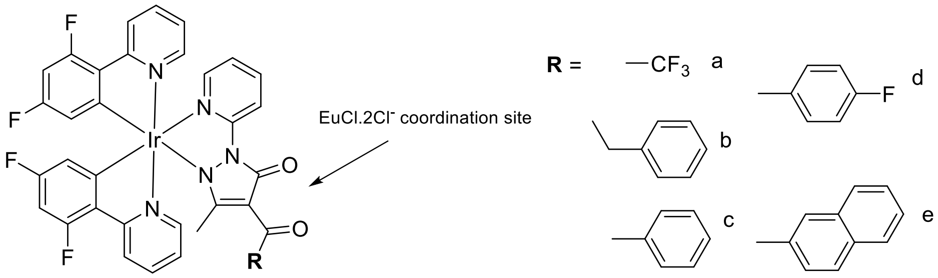

4a-e

Figure 1.47. Structures of the Ir(III) complexes reported.[108]

The study showed that the energy-transfer process from Ir(III) → Eu(III) is affected by the triplet energy level of the ligand (**Fig. 1.48**).

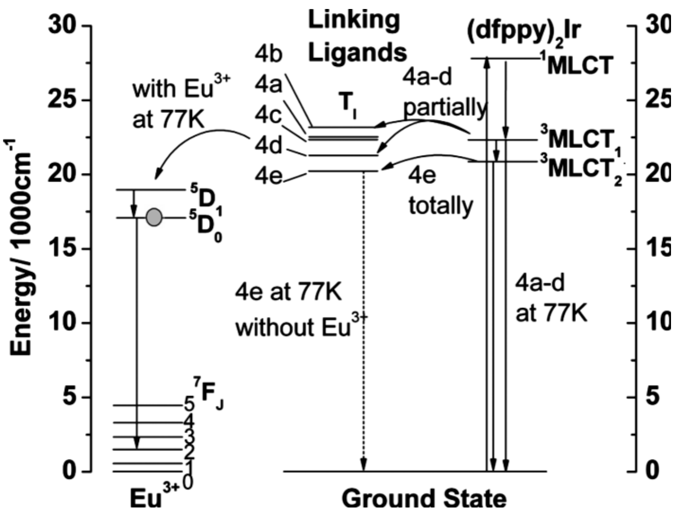

Figure 1.48. Schematic representation of the energy-transfer process for the Ir/Eu systems.[108]

Complete energy-transfer is observed when the triplet energy level of the ligand was lower than the ^{3}MLCT energy levels of the Ir and higher than the excited state levels of Eu, as was seen for complex 4e. This implies a stepwise energy-transfer mechanism with the ligand triplet state acting as a spatial and energetic intermediate between Ir-based and Eu-based excited states. When the triplet energy level was similar or slightly higher than the ^{3}MLCT energy levels of Ir, a mixture of emission from Ir(III) and Eu(III) is observed (in the cases of complexes 4a-d): this is because the energy-transfer is now incomplete or may involve back ET and cannot go through the intermediate triplet state of the ligand, so is slower, with the Ir-based excited state not being fully quenched.

A classic study showing d → f PEnT in Ir(III) and Eu(III) systems was reported by De Cola *et al.* in 2005 using a cyclometallated Ir(III) complex with a triazole-based spacer ligand and a Eu(III) terpyridine-based complex (**Fig. 1.49**).[109]

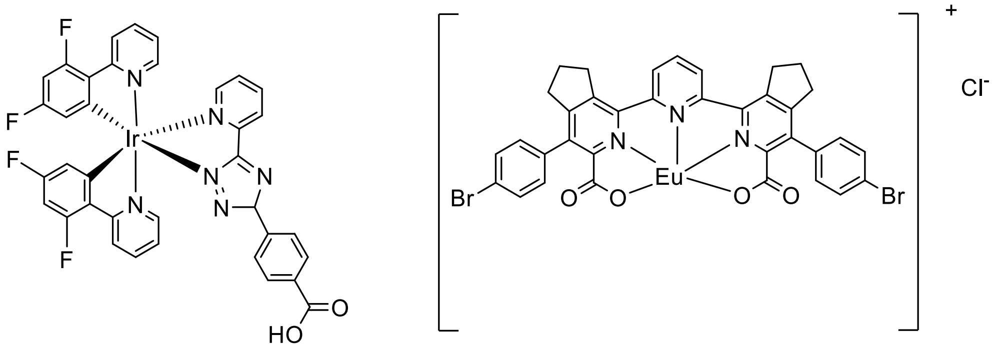

13 **14**

Figure 1.49. Chemical structures of the Ir(III) complex (**13**) and Eu(III) complex (**14**).

Complex **13** had a blue emission in CH_2Cl_2, MeOH or CH_3CN, with maxima at 460 and 491 nm (**Fig 1.50**). The complex had a quantum yield of emission, Φ, of 17% in deaerated solution of MeOH. The UV/Vis absorption spectrum showed a MLCT transition in the visible region and π-π* bands that were attributed to the ligand in the UV region.

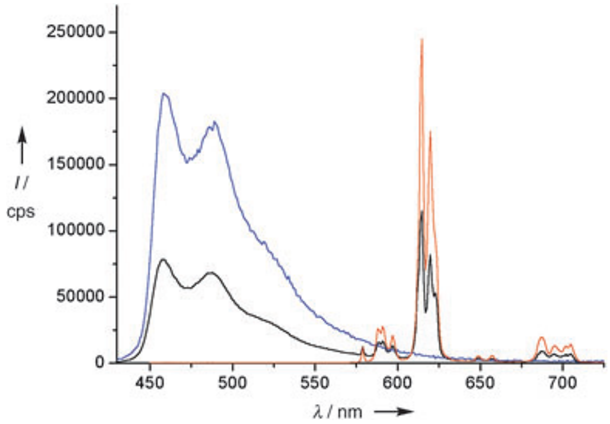

Figure 1.50. Relative steady-state emission spectra of solutions of complexes **13** (blue), **14** (red) and **15**, the dimer complex (black) in CD_3OD upon excitation at λ = 400 nm (complex **14** was excited at λ = 350 nm as it shows negligible absorption at λ = 400 nm; cps = counts per second). The solutions have identical absorption values at the excitation wavelength.[109]

Emission from complex **14** was mainly observed from the $^5D_0 \rightarrow {}^7F_2$ transition centred at 615 nm. Although this transition is an electric-dipole emission that is forbidden in the free ion, the Eu(III) centre had a strong asymmetric or strongly interacting ligand field, therefore enhancing the transition.[110] The quantum yield of emission of the complex in an air-equilibrated solution in D_2O was 33%.

Reaction of **13** and **14** gave complex **15**, in which two units of complex **13** are bonded to the Eu(III) ion of complex **14** through the terminal hydroxide units. An energy transfer process was evident as only the Ir(III) component absorbed light at λ = 400 nm, however emission from the Eu(III) centre is observed in the spectra (see **Fig. 1.50** above). The complex showed an almost-white light emission, making it an interesting compound to investigate for the potential use in white electrophosphorescent devices.

The Ward group have also demonstrated a good example of a dual-emitting Ir(III)/Eu(III) dyad in 2011, using an Ir(III) complex with cyclometallated phenylpyridine-based ligands and a pyrazolylpyridine-based organic spacer unit (**Fig. 1.51**).[111]

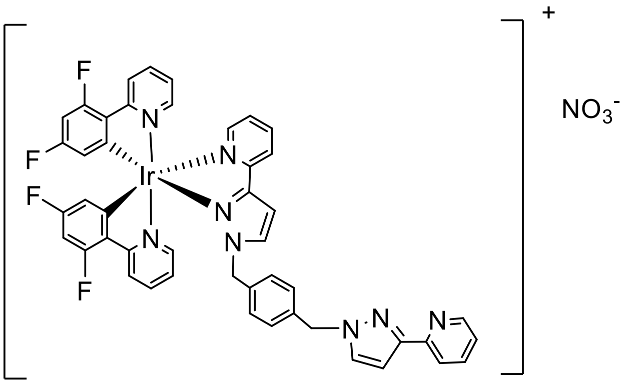

Ir.L

Figure 1.51. Chemical structure of the Ir(III) pyrazolylpyridine-based complex (Ir.L).

The complex had an emission maximum of 455 nm (≈ 22,000 cm^{-1}) in CH_2Cl_2 at room temperature, implying the presence of an excited state high enough in energy to populate Eu(III) excited states. The Ir.Ln dyads were prepared by titration of the Ir(III) complex with $Ln(hfac)_3.2H_2O$ in CH_2Cl_2 solution, where the two water molecules are displaced when the diimine ligand coordinates to Ln to give an eight-coordinated $Ln(hfac)_3$(diimine) unit. Upon titration with $Gd(hfac)_3.2H_2O$, the complex showed substantial quenching of Ir(III)-based luminescence. This was attributed to the possibility of a PET occurring from the excited state of the Ir unit to the pyrazolylpyridine unit coordinated to $Gd(hfac)_3$ to give short-lived Ir(IV)/diimine$^{\bullet -}$ charge-separated state, providing a quenching pathway. When the Ir(III) complex was titrated with $Eu(hfac)_3.2H_2O$, partial quenching of Ir(III) was observed with a simultaneous emission characteristic of Eu(III)-based emission. A very interesting observation was made where a balance of the blue and red luminescent components gave white light emission (**Fig. 1.52**).

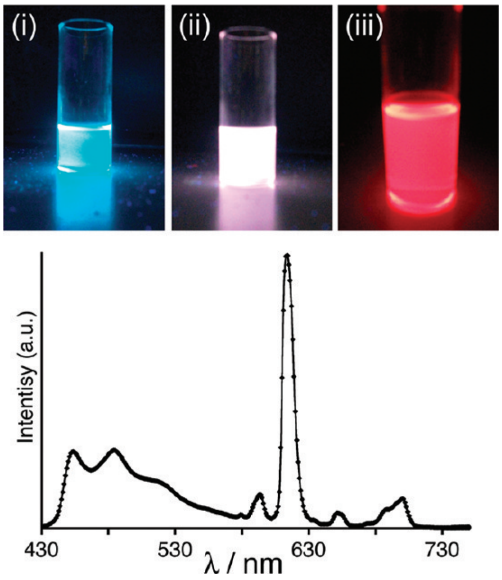

Figure 1.52. Above: Luminescence of the Ir.L complex titrated with Eu(hfac)$_3$.2H$_2$O at different points during the titration: (i) pure Ir.L complex showing characteristic blue emission; (ii) after the addition of 0.1 equivalents of Eu(hfac)$_3$.2H$_2$O; (iii) after the addition of 2 equivalents of Eu(hfac)$_3$.2H$_2$O when red Eu-based emission dominates. Below: Luminescence spectrum of white-light emitting mixture. Taken from Ref. 111.

Good white-light emission was observed from the sample when 0.1 equivalents of Eu(hfac)$_3$.2H$_2$O was added, where the mixture consisted of 90% free Ir.L complex and 10% of the dyad Ir.L.Eu with the CIE coordinates (which defines standard white light at x = 0.31 and y = 0.33) given as x = 0.34 and y = 0.32. Although white-light emission was achieved, emission becomes dominated by the red component above 0.1 equivalents of Eu(hfac)$_3$.2H$_2$O, therefore decreasing the efficiency of the Ir → Eu energy transfer process would result in a better blue-to-red ratio of emission, nonetheless this study clearly shows a combination of Ir(III) and Eu(III) fluorophores can be used to achieve white-light emission.

Further examples of Ir(III) chromophores implemented as sensitisers of Ln(III) luminescence by the Ward group are given in **Fig. 1.53**.[112, 113, 114, 115]

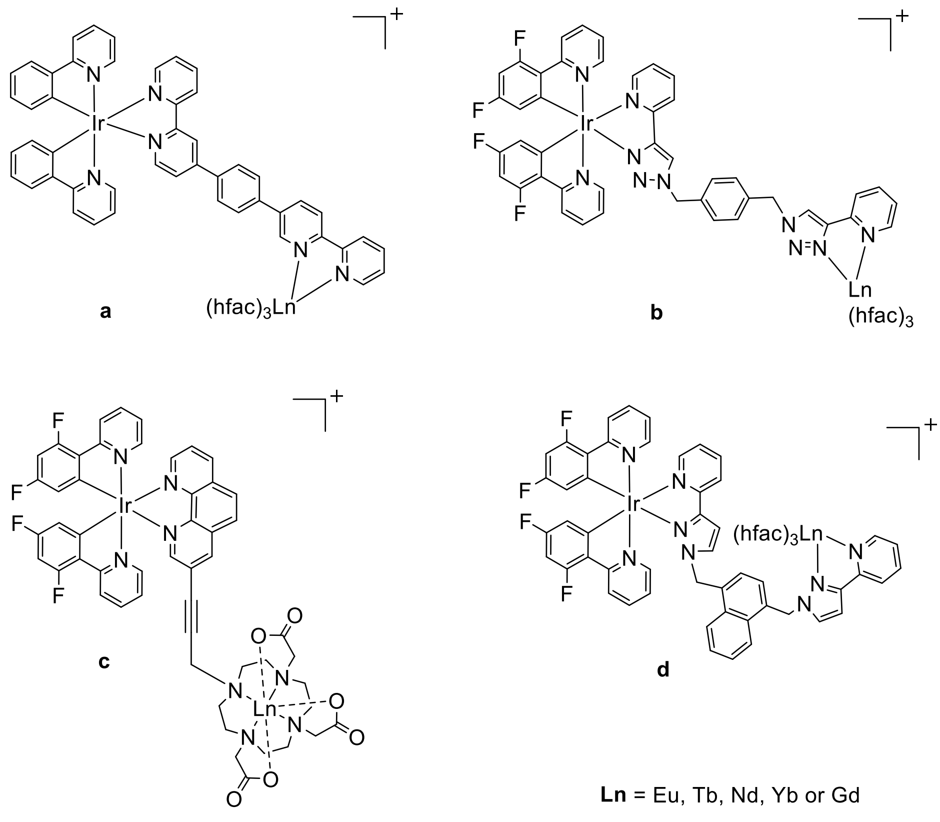

Ln = Eu, Tb, Nd, Yb or Gd

hfac = hexafluoroacetylacetonate

Figure 1.53. Examples of Ir(III) complexes **a**[112], **b**[113], **c**[114] and **d**[115] used as sensitisers for Ln(III) luminescence.

1.5 References

1. G. A. Crosby, W. G. Perkins and D. M. Klassen, *J. Chem. Phys.,* 1965, **43**, 1498.
2. V. Balzani and A. Juris, *Coord. Chem. Rev.,* 2001, **211**, 97-115.
3. A. Juris, V. Balzani, F. Barigelletti, S. Campagna, P. Belser and A. Von Zelewsky, *Coord. Chem. Rev.,* 1988, **84**, 85-277.
4. R. J. Watts, *J. Chem. Educ.,* 1983, **60**, 834.
5. B. Valeur, Molecular Fluorescence, Wiley-VCH, Weinheim, 2002.
6. A. Jablonski, *Nature*, 1933, **131**, 839.
7. L. Sun, H. Berglund, R. Davydov, T. Norrby, L. Hammartröm, P. Korall, A. Börje, C. Philouze, K. Berg, A. Tran, M. Andersson, G. Stenhagen, J. Mårtensson, M. Almgren, S. Styring and B. Åkermark, *J. Am. Chem. Soc.,* 1997, **119**, 6996.
8. M. S. Wrighton and D. L. Morse, *J. Am. Chem. Soc.,* 1974, **96**, 998.
9. J. V. Caspar and T. J. Meyer, *J. Phys. Chem.,* 1983, **87**, 952.
10. B. P. Sullivan and T. J. Meyer, *Organometallics,* 1986, **5**, 1500.
11. [a] S. T. Lam, N. Zhu and V. W. W. Yam, *Inorg. Chem.,* 2009, **48**, 9664.
    [b] V. W. W. Yam, V. C. Y. Lau and K. K. Cheung, *Organometallics,* 1995, **14**, 2749.
12. V. W. W. Yam, S. H. F. Chong, C. C. Ko and K. K. Cheung, *Organometallics,* 2000, **19**, 5092.
13. C. M. Che, H. Y. Chao, V. M. Miskowski, Y. Li and K. K. Cheung, *J. Am. Chem. Soc.,* 2001, **123**, 4985.
14. V. Fernandez-Moreira, M. L. Ortego, C. F. Williams, M. P. Coogan, N. D. Villacampa and M. C. Gilmeno, *Organometallics*, 2012, **31**, 5950.
15. D. J. Cárdenas, A. M. Echavarren, M. C. Ramirez de Arellano, *Organomettalics*, 1999, **18**, 3337.
16. J. A. G. Williams, A. Beeby, E. S. Davies, J. A. Weinstein and C. Wilson, *Inorg. Chem.,* 2003, **42**, 8609.
17. S.W. Botchway, M. Charnley, J. W. Haycock, A. W. Parker, D. L. Rochester, J. A. Weinstein and J. A. G. Williams, *Proc. Natl. Acad. Sci.,* U.S.A., 2008, **105**, 16071.

18. E. Holder, B. M. W. Langeveld and U. S. Schubert, *Adv. Mater.*, 2005, **17**, 1109.
19. Q. Pei, G. Yu, C. Zhang, Y. Yang and A. J. Heeger, *Science*, 1995, **269**, 1086.
20. M. S. Lowry and S. Bernhard, *Chem. Eur. J.*, 2006, **12**, 7970.
21. K. Lo, C. Chung and N. Zhu, *Chem. Eur. J.,* 2003, **9**, 475.
22. M. Wolgenannt, K. Tandon, S. Mazumdar, S. Ramasesha and Z. V. Vardeney, *Nature*, 2001, **409**, 494.
23. A. Tsuboyama, H. Iwawaki, M. Furugori, T. Mukaide, J. Kamatani, S. Igawa, T. Moriyama, S. Miura, T. Takiguchi, S. Okada, M. Hoshina and K. Veno, *J. Am. Chem. Soc.,* 2003, **125**, 12971.
24. T. Sajato, P. I. Djurovich, A. Tamayo, M. Yousufuddin, R. Bau, M. E. Thompson, R. J. Holmes and S. R. Forrest, *Inorg. Chem.,* 2005, **44**, 7992.
25. V. Balzani and S. Campagna, *Photochemistry and Photophysics of Coordination Compounds II*, Springer, Berlin Heidelberg, 2007, 147.
26. P. J. Hay, *Phys. Chem. A,* 2002, **106**, 1634.
27. S. D. Cummings and R. Eisenberg, *J. Am. Chem. Soc.,* 1996, **118**, 1949.
28. E. Orselli, G. T. Kottas, A. E. Konradsson, P. Coppo, R. Fröhlich, L. De Cola, A. van Dijken, M. Büchel and H. Börner, *Inorg. Chem.,* 2007, **46**, 11082.
29. S. Sprouse, K. A. King, P. J. Spellane and R. J. Watts, *J. Am. Chem. Soc.,* 1984, **106**, 6647.
30. Q. Zhao, S. Lin, M. Shi, C. Wang, M. Yu, L. Li, F., Li, T. Yi and C. Huang, *Inorg. Chem.* 2006, **45**, 6152.
31. M. Yu, Q. Zhao, L. Shi, F. Li, Z. Zhou, H. Yang, T. Yi and C. Huang, *Chem. Commun.,* 2008, **44**, 2115.
32. K. Ko, C. Chung and N. Zhu, *Chem. Eur. J.,* 2006, **12**, 1500.
33. C. Li, M .Yu, Y. Sun, Y. Wu, C. Huang and F. Li, *J. Am. Chem. Soc.,* 2011, **133**, 11231.
34. C. Li, Y. Liu, Y. Wu, Y. Sun and F. Li, *Biomaterials*, 2013, **34**, 1223.
35. J-X. Ru, L-P. Guan, X-L. Tang, W. Dou, X. Yao, W-M. Chen, Y-M. Liu, G-L. Zhang, W-S. Liu, Y. Meng and C-M. Wang, *Inorg. Chem.,* 2014, **43**, 11498.

36. C. Leung, H. Zhong. H. Yang, Z. Cheng, D. Chan, V. Ma, R. Abagyan, C. Wong and D. Mai, *Angew. Chem. Int. Ed.,* 2012, **51**, 9010.

37. H. Wajant, K. Pfizenmaier and P. Scheurich, *Cell Death Differ.,* 2003, **10**, 45.

38. B. B. Aggarwal, *Nat. Rev. Immunol.,* 2003, **3**, 745.

39. K. Chatzantoni and A. Mouzaki, *Curr. Top. Med. Chem.,* 2006, **6**, 1707.

40. M. Ikai and S. Tokito, *Appl. Phys. Lett.,* 2007, **79**, 156.

41. J. A. G. Williams, A. J. Wilkinson and V. L. Whittle, *Dalton Trans.,* 2008, 2081.

42. M. A. Baldon, D. F. O'Brien, M. E. Thompson and S. R. Forrest, *Phys. Rev. B: Condens. Matter Mater. Phys.,* 1999, **60**, 14422.

43. P. Chou and Y. Chi, *Eur. J. Inorg. Chem.,* 2006, 3319.

44. W. Yong and C. Ho, *J. Mater. Chem.,* 2009, **19**, 4457.

45. M. Klessinger and J. Michl, *Excited States, Photochemistry of Organic Molecules;* VCH, New York, 1995.

46. S. Tokito, *J. Photopolym. Sci. Technol.,* 2004, **17**, 307.

47. C. Adachi, R. C. Kwong, P. Djurovich, V. Adamovich, M. A. Baldo, M. E. Thompson and S. R. Forrest, *Appl. Phys. Lett.,* 2001, **79**, 2082.

48. S. J. Lee, K.-M. Park, K. Yang and Y. Kang, *Inorg. Chem.,* 2009, **48**, 1030.

49. H. Hong and T. Chen, *Mater. Chem. Phys.,* 2007, **101**, 170.

50. A. Endo, K. Suzuki, T. Yoshihara, S. Tobita, M. Yahiro and C. Adachi, *Chem. Phys. Lett.,* 2008, **460**, 155.

51. M. K. Nazeeruddin, R. Humphry-Baker, D. Berner, S. Rivier, L. Zuppiroli and M. Grätzel, *J. Am. Chem. Soc.,* 2003, **125**, 8790.

52. J. D. Slikner, A. A. Gorodetsky, M. S. Lowry, J. Wang, S. Parker, R. Rohl, S. Bernards and G. G. Malliaras, *J. Am. Chem. Soc.,* 2004, **126**, 2763.

53. A. B. Tamayo, S. Garon, T. Sajato, P. I. Djurovich, I. M. Tsyba, R. Bau and M. E. Thompson, *Inorg. Chem.,* 2005, **44**, 8723.

54. M. K. Nazeeruddin, R. T. Wegh, Z. Zhou, C. Klein, Q. Wang, F. De Angelis, S. Fantacci and M. Grätzel, *Inorg. Chem.,* 2006, **45**, 9245.

55. E. Soini and I. Haemmilä, *Clin. Chem.,* 1979, **25**, 353.

56. I. Hemmilä, T. Ståhlberg and P. Mottram, *Bioanalytical Applications of Labelling Technology,* 2nd ed., Wallac Oy: Turku Finland, 1995.

57. C. M. G. Dos Santos, A. J. Harte, S. J. Quinn and T. Gunnlaugsson, *Coord. Chem. Rev.,* 2008, **252**, 2512.
58. B. A. Hess, A. Kedziorski, L. Smentek and D. J. Bornhop; *J. Phys. Chem.* A., 2008, **112**, 2397.
59. Y. Fan, P. Yang, S. Huang, J Jiang, H. Lian and J. Lin, *J. Phys. Chem.* C., 2009, **113**, 7628.
60. A. de Bettencourt-Dias, *Dalton Trans.,* 2007, 2229.
61. D. M. Khreis, R. J. Curry, M. Somerton and W. P. Gillin, *J. Appl. Phys.,* 2000, **88**, 777.
62. P. He, H. H. Wang, S. G. Liu, W. Hu, J. X. Shi, G. Wang and M. L. Gong, *J. Electrochem. Soc.,* 2009, **156**, E46.
63. G. Urbain, *Acad. Sci. Paris,* 1906, **142**, 205.
64. S. Shionoya and W. M. Yen; *Phosphor. Handbook,* CRC Press Inc., Boca Raton, FL 33431, USA, 1999.
65. A. K. Levine and F. C. Palilla, *Appl. Phys. Lett.,* 1964, **5**, 118.
66. W. T. Carnall, P. R. Fields and K. Rajnak, *J. Chem. Phys.,* 1968, **49**, 4424.
67. J-C. G, Bünzli and C. Piguet, *Chem. Soc. Rev.,* 2005, **34**, 1048.
68. S. V. Eliseeva, M. Ryazano, F. Gumy, S. I. Troyanov, L. S. Lepnev, J-C. G. Bünzli and N. P. Kuzmina, *Eur. J. Inorg. Chem.,* 2006, 4809.
69. J-C. G. Bünzli, *Chem. Rev.,* 2010, **110**, 2729.
70. S. I. Weissman, *J. Chem. Phys.,* 1942, **10**, 214.
71. M. C. Heffern, L. M. Matosziuk and T. J. Meade, *Chem. Rev.,* 2014, **114**, 4496.
72. B. Alpha, J-M. Lehn and G. Mathis, *Angew. Chem. Int. Ed.,* 1987, **99**, 266.
73. S. Petloud, S. M. Cohen, J-C. G. Bünzli and K. N. Raymond, *J. Am. Chem. Soc.,* 2003, **125**, 13324.
74. S. V. Eliseeva and J-C. G. Bünzli, *Chem. Soc. Rev.,* 2010, **39**, 189.
75. D. L. Dexter, *J. Chem. Phys.,* 1953, **21**, 836.
76. T. Förster, *Discuss. Faraday Soc.,* 1959, **27**, 7.
77. V. Balzani, A. Juris and M. Venturi, *Chem. Rev.,* 1996, **96**, 759.
78. T. Lazarides, N. Tart, D. Sykes, S. Faulkner, S. Barbieri and M. D. Ward, *Dalton. Trans.,* 2009, 3971.

79. A. P. De Silva, D. B. Fox, A. J. M. Huxley and T. S. Moody, *Coord. Chem. Rev.,* 2000, **205**, 41.

80. A. Beeby, I. M. Clarkson, R. S. Dickins, S. Faulkner, D. Parker, L. Royale, A. S. de Sousa, J. A. G. Williams and M. Woods, *J. Chem. Soc., Perkin Trabs. 2,* 1999, 493.

81. R. M. Supkowski and W. D. Horrocks, *Inorg. Chim. Acta,* 2002, **340**, 44.

82. P. B. Glover, A. P. Bassett, P. Nockemann, B. M. Kariuki, R. Van Deun and Z. Pikramenou, *Chem. Eur. J.,* 2007, **13**, 6308.

83. S. Phimphivong and S. S. Saavedra, *Bioconjugate Chem.,* 1998, **9**, 350.

84. J. Yu, D. Parker, R. Pal, R. A. Poole and M. J. Cann, *J. Am. Chem. Soc.,* 2006, **128**, 2294.

85. S. J. Butler, L. Lamarque, R. Pal and D. Parker, *Chem. Sci.,* 2014, **5**, 1750.

86. E. A. Weitz, J. Y. Chang, A. H. Rosenfield and V. C. Pierre, *J. Am. Chem. Soc.,* 2012, **134**, 16099.

87. P. Imming, C. Sinning and A. Meyer, *Nat. Rev. Drug Discov.,* 2006, **5**, 821.

88. J. P. Overington, B. Al-Lazikani and A. L. Hopkins, *Nat. Rev. Drug Discov.,* 2006, **5**, 993.

89. B. McMahon, P. Mauer, C. P. McCoy, T. C. Lee and T. Gunnlaugsson, *J. Am. Chem. Soc.,* 2009, **131**, 17542.

90. D. Taylor, J. G. Hazenberg and T. C. Lee, *Nat. Mater.,* 2007, **6**, 263.

91. R. Parkesh, W. Gowin, T. C. Lee and T. Gunnlaugsson, *Org. Biomol. Chem.,* 2006, **4**, 3611.

92. J. Kido and Y. Okamoto, *Chem. Rev.,* 2002, **102**, 2357.

93. M. A. Katkora and M. N. Bochkarev, *Dalton Trans.,* 2010, **39**, 6599.

94. J. Kido, K. Nagai and Y. Ohashi, *Chem. Lett.,* 1990, 657.

95. A. de Bettencourt-Dias, *Dalton Trans.,* 2007, 2229.

96. N. Tessler, V. Medvedev, M. Kazes, S. Kan and U. Banin, *Science*, 2002, **295**, 1506.

97. T. Zhang, X. J. Zhu, C. C. W. Cheng, W. M. Kwok, H. L. Tam, J. H. Hao, D. W. J. Kwong, W. K. Wong and K. L. Wong, *J. Am. Chem. Soc.,* 2011, **133**, 20120.

98. E. L. Williams, J. Li and G. E. Jabbour, *Appl. Phys. Lett.,* 2006, **89**, 83506.

99. M. A. Kartkova, A. P. Pushkarev, T. V. Balashova, A. N. Konev, G. K. Fukin, S. Y. Ketkov and M. N. Bochkarev, *J. Mater. Chem.,* 2011, **21**, 16611.

100. H. Wei, G. Yu, Z. Zhao, Z. Liu, Z. Bian and C. Huang, *Dalton Trans.,* 2013, **42**, 8951.

101. M. D. Ward, *Coord. Chem. Rev.,* 2007, **251**, 1663.

102. N. Sabbatini, M. Guardigli and J. M. Lehn, *Coord. Chem. Rev.,* 1993, **123**, 201.

103. T. Lazarides, N. M. Tart, D. Sykes, S. Faulkner, A. Barbieri and M. D. Ward, *Dalton Trans.,* 2009, 3971.

104. M. Tropiano, C. J. Record, E. Morris, H. S. Rai, C. Allain and S. Faulkner, *Organometallics*, 2012, **31**, 5673.

105. S. Singaravadivel, M. Velayudham, E. Babu, P. M. Mareeswaran, K-W. Lu and S. Rajagopal, *J. Fluoresc.,* 2013, **23**, 1167.

106. T. Lazarides, D. Sykes, S. Faulkner, A. Barbieri and M. D. Ward, *Chem. Eur. J.,* 2008, **14**, 9389.

107. S. Faulkner, L. S. Natrajan, W. S. Perry and D. Sykes, *Dalton Trans.,* 2009, 3890.

108. W. Jiang, B. Lou, J. Wang, H. Lv, Z. Bian and C. Huang, *Dalton Trans.,* 2011, **40**, 11410.

109. P. Coppo, M. Duati, V. N. Kozhevnikov, J. W. Hofstraat and L. De Cola, *Angew. Chem. Int. Ed.,* 2005, **44**, 1806.

110. F. S. Richardson, *Chem. Rev.,* 1982, **82**, 541.

111. D. Sykes, I. S. Tidmarsh, A. Barbieri, I. V. Sazanovich, J. A. Weinstein and M. D. Ward, *Inorg. Chem.,* 2011, **50**, 11323.

112. N. M. Tart, I. Sazanovich, I. S. Tidmarsh and M. D. Ward, *Photochem. Photobiol. Sci.,* 2010, **9**, 886.

113. D. Sykes and M. D. Ward, *Chem. Commun.,* 2011, **47**, 2279.

114. E. Baggaley, D-K. Cao, D. Sykes, S. W. Botchway, J. A. Weinstein and M. D. Ward, *Chem. Eur. J.,* 2014, **20**, 8898.

115. D. Sykes, S. C. Parker, I. V. Sazanovich, A. Stephenson, J. A. Weinstein and M. D. Ward, *Inorg. Chem.,* 2013, **52**, 10500.

2

Photoinduced Energy-Transfer and Electron-Transfer

2.1 Introduction

When considering d → f energy-transfer, emission from lanthanides can be achieved using the antenna effect through two different mechanisms:

i. Photoinduced energy-transfer
ii. Photoinduced electron-transfer

This chapter looks at the syntheses, characterisation and photophysical properties of two blue-luminescent iridium (III) complexes and their use as sensitisers of Eu(III) and Tb(III) centres *via* these two mechanisms.

2.1.1 Photoinduced Energy-Transfer

Photoinduced energy-transfer (PEnT) is a well-studied process that can occur in two different ways. An electron from the donor excited state can be transferred to the LUMO of the acceptor, where a simultaneous electron is transferred from the HOMO of the acceptor to the vacant position of the lower-lying singly occupied molecular orbital of the donor. This process is known as Dexter energy-transfer.[1]

The second process also results in promotion of the acceptor to its excited state; however it occurs in a dipole-dipole mechanism with no exchange of electrons that can operate up to a distance of 100 Å between the donor and acceptor. This process is known as Förster energy-transfer.[2] Both these mechanisms are discussed in detail in Chapter 1.

2.1.2 Photoinduced Electron-Transfer

In the case of photoinduced electron-transfer (PET), a single electron moves from the excited state of the donor to the LUMO of the acceptor, forming a charge-separated state which results in the donor becoming cationic and the acceptor being anionic. This process can be modelled with the Rehm-Weller equation[3,4] where the overall free energy change for the process depends on the donor's oxidation potential and the acceptor’s reduction potential. The driving force for the reaction is the absorption of light, as long as the absorbed energy of the donor is higher than energy required for the formation of the donor-acceptor excited state. This is discussed in detail in Chapter 1.

2.1.3 Previous Work by the Ward Group

There has been interest from the Ward group and co-workers into the study of the mechanisms of energy-transfer in d/f dyad systems.[5,6,7,8]

Studies from the group have shown that d → f PEnT can occur over quite long distances of up to 20 Å in a d/f system *via* a Dexter-type mechanism.[6] This energy-transfer process is mediated by the bridging ligand orbitals and occurs faster through conjugated spacer units compared to saturated ones. The energy-transfer from the d-metal to the Ln(III) can therefore be somewhat controlled, which highlights the importance of selecting the appropriate spacer unit when considering the synthetic design of the system.

In addition to PEnT, the Ward group have also shown d → f energy-transfer can occur through a PET mechanism.[5,7] The group found that a charge-separated state that formed when an electron from the d-metal was transferred to the electron-deficient ligand coordinated to the Ln(III) (in some cases PET can occur directly to the lanthanide where the metal gets transiently reduced from Ln(III) to Ln(II) instead of the ligand) provided sufficient energy to sensitise from Ln(III) ions in the near-infrared region. Examples of these complexes are shown in **Fig. 2.01**.

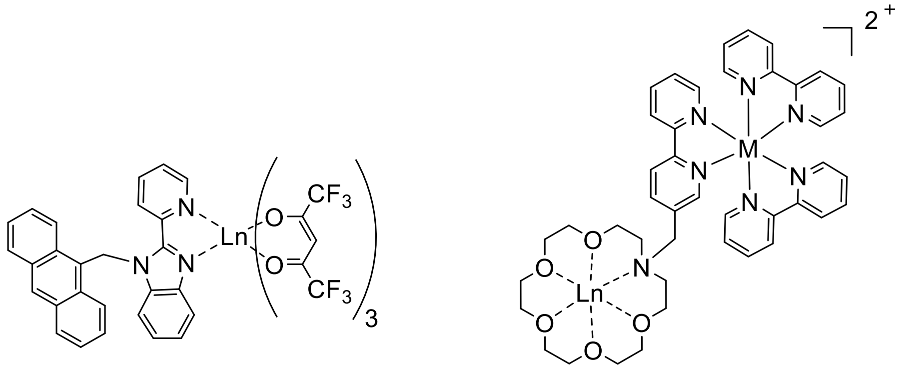

Ln = Nd, Gd, Er, Yb

M = Os, Ru
Ln = Nd, Yb

Figure 2.01. Examples of complexes prepared by the Ward group that display photoinduced electron-transfer from the donor to the acceptor (Ln).[5,7]

More recently, work from the group has focused on the synthesis of Ir(III) complexes that emit in the blue region of the visible spectrum.[8,9,10,11] These complexes were based on two cyclometallated 2-(2,4-difluorophenyl)pyridine units to Ir(III), containing a spacer unit with an available bidentate coordination site, [Ir(fppy)$_2$L]^n, for the Ln(III) (**Fig. 2.02**).

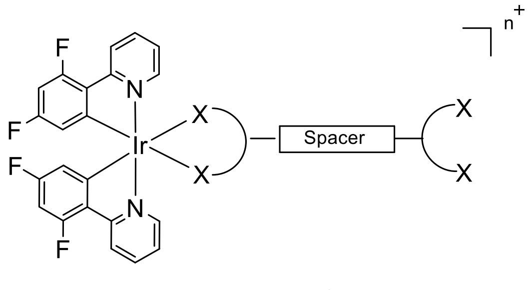

[Ir(fppy)$_2$L]^n

Figure 2.02. Example of the molecular architecture based on complexes researched within the Ward group.

As mentioned in Chapter 1, the fluorine atoms on the phenylpyridine ligands cause a blue-shift in emission from the Ir(III) centre when compared to its parent ppy complex, therefore the emission of these complexes was high enough in energy to excite Ln(III) centres that emit in the visible region (Eu and Tb). The advantages of generating emission from lanthanides in the visible region are discussed in Chapter 1.

To continue this work, two new Ir(III) complexes [Ir(fppy)$_2$L^{pytz}] and [Ir(fppy)$_2$L^{pic}] have been synthesised. Both have pendant bidentate binding sites which can be used to form Ir(III)/Ln(III) dyads. Their syntheses, characterisation and photophysical studies are reported in detail in this chapter.

2.2 Synthetic Studies

The synthetic details of all the products are described in full in Chapter 5. The first step for the synthesis of the complexes involved the synthesis of the Ir(III) μ-dichloro-bridged dimer, $[Ir_2(fppy)_4Cl_2]$, as described previously in the literature (**Scheme 2.01**).[12]

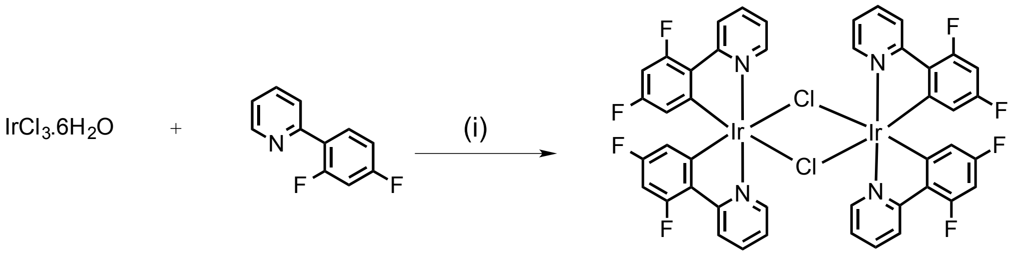

[Ir(fppy)$_4$Cl$_2$]

Scheme 2.01. Synthesis of $[Ir_2(fppy)_4Cl_2]$. (i) 2-ethoxyethanol/water (3:1), reflux 18 hours.

The reaction occurred under relatively mild conditions to give a good yield of the product. Metalation of the complex occurred *via* an electrophilic attack of the metal on the aromatic phenyl ring. The reaction was carried out in the dark by covering the reaction flask in foil. This was done to ensure high yields were achieved by blocking light in the reaction medium as some iridium compounds are known to be photosensitive.

It was reported in the literature that the obtained product is the *meso*-isomer, where the fppy groups were in the *trans* position relative to each other. No purification steps were necessary as the ^{1}H NMR spectrum and mass spectrum showed the complex to be pure.

2.2.1 [Ir(fppy)$_2$L^{pytz}]

[Ir(fppy)$_2$L^{pytz}] was synthesised using a 1,2,4-triazole-based spacer unit (L^{pytz}). A triazole unit was selected as iridium-triazole complexes are known to have emission in the blue region of the visible spectrum.[13] The L^{pytz} unit contains an N,N'-donor bidentate chelating site at which a $[Ln(hfac)_3]$ unit binds to during the titration to form the Ir(III)/ Ln(III) dyad in CH_2Cl_2.

L^{pytz} was synthesised from 4-amino-3,5-di-2-pyridyl-4H-1,2,4-triazole (Sigma-Aldrich) by elimination of the NH_2 group at position 4 of the N group of the triazole ring.[14] This was achieved by forming a diazonium group on the triazole which allowed elimination of $N_{2\ (g)}$ to form the desired compound in high yields. $[Ir(fppy)_2L^{pytz}]$ was then synthesised from this with the subsequent reaction of L^{pytz} with $[Ir_2(fppy)_4Cl_2]$ (**Scheme 2.02**). Excess L^{pytz} was used in the reaction with $[Ir_2(fppy)_4Cl_2]$ in order to minimise the formation of the dinuclear complex, in which an Ir(III) unit could bind to each of the bidentate sites of the L^{pytz} unit.

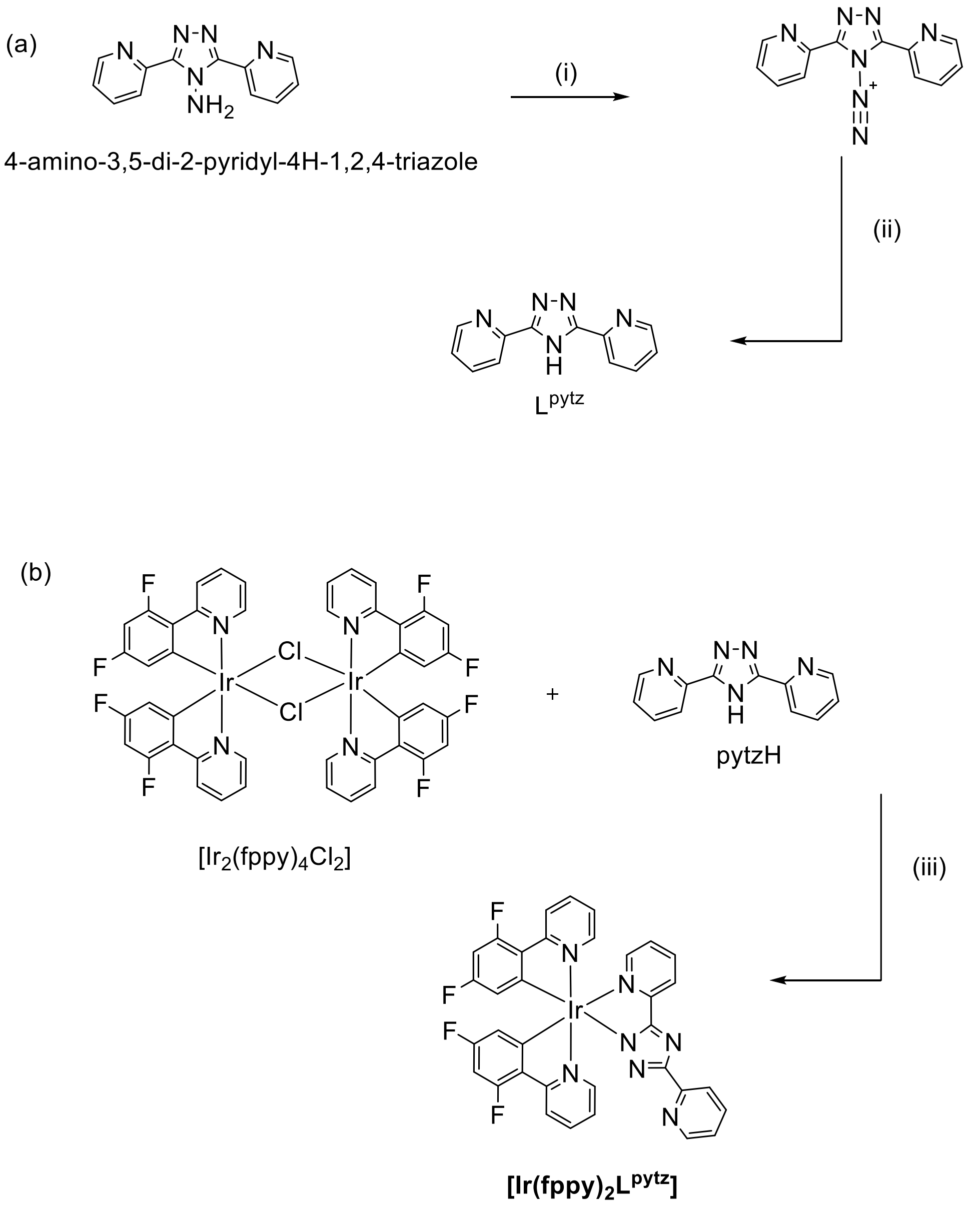

Scheme 2.02. (a) Synthesis of L^{pytz} : (i) $HNO_{3\,(aq)}$, $NaNO_2$, 0°C, 30 min. (ii) NH_3OH (3 M). (b) Synthesis of $[Ir(fppy)_2L^{pytz}]$: (iii) MeOH/CH_2Cl_2 (2:1), reflux, $N_{2\,(g)}$, 18 hours.

It was necessary to purify the final complex by column chromatography twice on silica gel (CH_2Cl_2/MeOH, 99:1 and then CH_3CN). Purity of the complex was confirmed by ^{1}H NMR spectroscopy (**Fig. 2.03**), mass spectrometry and elemental analysis. The integrals of the ^{1}H NMR spectrum showed the presence of 20 H atoms which correlated with the number of the atoms present in the complex. The absence of the nitrogen-bound H atom showed that coordination to the metal centre occurred through the deprotonation of the N atom of the triazole ring.

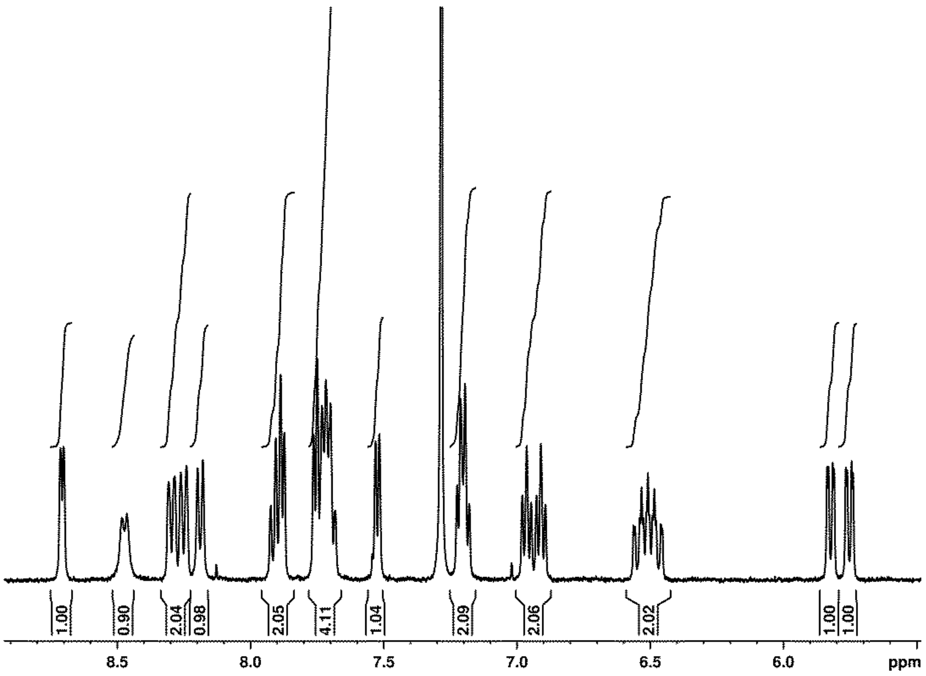

Figure 2.03. ^{1}H NMR (400 MHz, $CDCl_3$) spectrum of [Ir(fppy)$_2$L^{pytz}] after purification by column chromatography.

2.2.2 [Ir(fppy)$_2$L^{pic}]

[Ir(fppy)$_2$L^{pic}] was synthesised *via* a different route from the previous complex. The complex contains a picolinate unit with a pendant hydroxy group. 3-Hydroxypicolinic acid (Sigma Aldrich) was used as a ligand as Ir(III) complexes containing a picolinate unit also have emission in the blue region of the visible spectrum.[15]

The pendant hydroxy group was fundamental as it could be functionalised to build the bridging ligand onto the complex. The complex was synthesised in three steps, which involved the synthesis of the iridium-picolinate [Ir-pic] complex from [Ir$_2$(fppy)$_4$Cl$_2$] first. The spacer unit was synthesised and then attached to the picolinate complex to form the product (**Scheme 2.03**).

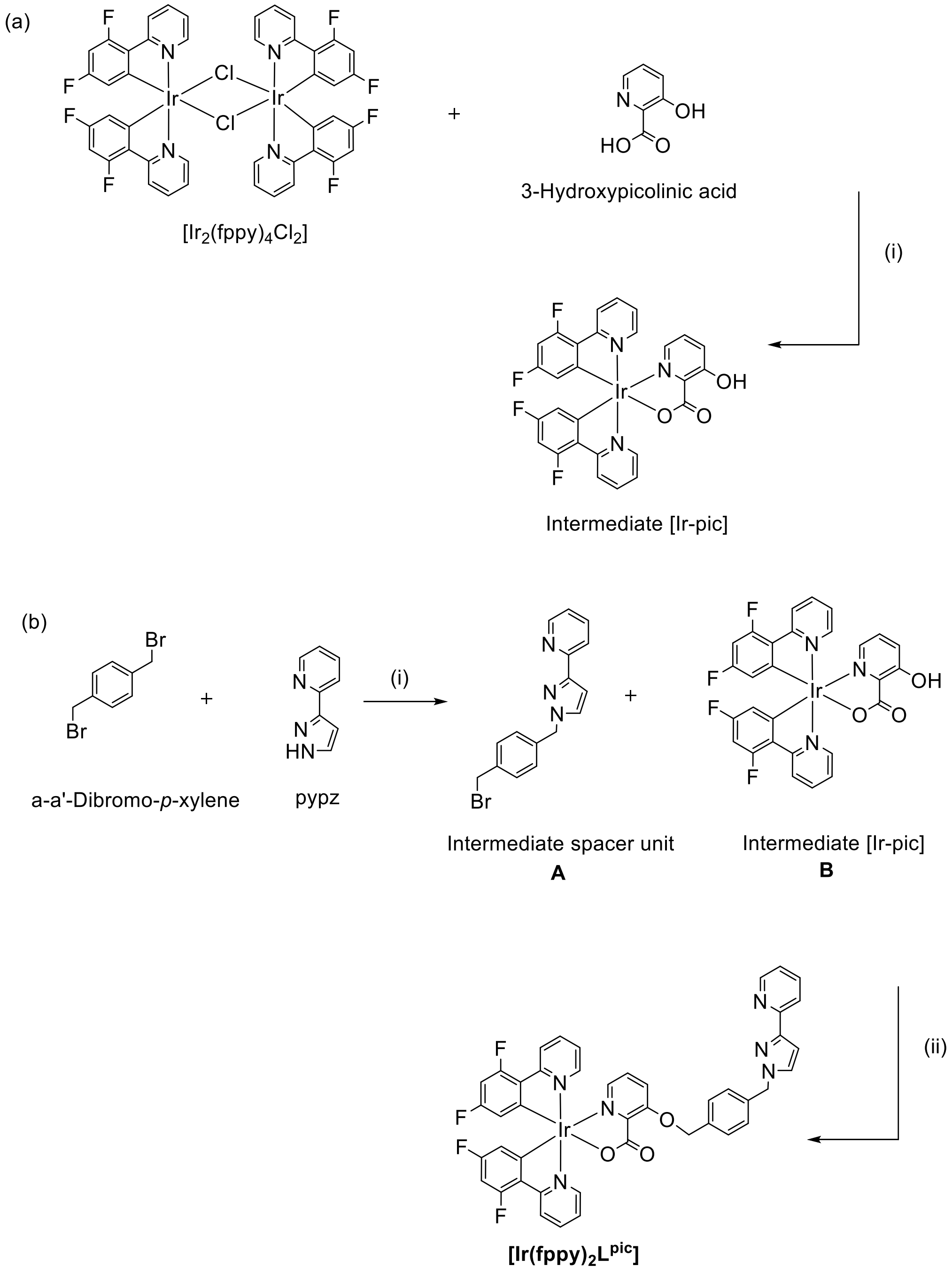

Scheme 2.03. Synthesis of [Ir(fppy)$_2$L^{pic}]: a) synthesis of the [Ir-pic] intermediate: (i) Na_2CO_3, 2-ethoxyethanol, reflux, $N_{2\,(g)}$, 18 hours: b) synthesis of spacer unit and [Ir(fppy)$_2$L^{pic}]: (i) 1 M NaOH $_{(aq)}$, THF/H_2O (1:1), room temperature, 2 days: (ii) K_2CO_3, acetone, reflux, $N_{2\,(g)}$, 48 hours.

The pendant group on the complex was a chelating pyridyl pyrazole (pypz) unit.[16] For the same reason mentioned for the previous complex, pypz was used for its N,N'-donor bidentate chelating site at which a [Ln(hfac)$_3$] unit could bind during titration to form dinuclear Ir(III)/ Ln(III) dyads in CH_2Cl_2.

A suitable aromatic group was necessary to bridge the pypz unit to the Ir-picolinate complex as this facilitated the energy-transfer from Ir(III) to the Ln(III) centre. The suitability of spacer units for energy-transfer is discussed in detail in Chapter 1. α,α'-Dibromo-*p*-xylene (Sigma Aldrich) was used to bridge the Ir(III) unit to pypz as both the NH group of pypz and the OH group of the picolinate unit could undergo alkylation with the dibromoxylene under relatively mild conditions, with the Br atoms acting as leaving groups. This was achieved in two steps; first by addition of dibromoxylene to pypz in a 4:1 ratio. In this reaction dibromoxylene was used in a 4:1 excess (dibromoxylene:pypz) in order to minimise substitution of pypz onto both sides of the dibromoxylene. This intermediate **A** (**Scheme 2.03**) was purified by column chromatography on silica gel (CH_2Cl_2/MeOH, 99:2) to give the intermediate spacer unit in high yield. The second step involved reaction of the intermediate unit **A** with the hydroxyl group on the [Ir-pic] complex **B** to give the final complex [Ir(fppy)$_2$L^{pic}].

[Ir(fppy)$_2$L^{pic}] was purified by column chromatography on silica gel (CH_2Cl_2/MeOH, 90:10). The yield for the synthesis of this complex was lower than that for the synthesis of the previous complex (20% and 87% respectively). Purity of the complex was confirmed by ^{1}H NMR spectroscopy (**Fig. 2.04**), mass spectrometry and elemental analysis.

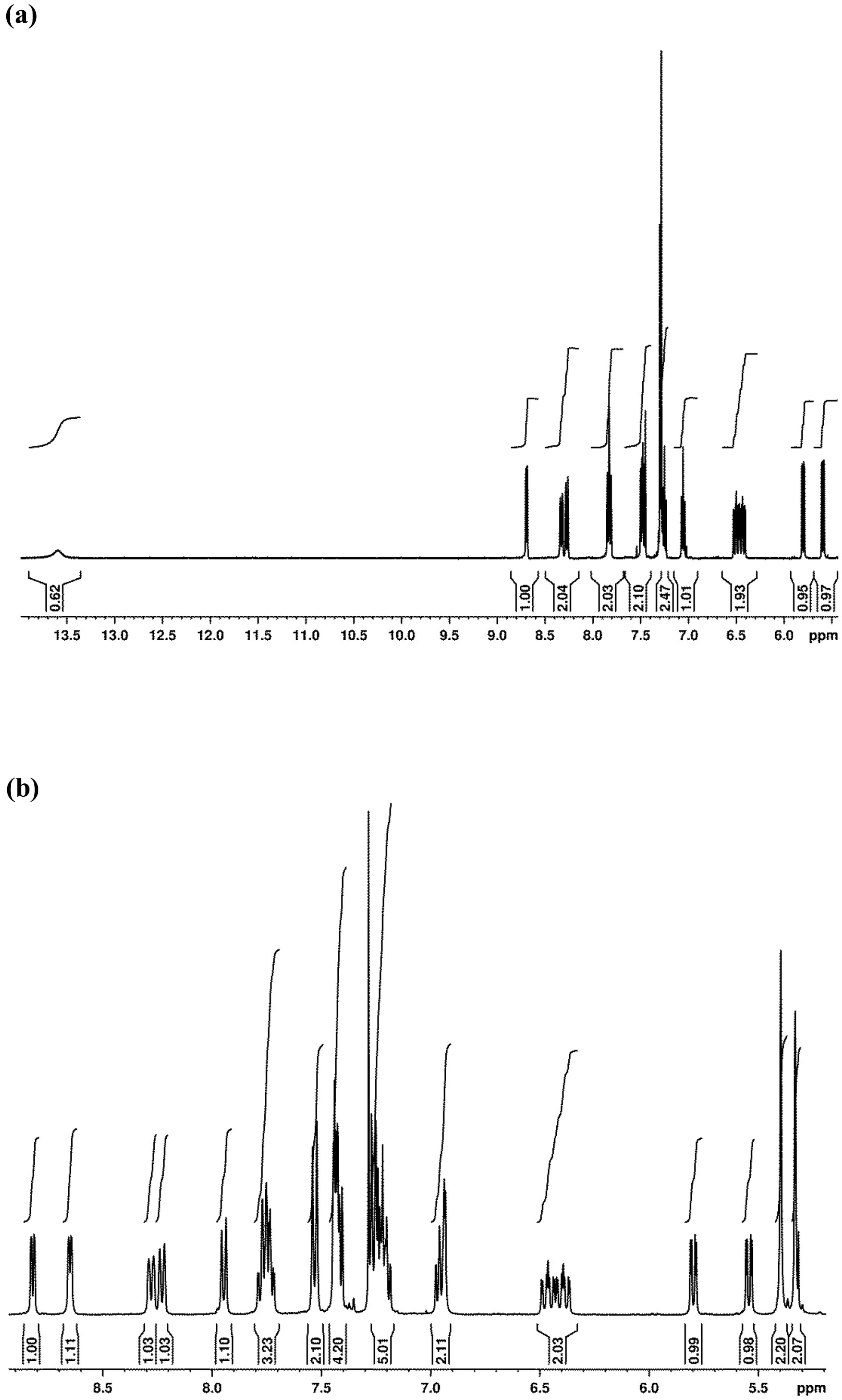

Figure 2.04. ^{1}H NMR (400 MHz, $CDCl_3$) spectrum of: a) the intermediate [Ir-pic] and b) [Ir(fppy)$_2$L^{pic}] after purification by column chromatography.

When comparing the intermediate [Ir-pic] complex **B** to the final product, additional aromatic peaks were observed in the ^{1}H NMR spectrum for the final complex. The additional aromatic peaks (from the pypz and phenyl units) are not well resolved as they are partly obscured by the aromatic peaks of the phenylpyridine and picolinate groups on the Ir(III) centre, however when the aromatic region was integrated, it contained 25 H atoms which correlates to the number of aromatic protons in the complex. Two new singlet peaks were also observed at δ_H = 5.40 and 5.33 ppm which gave further confirmation that the final product was successfully synthesised. These peaks are from the two alkyl CH_2 peaks which are typically observed in this region of the spectrum.

2.3 X-ray Crystallography

2.3.1 [Ir(fppy)$_2$L^{pytz}]

Crystals of the complex were grown by slow vapour diffusion in CH_2Cl_2 and hexane and the molecular structure was identified by X-ray crystallography (**Fig. 2.05**). The structure was resolved by direct methods and refined to give a final R1 value of 0.04. Crystal data and structure refinement are given in appendix A1.

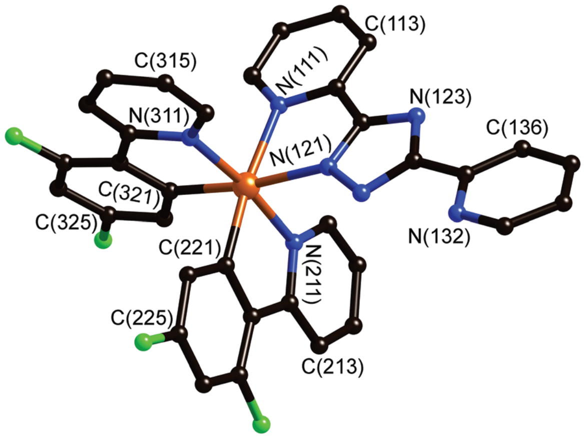

Figure 2.05. Structure of [Ir(fppy)$_2$L^{pytz}] from crystallographic data.

The crystal structure showed that the pendant bidentate site of the pytz compound involved N(132) of the pyridyl ring and either N^2 or N^4 position of the triazole ring, depending on the orientation of the pendant pyrdiyl ring. It was also evident that the triazole ring of the pytz unit is coordinated through the N^1 atom [N(121)].

Unit cell packing showed π-π stacking interactions of the phenyl groups of the coordinate phenyl pyridine substituents with a distance of 3.279 Å (**Fig. 2.06**). Hydrogen to fluorine H-bonding interactions were also observed with a bond distance of 2.330 Å. This is highlighted between H(214) of a pyridyl ring and F(228) of a phenyl ring in **Fig. 2.07**.

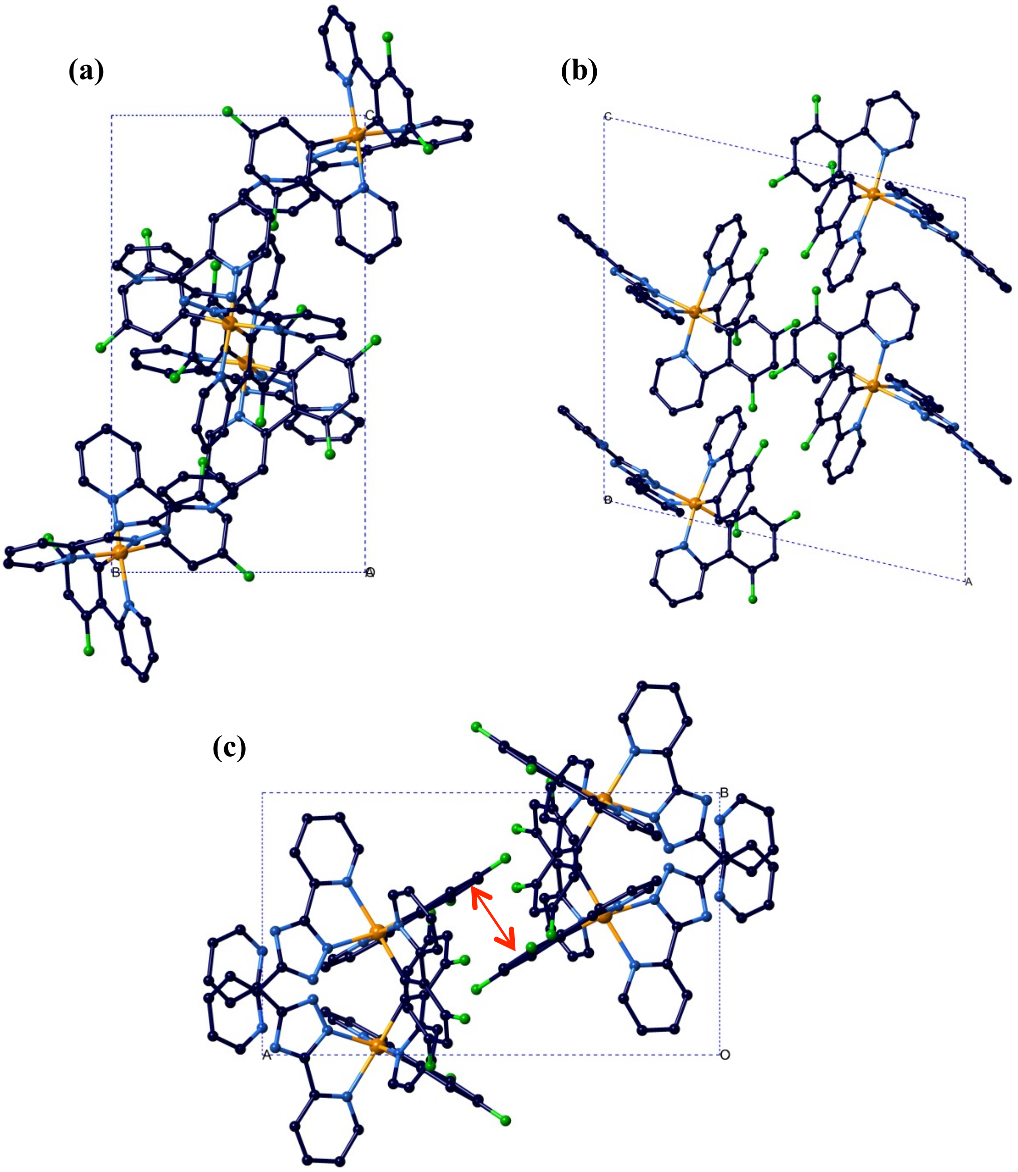

Figure 2.06. Unit cell displaying the packing of the (a) a-face (b) b-face and (c) c-face. π-π stacking interactions of the phenyl groups is observed between the phenyl units of the phenylpyridine groups (red arrow).

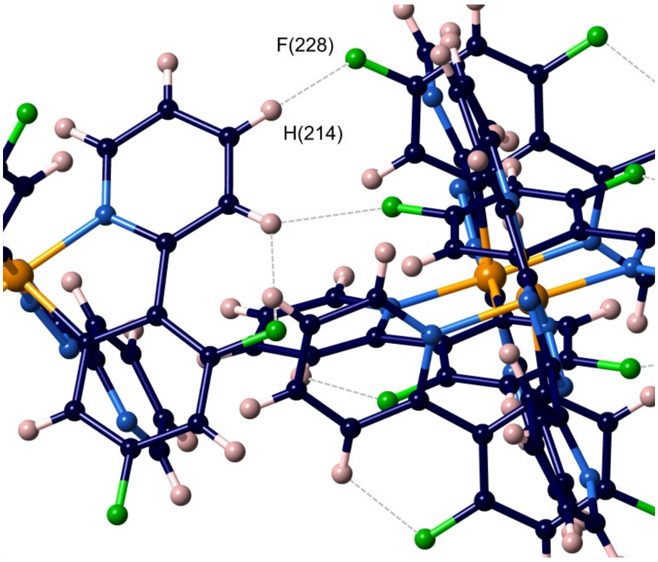

Figure 2.07. Hydrogen-bonding interactions between H(214) of a pyridyl ring and F(228) of a phenyl ring.

The ORTEP plot is given in **Fig. 2.08** below.

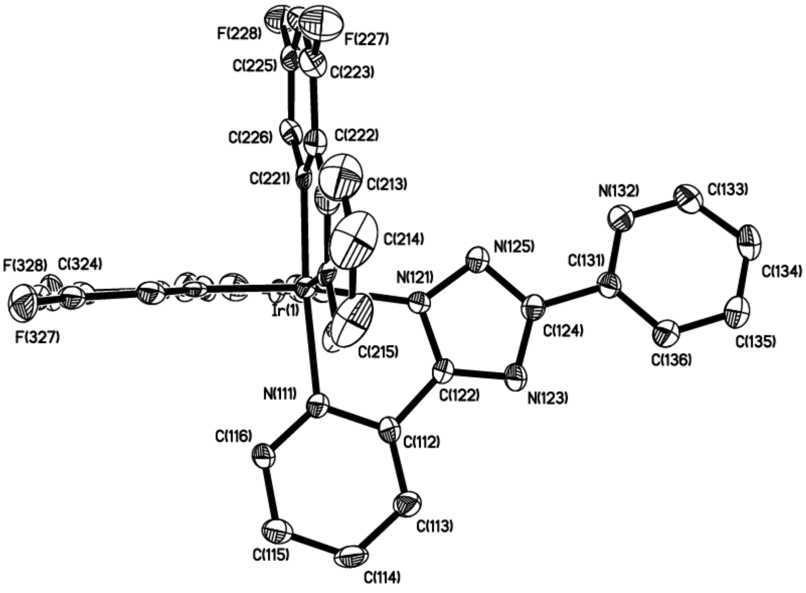

Figure 2.08. ORTEP plot of [Ir(fppy)$_2$L^{pytz}] at 50% probability.

2.4 Luminescence Properties of [Ir(fppy)$_2$L^{pytz}]

2.4.1 UV/Vis Absorption

The UV/Vis spectrum of [Ir(fppy)$_2$L^{pytz}] was recorded in aerated CH_2Cl_2 at room temperature (**Fig. 2.09**).

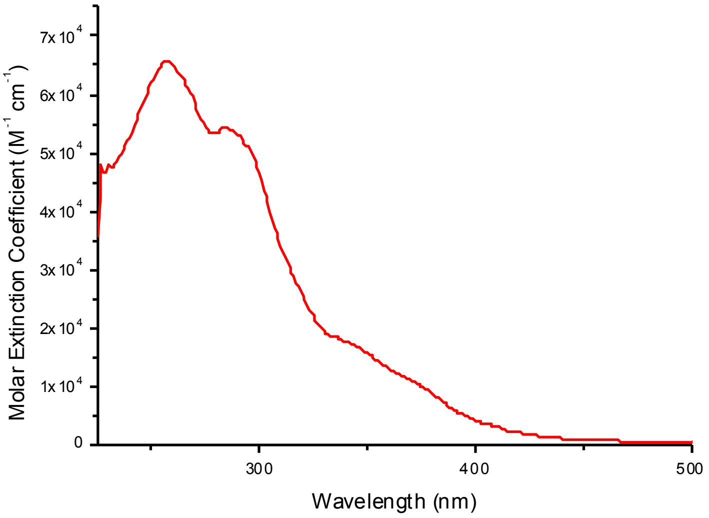

Figure 2.09. UV/Vis absorption spectrum of [Ir(fppy)$_2$L^{pytz}] [7.10 × 10^{-6} M] in CH_2Cl_2 at 298 K.

Tentative assignment of the spectrum is provided in **Table 2.01**.

λ_{max}/nm	Absorption ε/M^{-1} cm^{-1}	Assignment
259	65,000	π-π*
288	54,000	π-π*
346	17,000	MLCT (sh)
371	11,000	MLCT (sh)
453	1,000	MLCT (broad)

Table 2.01. UV/Vis absorption data for [Ir(fppy)$_2$L^{pytz}] [7.10 × 10^{-6} M] in CH_2Cl_2 at 298 K.

The high-energy absorption bands at (< 346 nm) are assigned to intraligand π-π* transitions localised on the coordinated ligands. The highest energy absorption at 259 nm is due to transitions centred on the fluorinated ppy ligands and the absorption at 288 nm is attributed to the transitions centred on the triazole ligand.[13] The weaker lower-energy transitions (346-453 nm) are attributed to the spin-allowed ^{1}MLCT and spin-forbidden ^{3}MLCT transitions which are typical for complexes containing heavy metal atoms resulting in strong spin-orbit coupling.[17] The excitation spectrum was measured and overlaid with the absorption spectrum (**Fig. 2.10**). The good match between these 2 spectra indicates that the emission observed emanates from the compound.

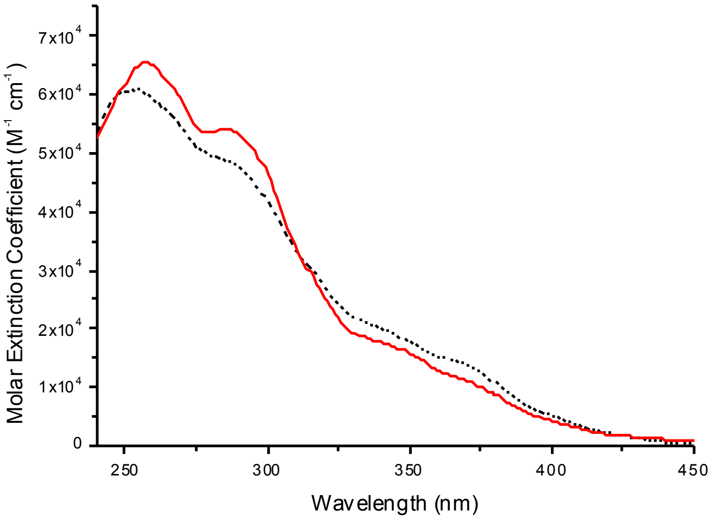

Figure 2.10. Excitation spectrum of [Ir(fppy)$_2$L^{pytz}] (registered at 460 nm) (black dashed line) overlaid with the absorption spectrum (red line) in CH_2Cl_2.

2.4.2 Emission Properties

The luminescence spectrum of [Ir(fppy)$_2$L^{pytz}] was recorded in CH_2Cl_2 at room temperature. The emission of the complex was blue (λ_{max} = 460 nm). The complex was designed to emit blue light as this means that the excited state energy is high enough to sensitise Eu(III) and Tb(III). The emission spectrum of the complex is given in **Fig. 2.11**.

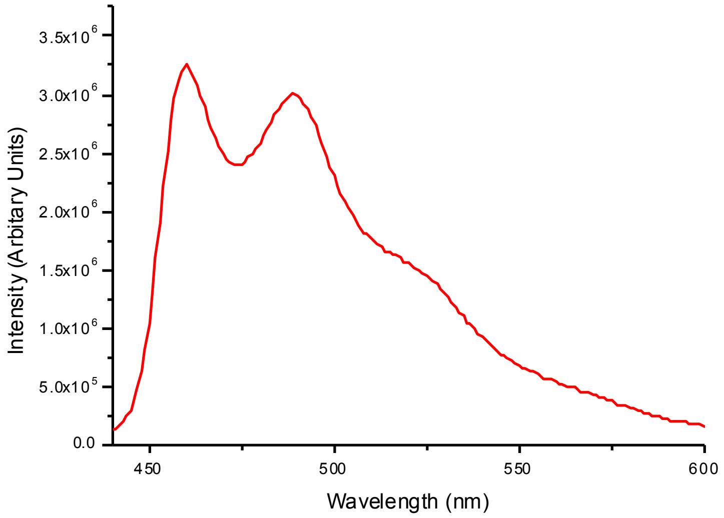

Figure 2.11. Emission spectrum of [Ir(fppy)$_2$L^{pytz}] [1.30 × 10^{-4} M] in CH_2Cl_2 at 298 K. Excitation at 425 nm.

The emission spectrum in CH_2Cl_2 is typical of Ir(fppy)$_2$L-type complexes. The vibronic structure of the emission band indicated a large amount of ^{3}LC character with the excited state being a mixture of ^{3}LC and ^{3}MLCT states.[18,19] The complex has a luminescence lifetime of 140 ns in air-equilibrated CH_2Cl_2. In EtOH/MeOH (4:1) glass at 77 K there was a small rigidochromic shift of the emission maximum from 460 nm to 452 nm (**Fig. 2.12**), giving a triplet excited state energy of 22,100 cm^{-1}. The fast solvent reorganisation at room temperature can stabilise the charge transfer state before emission takes place, therefore the stabilisation of charge transfer states is impeded at 77 K which explains the blue-shift in the emission wavelength.[20] A strong increase in emission intensity was also observed at 77 K which can be attributed to the impediment of the non-radiative relaxation processes, such as internal conversion, which compete with the radiative relaxation pathways at room temperature. The emission of complex had a quantum yield of $\phi = 0.034$ in aerated CH_2Cl_2 which was calculated against a known standard.[21]

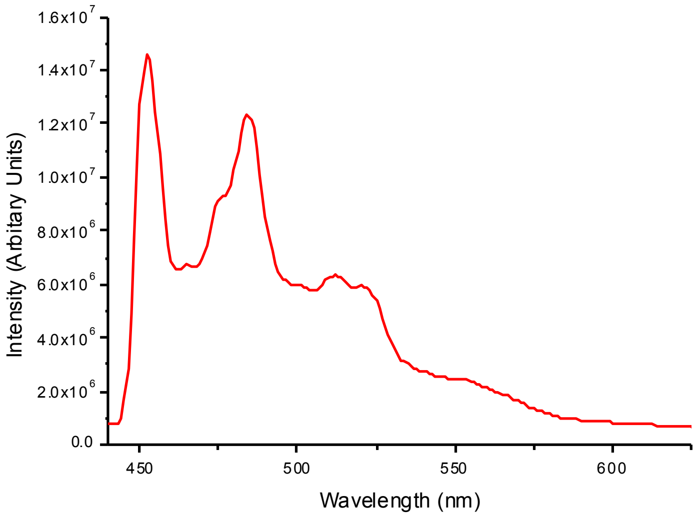

Figure 2.12. Emission spectrum of [Ir(fppy)$_2$L^{pytz}] [1.30 × 10^{-4} M] at 77 K in EtOH/MeOH (4:1, v/v). Excitation at 425 nm.

2.4.3 Titration with [Eu(hfac)$_3$.2H$_2$O]

The Ir(III)/Eu(III) dyad was prepared by titration of [Eu(hfac)$_3$.2H$_2$O] to a solution of [Ir(fppy)$_2$L^{pytz}] in CH$_2$Cl$_2$ at room temperature.[7,9] Binding of [Eu(hfac)$_3$] occurs at the pendant triazole-pyridine site with the displacement of the two water molecules from the Eu(III) coordination sphere (**Scheme 2.04**).

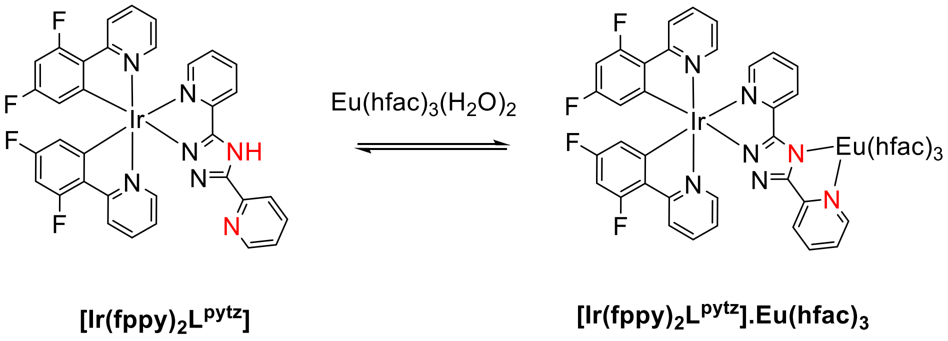

Scheme 2.04. Binding of [Eu(hfac)$_3$] to the pendant triazole-pyridine site (red) of [Ir(fppy)$_2$L^{pytz}].

Addition of [Eu(hfac)$_3$.2H$_2$O] occurred until no significant change in Ir(III) – based luminescence was observed, at which point it was considered the formation of the Ir(III)/Eu(III) dyad was complete. The emission spectra of the titration are given in **Fig. 2.13**.

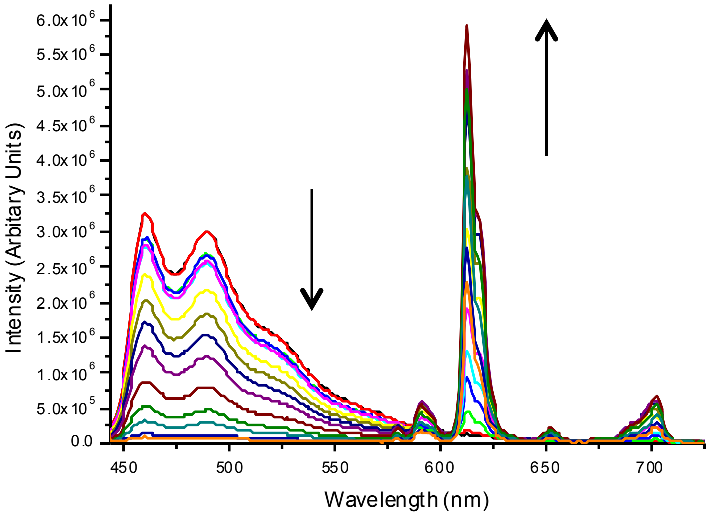

Figure 2.13. Emission spectra of [Ir(fppy)$_2$L^{pytz}] [1.30 × 10^{-4} M] titrated with [Eu(hfac)$_3$.2H$_2$O] [1.24 × 10^{-3} M] in CH$_2$Cl$_2$ at 298 K. Excitation at 425 nm.

As mentioned previously, the Ir(III) complex has a triplet energy level of 22,100 cm^{-1}, which is considerably higher than the luminescent f-f energy level of the Eu(III) species which is at around 17,500 cm^{-1}. Therefore energy-transfer from Ir(III) to Eu(III) is allowed with no BET process. Upon addition of [Eu(hfac)$_3$.2H$_2$O], quenching of Ir(III)–based emission was observed with a simultaneous increase in Eu(III)–based emission, where the manifold of Eu(III) emission peaks observed at λ_{max} of 578 nm, 590 nm, 612 nm, 650 nm and 700 nm are attributed to the $\{^5D_0 \rightarrow {}^7F_0\}$, $\{^5D_0 \rightarrow {}^7F_1\}$, $\{^5D_0 \rightarrow {}^7F_2\}$, $\{^5D_0 \rightarrow {}^7F_3\}$, and $\{^5D_0 \rightarrow {}^7F_4\}$ transitions of Eu(III) respectively.

The excitation wavelength was set at 425 nm into the Ir-based absorption manifold in order to ensure there was no direct excitation of the Eu(III) complex. Ir-based emission is almost completely quenched after 500 μL addition (2 molar equivalents) of [Eu(hfac)$_3$.2H$_2$O] and the intensity of the sensitised Eu-based emission is very high, indicating essentially complete Ir → Eu PEnT as a result of a short and fully conjugated bridging ligand pathway in the complex.

Lifetime measurements were recorded throughout the titration; only a single exponential decay for Ir-based luminescence was observed with a lifetime of *ca.* 140 ns assigned to the unquenched Ir(III) before the Ir(III)/Eu(III) dyad formed. This lifetime remained consistent until the end of the titration and a shorter-lived lifetime was not observed. This confirmed that Ir(III)-based emission was fully quenched in the Ir(III)/Eu(III) dyad. Although residual emission of Ir (III) was observed at the end of the titration, this was very weak and was attributed to traces of the free complex (**scheme 2.04**).

The conjugated bridging pathway of the complex enabled a Dexter-type energy-transfer *via* the electronic coupling between the metal centres.[1,6] Purely Förster-type energy-transfer was ruled out due to poor spectral overlap between the Ir-centred emission and the weak Eu-based f-f absorption manifold, therefore the critical distance for Förster-type energy-transfer is *ca*. 3 Å based on previous calculations from the Ward group.[8]

White light emission was achieved during the titration upon 150 μL addition (0.6 molar equivalents) of [Eu(hfac)$_3$.2H$_2$O] due to a balance of red/blue components (**Fig. 2.14**) with CIE coordinates of (0.29, 0.33).

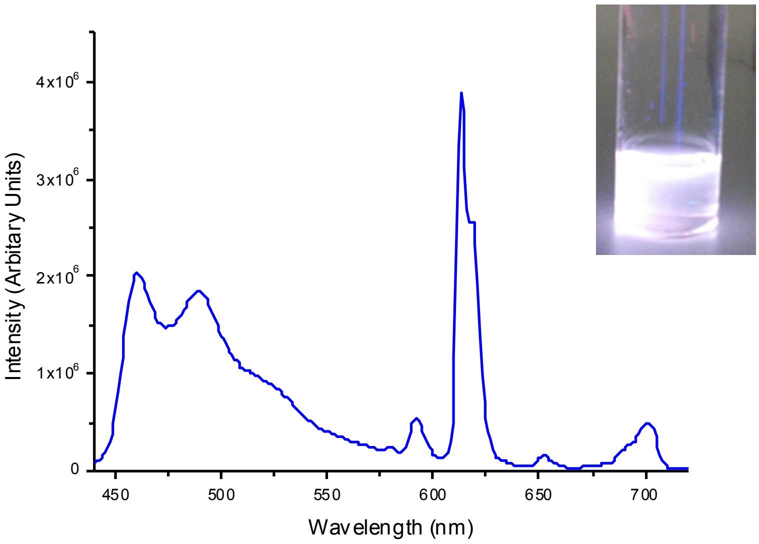

Figure 2.14. Emission spectrum of [Ir(fppy)$_2$L^{pytz}] during 0.6 equivalent addition of [Eu(hfac)$_3$.2H$_2$O] in CH$_2$Cl$_2$ to give emission of white light from a balance of blue (Ir-based) and red (Eu-based) emission.

As white emission was observed at only 0.6 molar equivalent addition of [Eu(hfac)$_3$.2H$_2$O], the colour was a result of a combination of blue emission from the free (unbound) [Ir(fppy)$_2$L^{pytz}] and red emission from the bound complex, [Ir(fppy)$_2$L^{pytz}].Eu(hfac)$_3$; the two compounds were in equilibrium at that stage of the titration. Nonetheless, the titration showed good complementarity of the two spectral colours (blue and red) from the Ir-based and Eu-based emission to give a white-light emitting system.

2.4.4 Titration with [Tb(hfac)$_3$.2H$_2$O]

The photophysical behaviour of [Ir(fppy)$_2$L^{pytz}] was also studied in the same manner as above using [Tb(hfac)$_3$.2H$_2$O]. The emission spectra of the titration are given in **Fig. 2.15**.

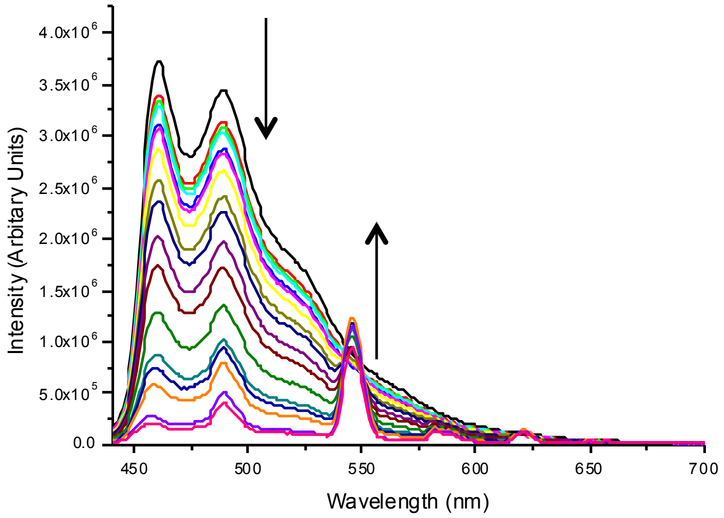

Figure 2.15. Emission spectra of [Ir(fppy)$_2$L^{pytz}] [1.30 × 10^{-4} M] titrated with [Tb(hfac)$_3$.2H$_2$O] [1.30 × 10^{-3} M] in CH$_2$Cl$_2$ at 298 K. Excitation at 425 nm.

Typical Tb(III) emission peaks grew in during the titration with the peak at 545 nm being most intense, resulting from the $^5D_4 \rightarrow {}^7F_5$ transition. Quenching of the Ir(III) component was observed with a simultaneous increase in the intensity of the Tb(III) component. Near-complete quenching (>90%) was observed after 1500 µL addition (≈ 7 equivalents) of [Tb(hfac)$_3$.2H$_2$O]. Time-resolved measurements again showed a single exponential decay of the lifetime of *ca.* 140 ns associated with the Ir centre, without a second lifetime throughout the titration. This suggested that the Ir(III)-based emission was fully quenched in the Ir(III)/Tb(III) dyad. The lifetime of Ir(III) that was observed at the end of the titration was attributed to traces of the free complex.

The intensity of the Tb(III)-based emission was very weak when compared to the titration with the Eu(III) analogue. This can be justified by the fact that emissive $^5D_4$ level of Tb(III) is around 20,400 cm^{-1}, which is approximately 1700 cm^{-1} lower than that of the Ir(III) excited state, therefore thermally-activated back energy-transfer to the Ir-based excited state followed by non-radiative decay would be expected. This was in agreement with previous work by Sato and Wada who showed that optimal sensitisation of Tb(III) triplet states required an energy-gap of 2000-3000 cm^{-1} to avoid back energy-transfer.[22]

2.4.5 Titration with [Gd(hfac)$_3$.2H$_2$O]

The complex was also titrated with [Gd(hfac)$_3$.2H$_2$O] in the same manner described previously. Gd(III) was used as a control experiment because the lowest excited state of is approximately 10,000 cm^{-1} higher ($^6P_{7/2}$ ≈ 32,000 cm^{-1}) than the Ir(III) ^{3}LC/^{3}MLCT states. Therefore no direct energy-transfer could occur to the lanthanide ion, however the electronic and structural effects of Eu(III) and Tb(III) was mimicked when attached to the pendant triazole-pyridine unit. The emission spectra measured during the titration are given in **Fig. 2.16**.

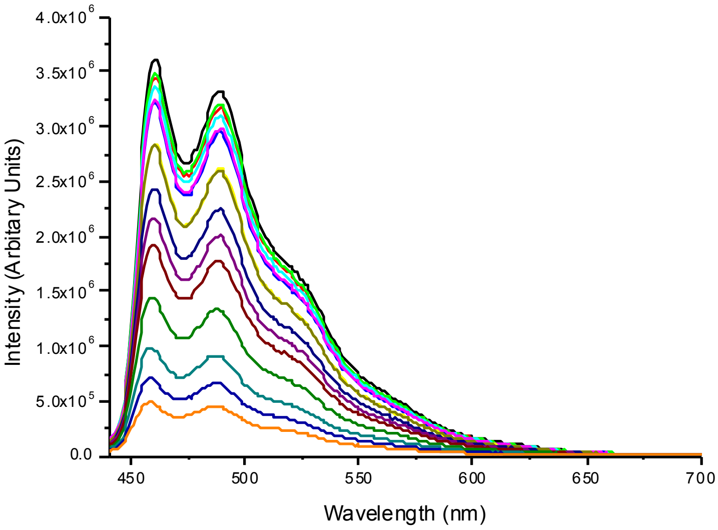

Figure 2.16. Emission spectra of [Ir(fppy)$_2$L^{pytz}] [1.30 × 10^{-4} M] titrated with [Gd(hfac)$_3$.2H$_2$O] [1.23 × 10^{-3} M] in CH$_2$Cl$_2$ at 298 K. Excitation at 425 nm.

An interesting observation was made during the titration in that the emission of Ir(III) showed near-complete quenching with the addition of Gd(III). Lifetime measurements showed a single component of *ca.* 140 ns from the Ir(III) centre, however after *ca.* 1 molar equivalent addition of [Gd(hfac)$_3$] a shorter second component of *ca.* 50 ns was observed. This was attributed to the partially quenched Ir(III) luminescence in the Ir(III)/Gd(III) dyad. This was not expected, as a PEnT process to Gd(III) could not occur. This could be explained by a different quenching mechanism. In 2007 the

Ward group reported how, in an anthracene-Gd dyad, the anthracene-based luminescence was completely quenched when bound to [Gd(hfac)$_3$] due to an electron-transfer mechanism.[5] The anthracene contained a pendant benzimidazolyl-pyridine unit, thus had an N^N binding site for the lanthanide (**Fig. 2.17**), like the [Ir(fppy)$_2$L^{pytz}] complex. The anthracene acted as an electron-donor which resulted in a PET to the diimine N^N unit which generated an (anthracenyl)$^{\bullet+}$ / (N^N)$^{\bullet-}$ state.

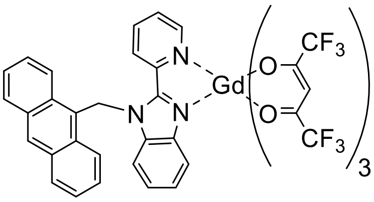

Figure 2.17. Benzimidazolyly-pyridine containing anthracene complex bound to [Gd(hfac)$_3$] reported by the Ward group.[5]

PET properties of Ir(III) complexes based on [Ir(N^C)$_2$N^N]$^+$ architecture (where N^C denotes a phenypyidine unit and N^N denotes a diimine moiety) have been reported by the Bernhard group where a series of these complexes were used for the catalytic reduction of protons from water for H_2 generation.[23,24]

These reports for the occurrence of electron-transfer based quenching mechanisms for Ir(III) complexes and the ability of [Gd(hfac)$_3$] to facilitate this mechanism supports the suggested PET mechanism for the quenching of the Ir(III)-based luminescence of [Ir(fppy)$_2$L^{pytz}].

2.4.6 Quantum Yield of Emission of [Ir(fppy)$_2$L^{pytz}]

The quantum yield (Φ) of [Ir(fppy)$_2$L^{pytz}] was calculated to be $\Phi = 0.034$ by measuring against Ir(ppy)$_3$ as a standard in aerated CH_2Cl_2. This standard was calibrated against the same molecule in aerated toluene ($\Phi = 0.04$) and against Ru(bpy)$_3$.Cl_2.$6H_2O$ in aerated water ($\Phi = 0.042$).[21,25,26]

The quantum yield was calculated using **Equation 2.01** below:

$$\Phi_s = \Phi_r \times \left(\frac{I_s}{(1-10^{-A})_s}\right) \times \left(\frac{(1-10^{-A})_r}{I_r}\right) \times \left(\frac{\eta_s^2}{\eta_r^2}\right)$$

Equation 2.01. Φ = Quantum yield, *A* = absorbance at excitation wavelength, *I* = integrated emission intensity, η = solvent refractive index, *s* = sample, *r* = reference.

2.5 Luminescence Properties of [Ir(fppy)$_2$L^{pic}]

2.5.1 UV/Vis Absorption

The UV/Vis spectrum of [Ir(fppy)$_2$L^{pic}] was recorded in aerated CH_2Cl_2 at room temperature (**Fig. 2.18**).

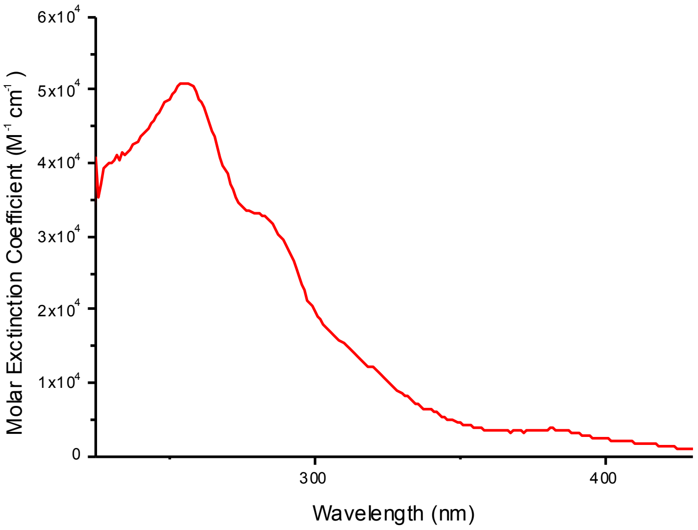

Figure 2.18. UV/Vis spectrum of complex [Ir(fppy)$_2$L^{pic}] [5.21 × 10^{-6} M] in CH_2Cl_2 at 298 K.

Assignment of the spectrum is provided in **Table 2.02** below.

λ_{max}/nm	Absorption ε/M^{-1} cm^{-1}	Assignment
256	51,000	π-π*
284	32,000	π-π*
322	11,000	MLCT (sh)
383	3,600	MLCT (sh)
413	1,800	MLCT (broad)

Table 2.02. UV/Vis absorption data for [Ir(fppy)$_2$L^{pic}] [5.21 × 10^{-6} M] in CH_2Cl_2 at 298 K.

The profile of the spectrum was similar to that of the triazole complex; the high-energy absorption bands (<320 nm) are assigned to π-π* transitions localised on the coordinated ligands. The lower energy transitions are weaker (320-420 nm) and these can be attributed to the spin-allowed ^{1}MLCT and spin-forbidden ^{3}MLCT transitions. The excitation spectrum was measured and overlaid with the absorption spectrum (**Fig. 2.19**). The good match between these 2 spectra indicates that the emission observed emanates from the compound.

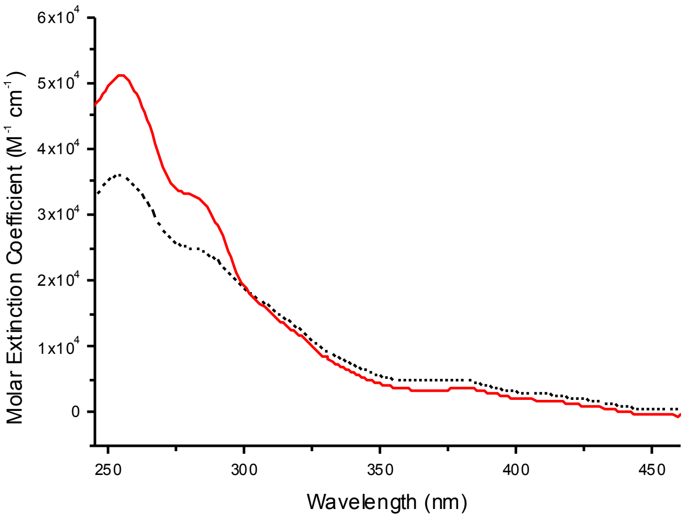

Figure 2.19. Excitation spectrum of [Ir(fppy)$_2$L^{pic}] (registered at 470 nm) (black dashed line) overlaid with the absorption spectrum (red line) in CH_2Cl_2.

2.5.2 Emission Properties

The emission spectrum of [Ir(fppy)$_2$L^{pic}] was also recorded in CH_2Cl_2 at room temperature. The complex had a slightly lower excited state energy (λ_{max} = 472 nm) than the triazole complex. The emission spectrum of the complex is given in **Fig. 2.20**.

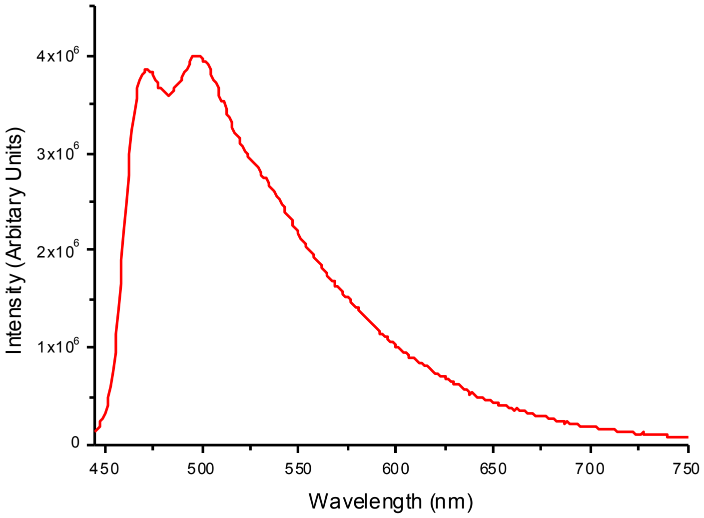

Figure 2.20. Emission spectrum of [Ir(fppy)$_2$L^{pic}] [1.04 x 10^{-4} M] in CH_2Cl_2 at 298 K. Excitation at 441 nm.

The highest-energy component of the spectrum was at 472 nm and a second intense band was observed at 495 nm. The emission band had a vibronic structure; indicative of a large amount of ^{3}LC character. The typical mixtures of ^{3}LC and ^{3}MLCT states were the main excited states of the complex. The emission recorded at 77 K in EtOH/MeOH (4:1) glass showed a small hypsochromic shift to 458 nm (**Fig. 2.21**), consistent with the ^{3}LC state. There was also a strong increase in the intensity of emission which was attributed to the impediment of the nonradiative relaxation processes. The emission of the complex had a quantum yield of $\phi = 0.04$ in aerated CH_2Cl_2 which was calculated against a known standard.[21]

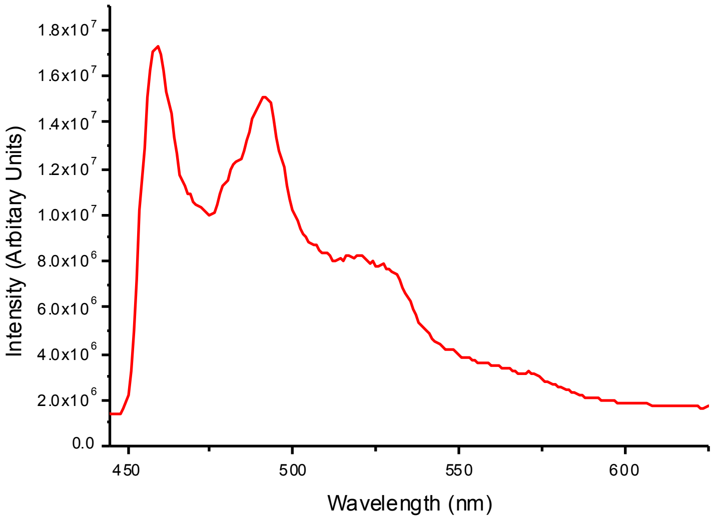

Figure 2.21. Emission spectrum of [Ir(fppy)$_2$L^{pic}] [1.04 × 10^{-4} M] at 77 K in EtOH/MeOH (4:1, v/v). Excitation at 441 nm.

2.5.3 Titration with [Eu(hfac)$_3$.2H$_2$O]

The Ir(III)/Eu(III) dyad was prepared by titration of [Eu(hfac)$_3$.2H$_2$O] to a solution of [Ir(fppy)$_2$L^{pic}] in CH$_2$Cl$_2$ at room temperature. Binding of [Eu(hfac)$_3$] occurs at the pendant pyridyl-pyrazole site with the displacement of the two water molecules from the coordination sphere (**Scheme 2.05**).

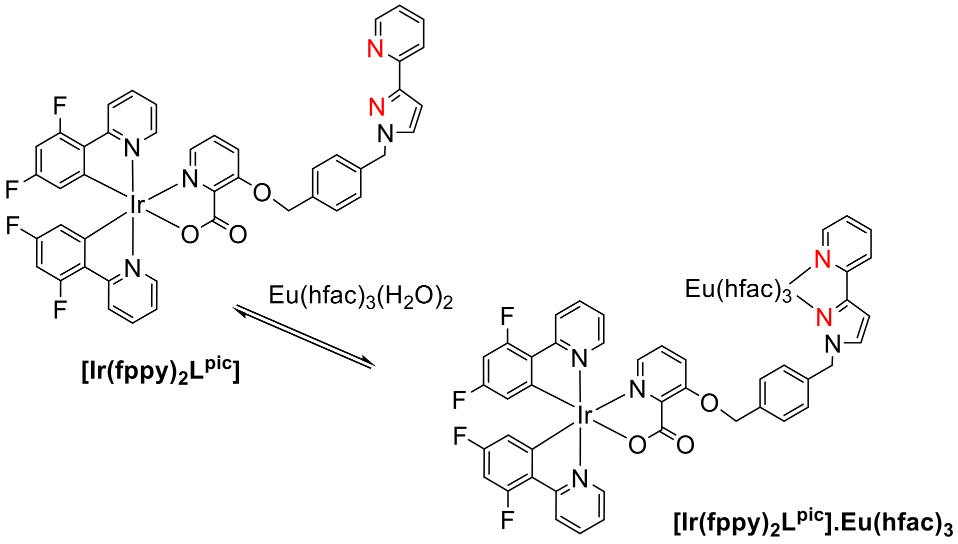

Scheme 2.05. Binding of [Eu(hfac)$_3$] to the pendant pyridyl-triazole site (red) of [Ir(fppy)$_2$L^{pic}].

Addition of [Eu(hfac)$_3$.2H$_2$O] was continued until no significant change in Ir(III) – based luminescence was observed, at which point it was considered the formation of the Ir(III)/Eu(III) dyad was complete. The emission spectra recorded during the titration is given in **Fig. 2.22**.

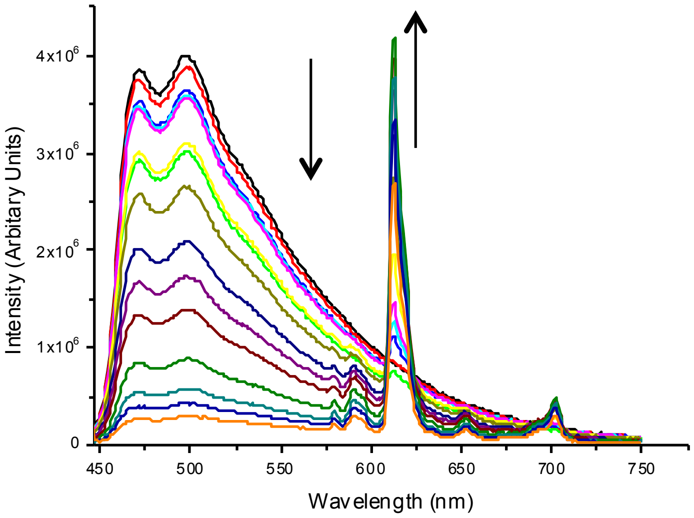

Figure 2.22. Emission spectra of [Ir(fppy)$_2$L^{pic}] [1.04 × 10^{-4} M] titrated with [Eu(hfac)$_3$.2H$_2$O] [1.24 × 10^{-3} M] in CH$_2$Cl$_2$ at 298 K. Excitation at 441 nm.

The emission colour of the complex was cyan before Eu(hfac)$_3$.2(H$_2$O) was added. [Ir(fppy)$_2$L^{pic}] has a triplet energy level of 21,800 cm^{-1} which allows energy-transfer to Eu(III) with no BET process. Upon addition of Eu(hfac)$_3$.2(H$_2$O) the manifold of Eu(III) emission peaks with λ_{max} of 578 nm, 590 nm, 612 nm, 650 nm and 700 nm was observed, attributed to the Eu(III) ($^5D_0 \rightarrow {}^7F_0$), ($^5D_0 \rightarrow {}^7F_1$), ($^5D_0 \rightarrow {}^7F_2$), ($^5D_0 \rightarrow {}^7F_3$) and ($^5D_0 \rightarrow {}^7F_4$) transitions respectively. The excitation wavelength was set to 441 nm into the Ir-based absorption manifold, in order to ensure there was no direct excitation of the Eu(III) complex. There was a steady decrease in the Ir(III) based luminescence after upon addition of Eu(hfac)$_3$.2H$_2$O. The Ir(III)-centred emission intensity of the complex was quenched by >90% after 700 μL (2 equivalents) addition of Eu(hfac)$_3$.2H$_2$O.

The decay trace of the free Ir(III) complex showed a biexponential decay with 100 ns as the major component and a minor component of 240 ns. During the titration, a three exponential decay was observed, where the two Ir(III) lifetimes remained at *ca*. 250 ns and 100 ns, however a dominant short-lived component of ~13 ns was observed which corresponded to the quenched Ir(III)-based emission of the Ir(III)/Eu(III) dyad.

2.5.4 Titration with [Tb(hfac)$_3$.2H$_2$O]

[Ir(fppy)$_2$L^{pic}] was also titrated with [Tb(hfac)$_3$.2H$_2$O]. The luminescence spectra recorded during the titration are given in **Fig. 2.23**.

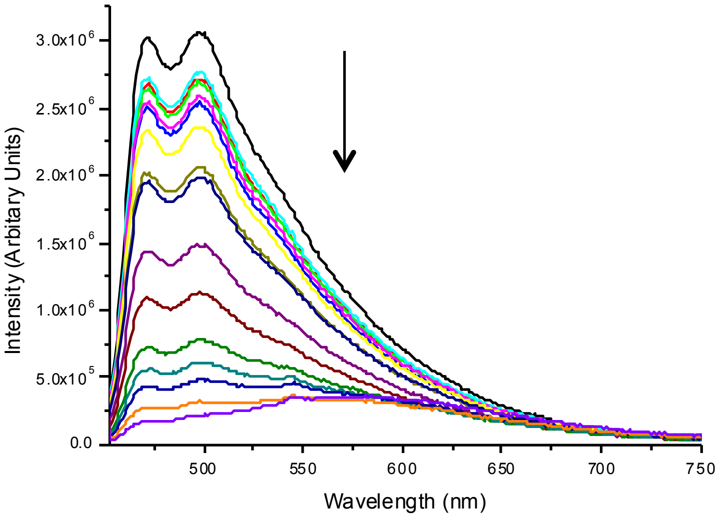

Figure 2.23. Emission spectra of [Ir(fppy)$_2$L^{pic}] [1.04 × 10^{-4} M] titrated with [Tb(hfac)$_3$.2H$_2$O] [1.28 × 10^{-3} M] in CH_2Cl_2 at 298 K. Excitation at 441 nm.

Upon addition of Tb(hfac)$_3$.2(H$_2$O) the intensity of the Ir(III) based emission intensity decreased by a similar amount (>90%) to the titration with [Eu(hfac)$_3$.2H$_2$O]. Unlike the titration with Eu(III), the manifold of narrow Tb(III) emission peaks was not observed as the excited state energy of the complex at 21,800 cm^{-1} means the Ir → Tb energy-transfer gradient is only around 1400 cm^{-1}, therefore thermally activated Tb → Ir BET was allowed, quenching any Tb-based emission.

There was also a loss of the fine structure, accompanied by a red-shift of the Ir-based emission during the titration, which lead to a broad and featureless spectrum in the Ir(III)/Tb(III) dyad. The Ir(III)-based lifetimes during the titration were similar to the titration with [Eu(hfac)$_3$.2H$_2$O], where the data required a three exponential decay for a satisfactory fit. The short-lived component of ~20 ns was ascribed to the residual Ir(III) emission from the Ir(III)/Tb(III) dyad.

2.5.5 Titration with [Gd(hfac)$_3$.2H$_2$O]

[Ir(fppy)$_2$L^{pic}] was also titrated with Gd(hfac)$_3$.2H$_2$O. The emission spectra recorded during the titration are given in **Fig. 2.24**.

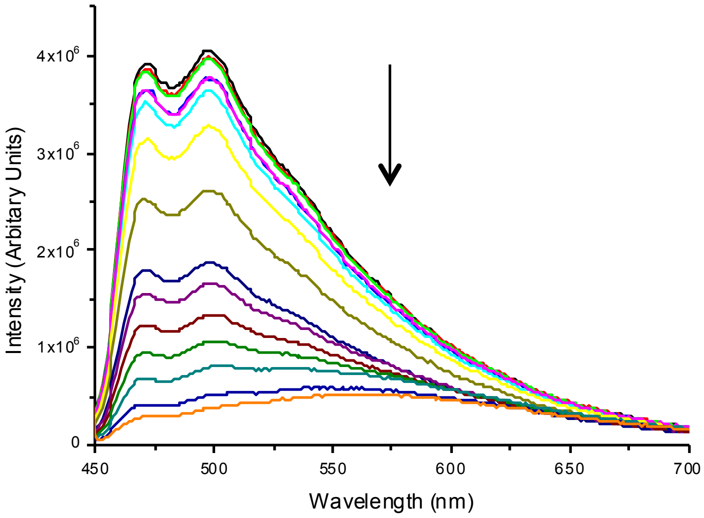

Figure 2.24. Emission spectra of [Ir(fppy)$_2$L^{pic}] [1.04 × 10^{-4} M] titrated with [Gd(hfac)$_3$.2H$_2$O] [1.23 × 10^{-3} M] in CH$_2$Cl$_2$ at 298 K. Excitation at 441 nm.

Gd(hfac)$_3$.2H$_2$O again was used as a control experiment. There cannot be any Ir(III) → Gd(III) PEnT as the energy of the lowest excited state of Gd(III) is approximately 10,000 cm^{-1} higher than the Ir(III) excited state. Interestingly the spectrum displayed a similar result to the Tb(III) analogue where substantial quenching of the Ir(III)-based emission was observed accompanied by a red-shift in the residual spectrum. The lifetime measurements were identical to that of the previous titrations where a third component of ~18 ns was observed from the quenched Ir(III) luminescence of the Ir(III)/Gd(III) dyad. Direct energy-transfer was ruled out as the quenching mechanism as it was not possible for the Ir(III)/Gd(III) dyad and energetically unlikely for the Ir(III)/Tb(III) dyad. A likely explanation for this observation is that PET is occurring from the Ir(III) centre to the coordinated pyridine-pyrazole unit of the bound complex and this occurs equally well in the Ir(III)/Tb(III) and Ir(III)/Gd(III) dyads. This is discussed in further detail later in this chapter.

2.5.6 Quantum Yield of Emission of [Ir(fppy)$_2$L^{pic}]

The quantum yield (Φ) of [Ir(fppy)$_2$L^{pic}] was calculated to be Φ = 0.04 in aerated CH$_2$Cl$_2$ by measuring against Ir(ppy)$_3$ as a standard. This standard was calibrated against the same molecule in aerated toluene (Φ = 0.04) and against

$Ru(bpy)_3.Cl_2.6H_2O$ in aerated water (Φ = 0.042).[21,25,26] The quantum yield was calculated using **Equation 2.01** described previously.

2.5.7 Conclusion of the Photophysical Properties

Both [$Ir(fppy)_2L^{pytz}$] and [$Ir(fppy)_2L^{pic}$] described showed the same pattern of quenching, with the Ir(III)-based luminescence being quenched during the titrations with [$Gd(hfac)_3.2H_2O$]. In these cases, photoinduced energy-transfer was ruled out as the quenching mechanism as this was energetically impossible.

The quenching mechanism in the Ir(III)/Gd(III) dyads was likely to be *via* photoinduced electron-transfer, by the formation of [$Ir^{IV}]^{\bullet}$-N'$N^{\bullet -}$ charge separated species. The formation of the species would be made possible due to the [N'N] coordinating group being made electron-deficient when coordinated to the electropositive lanthanide ions. Previous research was found to support this behaviour in Ir(III) complexes.[5,24,27,28] Additionally, luminescence from Eu(III) and Tb(III) could have been generated indirectly from the [$Ir^{IV}]^{\bullet}$-N'$N^{\bullet -}$ charge-separated species provided there was sufficient energy in the collapse of the species by back electron-transfer.

When the emission of the Ir(III)/Eu(III) and Ir(III)/Tb(III) dyads were compared with that of the Ir(III)/Gd(III) dyads, additional quenching was observed. The most probable mechanism for this is additional Dexter energy-transfer which is supported by evidence from previous research in the Ward group.[6,8]

For [$Ir(fppy)_2L^{pic}$], the rate constant for the photoinduced electron-transfer process in the Ir(III)/Gd(III) dyad was calculated from the lifetimes obtained from the Ir/Gd dyad using **Equation 2.02**.

$$k_{PET} = \tau_q^{-1} - \tau_u^{-1}$$

Equation 2.02. k_{PET} = Rate of photoinduced electron-transfer, τ_q = lifetime of quenched Ir(III), τ_u = lifetime of unquenched Ir(III).

The lifetimes of 100 ns and 18 ns for τ_u and τ_q respectively gave a k_{PET} of 5×10^7 s^{-1}.

Using **Equation 2.02**, the Dexter energy-transfer rate constant (k_{EnT}) was calculated to be 2×10^7 s^{-1} using the difference between the quenched Ir(III) lifetimes of the Ir(III)/Gd(III) (18 ns) and Ir(III)/Eu(III) dyads (5 ns). This value was in the same order as the PET process.

The PET rate constant of $[Ir(fppy)_2L^{pytz}]$ was calculated using the lifetimes of the Ir(III)/Gd(III) dyad, where the Ir(III)-based lifetime of 140 ns was quenched to 50 ns. This gave a k_{PET} of 1.3×10^7 s^{-1}. As a second lifetime of the quenched Ir(III) was not observed in either the Ir/Eu or the Ir/Tb dyads, therefore the rate of energy-transfer could not be calculated. Although the complex $[Ir(fppy)_2L^{pic}]$ contained saturated methylene bridging groups, the near complete quenching observed in the Ir(III)/Gd(III) dyad could be explained by the presence of the anionic carboxylate group of the picolinate ligand, making the Ir centre electron-rich. Previous work from the Hong group showed there was a reduction of the Ir(III)/Ir(IV) redox potential by 0.13 V when a neutral bipyridyl (bpy) ligand was replaced with a picolinate ligand.[29] Cyclic voltammetry measurements were carried out on $[Ir(fppy)_2L^{pic}]$ (**Fig. 2.25**) which showed a symmetric wave which suggested a reversible one-electron couple at +0.87 V *vs* Fc/Fc^+ in CH_2Cl_2. When the Hong group compared two isostructural Ir(III) complexes, one containing a bpy ligand and the other containing a picolinate ligand, the Ir(III)/Ir(IV) redox potential of the picolinate-containing complex was reduced (by 0.37 V), with a stabilisation energy of *ca.* 3000 cm^{-1} *vs* the bpy complex. $[Ir(fppy)_2L^{pic}]$ gave a similar value (~ 3400 cm^{-1}) when compared to the reported bpy complex.

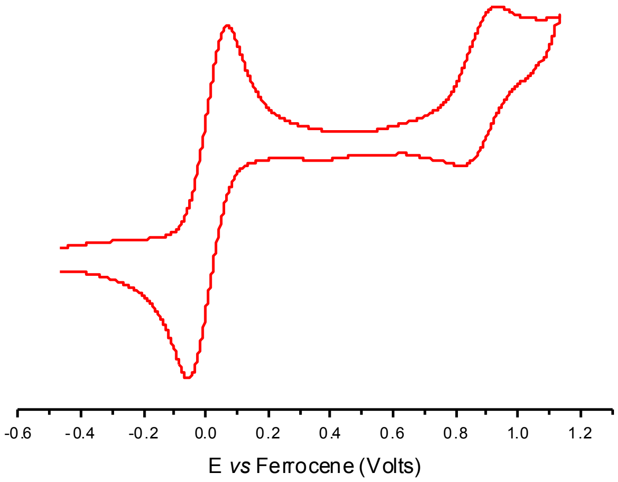

Figure 2.25. Cyclic voltammogram of [Ir(fppy)$_2$L^{pic}] *vs* Fc/Fc$^+$ in CH$_2$Cl$_2$ (0.1M *n*-Bu$_4$NPF$_6$) at 100 mVs^{-1}. (E$_{1/2}$ = 0.87 V, ΔE$_p$ = 50 mV).

[Ir(fppy)$_2$L^{pic}] is a poorer energy donor than [Ir(fppy)$_2$L^{pytz}], however it is a better electron donor and the extent of Ir-based quenching of the Ir(III)/Gd(III) dyad confirms that a PET process operates in parallel with direct energy-transfer in the Ir(III)/Eu(III) and Ir(III)/Tb(III) dyads.

2.6 Chapter Conclusion

The synthesis and photophysical properties of two blue-luminescent Ir(III) complexes were reported. The complexes were synthesised in relatively good yields and fully characterised. The photophysical studies showed that the complexes were able to generate sensitised luminescence from Eu(III) and Tb(III) centres. The mechanism of this was shown to be a combination of photoinduced energy-transfer and photoinduced electron-transfer mechanisms.

A PET process was clearly evident from the control studies using Ir(III)/Gd(III) dyads, where Ir(III)-based quenching was observed from these dyads even though Gd could not act as an energy-acceptor, whereby a $[\mathrm{Ir}^{\mathrm{IV}}]^{\bullet}$-N'$\mathrm{N}^{\bullet -}$ charge separated species could be formed by PET. A Dexter-type energy-transfer process was also evident by the fact that the Ir(III)/Eu(III) and Ir(III)/Tb(III) dyads displayed more quenching of the Ir(III)-based excited state compared to the Ir(III)/Gd(III) dyads.

For the Ir(III)/Eu(III) dyads, Ir(III)-based emission of $[\mathrm{Ir(fppy)_2L^{pytz}}]$ was completely quenched due to excellent energy-transfer from the Ir centre to the Eu centre, facilitated by a fully conjugated and short bridging ligand. Neither of the complexes were able to generate efficient Tb(III)-based luminescence, due to thermally-activated back energy-transfer from Tb(III) $^5D_4$ state to the Ir-based excited state as result of the small energy-transfer gradient (~1800 $\mathrm{cm^{-1}}$). In order for the Ir complexes to be good Tb sensitisers, Ir-based emission would need to be blue-shifted so the energy-transfer gradient would be increased thus avoiding thermally-activated back energy-transfer.

Further studies are required in order to determine if both complexes could be used as potential candidates for light-emitting electrochemical cells or OLED devices.[30,31]

2.7 References

1. D. L. Dexter, *J. Chem. Phys.,* 1953, **21**, 836.
2. T. Förster, *Discuss. Faraday Soc.,* 1959, **27**, 7.
3. D. Rehm and A. Weller, *Isr. J. Chem.,* 1970, **8**, 251.
4. D. Rehm and A. Weller, *Ber. Bunsenges. Phys. Chem.,* 1969, **73**, 834.
5. T. Lazarides, M. A. H. Alamiry, H. Adams, S. J. A. Pope, S. Faulkner, J. A. Weinstein and M. D. Ward, *Dalton Trans.,* 2007, 1484.
6. T. Lazarides, D. Sykes, S. Faulkner, A. Barbieri and M. D. Ward, *Chem. Eur. J.,* 2008, **14**, 9389.
7. T. Lazarides, N. M. Tart, D. Sykes, S. Faulkner, A. Barbieri and M. D. Ward, *Dalton Trans.,* 2009, 3971
8. D. Sykes, I. S. Tidmarsh, A. Barbieri, I. V. Sazanovich, J. A. Weinstein and M. D. Ward, *Inorg. Chem.,* 2011, **50**, 11323.
9. D. Sykes and M. D. Ward, *Chem. Commun.,* 2011, **47**, 2279.
10. R. M. Edkins, D. Sykes, A. Beeby and M. D. Ward, *Chem. Commun.,* 2012, **48**, 9979.
11. D. Sykes, S. C. Parker, I. V. Sazanovich, A. Stephenson, J. A. Weinstein and M. D. Ward, *Inorg. Chem.,* 2013, **52**, 10500.
12. S. Sprouse, K. A. King, P. J. Spellane, R. J. Watts, *J. Am. Chem. Soc.,* 1984, **106**, 6647.
13. E. Orselli, G. S. Kottas, A. E. Konradsson, P. Coppo, R. Fröhlich, L. De Cola, A. van Dijken and H. Börner, *Inorg. Chem.,* 2007, **46**, 11082.
14. A. K. Levine and F. C. Palilla, *Appl. Phys. Lett.,* 1964, **4**, 118.
15. C. Adachi, R. C. Kwong, P. Djurovich, V. Adamovich, M. A. Baldo, M. E. Thompson and S. R. Forrest, *Appl. Phys. Lett.,* 2001, **79**, 2082.
16. A. J. Amoroso, A. M. C. Thompson, J. C. Jeffery, P. L. Jones, J. A. McCleverty and M. D. Ward, *J. Chem. Soc., Chem. Comm.,* 1994, 2751.
17. M. G. Colombo, A. Hauser and H. U. Güdel, *Inorg. Chem.,* 1993, **32**, 3088.
18. T. Sajoto, P. I. Djurovich, A. B. Tamayo, J. Oxgaard, W. A. Goddard and M. E. Thompson, *J. Am. Chem. Soc.,* 2009, **131**, 9813.
19. L. Flamingi, A. Barbieri, C. Sabatini, B. Ventura and F. Barigelletti, *Top. Curr. Chem.,* 2007, **281**, 143.

20. A. Juris, V. Balzani, F. Barigelletti, S. Campagna, P. Belser and A. Von Zelewsky, *Coord. Chem. Rev.,* 1988, **84**, 85.
21. K. A. King, P. J. Spellane and R. J. Watts, *J. Am. Chem. Soc.,* 1985, **107**, 1431.
22. S. Sato and M. Wada, *Bull. Chem. Soc. Jpn.,* 1970, **43**, 1955.
23. J. I. Goldsmith, W. R. Hudson, M. S. Lowry, T. H. Anderson and S. Bernhard, *J. Am. Chem. Soc.,* 2005, **127**, 7502.
24. L. L. Tinker, N. D. McDaniel, P. N. Curtin, C. K. Smith, .M. J. Ireland and S. Bernhard, *Chem. Eur. J.,* 2007, **13**, 8726.
25. E. B. Namdas, A. Ruseckas and D. W. Samuel, *J. Phys. Chem. B.,* 2004, **108**, 1570.
26. K. Suzuki, A. Kobayashi, S. Kaneko, K. Takehira, T. Yoshihara, H. Ishida, Y. Shiina, S. Oishi and S. Tobita, *Phys. Chem. Chem. Phys.,* 2009, **11**, 9850.
27. W. D. Horrocks, Jr. J. P. Bolender, W. D. Smith and R. M. Supkowski, *J. Am. Chem. Soc.,* 1997, **119**, 5972.
28. S. Faulkner, B. P. Burton-Rye, T. Khan, L. R. Martin, S. D. Wray and P. J. Skabara, *Chem. Commun.,* 2002, 1668.
29. T.-H. Kwon, O. H. Oh, I.-S. Shin and J.-I. Hong, *Adv. Funct. Mater.,* 2009, **19**, 711.
30. J. D. Slinker, A. A. Gorodetsky, M. S. Lowry, J. J. Wang, S. Parker, R. Rohl, S. Bernhard and G. G. Malliaras, *J. Am. Chem. Soc.,* 2004, **126**, 2763,
31. T. Hu, .L He, L. Duan and Y. Qiu, *J. Mater. Chem.,* 2012, **22**, 4206.

3

Water Soluble Complexes for Cell Imaging

3.1 Introduction

This chapter focuses on further work based on the architecture of the complex [Ir(fppy)$_2$L^{pytz}] reported previously in Chapter 2 (**Fig. 3.01**) for cell imaging.

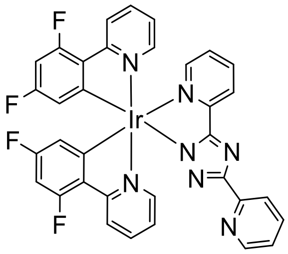

[Ir(fppy)$_2$L^{pytz}]

Figure 3.01. Structure of [Ir(fppy)$_2$L^{pytz}] reported in Chapter 2.

3.1.1 Water Solubility

When considering the design of an Ir(III) complex for the purpose of cell imaging, a crucial factor for a complex to be suitable is that it needs to be water soluble, thus allowing cell membrane permeation. The simplest method to do this is to functionalise the cyclometallating groups with water soluble units. One synthetic strategy employed to enable cell permeation is to functionalise complexes with amino acid groups. A few examples are shown in **Fig. 3.02** by the Lo and Velders group where either the phenyl or the pyridine group of the cyclometallated phenylpyridine units was functionalised.[1,2]

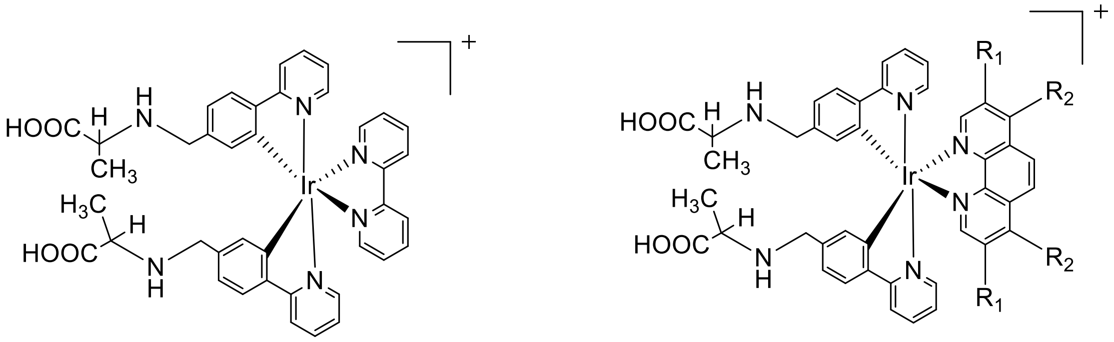

R_1=R_2= H or

R_1=R_2= CH_3 or

R_1= H, R_2= C_8H_5

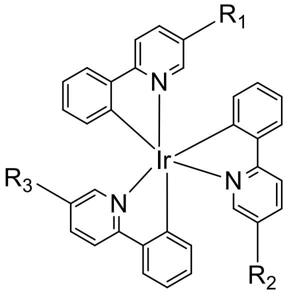

R_1=R_2=R_3= CONHAlaOH or

R_1= CONHLysOMe, R_2=R_3= H or

R_1=R_2= CONHLysOMe, R_3= H or

R_1=R_2=R_3= CONHLysOMe

Figure 3.02. Ir(III) complexes functionalised with amino acid groups that were used as cell imaging agents (below) and luminescent cross-linkers for biomolecules (above).

The amino acid groups enabled to complexes to be water soluble and also allowed good cellular uptake.

Water solubility of a complex can also be improved by attaching a polar polyethylene glycol (PEG) chain onto the cyclometallating ligand, as reported by Lo *et al* (**Fig. 3.03**) in 2010.[3]

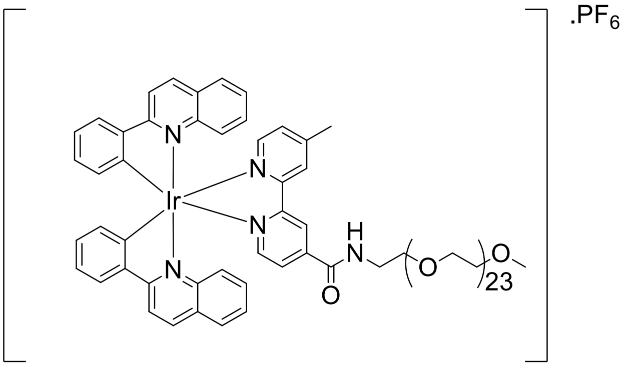

Figure 3.03. An Ir(III) complex reported by the Lo group which was functionalised with a PEG group.

The study reported that the advantage of using PEG chains meant the complex exhibited relatively low cytotoxicity (compared to cisplatin) which was attributed to the long PEG chains which protected the complex from (i) interacting non-specifically with the extracellular proteins and (ii) triggering immunogenicity and antigenicity inside the cells.[4,5]

This study highlights that the low cytotoxicity and high biocompatibility of PEG complexes are highly advantageous for live-cell imaging applications.

3.1.2 pH Sensitivity

In 1999 Licini and Williams reported a bis-terpyridine complex of Ir(III) incorporating a pendent pyridyl group (**Fig. 3.04**) where the luminescence showed pH sensitivity.[6]

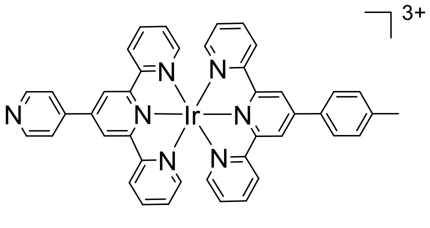

Figure 3.04. Chemical structure of the Ir(III) bis-terpyridine complex reported by Licini and Williams.

Upon protonation of the complex, there were significant effects on the luminescence: the intensity of emission was reduced by *ca*. 8-fold in an acidic environment ($pH < 7$). A luminescence lifetime reduction was also observed from 4.7 μs at pH 7 to 0.48 μs at pH 2. Protonation occurred at the pendant pyridine resulting in an increase in the overall charge of the complex from +3 to +4.

A pH sensitive complex may be advantageous for biological imaging, such as detecting tumour cells. A comprehensive study conducted by Wike-Hooley and co-workers showed that healthy tissue and muscle has a pH range of 7-8, whereas tumour tissues have a wider range of 5.8-7.6.[7] It is also advantageous to probe intracellular pH as it can provide information on how physiological processes (muscle contractions, apoptosis, ion transport etc.) affect the pH within the cell.[8]

As $[Ir(fppy)_2L^{pytz}]$ (reported in Chapter 2) contains a pendant pyridine group, the emission properties of the complex were investigated across a pH range in order to determine whether the complex was pH sensitive. The complex was functionalised with polyethylene glycol (PEG) chains in order to make it water-soluble, thus allowing its cell-imaging properties to be investigated. In addition, control complexes in which the pyridine group was replaced with a tolyl group to remove the pH sensitivity were also synthesised.

The syntheses, characterisation, photophysical properties and cell imaging properties of these complexes are discussed in this chapter.

3.2 Synthetic Studies of [Ir(fppy)$_2$L^{tol}].(PF$_6$)

The synthetic details of all the products are described in full in Chapter 5. The synthesis of [Ir(fppy)$_2$L^{pytz}] is given in Chapter 2. As this chapter looks at the behaviour of emission when the pendant pyridine of the L^{pytz} is protonated under acidic conditions, a control complex was synthesised in which the pH-sensitive pyridyl group is replaced with a tolyl group.

The synthesis of the ligand L^{tol} was taken from literature and is given in **Scheme 3.01** below.[9]

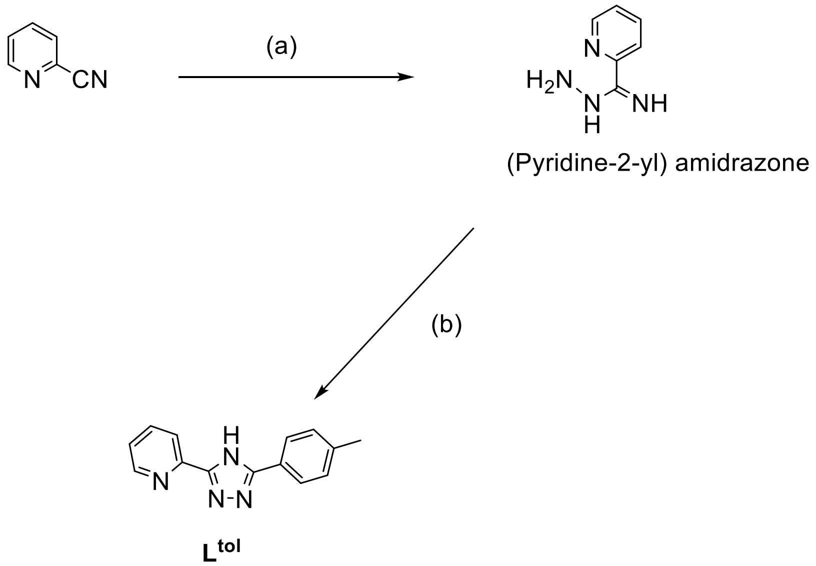

Scheme 3.01. Synthesis of L^{tol}. (a) $N_2H_4.H_2O$, EtOH. (b) (i) *p*-toluoyl chloride, DMAA/THF, 0°C. (ii) CH_2Cl_2, RT. (iii) Glycerol, 190°C.

L^{tol} was used as the control ligand, as it is analogous to L^{pytz}, however a pendant pyridine group is replaced by a tolyl group (**Fig. 3.05**). This would then confirm if protonation occurs on the pyridine site when measuring the luminescence of the Ir(III) complexes during a pH titration.

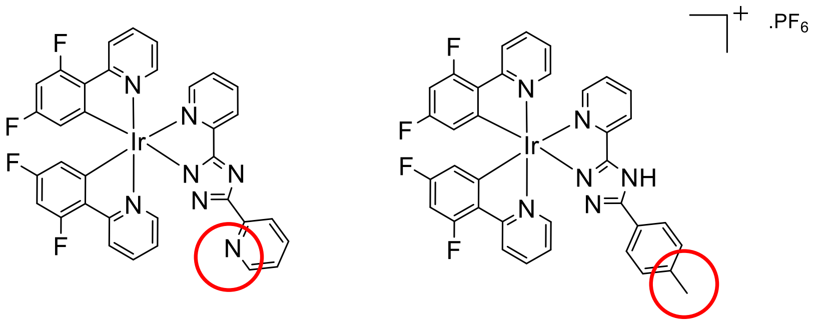

[Ir(fppy)$_2$L^{pytz}]

[Ir(fppy)$_2$L^{tol}].(PF$_6$)

Figure 3.05. Modification of [Ir(fppy)$_2$L^{pytz}] where the pyridine group is replaced by a tolyl group to give [Ir(fppy)$_2$L^{tol}].(PF)$_6$.

[Ir(fppy)$_2$L^{tol}].(PF)$_6$ was then synthesised by reacting L^{tol} with [Ir$_2$(fppy)$_4$Cl$_2$] (**Scheme 3.02**).

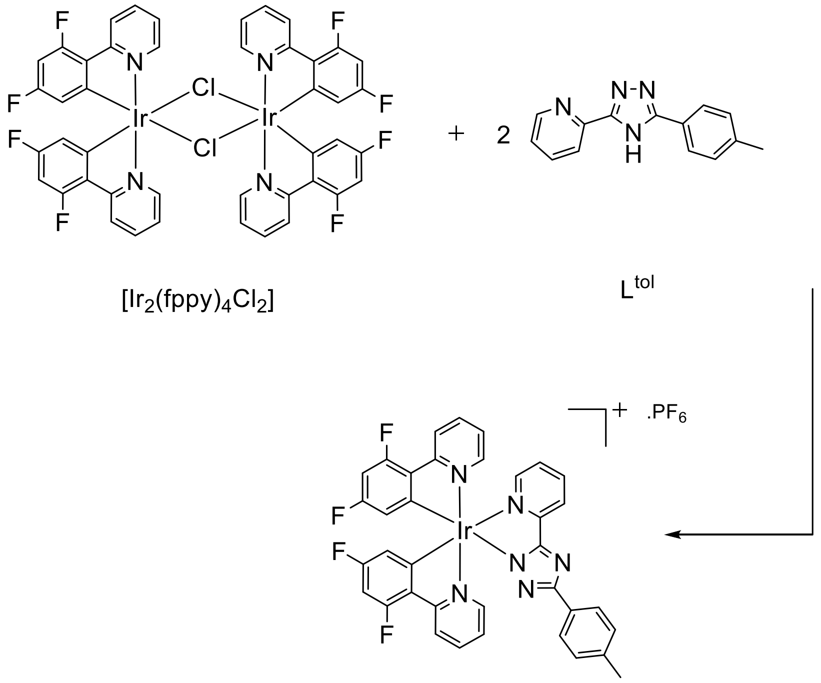

[Ir$_2$(fppy)$_4$Cl$_2$]

L^{tol}

[Ir(fppy)$_2$L^{tol}].(PF$_6$)

Scheme 3.02. Synthesis of [Ir(fppy)$_2$L^{tol}].(PF)$_6$ MeOH/CH$_2$Cl$_2$ (2:1), reflux, N$_{2\ (g)}$, 18 hours.

Purification of the complex was achieved by column chromatography on silica gel (CH_2Cl_2/MeOH, 99:1 and then CH_3CN/H_2O, 99:1) with a yield of 58%. Purity of the complex was confirmed by ^{1}H NMR spectroscopy (**Fig. 3.06**), mass spectrometry and elemental analysis. The integrals of the ^{1}H NMR spectrum showed the presence of 20 aromatic H atoms that correlated with the number of independent H atoms present in the complex, and a singlet peak corresponding to 3 H atoms of the tolyl group with a chemical shift at 2.44 ppm.

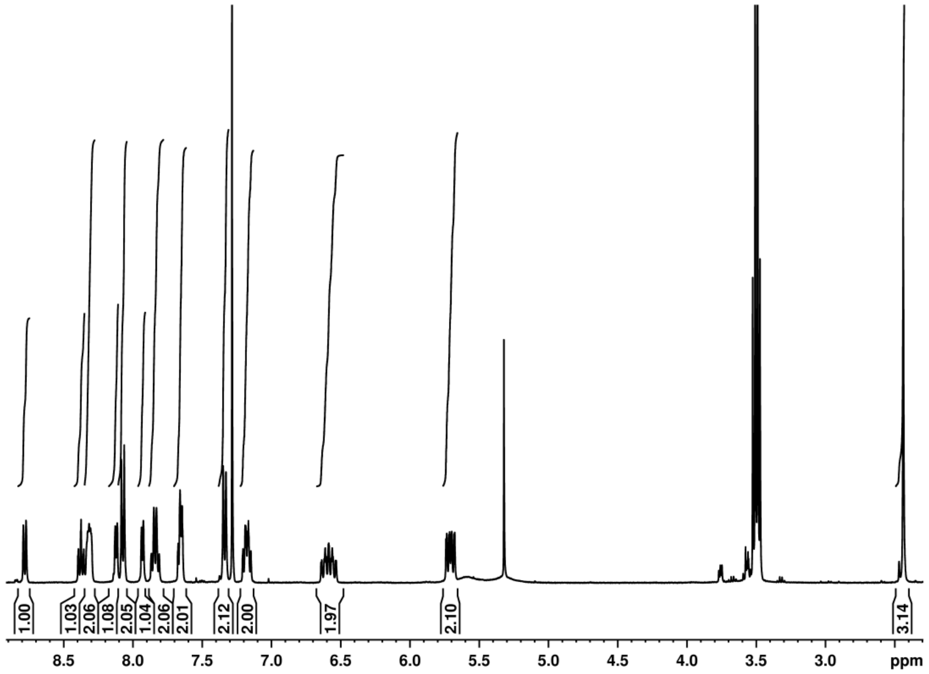

Figure 3.06. ^{1}H NMR (400 MHz $CDCl_3$) spectrum of $[Ir(fppy)_2L^{tol}].(PF)_6$ after purification by column chromatography.

The singlet peak and quartet peak observed with chemical shifts of 5.30 ppm and 3.48 ppm, respectively, are attributed to the presence of residual CH_2Cl_2 and Et_2O.

3.3 X-ray Crystallography

3.3.1 [Ir(ppy)$_2$L^{tol}].(PF)$_6$

Crystals of the complex were grown by slow vapour diffusion of hexane into a solution of the complex in CH_2Cl_2 and the molecular structure was determined by X-ray crystallography (**Fig. 3.07**). The structure was resolved by direct methods and refined to give a final R1 value of 0.063. Crystal data and structure refinement are given in appendix A2.

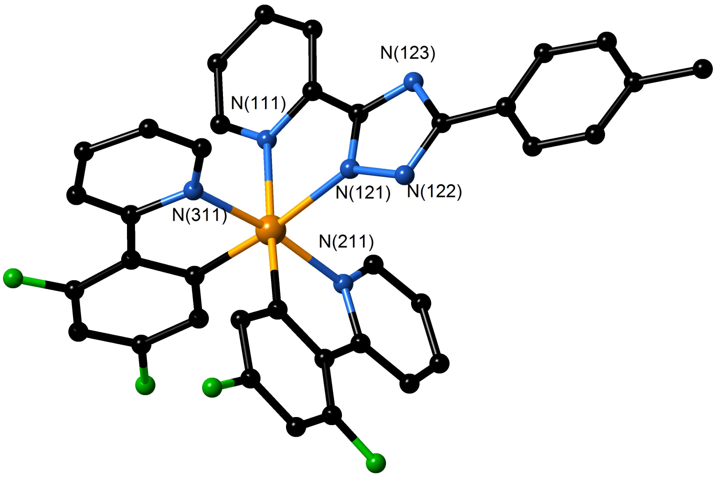

Figure 3.07. Structure of [Ir(ppy)$_2$L^{tol}].(PF)$_6$ from crystallographic data.

The crystal structure showed that the triazole ring is coordinated to the Ir(III) centre through the N^1 atom [N(121)]. The unit cell packing of the complex is given in **Fig. 3.08**. The Ir core has the usual arrangement of trans-pyridines and cis-phenyl groups.

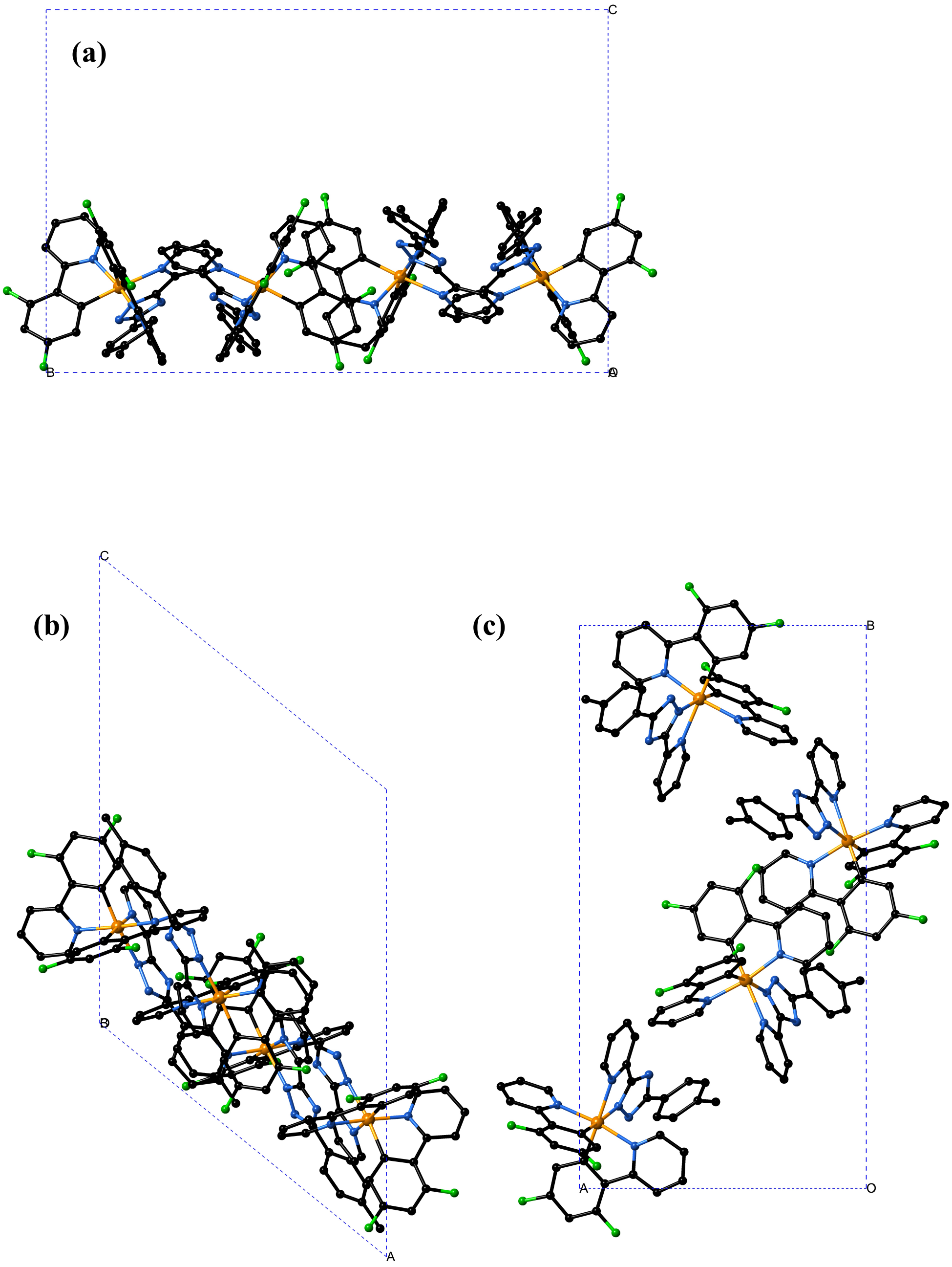

Figure 3.08. Unit cell displaying the packing of the (a) a-face (b) b-face and (c) c-face.

Close inspection of the crystal structure showed π-π stacking of the ppy groups with separation between overlapping aromatic rings with a bond distance of *ca.* 3.3 Å. Hydrogen to fluorine H-bond interactions were also observed between the F groups of the phenyl ring and the H groups of the pyridine ring, with a bond distance of *ca*. 2.2 Å. These bonding interactions are shown in **Fig. 3.09**.

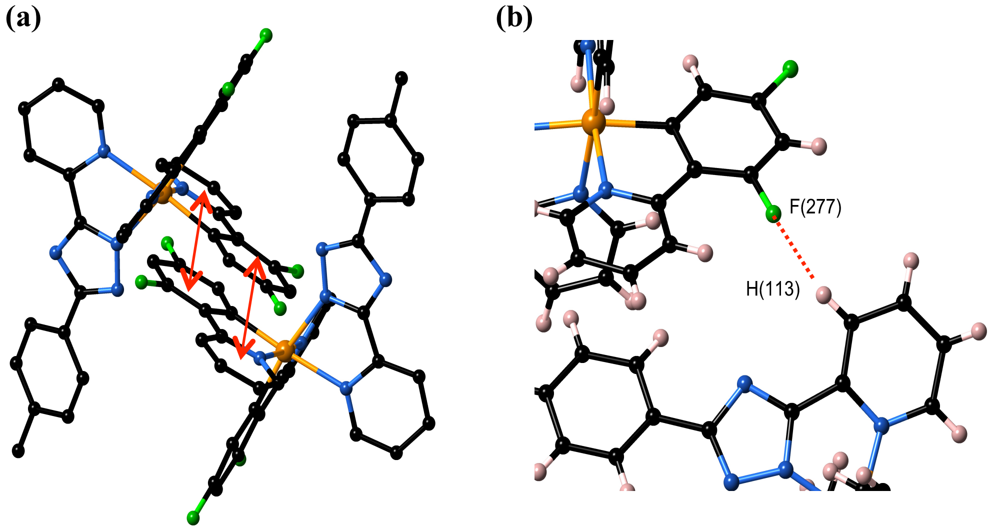

Figure 3.09. (a) π-π stacking interactions between the ppy units (highlighted in red). (b) Hydrogen-bonding interactions between H(113) of a pyridine ring a F(227) of a phenyl ring. The ORTEP plot is given in **Fig. 3.10** below.

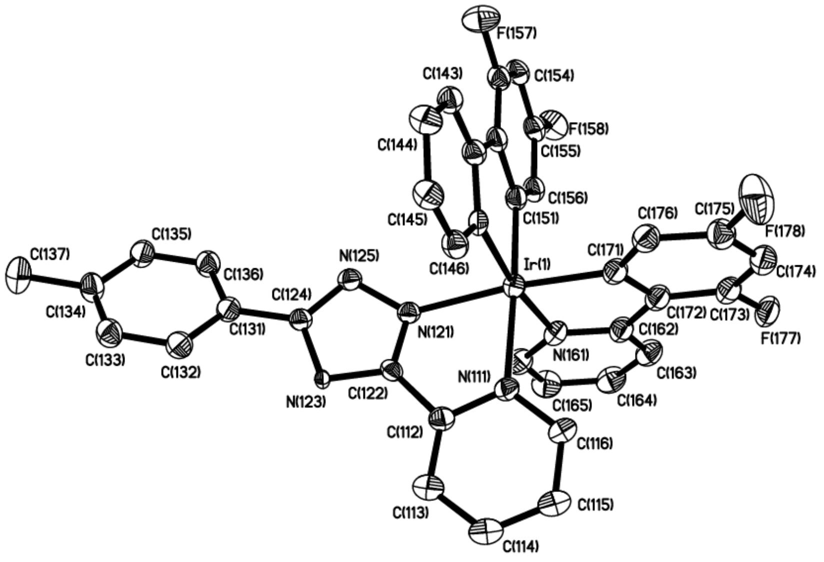

Figure 3.10. ORTEP plot of $[Ir(ppy)_2L^{tol}].(PF)_6$ at 50% probability.

3.4 pH Titrations of $[Ir(fppy)_2L^{pytz}]$ and $[Ir(fppy)_2L^{tol}].(PF)_6$

The emission properties of the $[Ir(fppy)_2L^{pytz}]$ and $[Ir(fppy)_2L^{tol}].(PF)_6$ were measured over a pH range of 2 – 14 in DMF/H_2O (1:1) (**Fig. 3.11**).

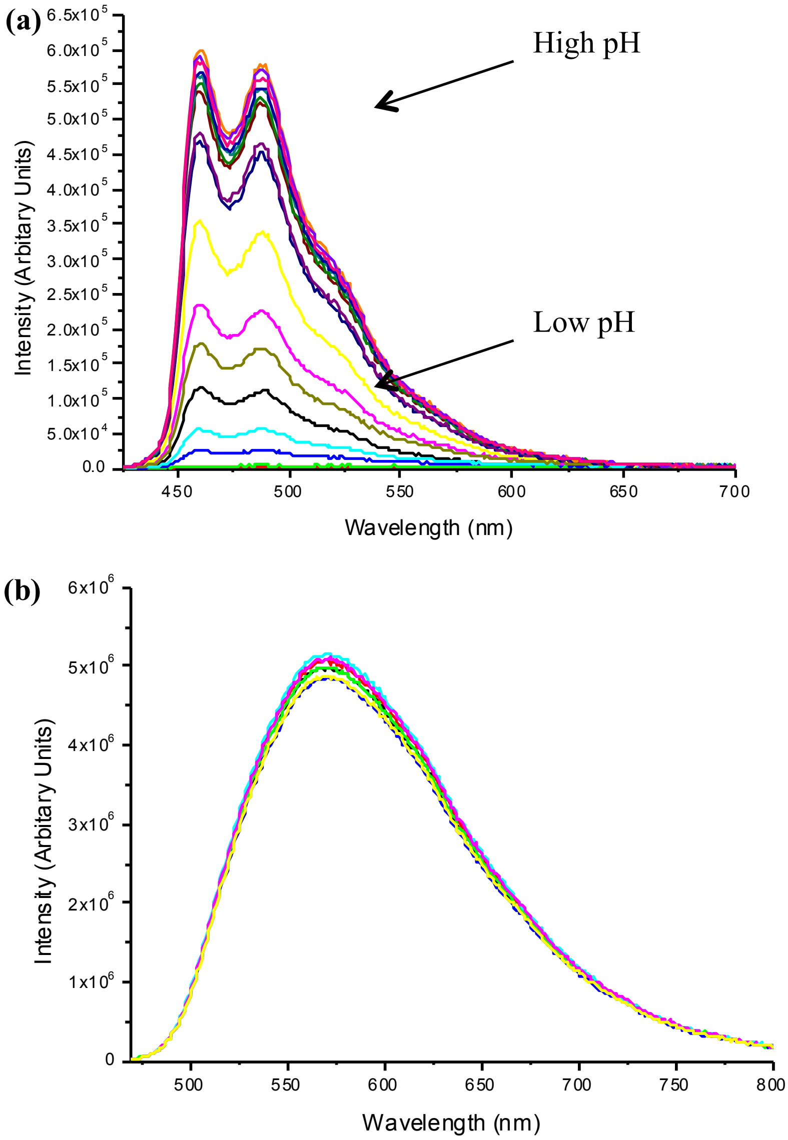

Figure 3.11. (a) Emission spectra of $[Ir(fppy)_2L^{pytz}]$ [1.3×10^{-4} M] between pH 2 and 14 in DMF/H_2O (1:1) at 298 K. Excitation at 425 nm. (b) Emission spectra of $[Ir(fppy)_2L^{tol}].(PF)_6$ [1.2×10^{-4} M] between pH 2 and 10 in DMF/H_2O (1:1) at 298 K. Excitation at 460 nm.

The emission properties of the complexes were recorded in a mixture of DMF/H_2O due to the poor solubility of the complexes in H_2O. In order to dissolve the complexes in H_2O, they were initially dissolved in a solution of DMF, and then equivalent portions of H_2O were added to this.

The emission intensity of [Ir(fppy)$_2$L^{pytz}] decreased significantly with a decrease in the pH. This observation is attributed to the protonation of the pendant pyridine unit, resulting in quenching of the emission due to PET to the positively charged pyridinium group, which is a good electron acceptor. By plotting the intensity at a set wavelength over pH range, it was possible to observe the pH range where quenching was most significant (**Fig. 3.12**).

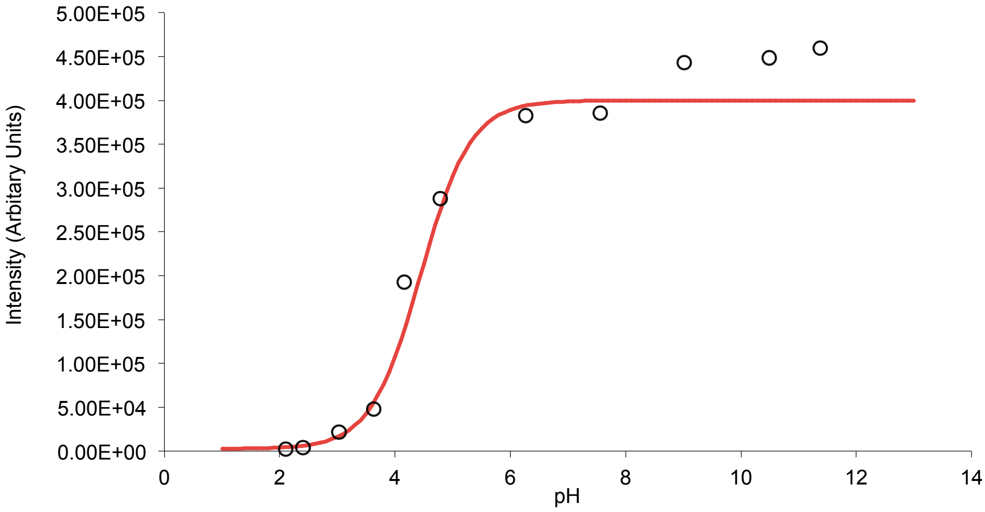

Figure 3.12. pH curve of [Ir(fppy)$_2$L^{pytz}] taken at 470 nm.

The emission intensity of the complex was quenched by 87% between pH 6 and 4 where protonation of the pyridine unit occurs.

In contrast there was no change in the emission intensity of [Ir(fppy)$_2$L^{tol}].(PF)$_6$ across the pH range. This confirmed that the pyridine group is involved in the protonation and not the triazole nitrogen atoms.

The pH sensitivity of [Ir(fppy)$_2$L^{pytz}] could be a useful property as cell imaging agent as it may provide information in pH within a cell environment. A drawback for the complex is that it is not soluble in water, therefore water-soluble analogues of both $[Ir(fppy)_2L^{pytz}]$ and $[Ir(fppy)_2L^{tol}].(PF)_6$ were prepared.

3.5 Synthesis of the Water Soluble Complexes

The two complexes were made water soluble by functionalising them with polyethylene glycol (PEG) chains. As mentioned previously, PEG chains can be attached onto metal complexes making them water-soluble giving them high biocompatibility and low cytotoxicity within cells.[3]

Various synthetic routes were employed in order for the complexes to be successfully synthesised. These routes are reported below.

3.5.1 [Ir(ppy-PEG)$_2$L^{pytz}]

The initial step of the synthesis is given in **Scheme 3.02**, where triethylene glycol monomethyl ether was tosylated by treating it with *p*-toluenesulfonyl chloride.[10] Tosylation was important as tosyl groups are better leaving groups than alcohols during S_N2 reactions in the presence of a good nucleophile.

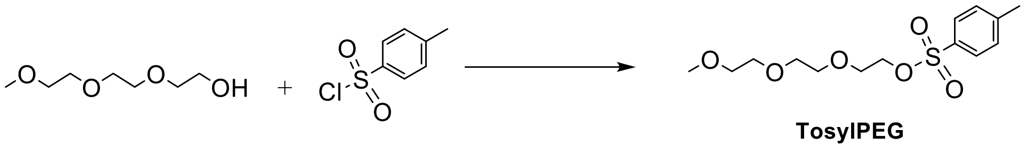

Scheme 3.02. Functionalisation of triethylene glycol monomethyl ether with a tosylate group. DMAP, CH_2Cl_2/Et_3N (2:1), $N_{2\,(g)}$, 18 hours.

A high yield of 90% was obtained for the synthesis of TosylPEG. In order the functionalise the complexes with the PEG chain, 4-(2-pyridyl)benzaldehyde was chosen. The aldehyde group on the phenylpyridine unit is easily reduced to an alcohol group, where the PEG chain could then be attached to this. **Scheme 3.03** shows the first unsuccessful route attempted in order to synthesise [Ir(ppy-PEG)$_2$L^{pytz}].

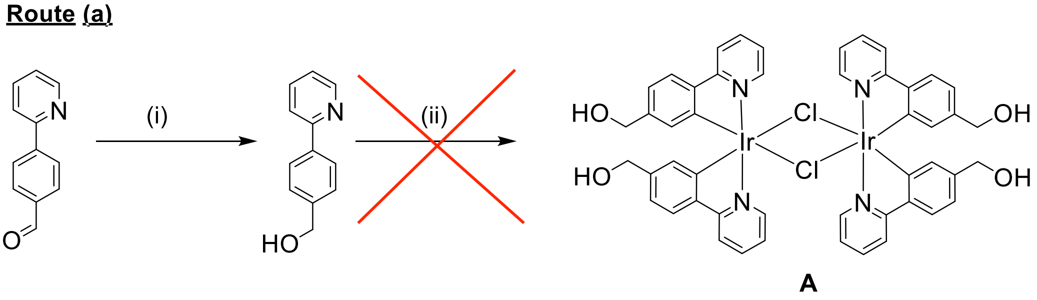

Scheme 3.03. Attempted synthesis of dimer **A**. (i) $NaBH_4$, Na_2CO_3, EtOH. (ii) Ir(III)$Cl_3.6H_2O$, 2-ethoxyethanol/H_2O (3:1), $N_{2\ (g)}$.

The first step of the synthesis was taken from literature,[11] where reduction of the aldehyde with sodium borohydride afforded the alcohol derivative with a 94% yield. For the second step, the synthesis of the Ir(III) dimer **A** was attempted however the product was not obtained. The synthetic route was altered (**Scheme 3.04**) in which the alcohol groups would be functionalised with the PEG chains before attempting to form the dimer.

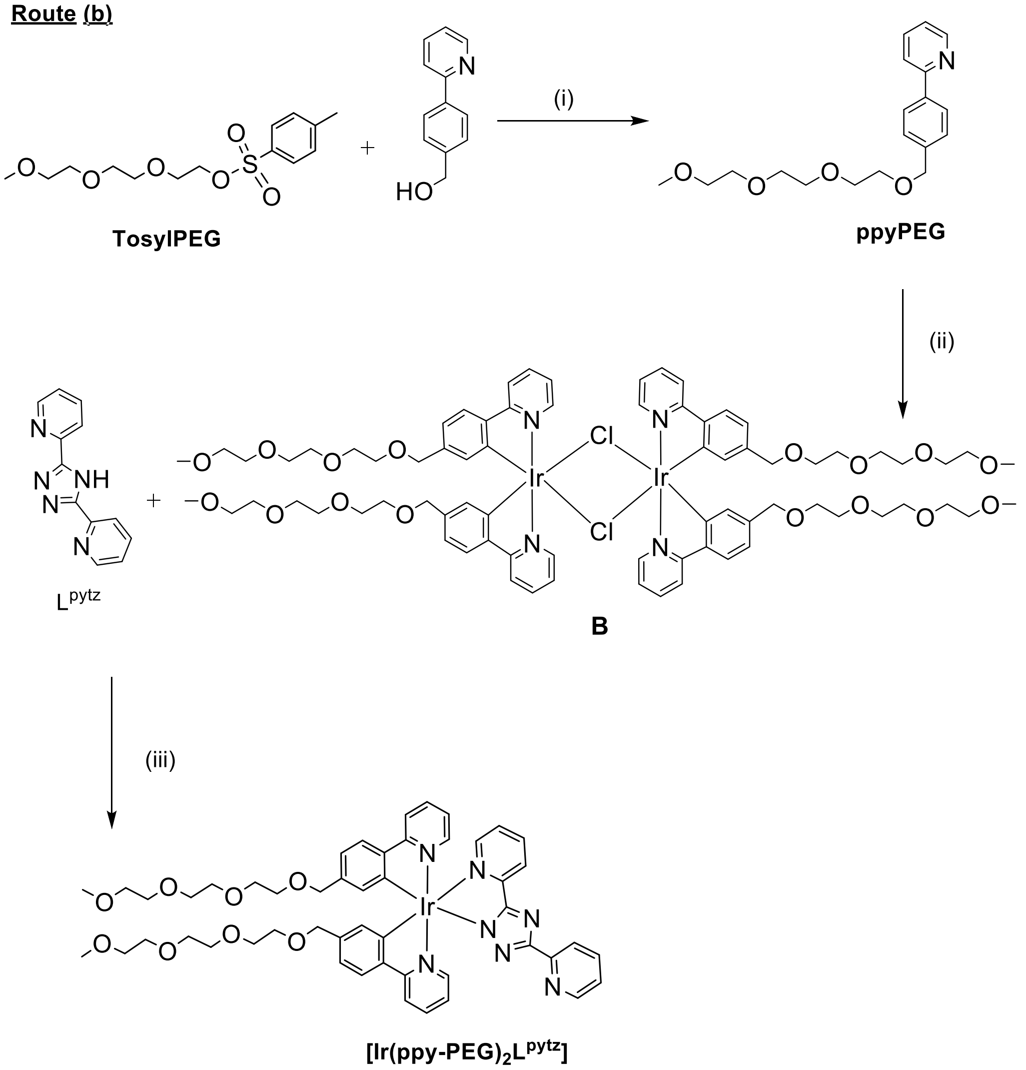

Scheme 3.04. Alternative route (b) for the synthesis of $[Ir(ppy\text{-}PEG)_2L^{pytz}]$. (i) NaH, THF/DMF (1:1), $N_{2\,(g)}$. (ii) $Ir(III)Cl_3.6H_2O$, 2-ethoxyethanol/H_2O (3:1), $N_{2\,(g)}$. (iii) MeOH/CH_2Cl_2 (2:1), $N_{2\,(g)}$.

The first step of the synthesis involved functionalising the alcohol group of ppy with the PEG chain, which gave a yield of 37% after purification by silica gel chromatography.

In the second step, ppyPEG was reacted with $Ir(III)Cl_3.6H_2O$ to form dimer **B**. This was then obtained was relatively low, ~ 17%, which is not typical for synthesis of Ir(III) chloro-dimers where yields are generally above 80%. The third step of the reaction involved the cyclometallation of L^{pytz} with dimer **B**. The presence of the product was confirmed by electrospray mass spectroscopy; however despite two purification steps by column chromatography on silica gel using CH_2Cl_2/MeOH (95:5), ^1H NMR spectroscopy showed that the obtained product was still impure. Further purification was not attempted as the amount of crude product obtained was very low. In order to improve the yield, the synthetic route was altered again (**Scheme 3.05**).

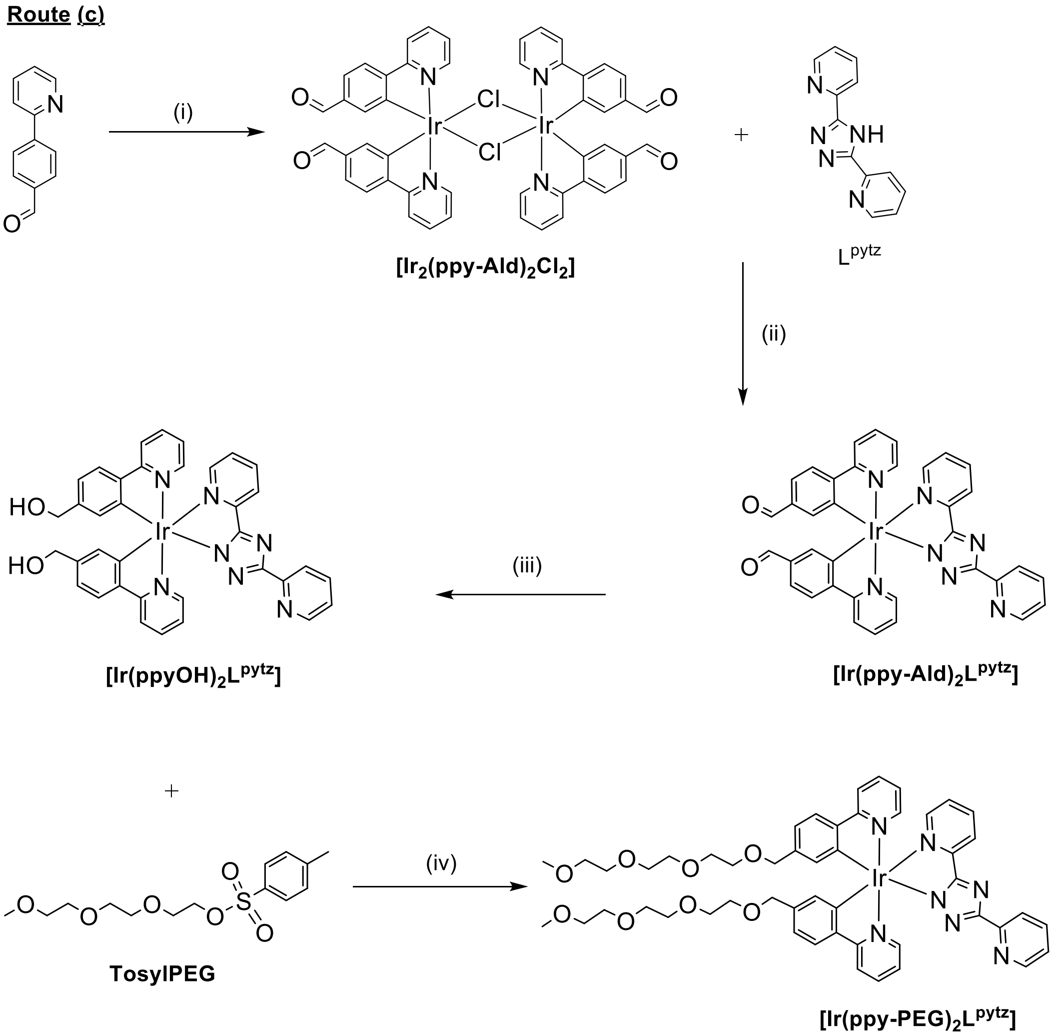

Scheme 3.05. Synthesis of [Ir(ppy-PEG)$_2$L^{pytz}] *via* an improved route (c). (i) Ir(III)$Cl_3.6H_2O$, 2-ethoxyethanol/H_2O (3:1), $N_{2\ (g)}$. (ii) MeOH/CH_2Cl_2 (2:1), $N_{2\ (g)}$. (iii) $NaBH_4$, Na_2CO_3, EtOH. (iv) NaH, THF/DMF (1:1), $N_{2\ (g)}$.

[Ir(ppy-PEG)$_2$L^{pytz}] was successfully synthesised using synthetic route (c). The initial step involved the synthesis of the Ir(III) dimer, [Ir_2(ppy-Ald)$_2Cl_2$], which was obtained in a 48% yield. L^{pytz} was then cyclometallated onto the Ir(III) centre to give the ppy aldehyde complex, [Ir(ppy-Ald)$_2$L^{pytz}]. This was purified by column chromatography twice on alumina gel using CH_2Cl_2/MeOH (99:1) followed by CH_3CN/H_2O (99:1), giving a yield of 78%. The aldehyde substituents were then reduced to alcohol groups in the third step to give [Ir(ppyOH)$_2$L^{pytz}]. This complex was purified by column chromatography on alumina gel using CH_2Cl_2/MeOH (95:5), with a high yield of 92%. This was then reacted with TosylPEG to give [Ir(ppy-PEG)$_2$L^{pytz}]. Initially the crude product was columned on alumina gel CH_2Cl_2/MeOH (99:1) however the ^{1}H NMR spectrum showed there were excess polyethylene glycol chains present (**Fig. 3.13**)

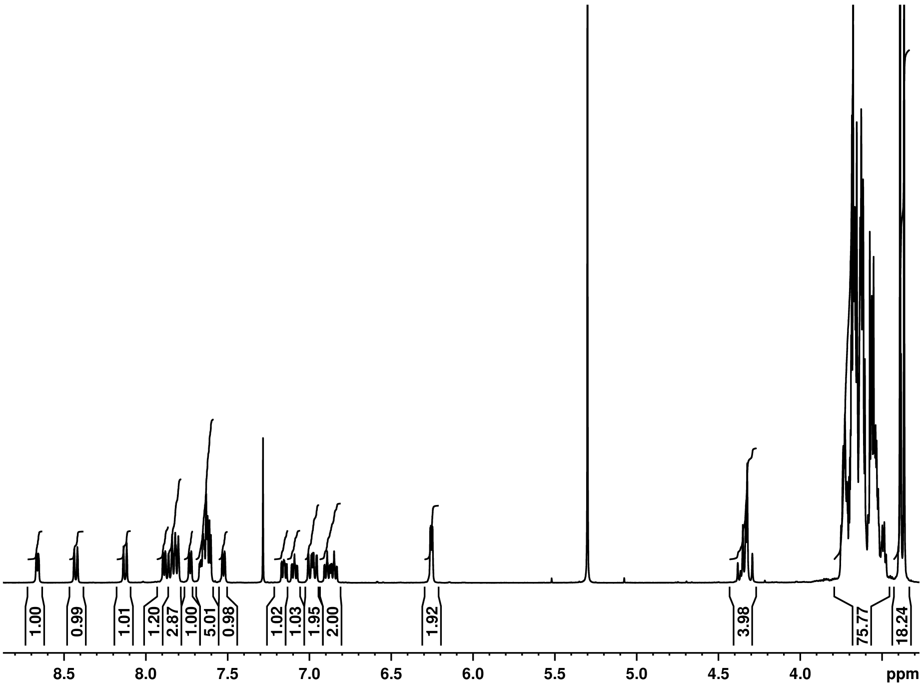

Figure 3.13. ^{1}H NMR (400 MHz $CDCl_3$) spectrum of [Ir(ppy-PEG)$_2$L^{pytz}] after the first purification step.

The aromatic region of the ^{1}H NMR spectrum integrated to the correct value of 22 aromatic H atoms in the complex. The signal for the two CH_2 groups on the ppy ligands is at 4.33 ppm where a multiplet peak is observed. The chemical shift range of the CH_2 groups on the PEG chains lies between 3.47 and 3.76 ppm in the spectrum and the CH_3 groups are observed at 3.38 ppm. Integration of these peaks showed there was a three fold of PEG protons. TLC analysis using various solvents on both silica and alumina gels showed poor separation between the complex and the excess PEG chains. The complex was therefore purified by HPLC using 60% H_2O (0.1% TFA) and 40% CH_3CN. Formation of the complex was confirmed by elemental analysis, mass spectrometry and purity was confirmed by ^1H NMR spectroscopy (**Fig. 3.14**).

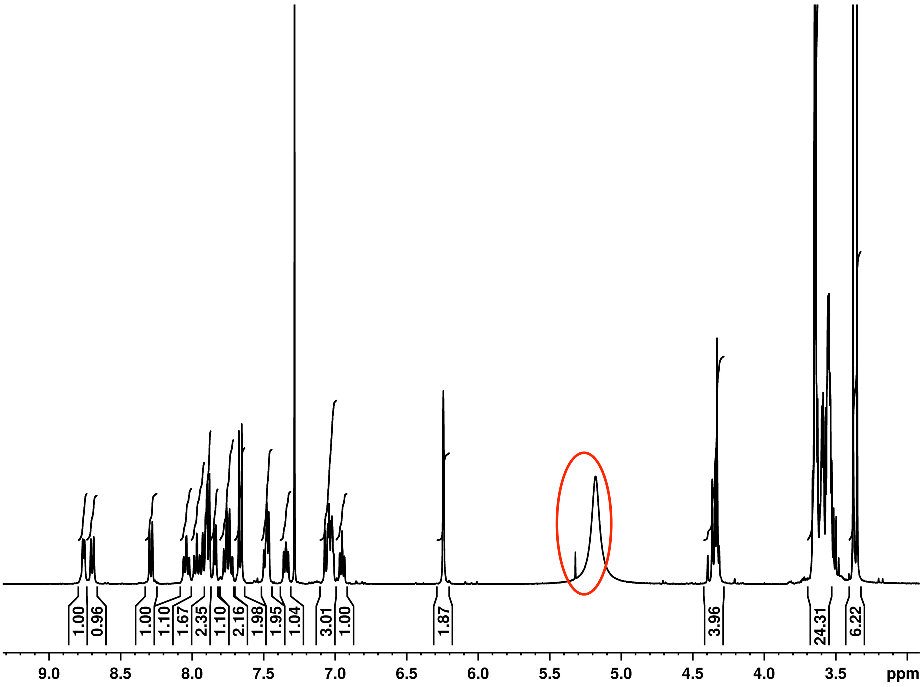

Figure 3.14. ^{1} H NMR (400 MHz $CDCl_3$) spectrum of $[Ir(ppy\text{-}PEG)_2L^{pytz}]$ after purification by HPLC.

The ^1H NMR spectrum showed the complex to be pure after purification by HPLC with the PEG CH_2 groups integrating to 24 H atoms and the two CH_3 groups integrating to 6 H atoms in the spectrum. An unexpected peak with a chemical shift of 5.18 ppm was observed in the spectrum (highlighted in red). Test with litmus paper confirmed presence of acid in the product, likely to be residual TFA from the HPLC purification stage. This peak was therefore likely to be a mixture of H_2O and H_3O^+. A signal for H_2O is not observed in the spectrum, but due to fast exchange on the NMR timescale, the observed peak at 5.18 ppm was likely to be an average of H_3O^+ and H_2O. To confirm this, the product was dissolved in CH_2Cl_2 and washed with

NaOH $_{(aq)}$. The ^{1}H NMR spectrum was recorded again, which showed the disappearance of the peak at 5.18 ppm (**Fig. 3.15**).

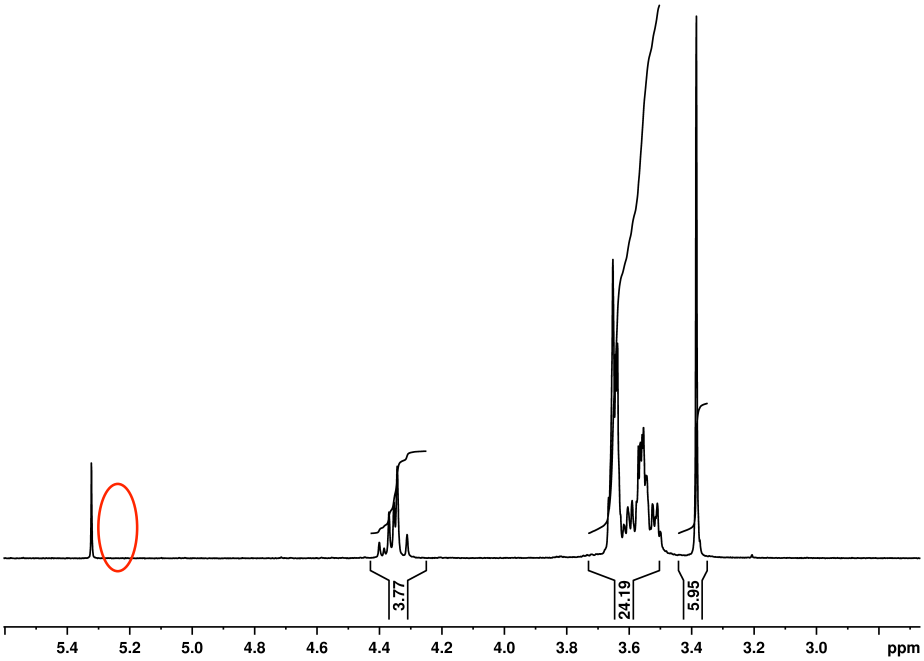

Figure 3.15. ^{1}H NMR (400 MHz $CDCl_3$) spectrum of [Ir(ppy-PEG)$_2$L^{pytz}] showing the disappearance of the peak at 5.18 ppm (highlighted in red).

The yield obtained for the final product was 25 %. Two fractions were obtained during the HPLC purification step. The first fraction contained the pure complex and the second fraction also contained the complex but also contained excess PEG. Therefore the yield could be improved upon by further purifying the second fraction.

3.5.2 [Ir(ppy-PEG)$_2$L^{tol}]

The synthetic route for the control complex was the same as route described above and shown in **Scheme 3.06** below.

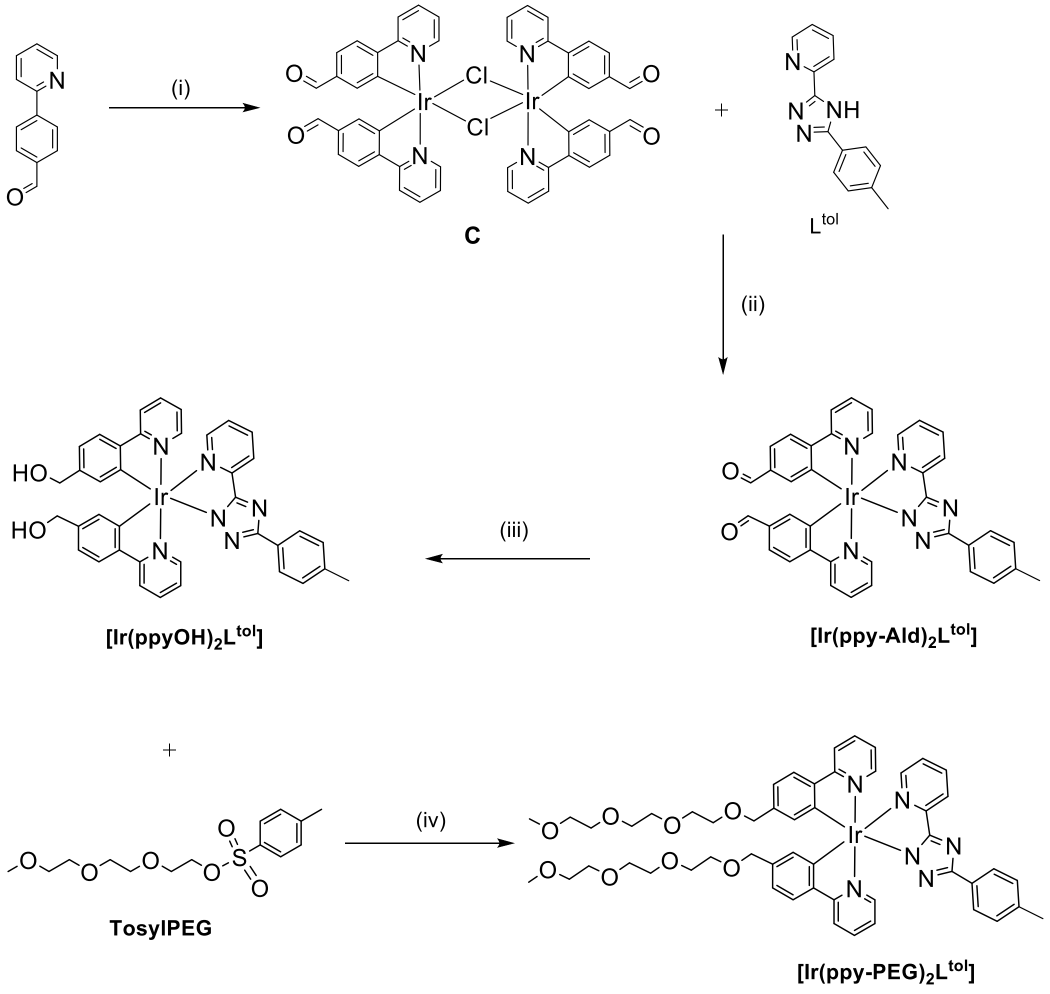

Scheme 3.06. Synthesis of [Ir(ppy-PEG)$_2$L^{tol}]. (i) Ir(III)Cl$_3$.6H$_2$O, 2-ethoxyethanol/H$_2$O (3:1), N$_{2\ (g)}$. (ii) MeOH/CH$_2$Cl$_2$ (2:1), N$_{2\ (g)}$. (iii) NaBH$_4$, Na$_2$CO$_3$, EtOH. (iv) NaH, THF/DMF (1:1), N$_{2\ (g)}$.

It was also necessary to purify [Ir(ppy-PEG)$_2$L^{tol}] by HPLC in 60 % CH$_3$CN and 40 % H$_2$O. Successful synthesis and purity of the product was confirmed by electrospray mass spectroscopy, elemental analysis and ^{1}H NMR spectroscopy, where the spectrum is given in **Fig. 3.16**.

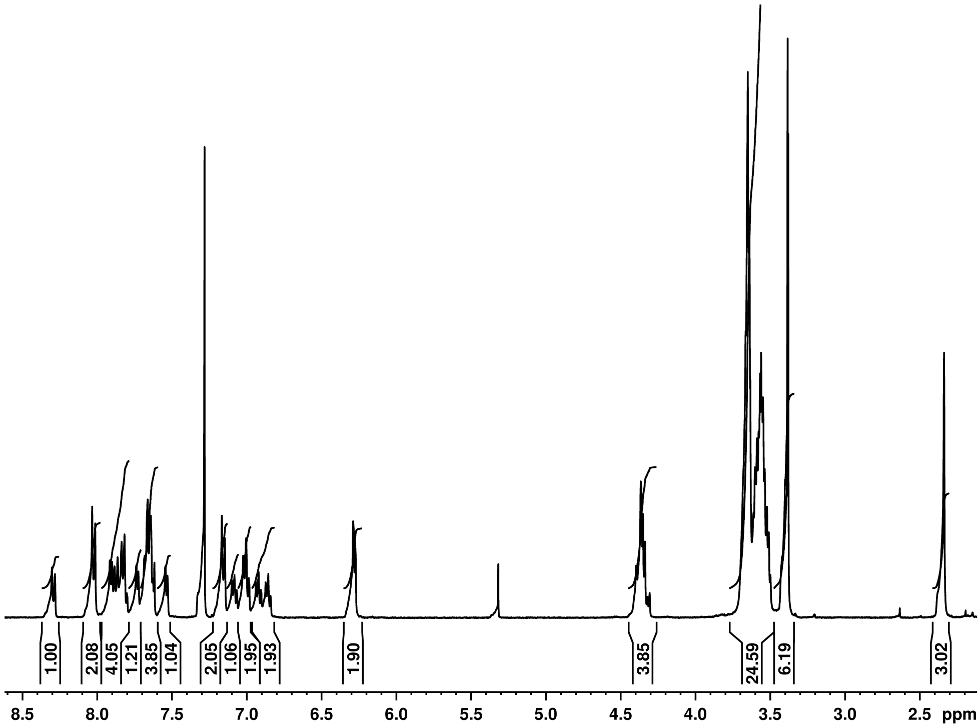

Figure 3.16. ^{1} H NMR (400 MHz $CDCl_3$) spectrum of [Ir(ppy-PEG)$_2$L^{tol}] after purification by HPLC.

The ^{1}H NMR spectrum shows the presence of 22 aromatic H atoms between 6.3 and 8.3 ppm. A multliplet at 4.36 ppm can be assigned to the two CH_2 substituents on the ppy units. The aliphatic protons of the PEG chains are found at 3.6 ppm (for the CH_2 units) and 3.4 ppm (for the terminal CH_3 units). The tolyl singlet CH_3 peak is observed at 2.35 ppm. A small peak at 5.3 ppm is attributed to the presence of residual CH_2Cl_2.

3.6 Luminescence Properties of [Ir(ppy-PEG)$_2$L^{pytz}]

3.6.1 UV/Vis Absorption

The UV/Vis spectra of [Ir(ppy-PEG)$_2$L^{pytz}] were recorded in aerated CH_2Cl_2, H_2O/DMSO (99.9/0.01), CH_3CN and toluene at 298 K (**Fig. 3.17**).

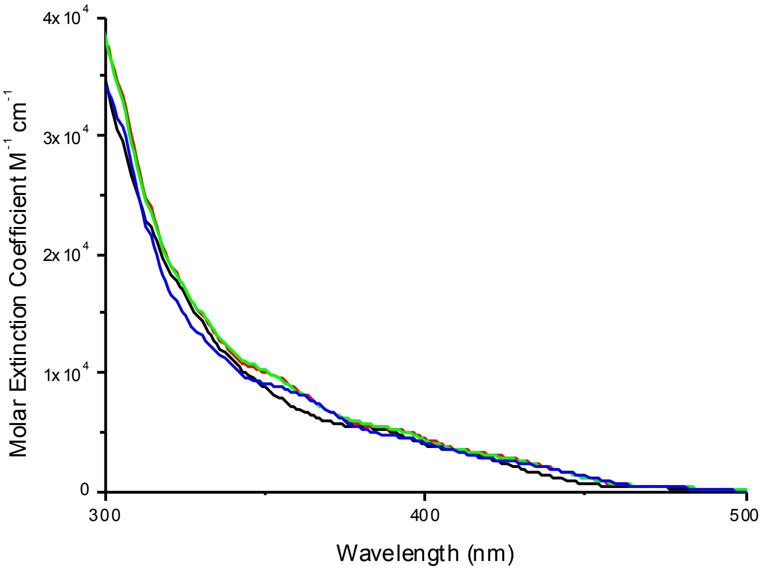

Figure. 3.17. UV/Vis absorption spectra of [Ir(ppy-PEG)$_2$L^{pytz}] [6.97 × 10^{-5} M] at 298 K in H_2O/DMSO (99.9/0.1) (black line), CH_3CN (green line) CH_2Cl_2 (red line) and toluene (blue line).

The complex was not completely soluble in H_2O therefore in order to measure the UV/Vis absorption spectrum, it was dissolved in a known volume of DMSO and then H_2O was added to this to give a solution of the complex in 0.1% DMSO and 99.9% H_2O.

The electronic absorption spectral data is given in **Table 3.01**.

Solvent	Absorption λ_{max}/nm (ε/M^{-1} cm^{-1})
CH_2Cl_2	352 sh (9870), 390 sh (5260) 426 sh (2870)
CH_3CN	354 sh (9520), 392 sh (5150), 428 sh (2660)
Toluene	356 sh (8672), 395 sh (4354), 431 sh (2360)
H_2O	385 sh (6110), 415 sh (3590)

Table 3.01. Electronic absorption data of [Ir(ppy-PEG)$_2$L^{pytz}] [6.97 x 10^{-5} M] at 298 K.

The intense region of absorption at λ < 300 nm is consistent with literature and can be tentatively assigned to spin-allowed intraligand π-π* transitions.[12,13,14] The less intense and poorly defined absorption bands and shoulders at λ > 350 nm can be assigned to spin-allowed and spin-forbidden MLCT transitions corresponding to (dπ(Ir) → π* (N^N and C^N)) transitions.[12,13,14] The excitation spectrum overlaid with the absorption spectrum is given in **Fig. 3.18** below. The good match between these 2 spectra indicates that the emission observed emanates from the compound.

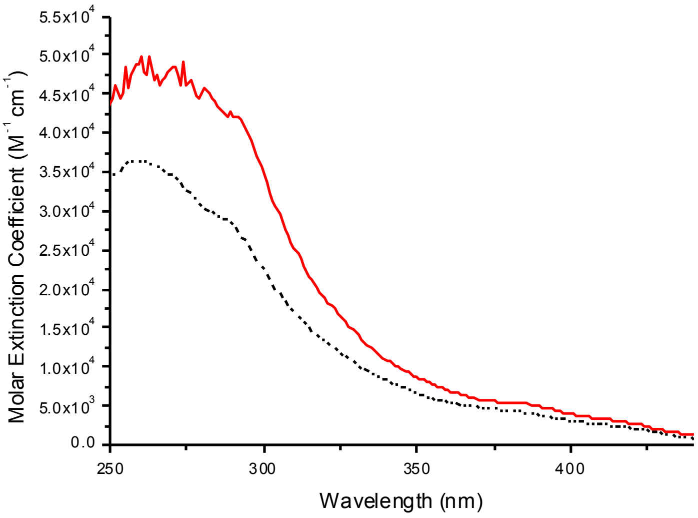

Figure 3.18. Excitation spectrum (black dashed line) of [Ir(ppy-PEG)$_2$L^{pytz}] (registered at 490 nm) overlaid with the absorption spectrum (red line) in CH_2Cl_2.

3.6.2 Emission Properties

The emission spectra and lifetimes of [Ir(ppy-PEG)$_2$L^{pytz}] were recorded in aerated CH_2Cl_2, H_2O/DMSO (99.9/0.01), CH_3CN and toluene at 298 K (**Fig. 3.19**).

The excitation wavelength varied for each solvent the complex was measured in (as emission was solvent dependent), to ensure the intensities of the complex in these solvents were directly comparable. Excitation wavelength was chosen to give an absorption of 0.1 in the UV/Vis spectrum for each solvent. Emission at 77 K was recorded in EtOH/MeOH (4:1) glass (**Fig. 3.20**). Summary of the photophysical data is given in **Table 3.02**.

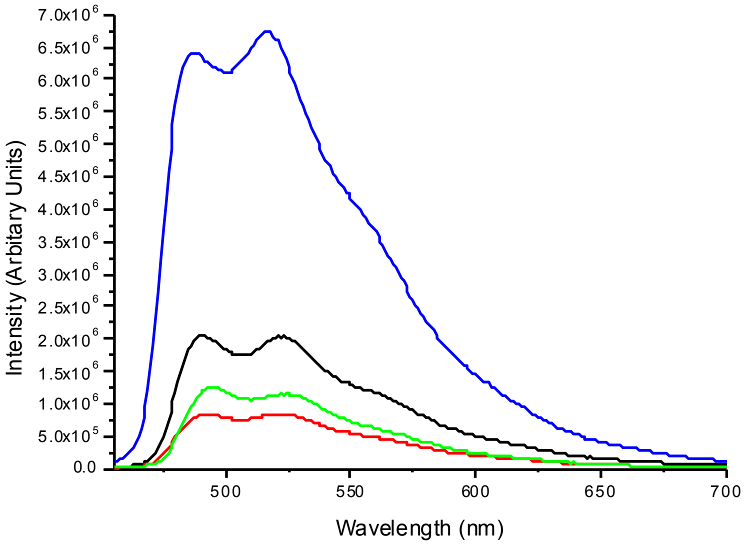

Figure 3.19. Emission spectra of [Ir(ppy-PEG)$_2$L^{pytz}] [6.97 × 10^{-5} M] at 298 K in H_2O/DMSO (99.9/0.01) (blue line, excitation at 436 nm), CH_2Cl_2 (black line, excitation at 446 nm), toluene (green line, excitation at 448 nm) and CH_3CN (red line, excitation at 446 nm). The optical density was 0.1 in every case so intensities are directly comparible.

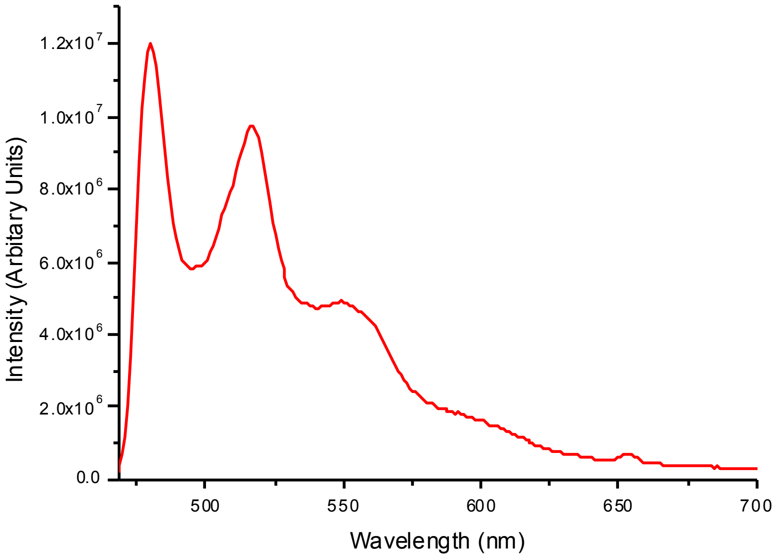

Figure 3.20. Emission spectrum of [Ir(ppy-PEG)$_2$L^{pytz}] [6.97 × 10^{-5} M] at 77 K in EtOH/MeOH (4:1, v/v). Excitation at 436 nm.

Solvent (T [K])	λ_{em} (nm)	τ_1, τ_2 (ns)
CH_2Cl_2 (298)	490, 521, 564 (sh)	290 (15%), 99 (85%)
CH_3CN (298)	492, 521, 561 (sh)	157 (10%), 45 (90%)
Toluene (298)	493, 522, 566 (sh)	173 (8%), 47 (92%)
glass (77)[a]	480, 516, 549, 601 (sh), 654	-
H_2O (298)	487, 516, 555 (sh)	557

Table 3.02. Photophysical data for [Ir(ppy-PEG)$_2$L^{pytz}] [6.97 × 10^{-5} M]. [a] EtOH/MeOH (4:1, v/v).

Under photoexcitation, [Ir(ppy-PEG)$_2$L^{pytz}] displayed green emission. The highest-energy emission maximum of the complex occurred between 487-493 nm in solution. The emission can be assigned to typical mixtures of ^{3}MLCT of the (dπ(Ir) → π* (N^N and C^N)) transitions.[12,13,14] Interestingly a small hypsochromic shift occurs when the complex is in H_2O, with an increase in emission intensity. These results may be justified by the fact that in an aqueous environment, there is an increase in the proximity of the PEG groups to the complex molecules. The local environment could therefore be considered to be nonpolar as the polyether groups are significantly less polar than water. This suggestion is supported by similar observations made on Ir(III)-PEG systems by the Lo group.[3,15] A longer-lived luminescence lifetime in water also complements this theory.

At 77 K an expected increase in emission intensity occurs. This is attributed to the impediment of the non-radiative relaxation processes, which compete with the radiative relaxation pathways at room temperature. A hypsochromic shift also occurs (~10 nm) as the charge transfer state is no longer stabilised by the fast solvent reorganisation that occurs at room temperature.[15] This shift is small, consistent with only a small degree of charge-transfer in the excited state, which has substantial ^{3}LC character.

The emission properties of [Ir(ppy-PEG)$_2$L^{pytz}] recorded during a pH titration are given in **Fig. 3.21**.

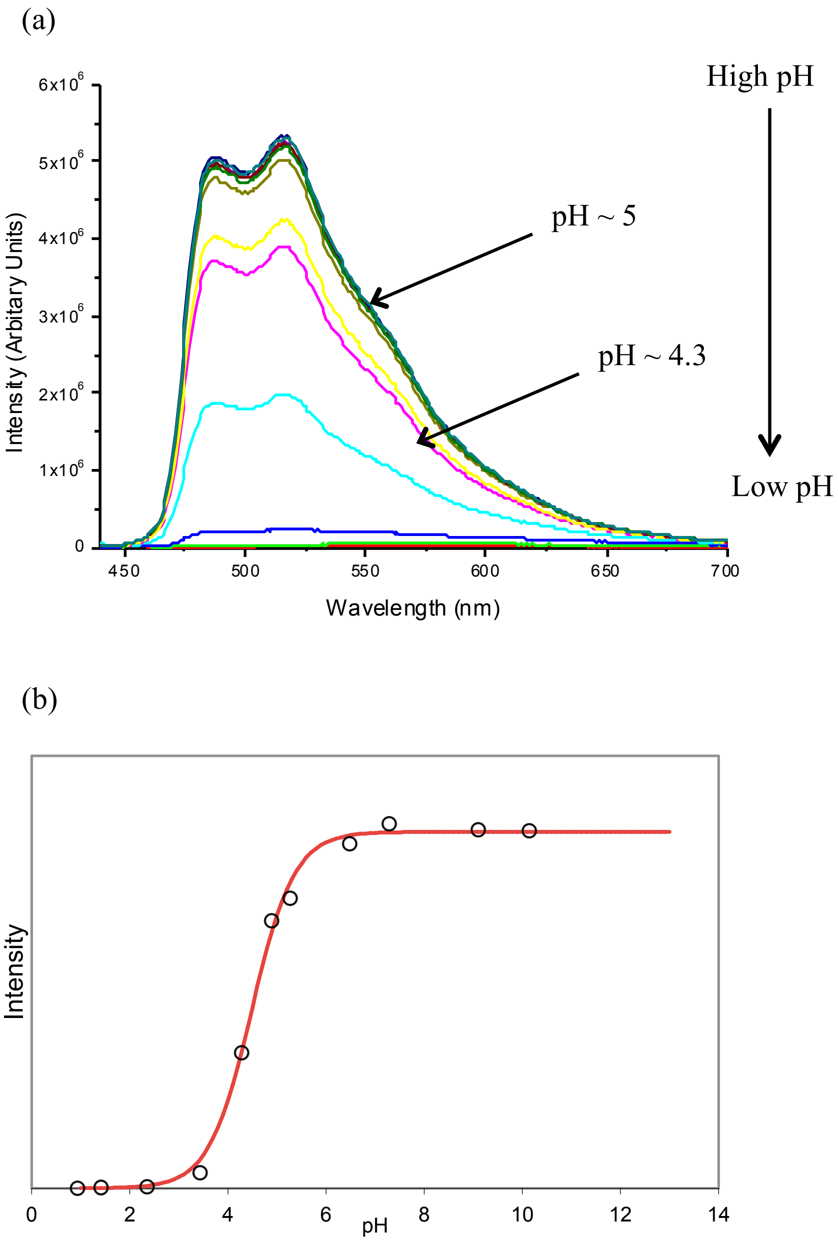

Figure 3.21. (a) Emission spectra of [Ir(ppy-PEG)$_2$L^{pytz}] [1.39 × 10^{-5} M] in H$_2$O/DMSO (99.9/0.1) during pH titrations at 298 K. (b) pH curve of [Ir(ppy-PEG)$_2$L^{pytz}] taken at 488 nm.

Under basic conditions, the emission of the complex did not change, however as expected, quenching was observed in an acidic environment in the same manner as the fluorinated analogue, [Ir(fppy)$_2$L^{pytz}], reported earlier. A PET process from the metal centre to the protonated pyridinium unit is likely to contribute to the quenching of the emission. The pH curve of the titration shows a significant change in emission intensity between pH 4-6. The intensity of emission from pH ~7 to pH ~4 was reduced by 63% and accompanied by a decrease in the lifetime of emission (from ~550 ns to ~350 ns).

3.6.3 Quantum Yield of Emission of [Ir(ppy-PEG)$_2$L^{pytz}]

The quantum yield (Φ) of [Ir(ppy-PEG)$_2$L^{pytz}] was calculated to be Φ = 0.027 by measuring against Ir(ppy)$_3$ as a standard in aerated CH_2Cl_2. This standard was calibrated against the same molecule in aerated toluene (Φ = 0.04) and against Ru(bpy)$_3$.Cl$_2$.6H$_2$O in aerated water (Φ = 0.042).[17,18,19]

The quantum yield was calculated using **Equation 3.01** below:

$$\Phi_s = \Phi_r \times \left(\frac{I_s}{(1-10^{-A})_s}\right) \times \left(\frac{(1-10^{-A})_r}{I_r}\right) \times \left(\frac{\eta_s^2}{\eta_r^2}\right)$$

Equation 3.01. Φ = Quantum yield, *A* = absorbance at excitation wavelength, *I* = integrated emission intensity, η = solvent refractive index, *s* = sample, *r* = reference.

3.7 Luminescence Properties of [Ir(ppy-PEG)$_2$L^{tol}]

3.7.1 UV/Vis Absorption

The UV/Vis spectra of [Ir(ppy-PEG)$_2$L^{tol}] were recorded in aerated CH_2Cl_2, H_2O/DMSO (95/5), CH_3CN and toluene at 298 K (**Fig. 3.22**).

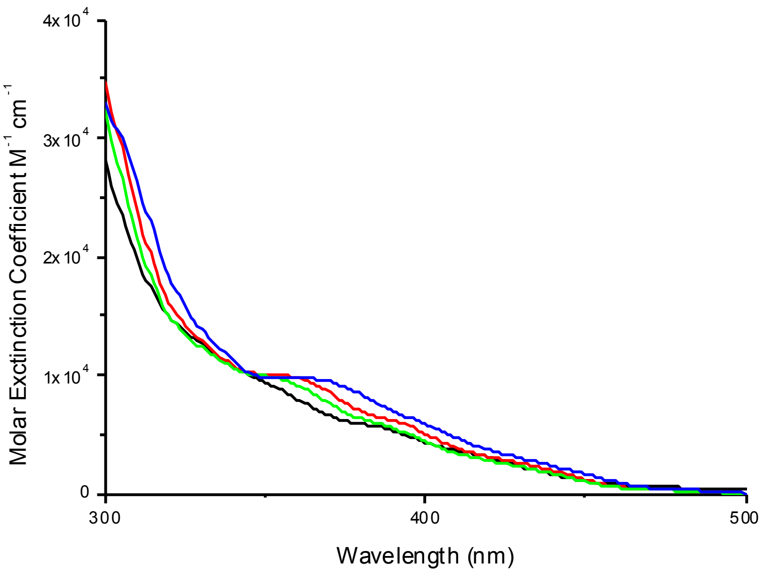

Figure 3.22. UV/Vis absorption spectra of [Ir(ppy-PEG)$_2$L^{tol}] [7.17 × 10^{-5} M] at 298 K in H_2O/DMSO (95/5) (black line), CH_3CN (green line) CH_2Cl_2 (red line) and toluene (blue line).

[Ir(ppy-PEG)$_2$L^{tol}] was initially prepared in a solution of H_2O/DMSO (99.9/0.1), however unlike the previous complex [Ir(ppy-PEG)$_2$L^{ptyz}], small precipitation was observed. The reason why this complex is slightly less soluble in water is likely to be as a result of changing a pyridine unit to a more hydrophobic tolyl group, thus affecting the overall solubility of the complex. Measurements were therefore recorded in H_2O/DMSO in a ratio of 95/5 respectively. Electronic absorption data are given in **Table 3.03**.

Solvent	Absorption λ_{max}/nm (ε/M^{-1} cm^{-1})
CH_2Cl_2	359 (9990), 395 sh (5750) 432 sh (2500)
CH_3CN	355 (9670), 394 sh (5160), 433 sh (2120)
Toluene	367 (9640), 397 sh (6100), 433 sh (2830)
H_2O	388 sh (5430), 416 sh (3320)

Table 3.03. Electronic absorption data of [Ir(ppy-PEG)$_2$L^{tol}] [7.17 × 10^{-5} M] at 298 K.

The absorption spectra of [Ir(ppy-PEG)$_2$L^{tol}] are very similar to its analogous pH sensitive complex, [Ir(ppy-PEG)$_2$L^{pytz}]. The observed intense absorption bands below 300 nm are tentatively assigned to spin-allowed intraligand π-π* transitions, with the less intense absorption bands and shoulders at > 350 nm being assigned to spin-allowed and spin-forbidden MLCT transitions corresponding to (dπ(Ir) → π* (N^N and C^N)) transitions. The excitation spectrum overlaid with the absorption spectrum is given in **Fig. 3.23** below. The good match between these 2 spectra indicates that the emission observed emanates from the compound.

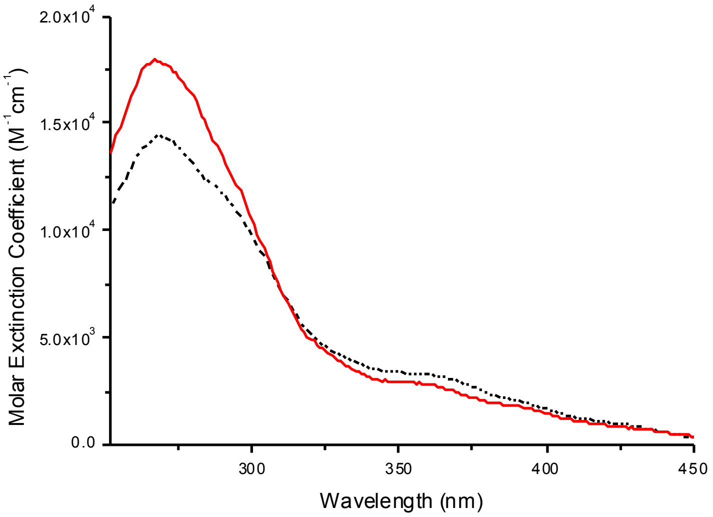

Figure 3.23. Excitation spectrum (black dashed line) of [Ir(ppy-PEG)$_2$L^{tol} (registered at 490 nm) overlaid with the absorption spectrum (red line) in CH_2Cl_2.

3.7.2 Emission Properties

The emission spectra and lifetimes of [Ir(ppy-PEG)$_2$L^{tol}] were recorded in aerated CH_2Cl_2, H_2O/DMSO (95/5), CH_3CN and toluene at 298 K (**Fig. 3.24**).

Emission at 77 K was recorded in EtOH/MeOH (4:1) glass (**Fig. 3.25**). A summary of the photophysical data is given in **Table 3.04**.

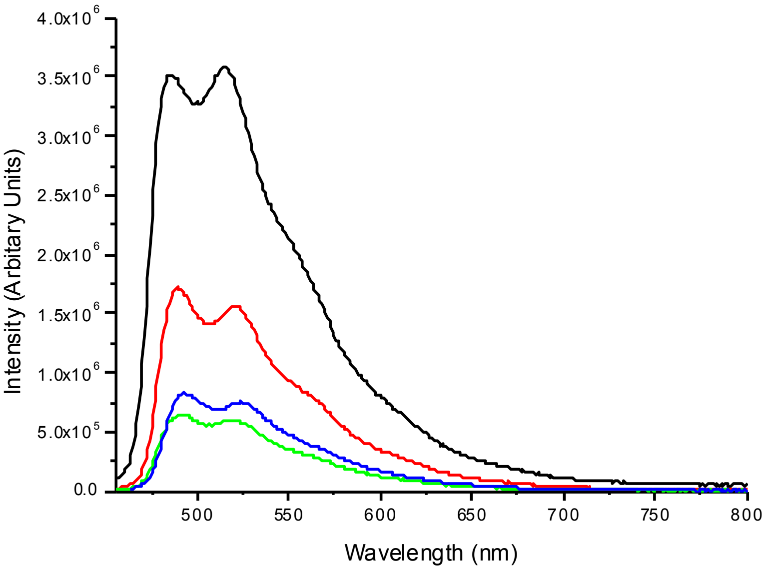

Figure 3.24. Emission spectra of [Ir(ppy-PEG)$_2$L^{tol}] [7.17 × 10^{-5} M] at 298 K in H_2O/DMSO (95/5) (black line, excitation at 445 nm), CH_2Cl_2 (red line, excitation at 448 nm), toluene (blue line, excitation at 454 nm) and CH_3CN (green line, excitation at 445 nm).

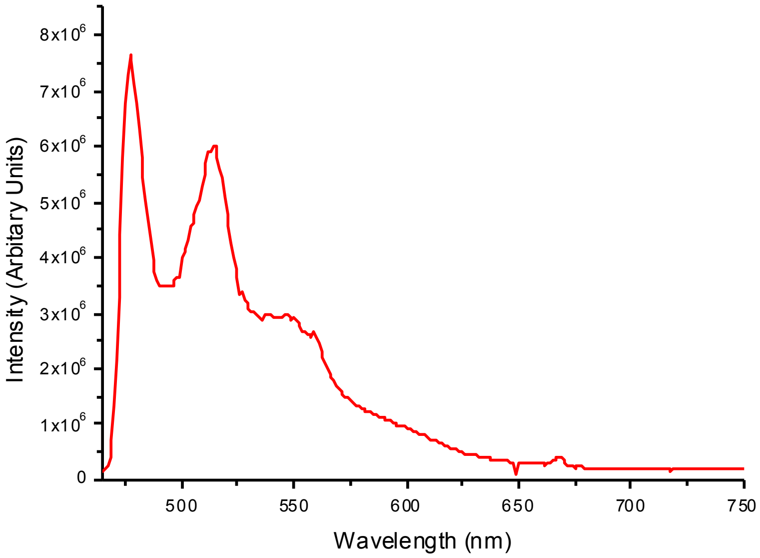

Figure 3.25. Emission spectrum of [Ir(ppy-PEG)$_2$L^{tol}] [7.17 × 10^{-5} M] at 77 K in EtOH/MeOH (4:1, v/v). Excitation at 445 nm.

Solvent (*T* [K])	λ_{em} (nm)	τ_1, τ_2 (ns)
CH_2Cl_2 (298)	489, 521, 564 (sh)	186 (11%), 89 (89%)
CH_3CN (298)	487, 519, 564 (sh)	188 (4%), 46 (96%)
Toluene (298)	492, 524, 566 (sh)	194 (4%), 46 (96%)
glass (77)[a]	477, 514, 545, 599(sh), 666	-
H_2O (298)	484, 515, 555 (sh)	528

Table 3.04. Photophysical data for [Ir(ppy-PEG)$_2$L^{tol}] [7.17 × 10^{-5} M]. [a] EtOH/MeOH (4:1, v/v).

Under photoexcitation, [Ir(ppy-PEG)$_2$L^{tol}] displayed green emission. The highest-energy emission maximum of the complex occurred between 484-492 nm depending on solvent. The emission profile was similar to that of [Ir(ppy-PEG)$_2$L^{tol}] and were assigned to typical mixtures of ^{3}MLCT of the (dπ(Ir) → π* (N^N and C^N)) transitions and ^{3}LLCT (π(N^C) → π*(N^N)) excited states. A small hypsochromic shift also occurred when the complex is in H_2O with a longer-lived luminescence lifetime and an increase in emission intensity. This evidence again may support the suggestion made for [Ir(ppy-PEG)$_2$L^{pytz}] that the PEG chains provide a protected and nonpolar local environment for the complex, however further investigation is needed to confirm this

As explained previously for [Ir(ppy-PEG)$_2$L^{pytz}], at 77 K an expected increase in emission intensity occurs along with a small hypsochromic shift (**Fig. 3.25**).

A pH titration was performed in H_2O/DMSO (95/5). The emission spectra from the titration are given in **Figure 3.26**.

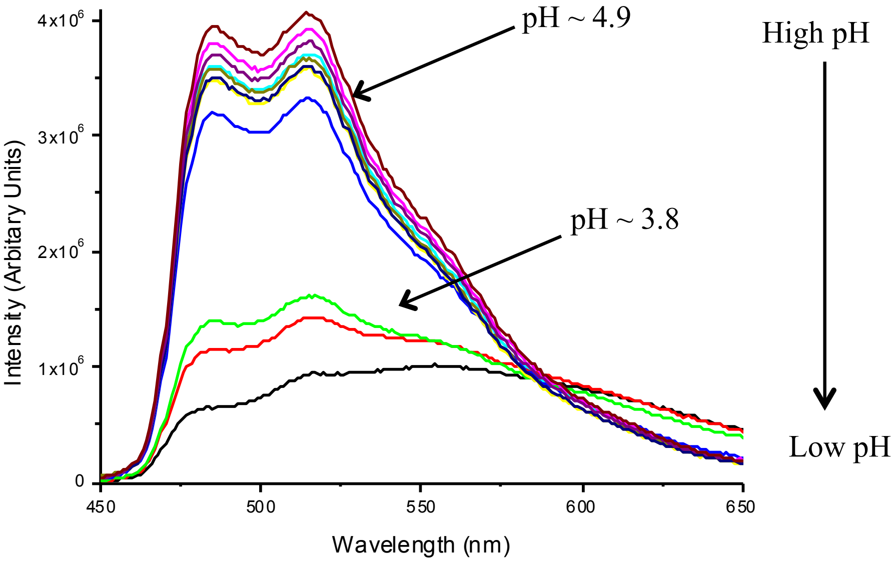

Figure 3.26. Emission spectra of [Ir(ppy-PEG)$_2$L^{tol}] [1.43 × 10^{-5} M] in H_2O/DMSO (95/5) during pH titrations at 298 K.

Under basic conditions, there was little change in the emission intensity of the complex. Interestingly, a partial quenching of emission intensity with a bathochromic shift to give a broad peak covering the spectral window from 550 to 650 nm was observed below pH ~ 4. This was unexpected, as protonation of the complex under acidic conditions cannot occur due to the absence of a pendant pyridine group. A comparison of time-resolved luminescence measurements for [Ir(ppy-PEG)$_2$L^{tol}] and [Ir(ppy-PEG)$_2$L^{pytz}] are give in **Table 3.05**.

pH (298 K)	[Ir(ppy-PEG)$_2$L^{tol}] τ_1, τ_2 (ns)	[Ir(ppy-PEG)$_2$L^{pytz}] τ_1 (ns)
Neutral	528	557
> 10	580	543
< 4	354 (96%), 114 (4%)	350

Table 3.05. Emission lifetimes of [Ir(ppy-PEG)$_2$L^{tol}] [1.43×10^{-5} M] and [Ir(ppy-PEG)$_2$L^{pytz}] [1.39×10^{-5} M] in H_2O/DMSO (99/5) and (99.9/0.1) respectively at 298 K.

Under basic conditions, both complexes had a single luminescence decay lifetime (~550 ns). Under acidic conditions, [Ir(ppy-PEG)$_2$L^{pytz}] had a shortened single lifetime (350 ns) whereas a biexponential decay for [Ir(ppy-PEG)$_2$L^{tol}] was observed with two shortened lifetimes (354 ns and 114 ns). Further time-resolved luminescence measurements were recorded for [Ir(ppy-PEG)$_2$l^{tol}] in different wavelength windows within the visible region under acidic conditions (**Table 3.06**).

Region (nm)	τ_1, τ_2 (ns) at pH 3.2
425-475	350
575-625	374 (83%), 146 (17%)
625-675	364 (80%), 143 (20%)

Table 3.06. Lifetimes of [Ir(ppy-PEG)$_2$L^{tol}] [7.43×10^{-5} M] between various windows of wavelengths, in H_2O/DMSO (99/5) under acidic conditions (pH = 3.2) at 298 K.

At pH 3.2, in the emission wavelength range of 425-475 nm, a single exponential lifetime was observed for the complex. The measured lifetimes between 575-675 nm (where the broad band occurs in the emission spectrum) showed biexponential decays with two shortened lifetimes. The most probable explanation for the partial quenching and bathochromic shift in emission in an acidic environment is the formation of aggregates in solution. The excitation spectra of the complex were recorded at pHs 10.8 and 3.2; where in each case the excitation wavelengths were set at λ_{ex} = 485 nm (the emission maxima of the complex) and 600 nm (the emission of the broad band in an acidic environment). The recorded spectra were identical at both acidic and basic environments and at different excitation wavelengths, suggesting that excimer formation was not feasible; suggesting an aggregation-induced bathochromic shift was the most probable explanation.

3.7.3 Quantum Yield of Emission of [Ir(ppy-PEG)$_2$L^{tol}]

The quantum yield (Φ) of [Ir(ppy-PEG)$_2$L^{tol}] was calculated to be Φ = 0.025 in aerated CH_2Cl_2 by measuring against Ir(ppy)$_3$ as a standard. This standard was calibrated against the same molecule in aerated toluene (Φ = 0.04) and against Ru(bpy)$_3$.Cl_2.$6H_2O$ in aerated water (Φ = 0.042).[17,18,19] The quantum yield was calculated using **Equation 3.01** As described previously.

3.8 Cell-Imaging Properties of [Ir(ppy-PEG)$_2$L^{tol}] and [Ir(ppy-PEG)$_2$L^{pytz}]

3.8.1 Cell Images

[Ir(ppy-PEG)$_2$L^{tol}] and [Ir(ppy-PEG)$_2$L^{pytz}] were utilised as phosphorescent dyes for live cell imaging using the MCF7 cell line. Measurements were taken by Dr Elizabeth Baggaley and the preliminary data is reported below. The two-photon microscopy images of the cells labelled with the complexes are given in **Fig. 3.27** below.

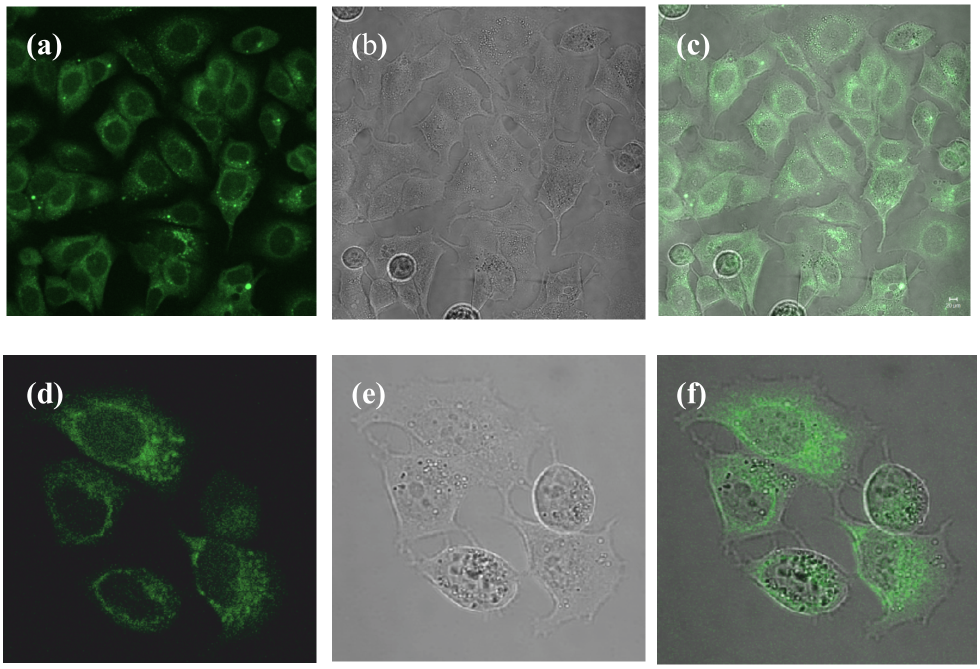

Figure 3.27. Two-photon (λ_{ex} = 780 nm) confocal microscopy images of MCF7 cells at 298 K with: (a) [Ir(ppy-PEG)$_2$L^{tol}] (25 µM, 4 hrs); (b) a differential interference contrast (DIC) image; (c) an overlay of the two images; (d) [Ir(ppy-PEG)$_2$L^{pytz}] (25 µM, 4 hrs); (e) DIC images and (f) overlay of the two images. The wavelength window for the images was taken between 480-510 nm.

The complexes were up taken into the cells and at 25 μM concentrations with a 4-hour incubation period, punctate staining for both of the complexes was observed. Under these conditions [Ir(ppy-PEG)$_2$L^{tol}] had brighter emission than [Ir(ppy-PEG)$_2$L^{pytz}].

Cell images were then taken with an increased concentration of [Ir(ppy-PEG)$_2$L^{tol}] to 50 μM whilst keeping the incubation time at 4 hours (**Fig. 3.28**).

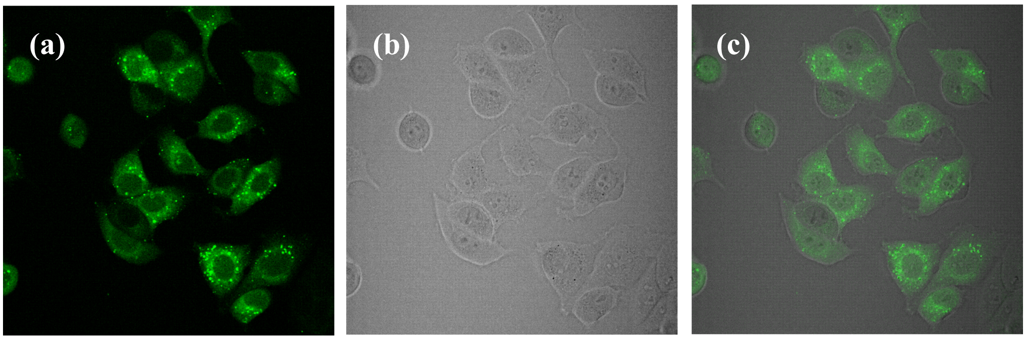

Figure 3.28. Two-photon (λ_{ex} = 780 nm) confocal microscopy images of MCF7 cells at 298 K with: (a) [Ir(ppy-PEG)$_2$L^{tol}] (50 μM, 4 hrs); (b) a DIC image and (c) an overlay of the two images. The wavelength window for the images was taken between 480–510 nm.

Upon increase in concentration of [Ir(ppy-PEG)$_2$L^{tol}], accumulation of the complex into cellular vesicles is observed, which is shown by the areas of bright punctate staining, however this is not seen for [Ir(ppy-PEG)$_2$L^{pytz}] even at higher concentrations (100 μM) (**Fig. 3.29**).

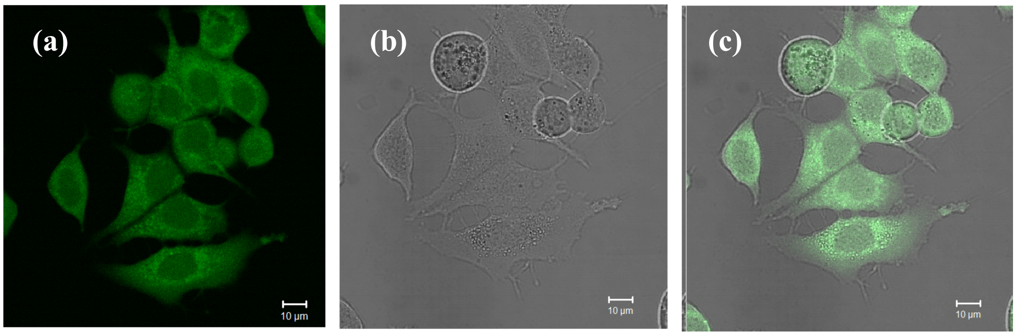

Figure 3.29. Two-photon (λ_{ex} = 780 nm) confocal microscopy images of MCF7 cells at 298 K with: (a) [Ir(ppy-PEG)$_2$L^{pytz}] (100 µM, 4 hrs); (b) a DIC image and (c) an overlay of the two images. The wavelength window for the images was taken between 480–510 nm.

Although no such obvious accumulation of [Ir(ppy-PEG)$_2$L^{pytz}] was observed, some modest punctate staining does appear around the perinuclear region of the cell. In each case, there was diffuse cytoplasmic emission.

The accumulation effect into cellular vesicles for [Ir(ppy-PEG)$_2$L^{tol}] becomes more pronounced when the incubation time was extended to 24 hours (**Fig. 3.30**).

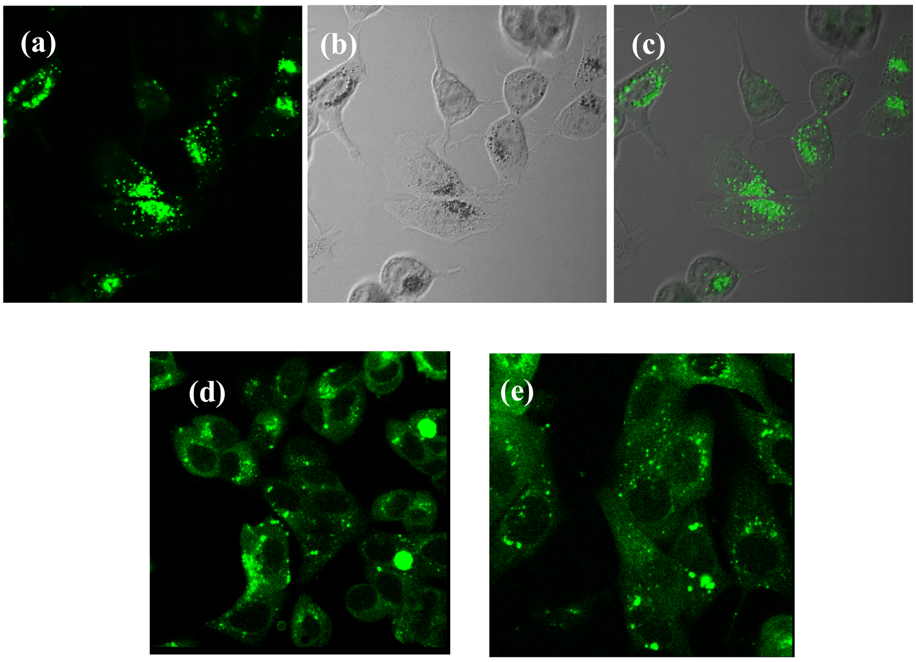

Figure 3.30. Two-photon (λ_{ex} = 780 nm) confocal microscopy images of MCF7 cells at 298 K with: (a) [Ir(ppy-PEG)$_2$L^{tol}] (50 μM, 24 hrs); (b) a DIC image; (c) an overlay of the two images; (d) [Ir(ppy-PEG)$_2$L^{tol}] (25 μM, 24 hrs) and (e) conventional confocal microscopy image (λ_{ex} = 405 nm) with [Ir(ppy-PEG)$_2$L^{tol}] (25 μM, 24 hrs). The wavelength window for the images was taken between 480–510 nm.

Interestingly the same staining pattern is not observed with [Ir(ppy-PEG)$_2$L^{pytz}] (**Fig. 3.31**). A likely cause for this observation could be that the complex is being quenched in areas of the cell where there is an acidic environment present.

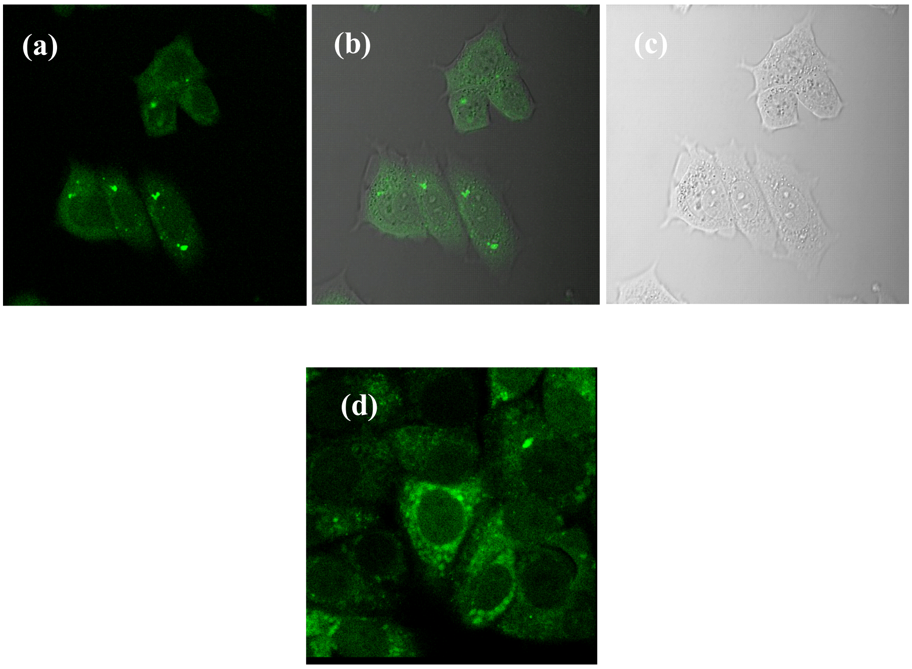

Figure 3.31. Two-photon (λ_{ex} = 780 nm) confocal microscopy images of MCF7 cells at 298 K with: (a) [Ir(ppy-PEG)$_2$L^{pytz}] (50 µM, 24 hrs); (c) a DIC image; (b) an overlay of the two images and (d) conventional confocal microscopy image (λ_{ex} = 405 nm). The wavelength window for the images was taken between 480–510 nm.

Emission from the two compounds is dissimilar, where typically a higher concentration of [Ir(ppy-PEG)$_2$L^{pytz}] is required to give better images, therefore it is probable that the method of uptake into cells could be different for each complex.

Images taken of the cells with [Ir(ppy-PEG)$_2$L^{tol}] at a longer wavelength window (650-710 nm) showed some red shifted emission (**Fig. 3.32**). This is consistent with the pH titration data reported earlier; where at very low pH a red shifted ground state aggregate was induced with a shorter emission lifetime.

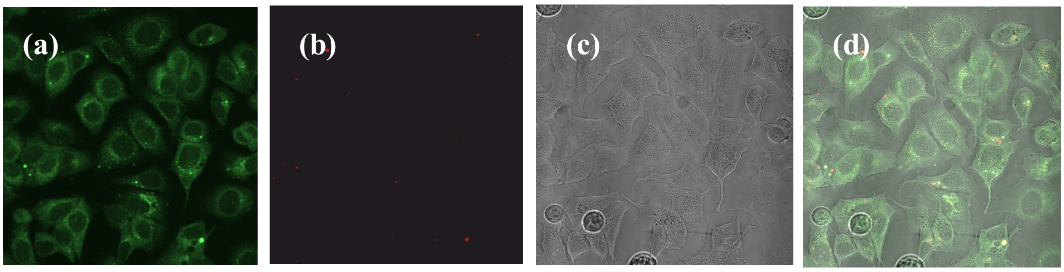

Figure 3.32. Two-photon (λ_{ex} = 780 nm) confocal microscopy images of MCF7 cells at 298 K with [Ir(ppy-PEG)$_2$L^{tol}] (25 µM, 4 hrs): (a) image window between 480-510 nm; (b) image window between 650-710 nm showing red-shifted emission (c) a DIC image and (d) an overlay of the images.

Z-stack images showed that emission from both complexes occurred from throughout the cell. These images are given in **Figure 3.33** along with the normalised emission spectra of the two complexes.

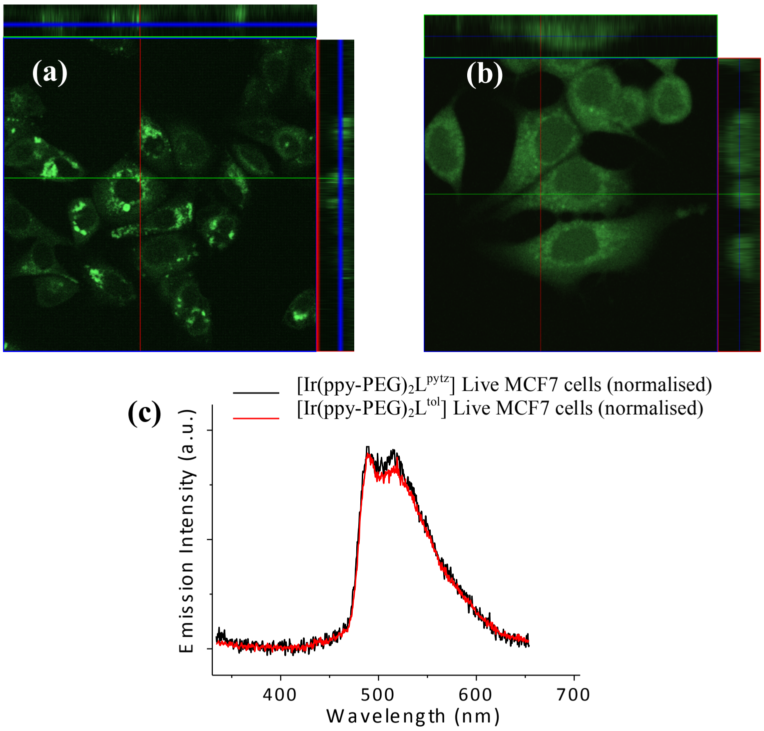

Figure 3.33. Z-stack image of (a) [Ir(ppy-PEG)$_2$L^{tol}] (25 µM, 24 hrs); (b) [Ir(ppy-PEG)$_2$L^{pytz}] (100 µM, 4 hrs) and (c) a normalised emission spectra of the complexes from within the cells.

3.8.2 Summary of the Cell Imaging

Preliminary cell-imaging studies have showed that incubation of MCF7 cells with [Ir(ppy-PEG)$_2$L^{tol}] and [Ir(ppy-PEG)$_2$L^{pytz}] at 25 μM for 4 hours resulted in efficient cellular uptake with obvious punctate staining in the cytoplasm. Both complexes can be excited in cellulo with 780 nm and 405 nm excitation light. More importantly, the fact that the complexes can undergo two-photon excitation at 780 nm highlights the fact that they are good candidates as cell imaging agents, as higher-energy single-photon excitation can have limits due to the fact that it has poor tissue penetration and can cause tissue/cell damage. Strong emission intensities of the complexes were still observed at higher concentrations (50 μM) and an increased incubation time of 24 hours. Z-scans confirmed that internalisation had occurred, with both complexes selectively localising in the cytoplasm rather than the nucleus or membranes.

Due to the similarity of the staining patterns of endosomes, lysosomes and mitochondria, it is difficult to identify where the complexes are localising within the cell. Further co-staining studies are necessary to gain better insight of where the complexes are staining, however it is probable that both complexes are staining more the one organelle.[20,21]

The pH responsive properties of [Ir(ppy-PEG)$_2$L^{pytz}], where emission is quenched at low pH, may affect the ability of the complex to act as an effective organelle stainer, however the differences between cellular emission intensities between both complexes indicate that the complexes may have a different mechanism of cell uptake. The fact that [Ir(ppy-PEG)$_2$L^{pytz}] can be protonated could allow electrostatic interaction of the complex with the negatively charged cell-membrane. Further studies are necessary in order to confirm this.

3.9 Chapter Conclusion

The synthesis and photophysical studies of three Ir(III) complexes were reported and the complexes were fully characterised. Of the three complexes, two were successfully utilised as phosphorescent cell imaging agents.

Photophysical studies of [Ir(ppy-PEG)$_2$L^{pytz}] and [Ir(ppy-PEG)$_2$L^{tol}] showed that incorporation of PEG groups onto the complexes enabled the complexes to be water soluble as well as enhancing the emission and lifetime properties of the complexes in aqueous solution (when compared to organic solution) possibly due to the close proximity of the PEG groups providing a nonpolar local environment for the complexes.

pH studies showed significant quenching of emission of [Ir(ppy-PEG)$_2$L^{pytz}] between pH 4-6, where near-complete quenching of emission was observed below pH 4. Using [Ir(ppy-PEG)$_2$L^{tol}] confirmed that quenching of emission of [Ir(ppy-PEG)$_2$L^{pytz}] occurred due to the protonation of the pendant pyridine group on the complex. Although partial quenching of [Ir(ppy-PEG)$_2$L^{tol}] occurred below pH 4 accompanied by a bathochromic shift in the emission, time-resolved measurements and excitation studies confirmed this was due to the formation of aggregates. Red-shifted emission observed between 650-710 nm in the cell-imaging studies also confirmed this.

Both complexes selectively stained the cytoplasm of MCF7 cells and good punctate staining was observed at various concentrations (25 μM, 50 μM and 100 μM) at 4 hour and 24 hour incubation times at room temperature. The mechanism of cell-uptake remains unclear and requires further investigation, however differences in intensities of cellular emission between the two complexes indicates that the complexes may have different uptake mechanisms into cells, highlighting the significance of utilising specific pendant groups on complexes when designing them.

Cytotoxicity measurements are necessary in order evaluate the biocompatibility of the complexes within the cells, along with co-staining studies in order to confirm which organelles the complexes are selectively staining, however it is probable that more than one organelle is being stained. The pH responsive nature of [Ir(ppy-PEG)$_2$L^{pytz}] where emission in quenched in acidic conditions may be disadvantageous for use as a specific organelle stainer.

3.10 References

1. K. K-W. Lo, C-K. Chung and N. Zhu, *Chem. Eur. J.,* 2003, **9**, 475.
2. P. Steunenberg, A. Ruggi, N. S. van der Berg, T. Buckle, J. Kuil, F. W. B. van Leeuwen and A. H. Velders, *Inorg. Chem.,* 2012, **51**, 2105.
3. S. P-Y. Li, H-W. Liu, K. Y. Zhang and K. K-W. Lo, *Chem. Eur. J.,* 2010, **16**, 8329.
4. P. Bailon and W. Berthold, *Pharm. Sci. Technol. Today,* 1998, **1**, 352.
5. J. M. Harris and R. B. Chess, *Nat. Rev. Drug Discovery,* 2003, **2**, 214.
6. M. Licini and J. A. G. Williams, *Chem. Commun.,* 1999, 1943.
7. J. L. Wike-Hooley, J. Hareman and J. S. Reinhold, *Radiother. Oncol.,* 1984, 343.
8. J. Casey, S. Grintein and J. Orlowski, *Nat. Rev. Mol. Cell Bio.,* 2010, **11**, 50.
9. E. Orselli, G. S. Kottas, A. E. Konradsson, P. Coppo, R. Fröhlich, L. De Cola, A. van Dijken and H. Börner, *Inorg. Chem.,* 2007, **46**, 11082.
10. P. S. Shirude, V. A. Kumar and K. N. Ganesh, *Eur. J. Org. Chem.,* 2005, 5207.
11. X. Zeng, A. S. Batsanov and M. R. Bryce, *J. Org. Chem.,* 2006, **71**, 9589.
12. K. A. King and R. J. Watts, *J. Am. Chem. Soc.,* 1987, **109**, 1589.
13. B. Schmid, F. O. Garces and R. J. Watts, *Inorg. Chem.,* 1994, **33**, 9.
14. F. Barigelletti and L. Flamigni, *J. Am. Chem. Soc.,* 1999, **121**, 5009.
15. S. P-Y. Li, C. T-S. Lau, M-W. Louie, Y-W. Lam, S. H. Chang and K. K-W. Lo, *Biomaterials,* 2013, **34**, 7519.
16. A. Juris, V. Balzani, F. Barigelletti, S. Campagna, P. Belser and A. Von Zelewsky, *Coord. Chem. Rev.,* 1988, **84**, 85.
17. K. A. King, P. J. Spellane and R. J. Watts, *J. Am. Chem. Soc.,* 1985, **107**, 1431.
18. E. B. Namdas, A. Ruseckas and D. W. Samuel, *J. Phys. Chem. B.,* 2004, **108**, 1570.
19. K. Suzuki, A. Kobayashi, S. Kaneko, K. Takehira, T. Yoshihara, H. Ishida, Y. Shiina, S. Oishi and S. Tobita, *Phys. Chem. Chem. Phys.,* 2009, **11**, 9850.
20. V. Fernandez-Moreira, F. L. Thorp-Greenwood and M. P. Coogan, *Chem. Commun.,* 2010, **46**, 186.

21. K. Y. Zhang, H-W. Liu, T. T-H. Fong, X-G. Chang and K. K-W. Lo, *Inorg. Chem.,* 2010, **49**, 5432.

4

Effect of Spacer Groups on d → f Energy-Transfer

4.1 Introduction

This chapter looks at the synthesis and characterisation of Ir(III)/Ln(III) complexes displaying Ir → Ln photoinduced energy-transfer and how the spacer group effects the photophysical properties for sensitised lanthanide emission.

4.1.1. Previous Research

In 2005 the De Cola group reported on the first known example of an Ir/Eu complex (**Fig. 4.01**) displaying white light emission.[1]

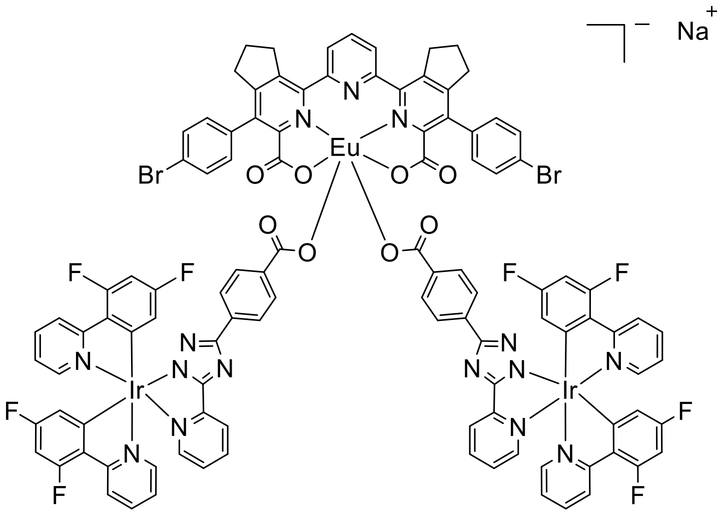

Figure 4.01. Structure of the Ir/Eu complex reported by the De Cola group.

Emission from the Ir(III) components of the complex was blue-green in colour (λ_{max} = 461 nm). Partial energy-transfer from the Ir(III) excited-state to Eu(III) resulted in red-coloured emission from the Eu(III) centre. The balance of these emissions was such that the overall emission of white light was achieved.

In 2012 the Ward group reported the preparation and photophysical properties of a macrocycle-appended naphthalimide derivative (**Fig. 4.02**) and the ability of this complex to also emit white light when Eu(III) is bound into the macrocycle centre.[2,3]

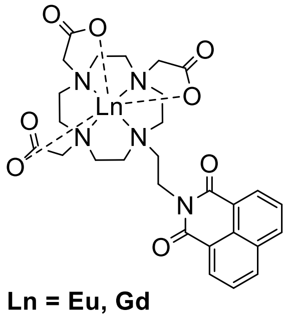

Figure 4.02. Structure of the macrocycle-appended naphthalimide derivative reported by the Ward group.

The interesting feature of this complex was that white light emission was achieved through a balance of red emission (from the Eu centre), blue emission (from the naphthalimide unit) and green emission (from aggregated naphthalimide units which generate excimers), displaying an example of a white-light emitting system that is composed of only one component rather than two or three luminophores.

There has been extensive research on complexes containing cyclen-based amino-carboxylate units.[4,5,6,7,8] These complexes are advantageous especially in biological applications as the carboxylic acid groups allow the complexes to be water-soluble and the lanthanide units are 'locked' into the cyclen centre through coordination to the N and O atoms as a result of the chelate effect which is strong with 7- or 8-dentate ligands. This makes the complex kinetically and thermodynamically stable which is important when the complexes are used in biological applications, as toxicity is reduced by preventing the lanthanide metals from dissociating from the ligands and leaching out into the biological systems.

An interesting example of implementing cyclen-based Ir(III) complexes as cell imaging agents was demonstrated by the Ward group in 2014, where a first example of cell imaging using two independent emission components from a dinuclear d/f complex was reported **(Fig 4.03).**[9]

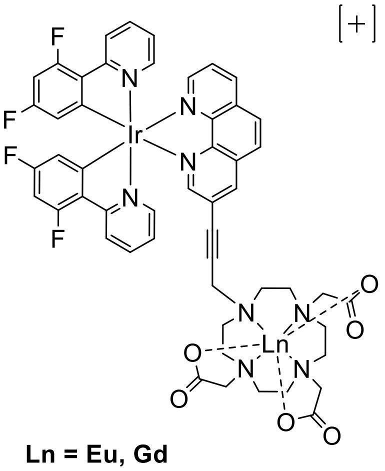

Figure 4.03. Structure of a Ir(III)/Ln(III) complex used as a cell imaging agent.

Two-photon excitation of the Ir(III) chromophore at 780 nm resulted in both green Ir(III)-based and red Eu(III)-based emission. Time-gated detection allowed identification of each emission component due to the large difference in emission timescale between Ir(III) emission (~µs) and Eu(III) emission (ms). In order to achieve this, a good balance of Ir(III)-based emission and Eu(III)-based emission is required; essentially the d → f energy transfer should not be too efficient (causing Ir(III)-based emission to become quenched) nor too inefficient (Eu(III)-based emission is too weak). In this example, the alkyne spacer group facilitated a good balance of d → f energy transfer to give emission from both Ir(III) and Eu(III).

In 2013 the Ward group also reported on a first example of an Ir(III)/Eu(III) dyad containing a naphtyl spacer unit which acted as an energetic and spatial stepping stone in the d → f energy transfer process (**Fig. 4.04**).[10]

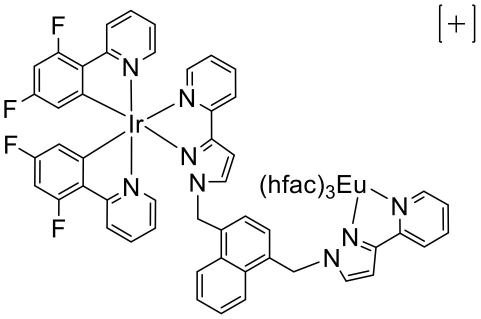

Figure 4.04. Structure of a Ir(III)/Eu(III) dyad containing a naphthyl spacer unit. Hfac = hexafluoroacetylacetonate.

Photophysical studies showed that the Ir(III)-based emission of the complex was nearly quenched by the naphthyl group to form a naphthyl-centred tripled state (^{3}nap). This resulted in sensitisation of Eu(III) emission occurring through two steps; First Ir-^{3}nap energy-transfer, followed by a ^{3}nap-Eu(III) energy-transfer step, therefore the ^{3}nap state acted like an intermediate stepping stone for two-stage d → f energy transfer.

There are multiple factors that control d → f energy-transfer and these factors are sometimes quite convoluted, however this study highlights the importance on the role of the spacer unit in controlling the energy-transfer process. This chapter looks at improving d → f energy-transfer through the use of a naphthyl spacer unit in Ir(III) complexes, as well as using cyclen-based units for potential duel-emitting cell imaging complexes.

4.2 [Ir(fppy)$_2$Lnap^{pic}]

4.2.1 Synthetic Studies

The synthetic details are described in full in Chapter 5. The initial synthesis for all the complexes involved the synthesis of the Ir(III) μ-dichloro-bridged dimer, [Ir$_2$(fppy)$_4$Cl$_2$], as described earlier in Chapter 2.

[Ir(fppy)$_2$Lnap^{pic}] was designed so that the energy-transfer process can be studied during titrations with lanthanides. It is structurally similar to [Ir(fppy)$_2$L^{pic}], which was described in Chapter 2, however the phenyl spacer unit has been changed to a naphthyl spacer unit (**Fig. 4.05**) in order to study how this affects the energy-transfer properties.

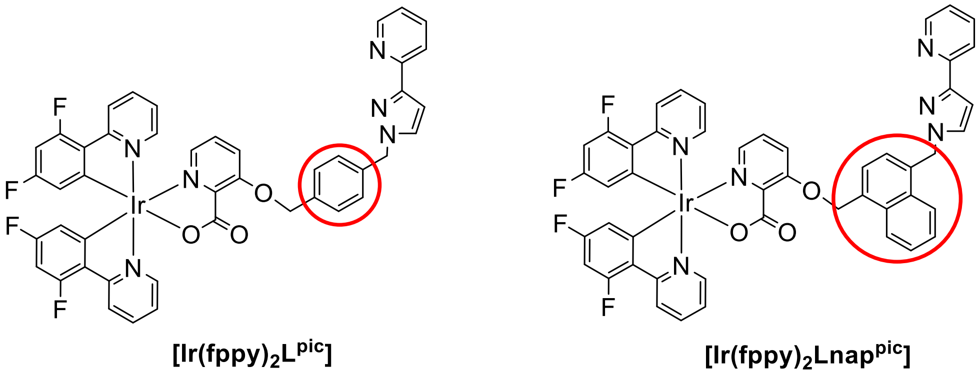

Figure 4.05. Chemical structures of [Ir(fppy)$_2$L^{pic}] (described in Chapter 2) and [Ir(fppy)$_2$Lnap^{pic}]. The phenyl spacer group has been replaced with a naphthyl spacer group (highlighted in red).

The initial step involved a Wohl-Ziegler Bromination[11] of 1,4-dimethylnaphthalene using 2.2 equivalents of *N*-bromosuccinimide (NBS) and a catalytic amount of the radical initiator aza-*bis*-isobutyronitrile (AIBN) to make 1,4-di(bromomethyl)naphthalene, shown in **Scheme 4.01**.

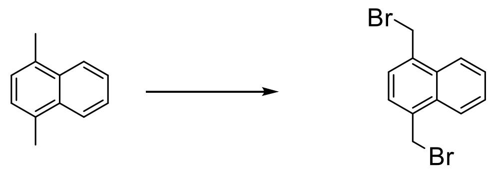

1,4-di(bromomethyl)naphthalene

Scheme 4.01. Synthesis of 1,4-di(bromomethyl)naphthalene. NBS (2.2 equiv), AIBN (cat.), CCl_4, reflux for 2 hours.

The product was obtained through crystallisation from toluene to give a yield of 52%.

Reaction of $[Ir_2(fppy)_4Cl_2]$ with 3-hydroxypicolinic acid gave the intermediate [Ir-pic]. This reaction is given in Chapter 2. The next step involved the reaction of this intermediate with 1,4-di(bromomethyl)naphthalene (**Scheme 4.02**).

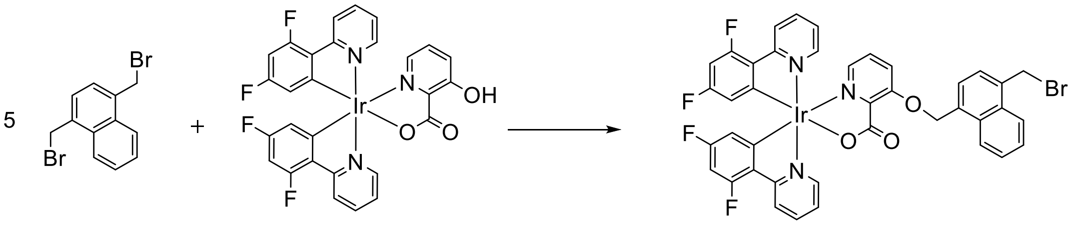

Intermediate [Ir-pic]

Intermediate [Ir-picnap]

Scheme 4.02. Synthesis of the intermediate [Ir-picnap]. K_2CO_3 (10 equiv), $N_{2\ (g)}$, acetone, 56°C, 48 hours.

In order to prevent two of the intermediate [Ir-pic] complexes reacting with one 1,4-dibromomethylnaphthalene unit, a 5:1 excess of the naphthalene to [Ir-pic] component was used as well as dissolving the naphthalene in a solution of acetone first, followed by slow addition of [Ir-pic] to this to ensure that the 1,4-di(bromomethyl)naphthalene was present in large excess.

Electrospray mass spectrometry confirmed the presence of the product, however ^1H NMR spectroscopy showed that purification was necessary. Initially purification was attempted by column chromatography on silica gel however the ^1H NMR spectrum still showed the presence of impurities. Due to a low yielding reaction, purification of the band containing the product was reattempted using prep TLC; however the ^1H

NMR spectrum once again showed the presence of impurities. It was suspected that the product was decomposing during the purification processes. Due to the low yield and suspected decomposition of the product by reaction of the pendant –CH_2Br group, a different synthetic route was developed (**Scheme 4.03**) where the 1,4-di(bromomethyl)naphthalene was reacted with pyridyl pyrazole (pypz) first to form nap^{pypz}, before attaching it onto the hydroxyl unit of the Ir(III) complex.

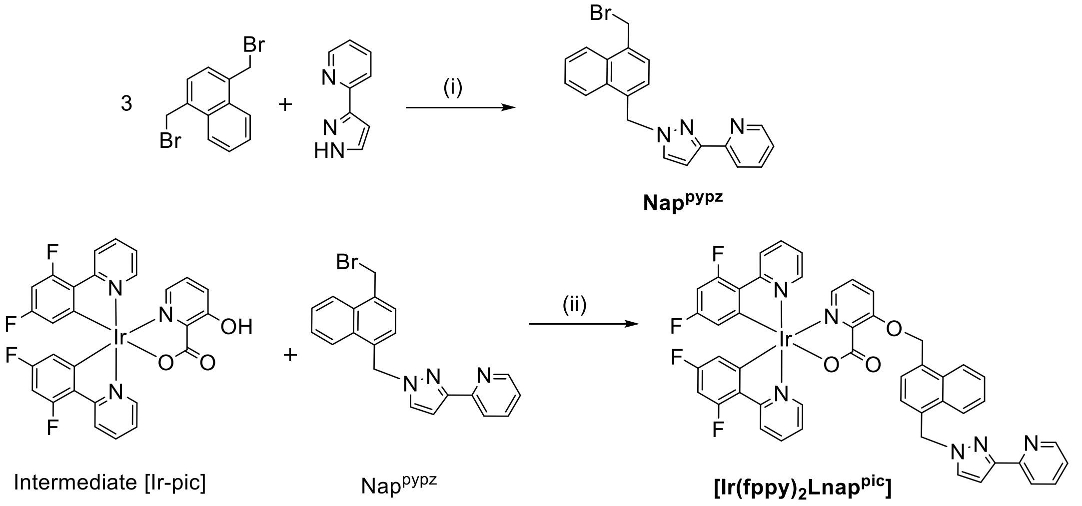

Scheme 4.03. (i) Synthesis of nap^{pypz}; NaOH $_{(aq)}$ (1M), THF, room temperature, 3 days. (ii) Synthesis of [Ir(fppy)$_2$Lnap^{pic}]; K_2CO_3 (10 equiv), $N_{2\,(g)}$, acetone, 56°C, 48 hours.

Nap^{pypz} was purified by column chromatography on silica gel. It was necessary to use the product within 24 hours of synthesis because decomposition of the product was observed after this period. In order to prevent pypz reacting on both sides of 1,4-di(bromomethyl)naphthalene, 3:1 excess of the 1,4-di(bromomethyl)naphthalene to pypz was used and the pypz was slowly added to a solution of the naphthalene. An overall yield of 63% was obtained for the preparation of nap^{pypz} in this way.

The second step of the reaction involved attaching the nap^{pypz} onto the intermediate [Ir-pic] complex. The presence of [Ir(fppy)$_2$Lnap^{pic}] in the crude product was confirmed by electrospray mass spectrometry. The product was purified by column chromatography, initially by alumina gel (in CH_2Cl_2/MeOH), followed by silica gel (in CH_3CN). The reaction afforded a yield of 25%. Confirmation of purity was given by the ^{1}H NMR spectrum (**Fig. 4.06**).

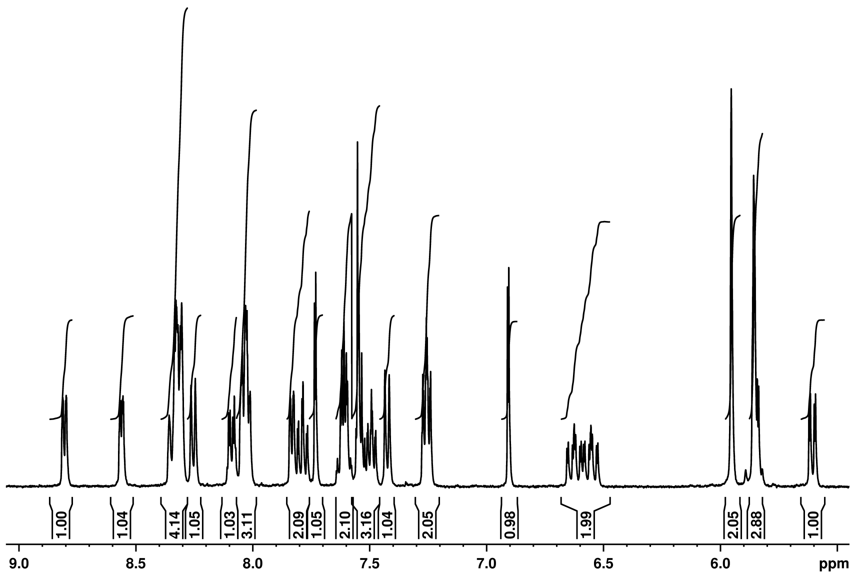

Figure 4.06. ^{1}H NMR (400 MHz Acetone-d$_6$) spectrum of [Ir(fppy)$_2$Lnap^{pic}] after purification.

Integration of the spectrum gave 31 H environments, which correlates with the number of H atoms present in the complex. The two peaks at δ_H = 5.95 and 5.85 ppm are from the two alkyl CH_2 group, however the peak at 5.85 ppm integrates as 3 H atoms due to the presence of a H atom lying at 5.84 ppm.

4.2.2 Photophysical Properties

The UV/Vis spectrum of [Ir(fppy)$_2$Lnap^{pic}] was recorded in aerated CH_2Cl_2 at room temperature (**Fig. 4.07**). Tentative assignment of the spectrum is given in **Table 4.01**.

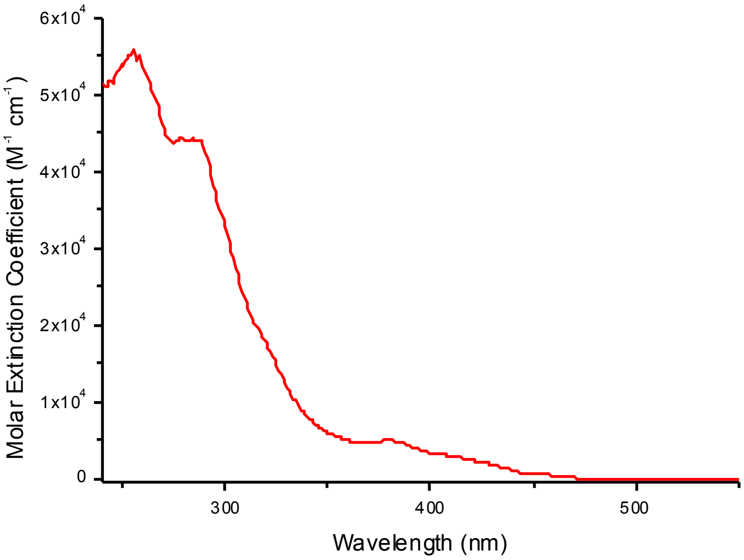

Figure 4.07. UV/Vis absorption spectrum of [Ir(fppy)$_2$Lnap^{pic}] [5.13 × 10^{-6} M] in aerated CH_2Cl_2 at 298 K.

Absorption		Assignment
λ_{max}/nm	ε/M^{-1} cm^{-1}	
255	56,000	π-π*
284	44,000	π-π*
318	18,000	MLCT (sh)
382	5,000	MLCT (sh)
418	2,500	MLCT (broad)

Table 4.01. UV/Vis absorption data of [Ir(fppy)$_2$Lnap^{pic}] [5.13 × 10^{-6} M] in aerated CH_2Cl_2 at 298 K.

The high-energy absorption bands (< 300 nm) are assigned to spin-allowed intraligand π-π* transitions localised on the coordinated ligands.[12,13,14] The less intense and poorly defined absorption bands and shoulders at λ > 300 nm can be assigned to spin-allowed and spin-forbidden MLCT transitions corresponding to (dπ(Ir) → π* (N^O and C^N)) transitions. The excitation spectrum was measured and overlaid with the absorption spectrum (**Fig. 4.08**). The good match between these 2 spectra indicates that the emission observed emanates from the compound.

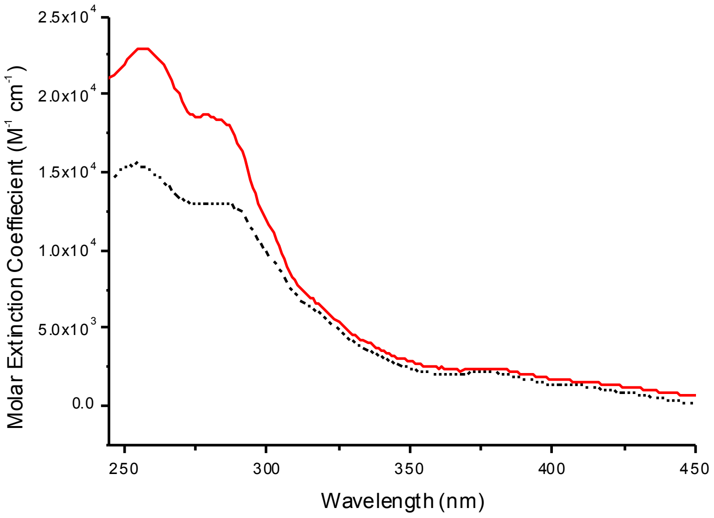

Figure 4.08. Excitation spectrum (black dashed line) of [Ir(fppy)$_2$Lnap^{pic}] (registered at 470 nm) overlaid with the absorption spectrum (red line) in CH_2Cl_2.

The emission spectrum of [Ir(fppy)$_2$Lnap^{pic}] was also recorded in CH_2Cl_2 at room temperature and is given in **Fig. 4.09**.

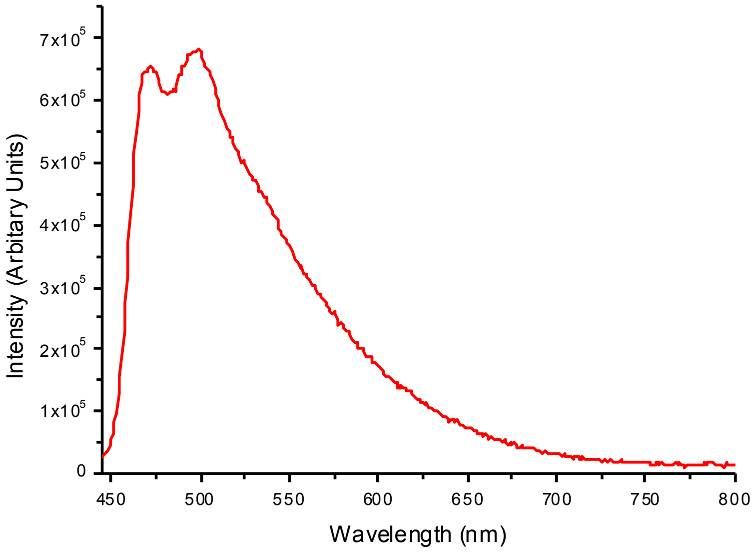

Figure 4.09. Emission spectrum of [Ir(fppy)$_2$Lnap^{pic}] [5.00 × 10^{-5} M] in aerated CH_2Cl_2 at 298 K. Excitation at 441 nm.

Two high-energy bands were observed at 470 nm and 500 nm in the spectrum. This vibronic fine-structure of the emission band is indicative of a large amount of ^{3}LC character with typical mixtures of ^{3}LC and ^{3}MLCT states being the main excited states of the complex.[24] A small hypsochromic shift to 460 nm was observed when the emission was recorded at 77 K in EtOH/MeOH (4:1) glass, which is consistent with the ^{3}LC state. There was also an increase in the intensity of emission which was attributed to the impediment of the nonradiative relaxation processes. The quantum yield (Φ) was measured against the standard Ir(ppy)$_3$ in CH_2Cl_2 at room temperature and had a value of $\Phi = 0.02$, which is half that of [Ir(fppy)$_2$L^{pic}]. Time-resolved luminescence measurements of the free complex showed it had a biexponential decay in aerated CH_2Cl_2 with lifetimes of $\tau_1 = 830$ ns (major component) and $\tau_2 = 200$ ns (minor component). A biexponential decay for this complex is consistent with previous data for [Ir(fppy)$_2$L^{pic}] which also had a bioexponential decay profile (see Chapter 2) and is likely to be as a result of a mixture of conformers being present in solution. Multi-exponential decay kinetics are commonly observed for these types of complexes.[16,17,18]

Luminescence measurements for [Ir(fppy)$_2$Lnap^{pic}] and [Ir(fppy)$_2$L^{pic}] were recorded at the same optical density (0.1 for both complexes), therefore the extent of quenching of Ir(III)-based emission of [Ir(fppy)$_2$Lnap^{pic}] can be calculated to be ~ 80% due to ^{3}Ir→nap PEnT (**Figure 4.10**).

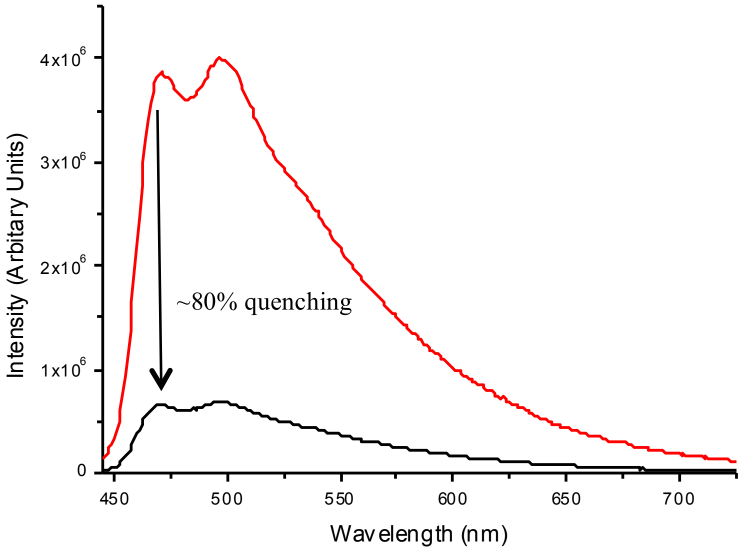

Figure 4.10. Emission spectra of [Ir(fppy)$_2$L^{pic}] [1.04 × 10^{-4} M] (red) and [Ir(fppy)$_2$Lnap^{pic}] [5.00 × 10^{-5} M] (black) in aerated CH_2Cl_2 at 298 K.

Interestingly the lifetimes of the Ir(III)-based emission of [Ir(fppy)$_2$Lnap^{pic}] were longer than the lifetimes of [Ir(fppy)$_2$L^{pic}] (830 ns and 200 ns *vs* 100 ns and 240 ns respectively). Weaker Ir(III)-based emission with longer-lived emission lifetimes is an unusual mix and is a result of the PEnT from ^{3}MLCT → nap. This is consistent with previous research by the Ward group on closely related systems.[10] The longer-lived emission lifetimes could be a result of either: (i) the naphthalene units providing the Ir(III) core steric protection from solvent/O_2 or (ii) the ‘reservoir effect’ with the non-emissive ^{3}nap state (due to the similarity in energies of ^{3}MLCT and ^{3}nap).[16,17] Phosphorescence from the ^{3}nap (although probable) is not observed due to the rate of collision-induced deactivation being faster than the rate of decay for phosphorescence in solution at room temperature.[10]

The Ir(III)/Ln(III) dyads were prepared by titration of [Ln(hfac)$_3$.2H_2O] to a solution of [Ir(fppy)$_2$Lnap^{pic}] in CH_2Cl_2 at room temperature. Binding of the [Ln(hfac)$_3$] molecules occurs at the pendant pyridyl-pyrazole site with the displacement of the two water molecules from the coordination sphere (**Scheme 4.04**).

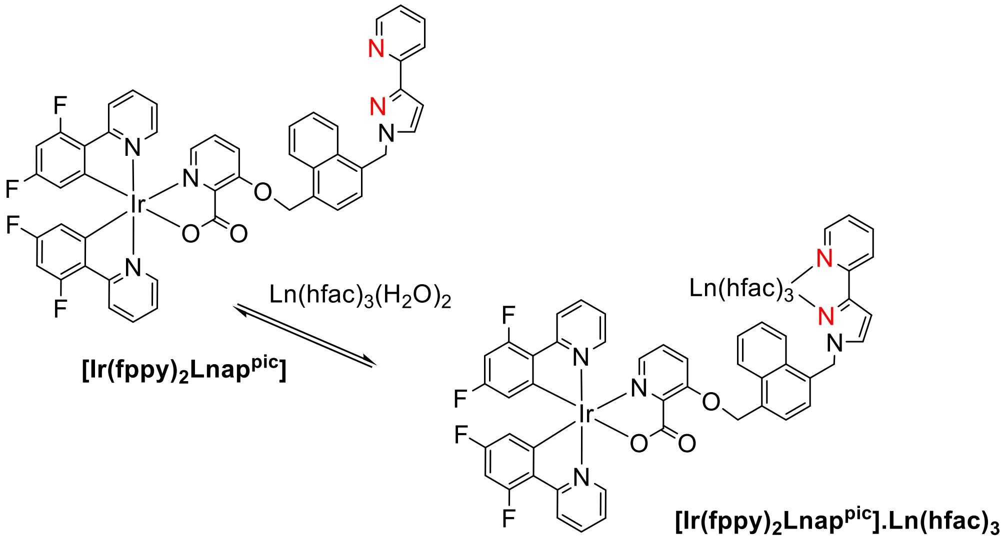

Scheme 4.04. Binding of [Ln(hfac)$_3$] to the pendant pyridyl-triazole site (red) of [Ir(fppy)$_2$Lnap^{pic}].

The complex was also titrated with [Gd(hfac)$_3$.2H$_2$O], which was used as a control experiment as there cannot be any Ir(III) → Gd(III) PEnT as the energy of the lowest excited state of Gd(III) is approximately 10,000 cm^{-1} higher than the Ir(III) excited state. The emission spectra obtained during the titration are given in **Fig. 4.11**.

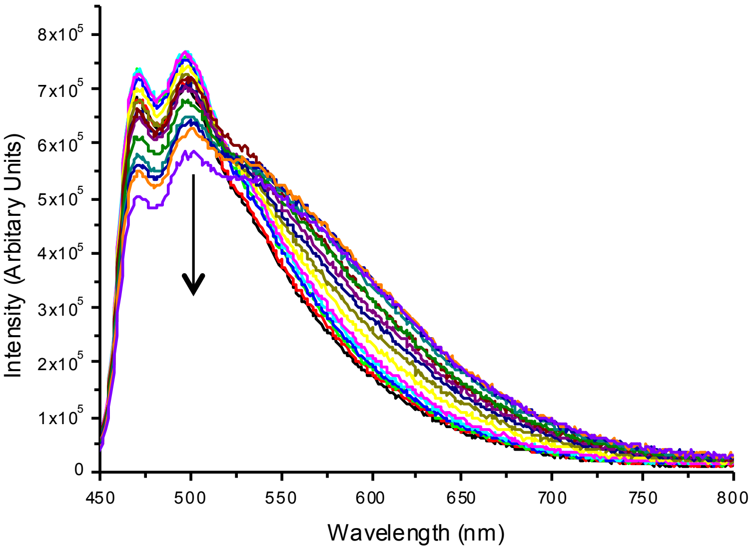

Figure 4.11. Emission spectra of [Ir(fppy)$_2$Lnap^{pic}] [5.00 × 10^{-5} M] titrated with [Gd(hfac)$_3$.2H$_2$O] [1.20 × 10^{-4} M] in aerated CH$_2$Cl$_2$ at 298 K. Excitation at 428 nm.

A small amount of quenching of the Ir(III)-based emission (~ 25%) at the end point of the titration is observed, with a slight bathochromic shift of the emission. Time-resolved luminescence measurements showed a decrease in the Ir(III) emission lifetimes from 824 ns and 210 ns, to 630 ns and 130 ns at the end point of the titration. Direct energy-transfer can ruled out as the quenching mechanism as it is not possible for the Ir(III)/Gd(III) dyad.

[Ir(fppy)$_2$Lnap^{pic}] was also titrated with [Tb(hfac)$_3$.2H$_2$O] and the luminescence spectra of the titration is given in **Fig. 4.12**.

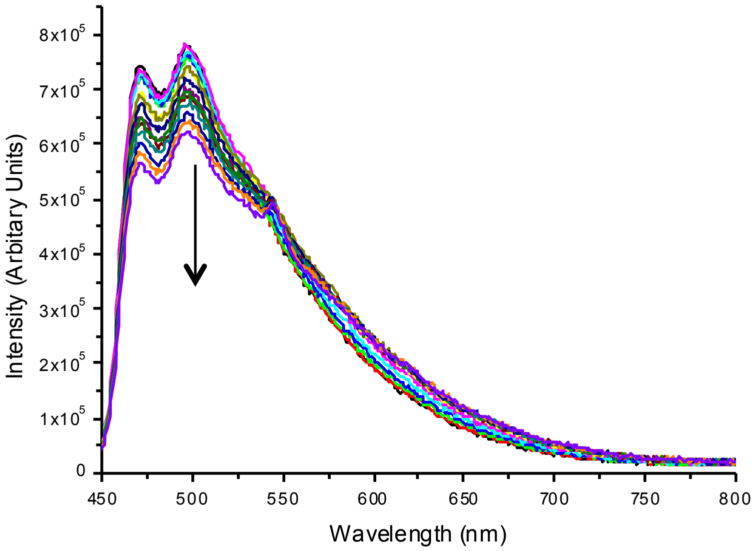

Figure 4.12. Emission spectra of [Ir(fppy)$_2$Lnap^{pic}] [5.00 × 10^{-5} M] titrated with [Tb(hfac)$_3$.2H$_2$O] [1.20 × 10^{-4} M] in aerated CH$_2$Cl$_2$ at 298 K. Excitation at 431 nm.

Titration of the complex with [Tb(hfac)$_3$.2H$_2$O] did not result in efficient sensitisation of the Tb(III) unit. The excited state energy of the Ir(III) complex at 21,700 cm^{-1} means thermally activated Tb → Ir BET can occur due to the Ir → Tb energy-transfer gradient being only around 1300 cm^{-1} (energy of Tb excited state = 20,400 cm^{-1}), therefore quenching the Tb-based emission. During the end of the titration, a small peak at 545 nm can observed in the emission spectra, which is attributed to the Tb(III) $^5D_4 \rightarrow {}^7F_5$ transition, however this is extremely weak. Additional quenching of the Ir(III)-based emission is observed (~20%) at the end-point of the titration. Time-resolved luminescence measurements again gave two lifetimes of *ca*. 860 ns and 170 ns throughout the titration. These lifetimes can be attributed to Ir(III)-based emission from the free complex (**Scheme 4.04**).

The titrations of [Ir(fppy)$_2$Lnap^{pic}] with [Tb(hfac)$_3$.2H$_2$O] and [Gd(hfac)$_3$.2H$_2$O] resulted in similar behaviour. The additional quenching of the Ir(III)-based emission suggests the possibility of a PET process occurring from Ir(III) → pypz to form a charge separated [Ir^{IV}]$^{\bullet}$-N'N$^{\bullet-}$ species, which is seen with [Ir(fppy)$_2$L^{pic}] in Chapter 2.

[Ir(fppy)$_2$Lnap^{pic}] was then titrated with [Eu(hfac)$_3$.2H$_2$O] until no significant change in Ir(III) – based luminescence was observed, at which point it was considered that the formation of the Ir(III)/Eu(III) dyad was complete. The emission spectra recorded during the titration are given in **Fig. 4.13**.

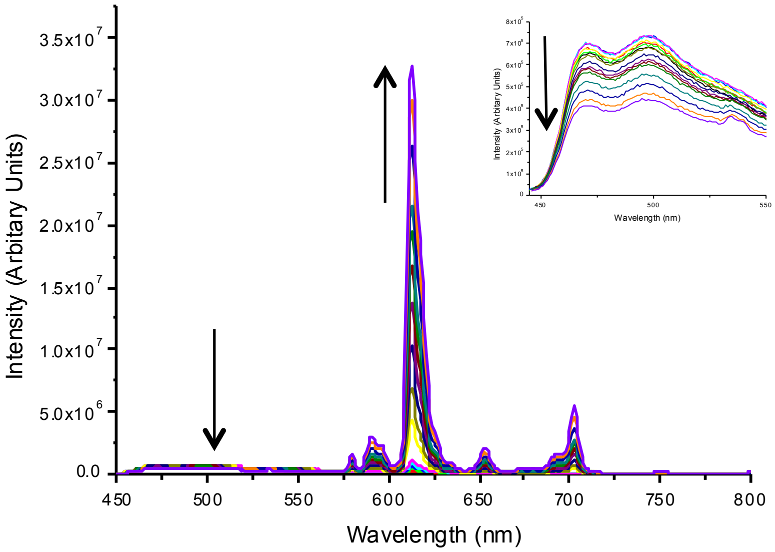

Figure 4.13. Emission spectra of [Ir(fppy)$_2$Lnap^{pic}] [5.00 × 10^{-5} M] titrated with [Eu(hfac)$_3$.2H$_2$O] [1.19 × 10^{-4} M] in aerated CH$_2$Cl$_2$ at 298 K. Top right: expansion of the Ir(III)-based emission between 450 nm and 550 nm. Excitation at 441 nm.

[Ir(fppy)$_2$Lnap^{pic}] has a triplet energy of 21,700 cm^{-1} for its excited state (determined by the highest-energy component in the 77 K emission spectrum) which allows energy-transfer to occur to the Eu(III) with no BET process. The excitation wavelength was chosen at 441 nm because the absorbance at that wavelength was always constant during the titration and to ensure that any free [Eu(hfac)$_3$.2H$_2$O] present in the solution would not be directly excited from the laser; therefore any observed Eu(III) emission can only be the direct result of sensitisation *via* d → f energy-transfer. From the emission spectra it is evident that Ir(III)-based emission is further quenched (~40%) at the end point of the titration and a simultaneous strong increase in emission of the Eu(III) component is observed. The quenching of Ir(III)-based emission is greater than in the Ir/Tb and Ir/Gd dyads and is attributed to small amount of Ir → Eu PEnT.

Direct comparison of the emission spectra to the phenyl-spaced analogue of the Ir(III) complex ([Ir(fppy)$_2$L^{pic}] (**Fig. 4.14**), discussed in Chapter 2 showed that in the case of the nap-spacer, there is a higher quantum yield for sensitised Eu(III) emission at the end point of the titration, suggesting that the nap unit is improving the energy-transfer to the Eu(III) centre.

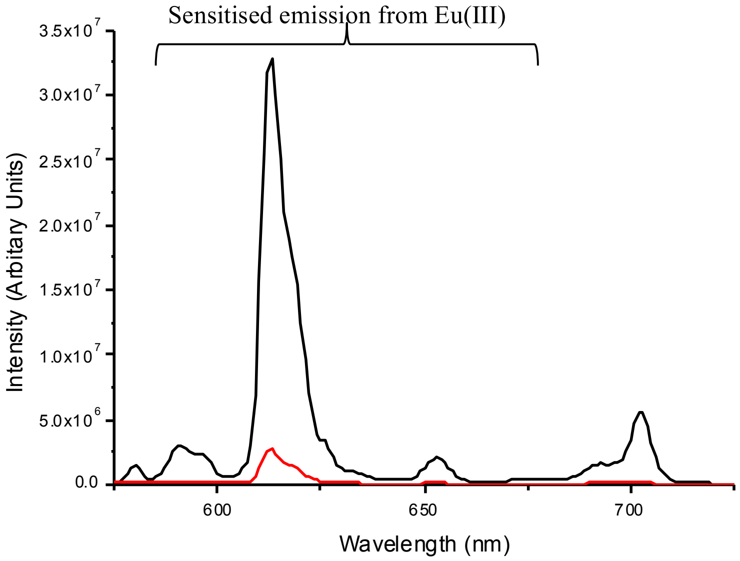

Figure 4.14. Emission spectra of [Ir(fppy)$_2$L^{pic}] [1.04 × 10^{-4} M] (red) titrated with [Eu(hfac)$_3$.2H$_2$O] [1.24 × 10^{-3} M] and [Ir(fppy)$_2$Lnap^{pic}] [5.00 × 10^{-5} M] (black) titrated with [Eu(hfac)$_3$.2H$_2$O] [1.19 × 10^{-4} M] in aerated CH$_2$Cl$_2$ at 298 K.

A third lifetime component of the Ir(III)-based emission was not observed for the Ir(III)/Eu(III) dyad during the titration with [Eu(hfac)$_3$.2H$_2$O]. A shortened third lifetime is likely due to quenching of Ir-emission from direct Ir(III) → Eu(III) energy-transfer however it could not be deconvoluted as it will be a minor percentage contribution. The two lifetimes of τ_1 = 830 ns and τ_2 = 200 ns were still detected and remained unchanged up to the end point of the titration and this can be attributed to free [Ir(fppy)$_2$Lnap^{pic}] present in solution (see **Scheme 4.04** from earlier).

4.2.3 Conclusion of the Photophysical Properties

The intensity of the Ir(III)-based emission is relatively weak in [Ir(fppy)$_2$Lnap^{pic}] when compared with [Ir(fppy)$_2$L^{pic}], as a result of PEnT from ^{3}MLCT → nap causing the Ir(III)-based emission to be quenched (~80%). Naphthalene emission is not observed due to collisional-deactivation in solution at room temperature. It is possible that the observed longer Ir(III) luminescence lifetimes of [Ir(fppy)$_2$Lnap^{pic}] is a result of either (i) steric protection of the Ir(III) core from O$_2$ or (ii) the well-established 'reservoir effect.[16,17,18,19] As the excited state energies of ^{3}MLCT (21,700 cm^{-1}) and

^{3}nap (21,200 cm^{-1})[16,20,21,22] are similar, photoexcitation could lead to thermal equilibrium between the two excited states, which has the effect of increasing the luminescence lifetimes.

Titration of [Ir(fppy)$_2$Lnap^{pic}] with [Eu(hfac)$_3$.2H$_2$O] results in strong emission peaks from Eu(III) being observed in the luminescence spectra. The sensitisation of Eu(III) emission is occurring from the ^{3}nap state, therefore acting as a 'stepping stone' resulting in a two-step energy-transfer process (**Fig. 4.15**).

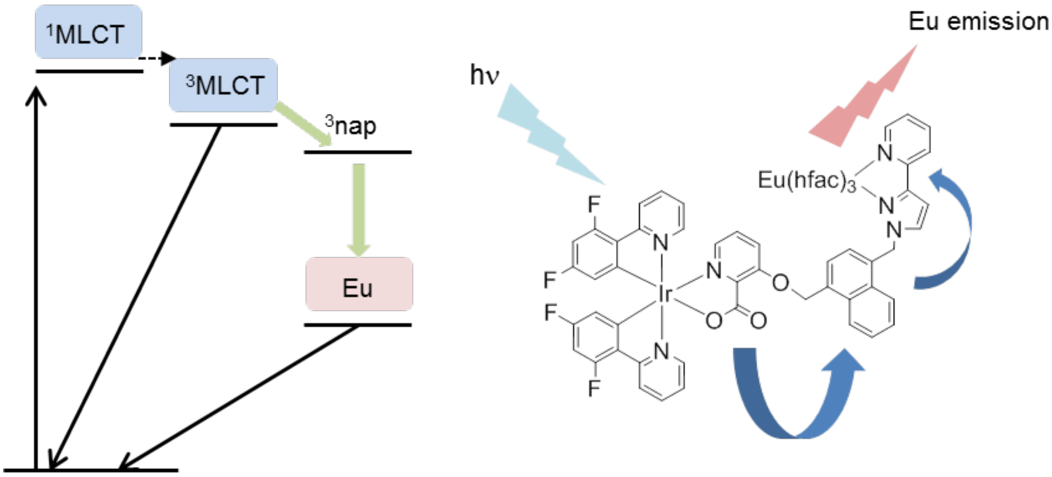

Figure 4.15. Schematic representation of the photophysical pathways for the sensitisation of Eu(III) through the nap spacer unit.

For the titrations of [Ir(fppy)$_2$Lnap^{pic}] with [Gd(hfac)$_3$.2H$_2$O] and [Tb(hfac)$_3$.2H$_2$O], partial quenching of the Ir(III) emission is observed (25% and 20% respectively). Ir → Ln PEnT can be ruled out as the Tb excited state level isn't low enough in energy to exclude BET and the Gd excited state is too high in energy (>10,000 cm^{-1}) to populate. The additional quenching is therefore attributed to PET from Ir → pypz (**Fig. 4.16**), as seen for [Ir(fppy)$_2$L^{pic}] in Chapter 2.

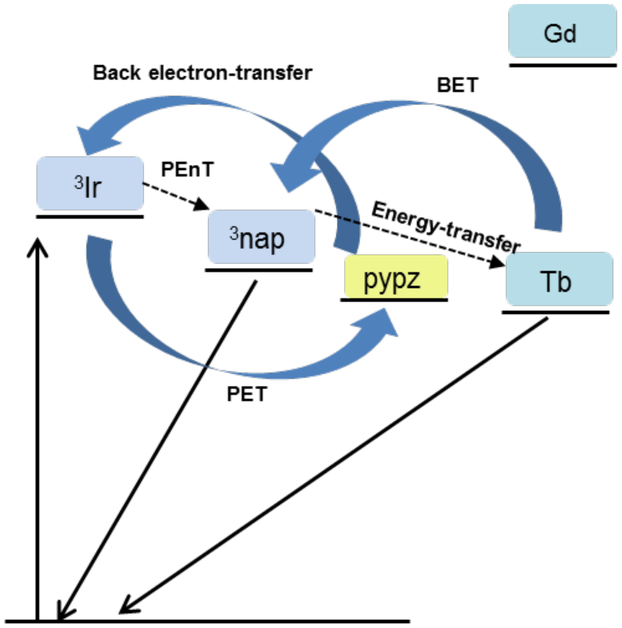

Figure 4.16. Schematic representing the possible photophysical processes occurring during titration of [Ir(fppy)$_2$Lnap^{pic}] with [Ln(hfac)$_3$.2H$_2$O].

Formation of a charge-separated species ([Ir^{IV}]$^{\bullet}$-(N'N)$^{\bullet-}$) would be possible due to the (N'N) coordinating group being electron-deficient when coordinated to electropositive lanthanide ions.

When comparing the extent of quenching of Ir(III) luminescence during the titrations with Gd(III), Tb(III) and Eu(III), the emission is quenched slightly more during the titration with Eu(III) (~40% quenching). This indicates there could be additional direct Ir → Eu PEnT. Further experimental investigations are required to confirm the most likely mechanism, although a combination of all processes cannot be ruled out.

This study highlights the complexity of sensitising lanthanides, making the ligand/complex-design not always straightforward.

4.3 [Ir(fppy)$_2$L^1]

4.3.1 Synthetic Studies

A d/f complex for the use as a dual luminescent cell imaging agent was designed and synthesised. The complex would contain a naphthalene spacer unit to facilitate good energy-transfer from Ir(III) to the lanthanide. A cyclen-carboxylate unit was incorporated into the complex as the lanthanide would strongly bind into the centre. The target complex is shown in **Fig. 4.17** and is based on the picolinate-nap architecture of the complex reported earlier in this chapter. The synthesis of the complex was not successful; however the attempted synthesis of this complex is discussed.

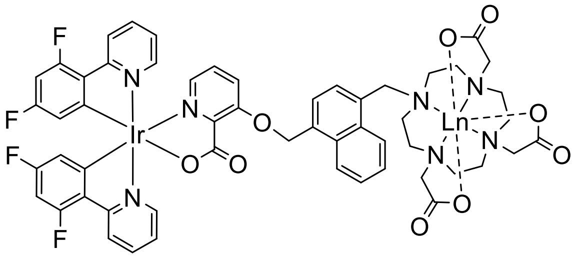

Figure 4.17. The target complex, [Ir(fppy)$_2$L^1], with a cyclen-carboxylate unit incorporated into it.

The first step of the synthesis is a literature method[23] and involved the addition of tertiary butyl acetate groups onto cyclen to form a triester compound, as shown in **Scheme 4.05**.

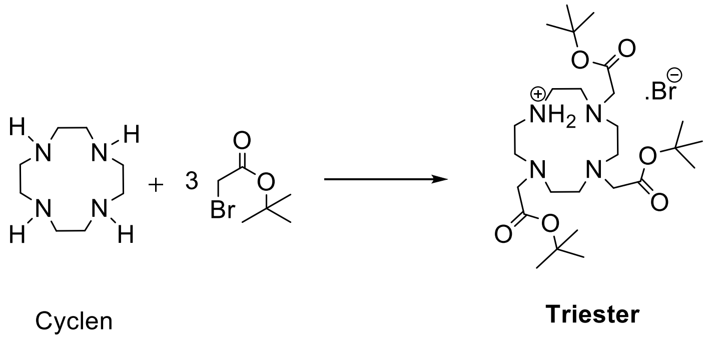

Scheme 4.05. Synthesis of the triester complex from cyclen. CH_3CN, $NaHCO_3$, 0°C 30 min, then stirred at room temperature for 2 days.

The reaction involved the alkylation of NH groups on the cyclen unit with *tert*-butyl bromoacetate, where the Br groups acted as leaving groups. Only three of the NH groups were alkylated, leaving an available NH site available for coordination onto the Ir(III) complex. In order to minimise alkylation on all four NH sites, the reaction was done at 0°C and 3 molar equivalents of *tert*-butyl bromoacetate was added to this dropwise over 30 minutes. The reaction was allowed to proceed at room temperature for 2 days. The product was crystallised in toluene to give a yield of 38%.

Synthesis of 1,4-(dibromomethyl)naphthalene is discussed earlier in this chapter. This was used in a reaction with Ir-pic (synthesis of this complex is given in Chapter 2) in an attempt to alkylate to OH group of the picolinate unit to form the Ir-picnap intermediate (**Scheme 4.06**).

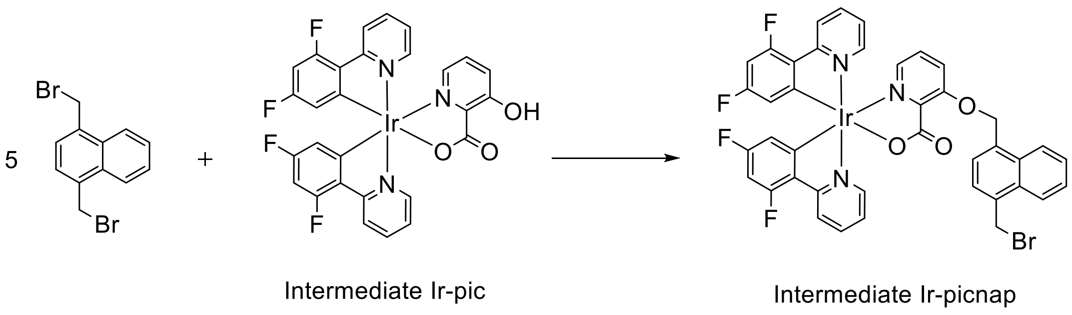

Scheme 4.06. Attempted synthesis of the intermediate Ir-picnap. K_2CO_3 (10 equiv), $N_{2\,(g)}$, acetone, 56°C, 48 hours.

This synthetic route was attempted previously and discussed earlier in the chapter. Due to difficulty in purification and low yield the product was not successfully obtained from this route, therefore a new synthetic route was designed, where the 1,4-di(bromomethyl)naphthalene [$(BrCH_2)_2$nap] was reacted with the triester (**Scheme 4.07**).

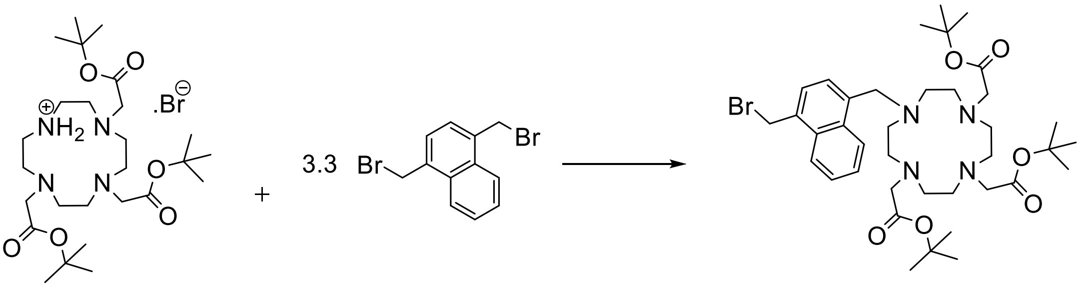

Triester^{nap} Intermediate

Scheme 4.07. Synthesis of the triester^{nap} intermediate. CH_2Cl_2, Cs_2CO_3, ^tBuNI, 40°C, 2 days, $N_{2\,(g)}$.

A few reaction conditions were attempted for the synthesis of the triester^{nap} intermediate. These are given in **Table 4.01** below.

	Solvent	Temperature	Reaction Time	Catalyst	Base
Method 1	CH_3CN	75°C	48 hours	none	Cs_2CO_3
Method 2	THF	25°C	72 hours	none	NaOH (2M)
Method 3	CH_2Cl_2	40°C	48 hours	^tBuNI	Cs_2CO_3

Table 4.01. Reaction conditions for the synthesis of the triester^{nap} intermediate.

The synthesis was unsuccessful for the first two methods. $(BrCH_2)_2$nap readily decomposes at ambient conditions within a day. It was suspected that for Method 1, the reaction was too high in temperature which led to the decomposition of the $(BrCH_2)_2$nap. For Method 2 it was suspected that the temperature was not high enough in energy to initiate the reaction. The synthesis was successful for Method 3, where CH_2Cl_2 was used as this has a low boiling point and the reagents had good solubility in it. ^tBuNI was used as a catalyst, where the I groups could replace the Br groups on the $(BrCH_2)_2$nap. This would result in the $(BrCH_2)_2$nap having better leaving groups and therefore facilitating the reaction. The reaction was monitored by electrospray mass spectrometry. After 48 hours, purification of the crude product was attempted by column chromatography; however the ^1H NMR spectrum showed that the product had decomposed during the purification. The reaction was attempted again however this time the crude product was purified by size-exclusion chromatography on Sephadex LH-20 in CH_2Cl_2. Electrospray mass spectrometry confirmed the presence of the product (22% yield), however the purity could not be determined as the ^1H NMR spectrum was too broad to assign, likely due to the fluxional nature of the triester unit. The reaction was continued and the synthesis of the complex was attempted (**Scheme 4.08**).

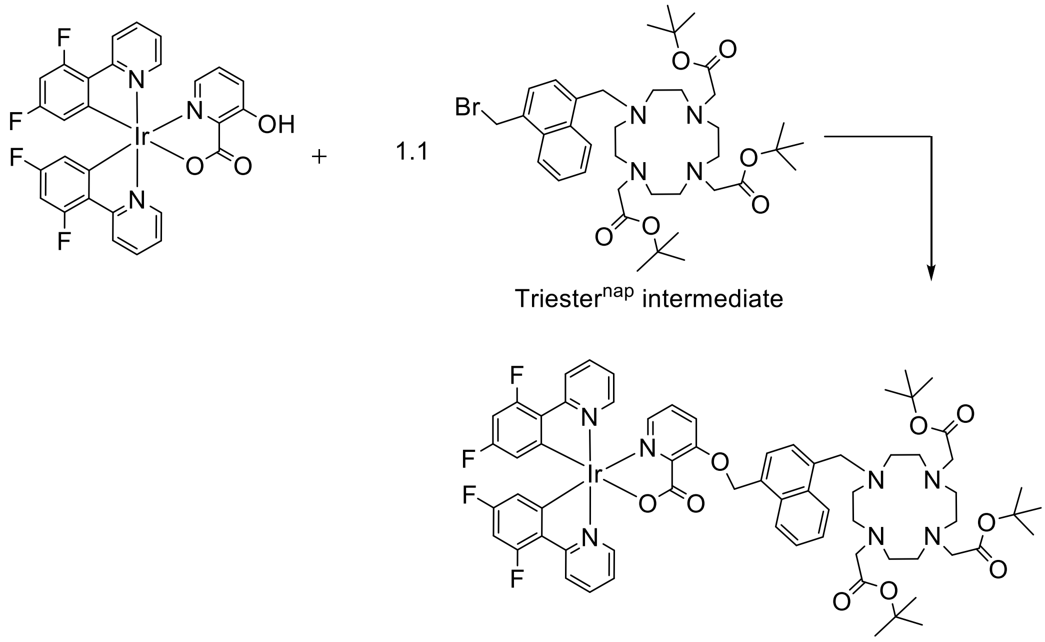

Scheme 4.08. Reaction of [Ir-pic] with the triester^{nap} intermediate. CH_3CN, KI, 65 °C, $N_{2\,(g)}$, 4 days.

The reaction was allowed to proceed for 4 days. Electrospray mass spectrometry showed the presence of the product; however the *m/z* peak corresponding to the [Ir-pic] starting material was also evident. ^1H NMR spectroscopy showed the presence of mainly the [Ir-pic] starting material. Due to low yields and difficulty in isolating the products throughout the synthesis, a different chelating ligand around the Ir centre was selected. This is discussed further in the next section.

4.4 [Ir(fppy)$_2$L^2]

4.4.1 Synthetic Studies

The target complex was modified in an effort to improve the synthesis. The picolinate unit was replaced with a pypz group (**Fig. 4.17**).

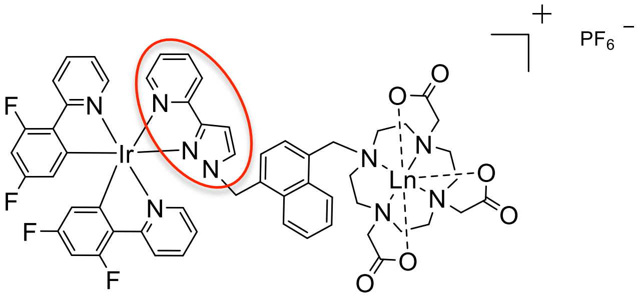

Figure 4.17. The modified target complex, [Ir(fppy)$_2$L^2], where the picolinate group has been replaced with a pypz group (highlighted in red).

The first step involved the synthesis of nap$^{\text{pypz}}$, followed by the alkylation of the NH group on the triester unit (**Scheme 4.09**).

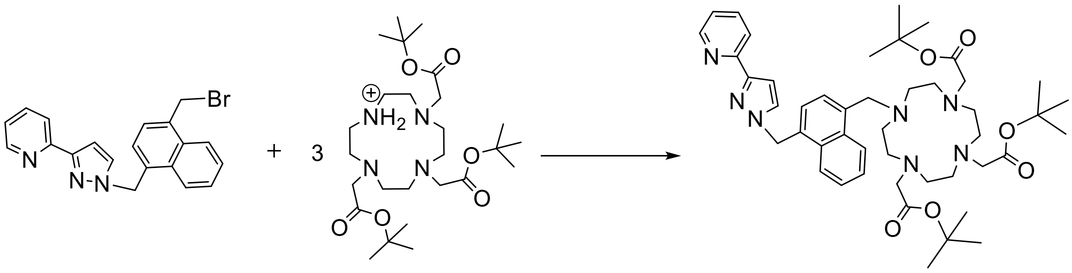

Nap$^{\text{pypz}}$ Triester **Pypz$^{\text{nap}}$-triester**

Scheme 4.09. Synthesis of the pypz$^{\text{nap}}$-triester ligand. CH_3CN, KI, Cs_2CO_3, 45 °C, $N_{2\,(g)}$, 18 hours.

The reaction was done under relatively mild conditions due to nap^{pypz} readily undergoing decomposition. The crude product was purified by size-exclusion column chromatography with Sephadex LH-20 in CH_2Cl_2 (39% yield). The ^{1}H NMR spectrum (**Fig. 4.19**) showed the compound to be relatively pure; however some free triester (~30%) was still present. This was evident by the presence of the presence of excess aliphatic H atoms in the spectrum. A *m/z* peak corresponding to the free triester group was also observed in the electrospray mass spectrum.

The reaction was continued without further purification of pypz^{nap}-triester as any free triester would not interfere with the next step of the reaction which is coordination to Ir(III) (**Scheme 4.10**).

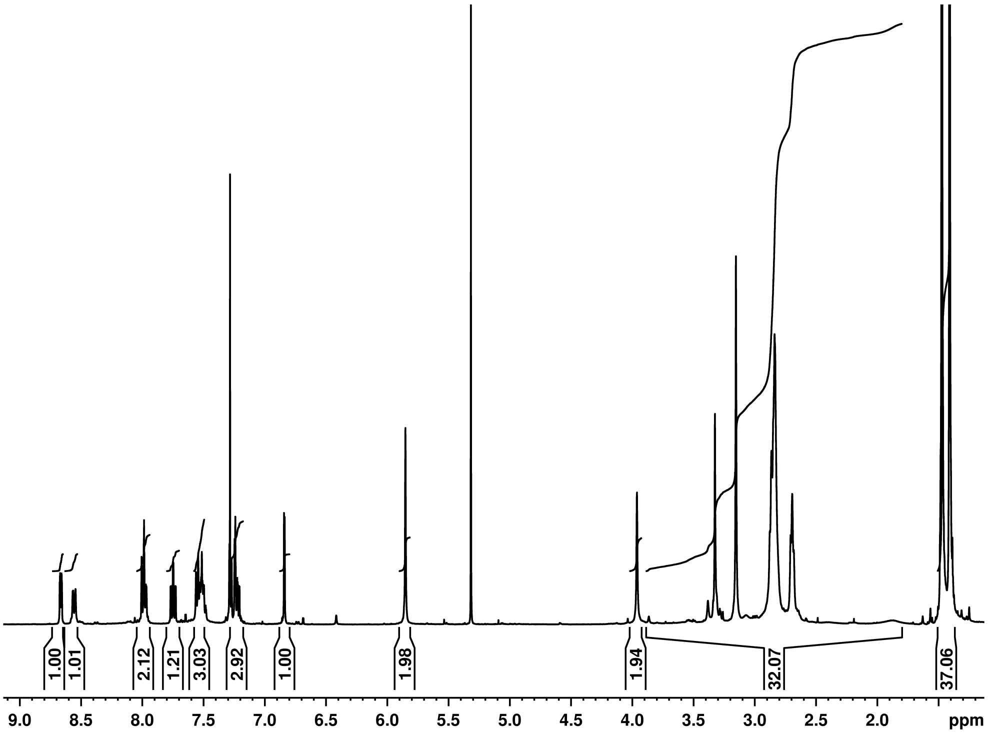

Figure 4.19. ^{1}H NMR (400 MHz $CDCl_3$) spectrum of pypz^{nap}-triester after purification.

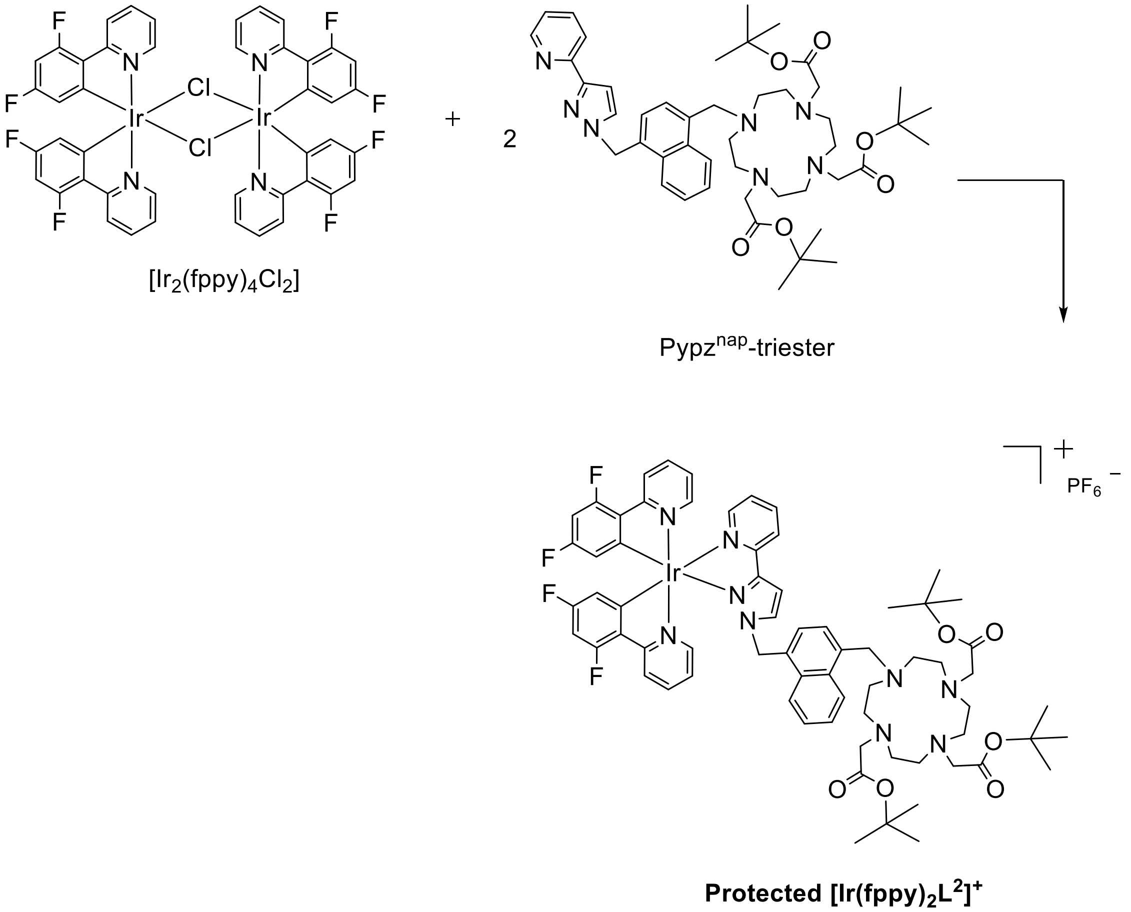

Scheme 4.10. Reaction of [$Ir_2(fppy)_4Cl_2$] with pypz^{nap}-triester. MeOH/CH_2Cl_2 (2:1), 45 °C, $N_{2\,(g)}$, 18 hours.

The crude was purified by column chromatography on silica gel in CH_2Cl_2/MeOH (99:1) and the product was obtained with a 45% yield. The ^{1}H NMR spectrum is given in **Fig. 4.20** and an expansion of the aromatic region is given in **Fig. 4.21**.

Two singlet peaks for the *tert*-butyl groups are observed at 1.50 ppm and 1.40 ppm. When integrated, the peak at 1.50 ppm accounts for ~ 18 H atoms and the second peak at 1.40 ppm accounts for ~ 9 H atoms. This is indicative of two of the *tert*-butyl groups being in the same chemical environment and the third group being in a different environment in relation to the other two groups. This is expected as rotation around the CH_2 group between the naphthalene and triester groups would result in the two nearest *tert*-butyl groups to be in the same chemical environment (**Fig. 4.22**).

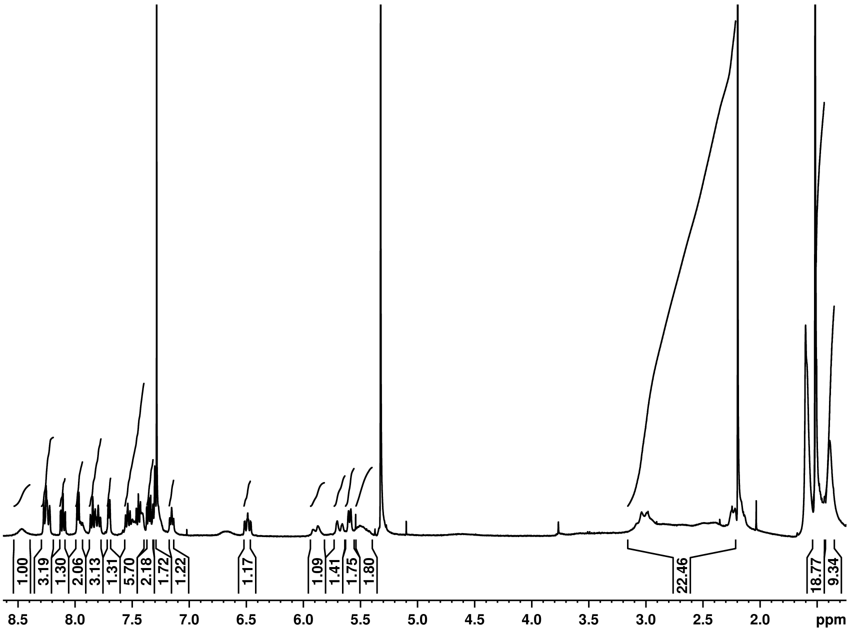

Figure 4.20 ^1H NMR (400 MHz $CDCl_3$) spectrum of protected $[Ir(fppy)_2L^2]^+$ after purification.

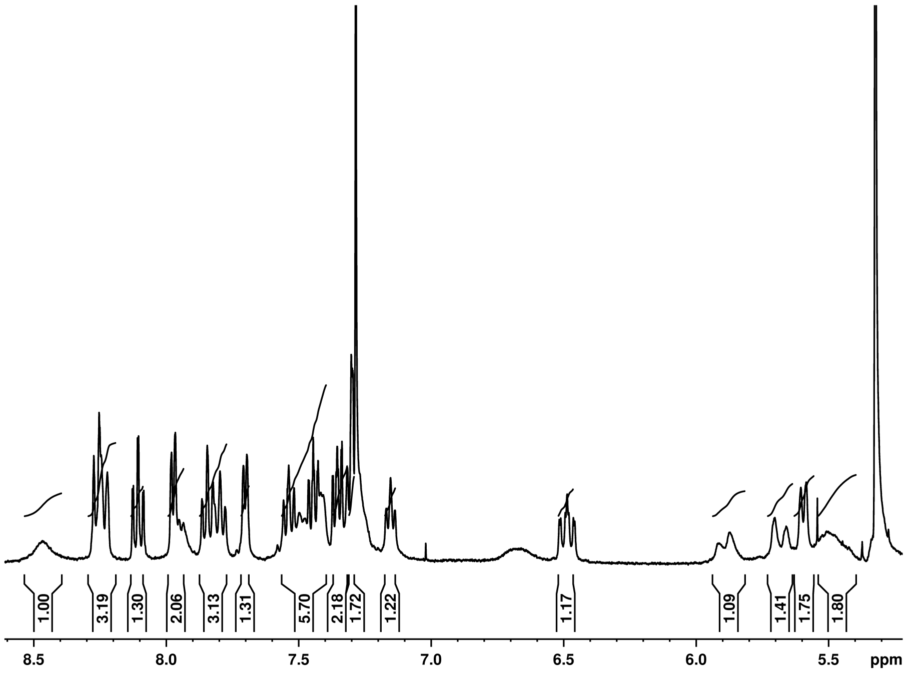

Figure 4.21. Expansion of the aromatic region in the ^{1}H NMR spectrum for protected $[Ir(fppy)_2L^2]^+$.

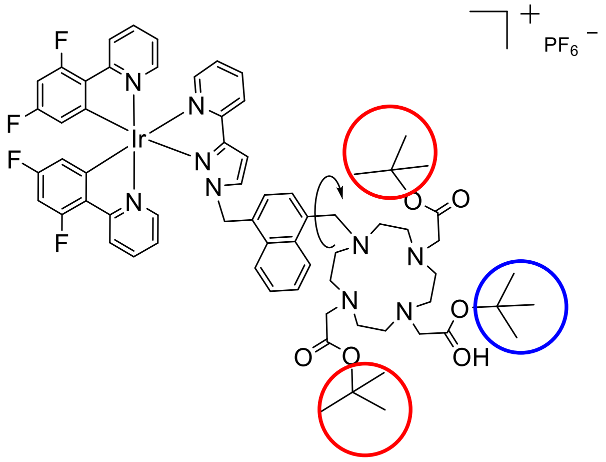

Figure 4.22. Protected $[Ir(fppy)_2L^2]^+$. The H atoms of the *tert*-butyl groups highlighted in red are in the same chemical environment and account for the peak at 1.50 ppm in the ^{1}H NMR spectrum. The H atoms of the *tert*-butyl group highlighted in blue are in a different chemical environment and account for the chemical shift at 1.40 ppm.

In order to bind Ln(III) ions to the complex, the protecting *tert*-butyl groups were removed by stirring the complex in TFA/CH_2Cl_2 at room temperature for 2 days. This gave the desired product containing the carboxylic acid groups available for binding to the Ln(III) ions (**Scheme 4.11**).

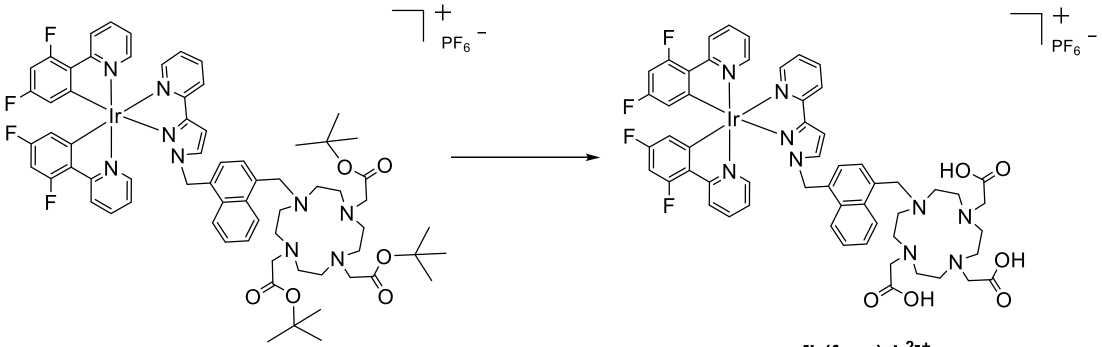

[Ir(fppy)$_2$L^2]$^+$

Scheme 4.11. Removal of the *tert*-butyl protecting groups to give [Ir(fppy)$_2$L^2]$^+$. TFA/CH_2Cl_2, room temperature, 2 days.

[Ir(fppy)$_2$L^2]$^+$ was isolated by dissolving it in a minimum volume of EtOH and triturating with diethyl ether (72% yield). The complex was characterised by ^{1}H NMR spectroscopy (**Fig. 4.23** with expansion of the aromatic region in **Fig. 4.24**), elemental analysis and electrospray mass spectroscopy.

Peaks observed at chemical shifts at 4.90 ppm, 3.50 ppm, 3.33 pm and 1.20 ppm in the ^{1}H NMR spectrum correspond to solvents (water, diethyl ether, methanol-d_4 and diethyl ether respectively). Integration of the aromatic H atoms correlates to the number of atoms present in the complex. Integration of the aliphatic CH_2H atoms on the cyclen derivative was not possible due to the presence of the solvent peaks (diethyl ether and methanol) in this region, however the *m/z* peak corresponding to the complex was observed in the mass spectrum as well as a single peak of the complex in the HPLC trace of the data, confirming the purity of the product.

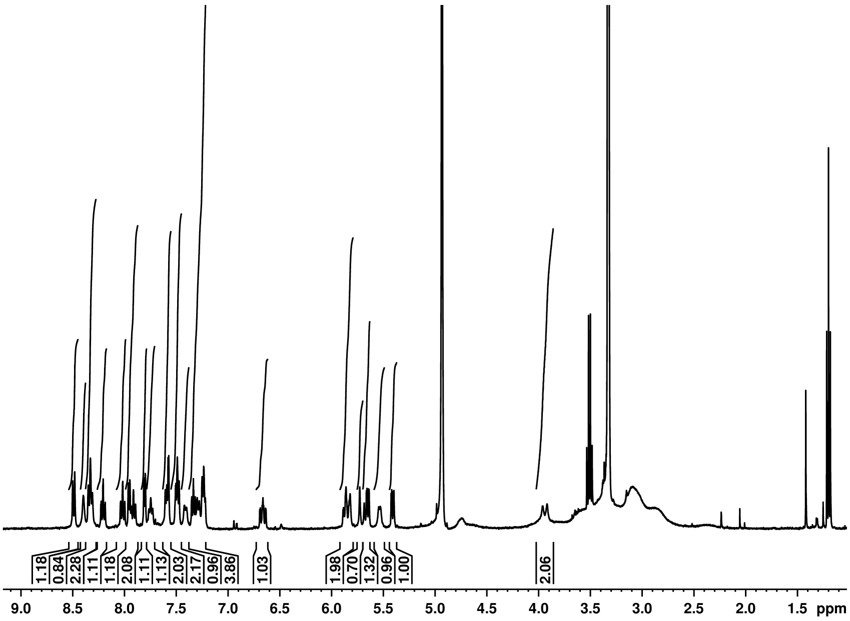

Figure 4.23. ^{1}H NMR (400 MHz CD_3OD) spectrum of $[Ir(fppy)_2L^2]^+$.

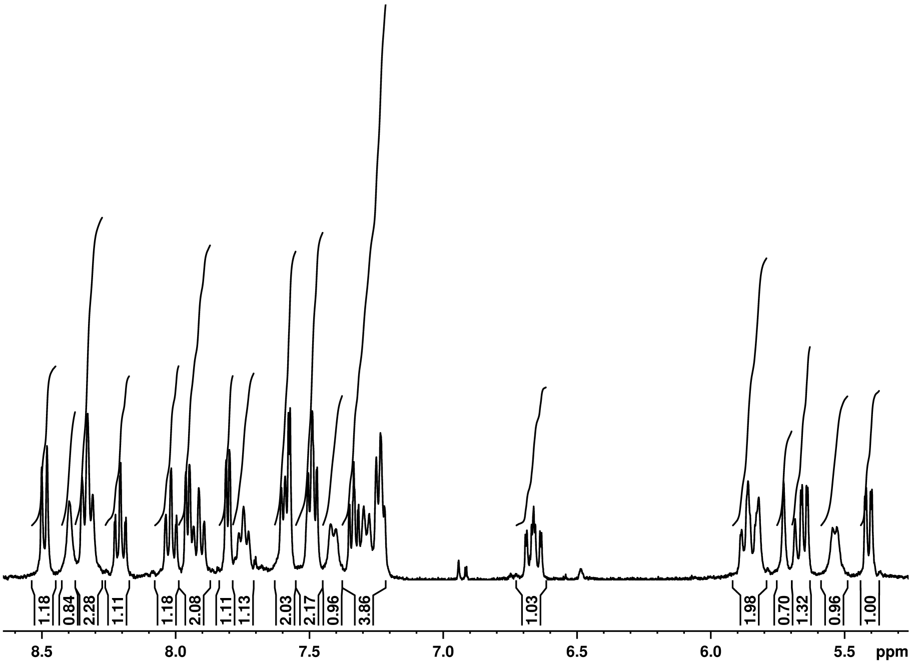

Figure 4.24. Expansion of the aromatic region in the ^{1}H NMR spectrum for $[Ir(fppy)_2L^2]^+$.

Complexation of Eu(III) and Gd(III) ions with $[Ir(fppy)_2L^2]^+$ was achieved by stirring $[Ir(fppy)_2L^2]^+$ with $Eu(OTf)_3$ and $Gd(OTf)_3$ in MeOH at 50°C for 2 days (**Scheme 4.12**). The complexes were isolated by dissolving the crude in water and adjusting the pH to ~ 10. The solids were removed by filtration and the pH of the filtrate was readjusted to pH ~ 7 to give the products (yields ~ 70%).

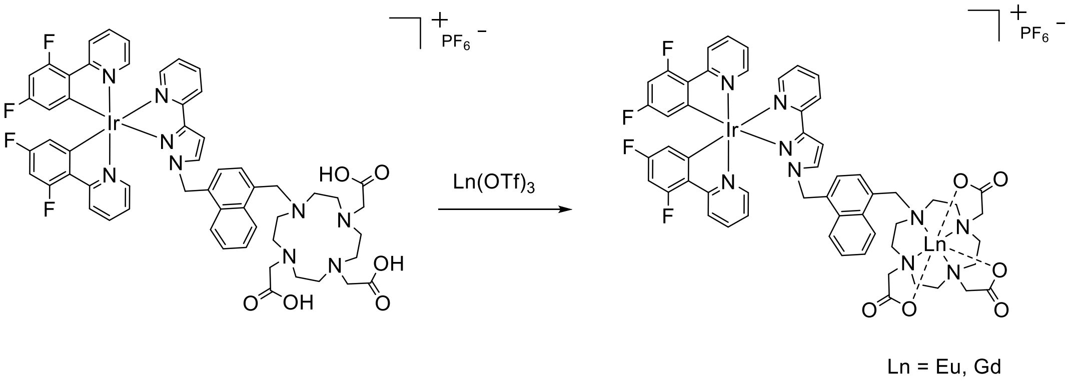

Scheme 4.12. Complexation of the Ln(III) ions with $[Ir(fppy)_2L^2]^+$. MeOH, room temperature, 2 days.

Due to the paramagnetic nature of the Ln(III) ions, it was not possible to obtain resolved ^{1}H NMR spectra of the complexes. The *m/z* ion peaks of the complexes were observed in the mass spectra and high-resolution mass spectra, with the correct isotopic distributions (**Fig. 4.25**), as well as a single peak in the HPLC traces correlating to the complexes.

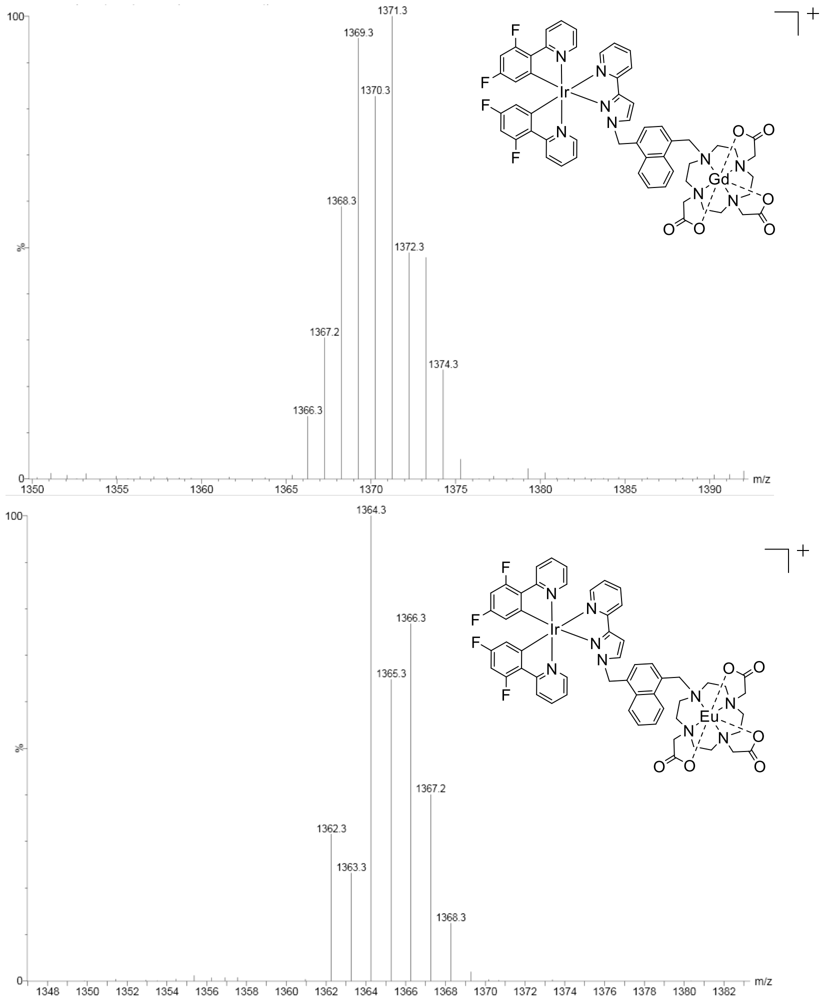

Figure 4.25. Electrospray mass spectra showing the peaks corresponding to $[Ir(fppy)_2L^2]^+$ containing Gd(III) (top spectrum) and Eu(III) (bottom spectrum).

4.4.2 Photophysical Properties

The UV/Vis spectrum of $[Ir(fppy)_2L^2]^+$ was recorded in aerated MeOH at room temperature (**Fig. 4.26**). Tentative assignment of the spectrum is given in **Table 4.02**.

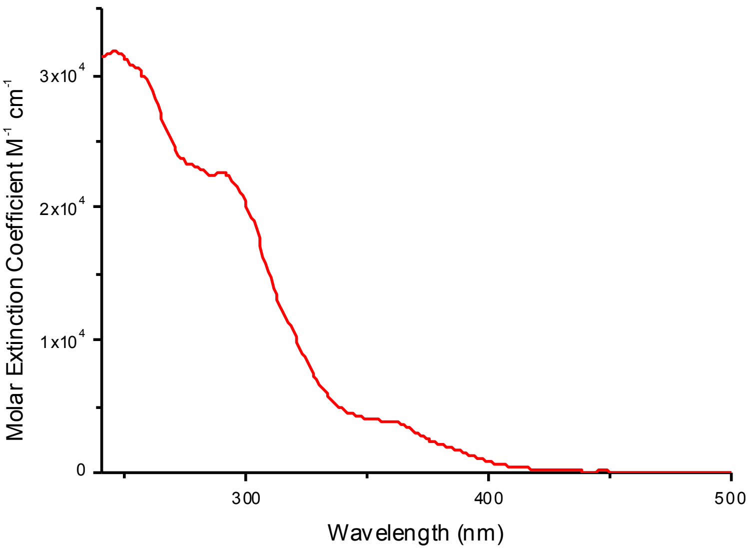

Figure 4.26. UV/Vis absorption spectrum of $[Ir(fppy)_2L^2]^+$ [5.55 × 10^{-5} M] in aerated MeOH at 298 K.

Absorption		Assignment
λ_{max}/nm	ε/M^{-1} cm^{-1}	
249	31,000	π-π*
292	22,000	π-π*
316	12,000	MLCT (sh)
365	4,000	MLCT
420	300	MLCT (broad)

Table 4.02. UV/Vis absorption data of $[Ir(fppy)_2L^2]^+$ [5.55 × 10^{-5} M] in aerated MeOH at 298 K.

The spin-allowed intraligand π-π* transitions localised on the coordinated ligands are observed in the high-energy region of the spectrum (< 300 nm). The transitions centred on the fluorinated ppy ligands are observed at 245 nm. The less intense and poorly defined absorption bands and shoulders at λ > 300 nm can be assigned to spin-allowed and spin-forbidden MLCT transitions corresponding to (dπ(Ir) → π* (N^N and C^N)) transitions.

The emission spectrum of $[Ir(fppy)_2L^2]^+$ was also recorded in MeOH at room temperature. The emission spectrum of the complex is given in **Fig. 4.27**.

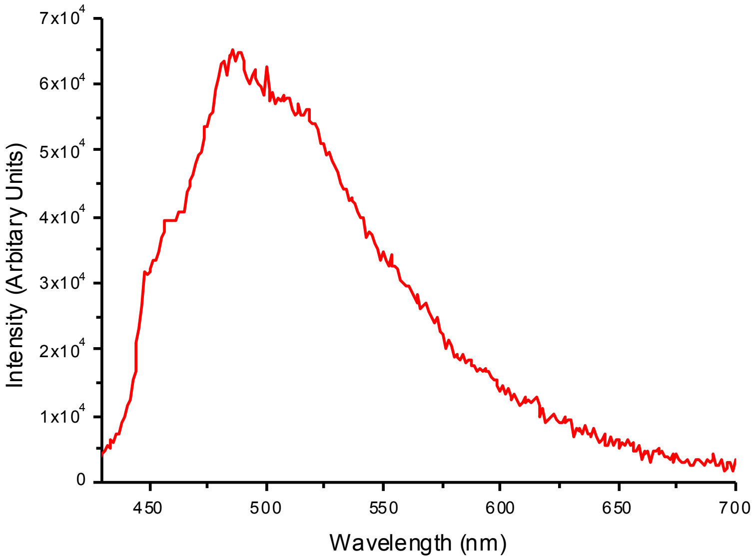

Figure 4.27. Emission spectrum of $[Ir(fppy)_2L^2]^+$ [1.11 × 10^{-4} M] in aerated MeOH at 298 K. Excitation at 398 nm.

The emission is broad and the intensity is very weak in comparison to the previous complexes measured at the same optical densities. This is indicative of quenching of the Ir(III)-based emission by the naphthalene group due to ^{3}Ir → ^{3}nap energy-transfer (as explained earlier). The quantum yield (Φ) of the complex was calculated against the standard $Ir(ppy)_3$ to be only 0.003 which is an order of magnitude lower when compared to the other Ir(III) complexes reported in previous chapters. This value is consistent with previous research on Ir(III) complexes containing nap spacer units[10] and is further evidence that Ir(III)-based emission is being quenched by the nap unit.

On comparison with $[Ir(fppy)_2Lnap^{pic}]$, $[Ir(fppy)_2L^2]^+$ has a larger ^{3}Ir → ^{3}nap energy gradient as the triplet energy is higher, therefore the Ir(III)-based emission is quenched better by ^{3}nap. This explains the significantly low quantum yield of $[Ir(fppy)_2L^2]^+$.

A hypsochromic shift to 448 nm (triplet energy = 22,300 cm^{-1}) was observed when the emission was recorded at 77 K in EtOH/MeOH (4:1) glass. There was also a significant increase in the intensity of emission. A more structured spectrum was also observed (**Fig. 4.28**). These observations are consistent with the impediment of the nonradiative relaxation processes at 77 K.

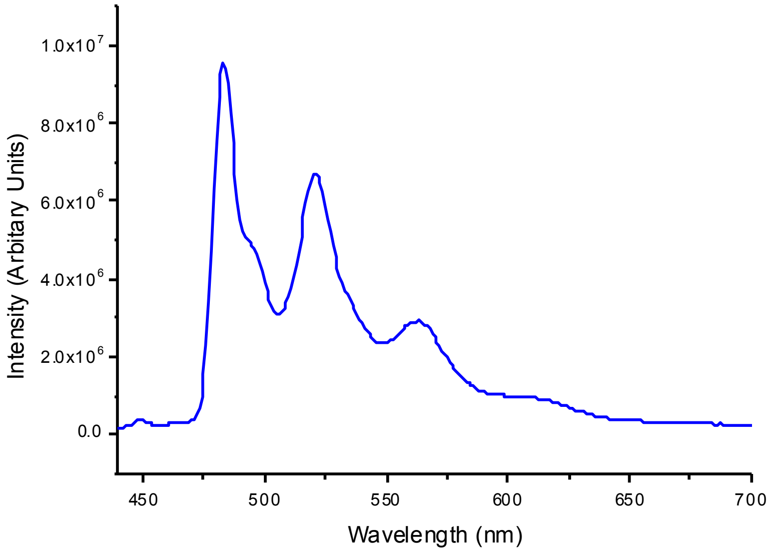

Figure 4.28. Emission spectrum of $[Ir(fppy)_2L^2]^+$ [1.11 × 10^{-4} M] in EtOH/MeOH (4:1) glass at 77 K. Excitation at 398 nm.

Time-resolved luminescence measurements of the complex gave a biexponential decay in aerated MeOH where τ_1 = 1.2 μs (46%) and τ_2 = 240 ns (54%). This very long lifetime of 1.2 μs is indicative of the 'reservoir effect' due to the establishment of a thermal equilibrium between the ^{3}Ir and ^{3}nap excited states during photoexcitation. As mentioned previously, a biexponential decay for this complex is consistent with previous data reported and is likely to be as a result of a mixture of conformers being present in solution.

The emission spectrum of the complex containing Gd(III) is given in **Fig. 4.29**. The complex has been abbreviated to [IrL^2•Gd].

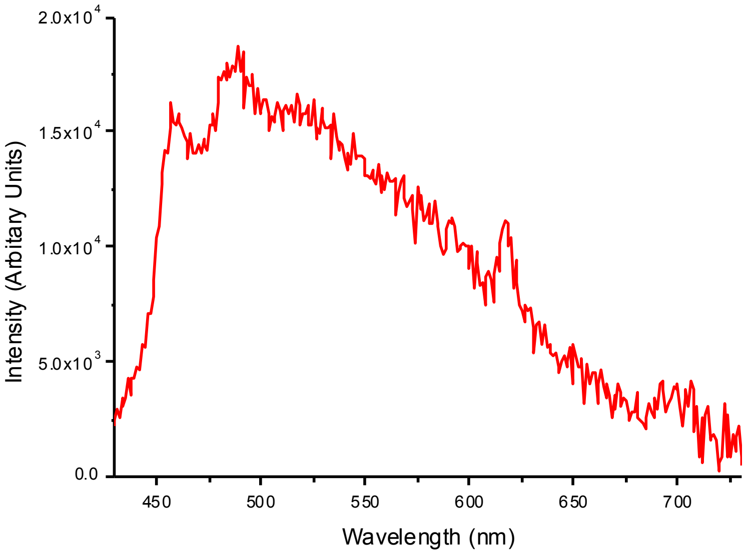

Figure 4.29. Emission spectrum of [IrL^2•Gd] [7.30 × 10^{-5} M] in MeOH at 298 K. Excitation at 380 nm.

No significant changes were observed in the emission spectrum of [IrL^2.Gd]. Like previous experiments, the Gd(III) complex is used as a control as the energy of the Gd(III) excited states are too high to populate (>10,000 cm^{-1}) by the Ir(III). Time-resolved luminescence measurements in MeOH gave two emission lifetimes of τ_1 = 1.4 μs (68%) and τ_2 = 200 ns (32%). These lifetimes are comparable to those of [Ir(fppy)$_2$L^2] as expected.

The emission spectrum of [IrL^2•Eu] is given in **Fig. 4.30**.

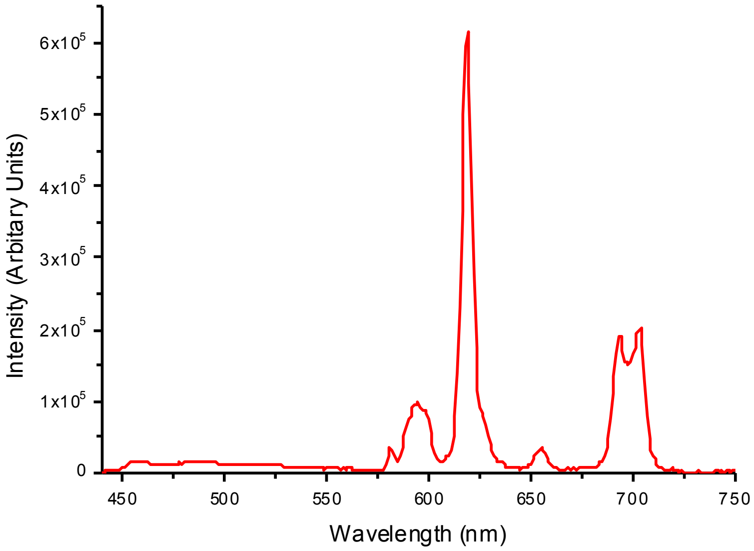

Figure 4.30. Emission spectrum of [IrL^2•Eu] [7.00 × 10^{-5} M] in MeOH at 298 K. Excitation at 383 nm.

As the Ir(III) complex has a triplet energy level that is considerably higher than the luminescent energy level of the Eu(III) species (17,500 cm^{-1}), Eu(III) acts as an energy acceptor with no BET process. In comparison to [IrL^2.Gd], there is also no significant change in the intensity of the Ir(III) emission, suggesting that energy-transfer to Eu(III) is occurring *via* a two-step process (^{3}Ir → ^{3}nap → Eu(III)) . This is consistent with data from the previous complex reported earlier in this chapter ([Ir(fppy)$_2$Lnap^{pic}]).

The lifetime of Eu(III)-based emission of the complex was measured in H_2O and D_2O (τ_{H_2O} = 0.65 μs and τ_{D_2O} = 1.88 μs). By using the Horrocks equation[24] (**Equation 4.01**), the q value was calculated to be ~ 1.

$$q = A\,(\frac{1}{\tau H_2O} - \frac{1}{\tau D_2O} - B)$$

Equation 4.01. Horrocks' equation for lanthanide quenching where q = number of coordinated molecules, A = 'inner sphere' correction factor and B = 'outer sphere' correction factor.

The q value of 1 indicates that when the complex is in H_2O, one H_2O molecule is bound to the Eu(III) centre, which causes the quenching of emission by non-radiative energy-transfer to stretching vibrations of the coordinate molecule. This accounts for the reduced lifetime in H_2O compared to D_2O (where quenching is less likely).

4.4.3 Conclusion of the Photophysical Properties

The intensity of Ir(III)-based emission from $[Ir(fppy)_2L^2]^+$ is low in comparison to the previous Ir(III) complexes reported. This is attributed to quenching of Ir(III)-based emission. The observed quenching is consistent with data on $[Ir(fppy)_2Lnap^{pic}]$ reported earlier, which also had a low intensity of Ir(III)-based emission. The quenching is a result of ^{3}MLCT → nap PEnT, which occurs efficiently due to the energy of the Ir(III) excited state being higher than the ^{3}nap excited state. As mentioned earlier, ^{3}nap emission is not observed due to collisional-deactivation in solution at room temperature.

Time-resolved luminescence measurements gave a biexponential decay with lifetimes of τ_1 = 1.2 μs and τ_2 = 240 ns. These lifetimes are considerably longer than the complexes reported in the previous chapters. Although it seems to be unusual for lifetimes to appear weak and long, these results are consistent with the 'reservoir effect' occurring between ^{3}MLCT and ^{3}nap excited states.

Addition of Gd(III) resulted in no change in the intensity of Ir(III)-based emission nor their lifetimes. As expected, PEnT from Ir(III) → Gd(III) was not observed due to the energy level of the Gd(III) excited-states are higher than the energy levels of the Ir(III) and ^{3}nap excited-states.

Strong intensity of Eu(III)-based emission of $[IrL^2{\bullet}Eu]$ was observed in the luminescence spectrum. Further quenching of Ir(III)-based emission was not observed in this case, which is unsurprising as the emission is already in a quenched state by the nap unit (also evident by the undetectable emission lifetimes). Sensitisation of Eu(III) emission is therefore occurring by a PEnT indirectly by energy-transfer from ^{3}Ir → nap, followed by ^{3}nap → Eu(III). These results correlate well with data from the titration of $[Ir(fppy)_2Lnap^{pic}]$ with $[Eu(hfac)_3.2H_2O]$.

The photophysical data for $[Ir(fppy)_2L^2]^+$ suggests it is not an ideal candidate for use as a dual emitting cell imaging agent. The nap spacer unit results in near-complete quenching of the Ir(III)-based emission resulting in very a low quantum yield. It does however provide good energy-transfer to the Eu(III), but overall the PEnT is too efficient. Ideally, there should a good balance of emission intensities of Ir(III) and Eu(III) for a dual d/f imaging agent. Because of this, the detection of Ir(III) emission in cells may prove too difficult. The cell imaging studies are ongoing and are not reported.

4.5 [Ir(fppy)$_2$L^3]

In order to achieve better balanced emission from Ir(III) and Eu(III) for use as a dual emitting d/f cell imaging agent, a complex was designed where a phenyl spacer unit was used instead of a naphthalene unit. The aim of this was to reduce quenching of Ir(III)-based emission by the intermediate nap unit. The structure of the complex is given in **Fig. 4.31** below. A very low yield was obtained for this complex; therefore the photophysical data is incomplete. The synthetic procedure and preliminary photophysical data are reported.

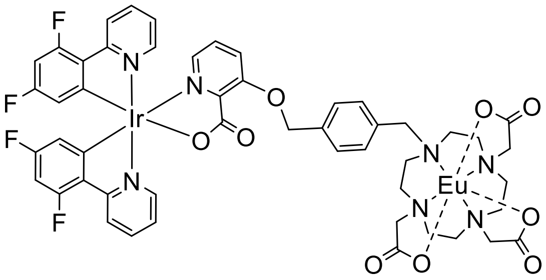

Figure 4.31. Chemical structure of [Ir(fppy)$_2$L^3].

4.5.1 Synthetic Studies

The first step of the reaction (**Scheme 4.13**) involved the alkylation of the pendant hydroxyl group on the picolinate unit of [Ir-pic] with α,α'-dibromo-*p*-xylene. The synthesis of [Ir-pic] is given in Chapter 2.

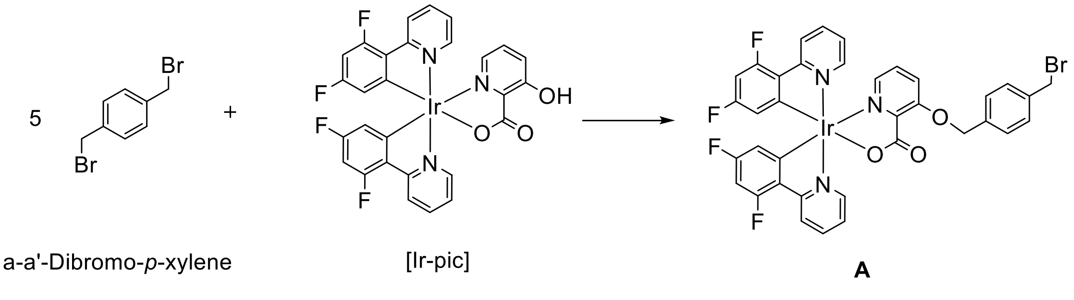

Scheme 4.13. Synthesis of intermediate **A**. Acetone, K_2CO_3, 56 °C, $N_{2\,(g)}$, 2 days.

The dibromoxylene was used in 5 times in excess in order to prevent dimerisation of Ir-pic to the dibromoxylene. The intermediate complex **A** was purified by column chromatography on silica gel in CH_2Cl_2/MeOH to give a 36% yield.

Intermediate **A** was then reacted with triester (**Scheme 4.14**).

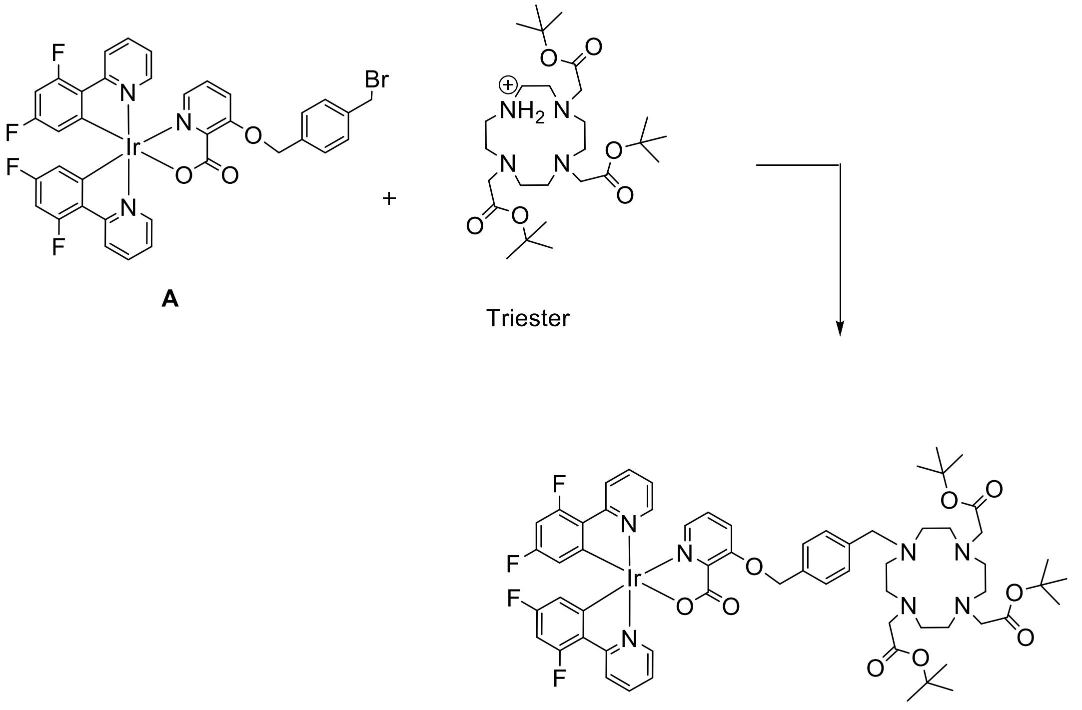

Scheme 4.14. Reaction of intermediate complex **A** with triester to form BOC protected [Ir(fppy)$_2$L^3]. CH_3CN, Cs_2CO_3, 82°C, $N_{2\,(g)}$, 24 hours.

The product was purified by column chromatography on silica gel in CH_2Cl_2/MeOH to give a yield of 27%. The ^{1}H NMR spectrum of the complex is given in **Fig. 4.32** and the expansion of the aromatic region is given in **Fig. 4.33**.

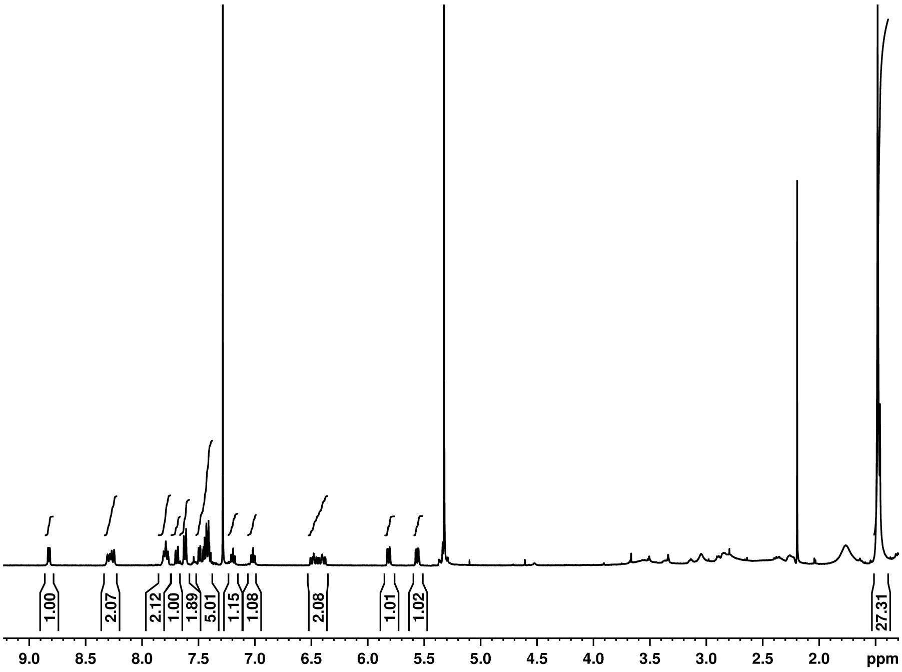

Figure 4.32. ^{1}H NMR spectrum (400 MHz $CDCl_3$) of BOC-protected [Ir(fppy)$_2$L^3].

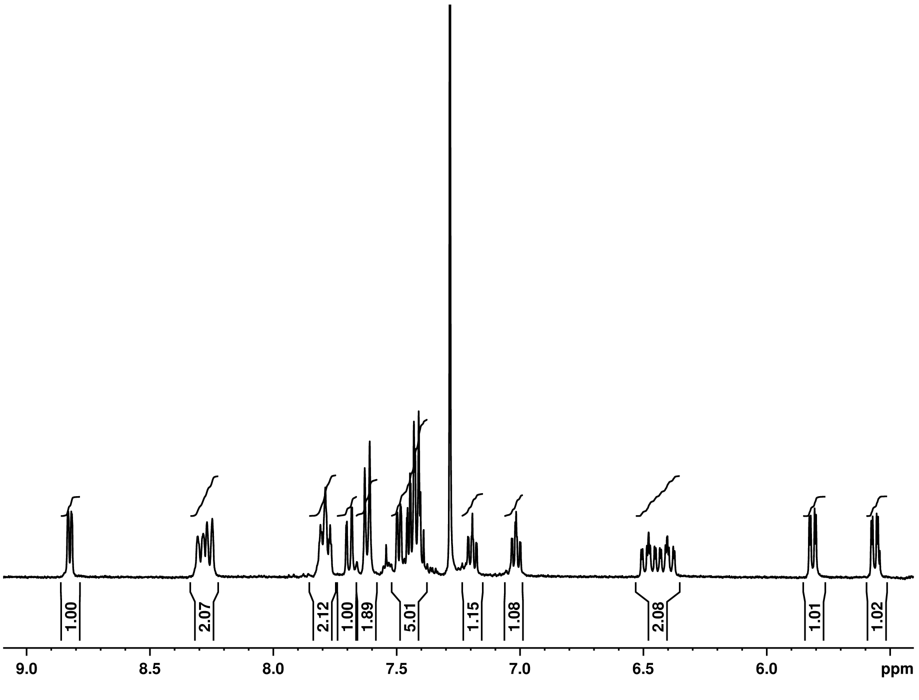

Figure 4.33. Expansion of the aromatic region in the ^{1}H NMR spectrum of BOC-protected [Ir(fppy)$_2$L^3].

Integration of the aromatic region of the spectrum gave the correct number of aromatic H atoms. The aliphatic region of the spectrum was not integrated due to the presence of acetone at chemical shift ~ 2.2 ppm. Integration of the *tert*-butyl H atoms at 1.4 ppm gave the correct number of H atoms which was further evidence of purity. The *m/z* peak of the complex was detected in the electrospray mass spectrum at 1328.

The BOC groups were removed by stirring the complex in TFA/CH_2Cl_2. The desired product was purified by size-exclusion column chromatography on Sephadex-LH20 in MeOH (23% yield). The ^1H NMR spectrum is given in **Fig. 4.34** and expansion of the aromatic region of the spectrum is given in **Fig. 4.35**.

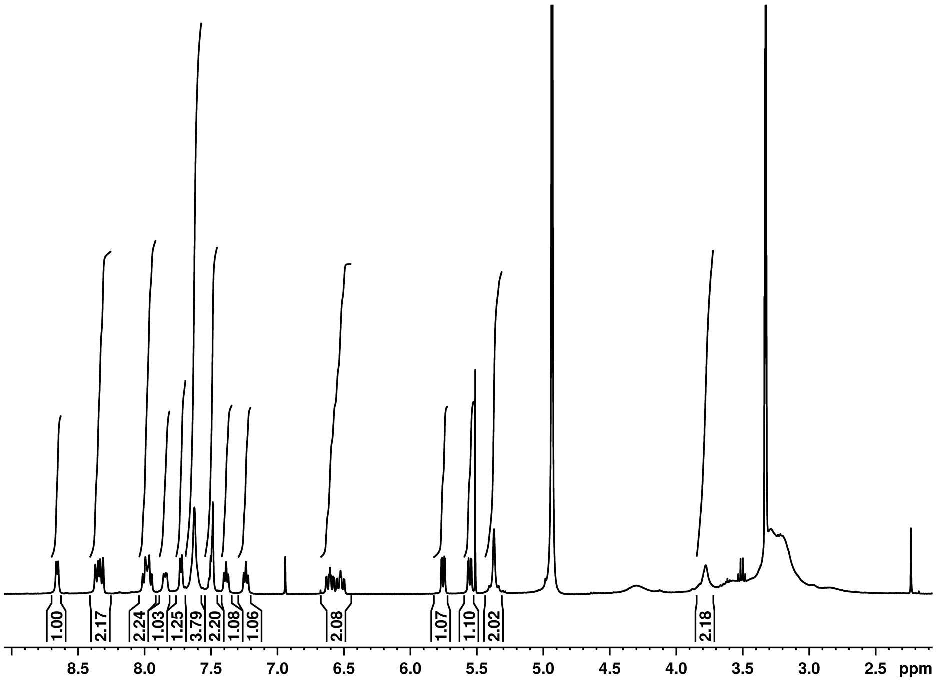

Figure 4.34. ^1H NMR spectrum (400 MHz CD_3OD) of [Ir(fppy)$_2$L^3].

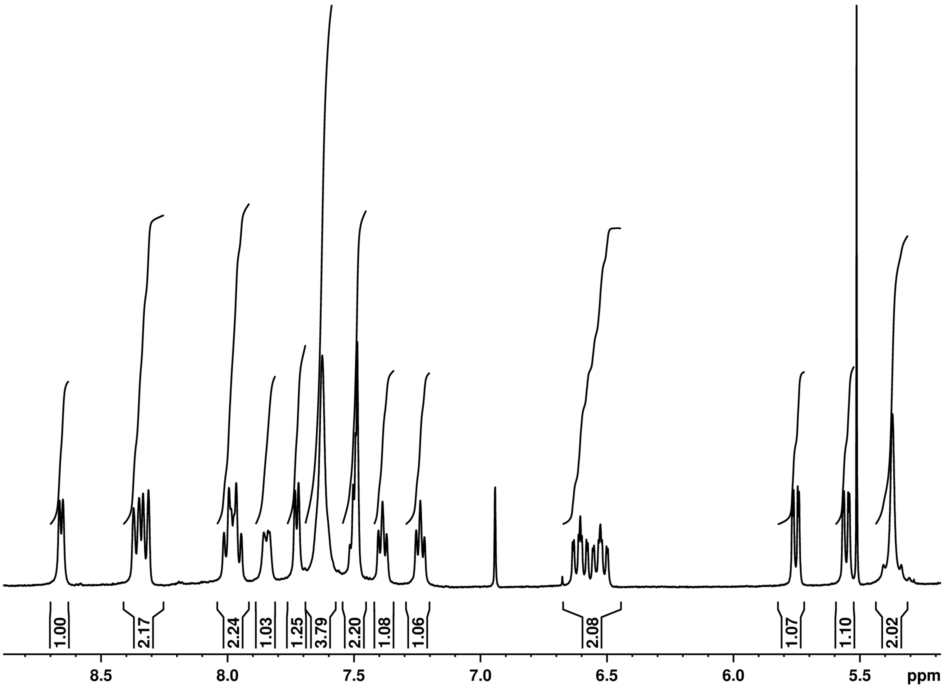

Figure 4.35. Expansion of the aromatic region in the ^{1}H NMR spectrum of [Ir(fppy)$_2$L^3].

Integration of the aromatic H atoms gave the correct numbers of atoms present in the complex. The aliphatic H atoms could not be integrated due to the presence of the MeOD solvent peak present in this region (~3.3 ppm). The peak observed at 4.9 ppm is attributed to H_2O. The *m/z* peak was observed in the electrospray mass spectrum and a single HPLC trace gave further evidence on the purity of the complex.

Eu(III) was coordinated to [Ir(fppy)$_2$L^3] by stirring with Eu(OTf)$_3$ in MeOH at 50°C for 2 days. The complex was isolated by size exclusion chromatography on Sephadex LH-20 in MeOH. The yield of this step was low ~ 26%. Purity was confirmed by electrospray mass spectrometry, high resolution mass spectrometry and observation of a single HPLC trace. The UV/Vis spectrum is given in **Figure 4.36**. Tentative assignment of the spectrum is given in **Table 4.03**.

Due to very low yields for the synthesis of [Ir(fppy)$_2$L^3], the Gd(III) analogue was not synthesised.

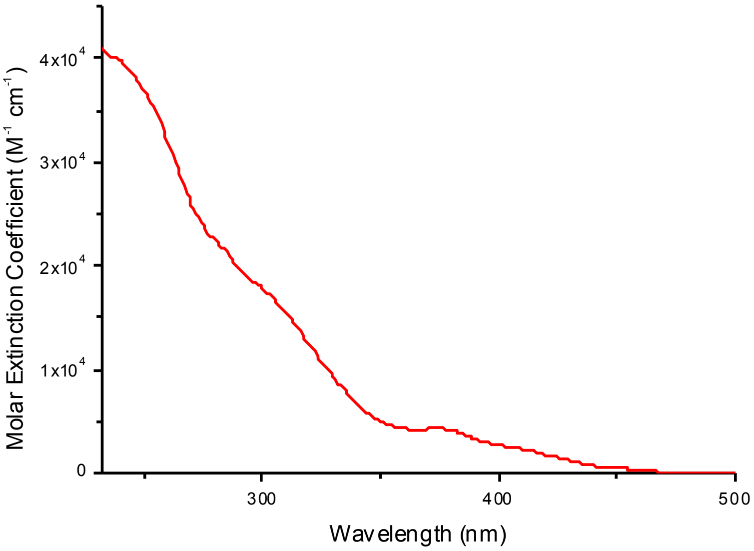

Figure 4.36. UV/Vis absorption spectrum of [IrL^3•Eu] [2.83 × 10^{-5} M] in aerated MeOH at 298 K.

Absorption		Assignment
λ_{max}/nm	ε/M^{-1} cm^{-1}	
251	40,000	π-π*
279	22,000	π-π*
322	15,000	MLCT
372	5,000	MLCT (broad)
456	2000	MLCT (broad)

Table 4.03. UV/Vis absorption data of [IrL^3•Eu] [2.83 × 10^{-5} M] in aerated MeOH at 298 K.

The spin-allowed intraligand π-π* transitions localised on the coordinated ligands are observed in the high-energy region of the spectrum (< 300 nm). The less intense and poorly defined absorption bands and shoulders at λ > 300 nm can be assigned to spin-allowed and spin-forbidden MLCT transitions corresponding to (dπ(Ir) → π* (N^O and C^N)) transitions.

The emission spectrum of [IrL^3•Eu] was also recorded in MeOH at room temperature. The emission spectrum of the complex is given in **Fig. 4.37**.

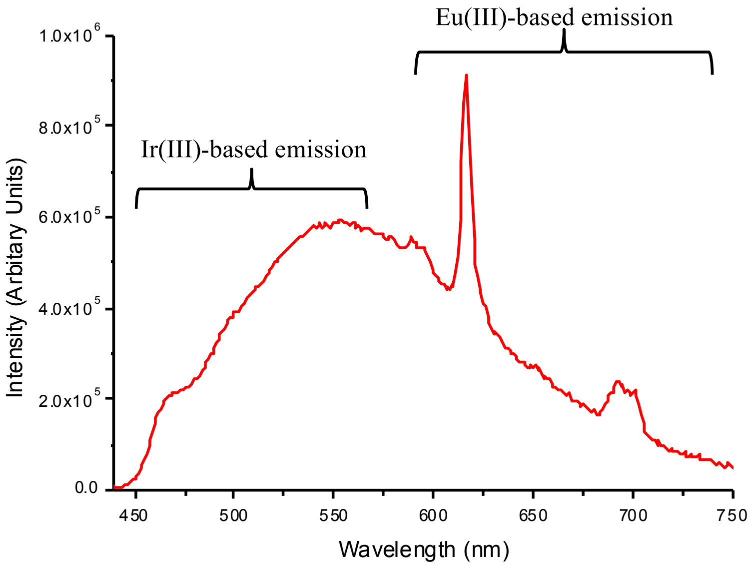

Figure 4.37. Emission spectrum of [IrL^3•Eu] [2.83 × 10^{-5} M] in aerated MeOH at 298 K. Excitation at 387 nm.

Under photoexcitation, the complex displayed a nice balance of both Ir(III)-based emission and Eu(III)-based emission. Eu(III)-based emission was observed with a series of sharp lines between 589 nm and 701 nm. The broad higher-energy emission (> 589 nm) is Ir(III)-based, displaying a good balance of d → f PEnT. Time-resolved luminescence measurements gave two Ir(III)-based emission lifetimes of τ_1 = 225 ns (minor component) and τ_2 = 42 ns (major component).

4.6 Chapter Conclusion

The synthesis and photophysical properties of four luminescent Ir(III) complexes are reported. Three of the complexes contained naphthalene spacer groups which resulted in quenching of Ir(III)-based emission, however efficient nap → Eu(III) PEnT was observed. The fourth complex, [Ir(fppy)$_2$L^3], contained a phenyl spacer unit which did not quench Ir(III)-based emission. Eu(III)-based emission was achieved with good balance between Ir(III)/Eu(III) emission in [IrL^3•Eu].

Ir(III)-based emission of [Ir(fppy)$_2$Lnap^{pic}] is quenched under photoexcitation due to ^{3}Ir → nap PEnT. Titration with [Eu(hfac)$_3$.2H$_2$O] showed strong sensitisation of Eu(III)-based emission. In this case, luminescence from Eu(III) is sensitised by a two-step energy-transfer process from ^{3}Ir → ^{3}nap → Eu(III).
Titration with [Tb(hfac)$_3$.2H$_2$O] showed little sensitisation of Tb(III) as the energy of the Tb(III) excited-state is too close to the energy of the Ir(III) excited state. It is also probable that a PET is occurring in tandem with PEnT, as partial quenching is also observed when the complex is titrated with [Gd(hfac)$_3$.2H$_2$O]. In this case it is not possible to populate the Gd(III) excited-states. PET could explain the additional quenching of Ir(III)-based emission observed in this case. There is evidence of [Ir(fppy)$_2$L^{pic}] (containing a phenyl spacer unit instead of naphthalene) from Chapter 2 that does display PET from Ir → pypz, therefore this shouldn't be ruled out. Further studies are necessary to determine the mechanism of Ir(III)-based quenching when the complex is bound to Ln(III) ions.

Photophysical studies of [Ir(fppy)$_2$L^2]$^+$ also showed that Ir(III)-based emission is quenched. This is consistent with the previous complex and is also attributed to ^{3}Ir → nap PEnT. [IrL^2•Eu] showed very efficient sensitisation of Eu(III), which was evident by the intensity of the Eu(III)-based emission. Ir(III)-based emission was almost completely quenched and undetectable by time-resolved luminescence studies. This is a disadvantage for use a dual-emitting cell imaging agent. Cell imaging studies are still necessary to confirm this, however it is likely that the Ir(III)-based emission will be too weak to detect.

Overall, the use of a naphthalene spacer unit showed improved d → f energy-transfer due to the nap unit acting as a 'stepping stone' in the energy-transfer process, however quenching of the extent of quenching of Ir(III)-based emission could limit the applications of the complex.

As a comparison, the use of a phenyl spacer unit in [IrL^3•Eu] resulted in good Ir(III) emission. Further photophysical studies on [Ir(fppy)$_2$L^3] are necessary. Measurements were not carried out due to the low yield of product obtained in the synthesis. The low yields also prevented the synthesis of the Gd analogue of the complex.

Sensitisation of Eu(III) emission is not as efficient in this case when compared to the previous naphthalene-based examples in this chapter, due to the d → f energy-transfer occurring directly from Ir(III) to Eu(III) rather than *via* a 'stepping stone'. In this case this is advantageous as a good balance of emission is achieved from both Ir(III) and Eu(III). This preliminary data is promising as it could be possible for the complex to be used in time-gated luminescence imaging and ratiometric sensing in cells.[25]

Future work on additional photophysical data and cell imaging studies would be beneficial to provide evidence of its usefulness as a cell imaging agent.

4.7 References

1. P. Coppo, M. Duatti, V. N. Kozhevnikov, J. W. Hofstraat and L. De Cola, *Angew. Chem. Int. Ed.,* 3005, **44**, 1806.
2. A. H. Shelton, I. V. Sazanovich, J. A. Weinstein and M. D. Ward, *Chem. Commun.,* 2012, **48**, 2749.
3. V. F. Plyusnin, A. S. Kupryakov, V. P. Grivin, A. H. Shelton, I. V. Sazanovich, A. J. H. M. Meijer, J. A. Weinstein and M. D. Ward, *Photochem. Photobiol. Sci.,* 2013, **12**, 1666.
4. A. J. Amoroso and S. J. A. Pope, *Chem. Soc. Rev.,* 2015, DOI: 10.1039/C4CS00293H.
5. T. J. Sørenson, A. M. Kenwright and S. Faulkner, *Chem. Sci.,* 2015, **6**, 2054.
6. C. M. Fisher, E. Fuller, B. P. Burke, V. Mogilireddy, S. J. A. Pope, A. E. Sparke, I. Déchamps-Olivier, C. Cadiou, F. Chuburu, S. Faulkner and S. J. Archibald, *Dalton Trans.,* 2014, **43**, 9567.
7. N. Sim, S. Gottschalk, R. Pal, J. Englemann, D. Parker and A. Mishra, *Chem. Sci.,* 2013, **4**, 3148.
8. T. Koullourou, L. S. Natrajan, H. Bhavsar, S. J. A. Pope, J. Feng, J. Narvainen, R. Shaw, E. Scales, R. Kauppinen, A. N. Kenwright and S. Faulkner, *J. Am. Chem. Soc.,* 2008, **130**. 2178.
9. E. Baggaley, D-K. Cao, D. Sykes, S. W. Botchway, J. A. Weinstein and M. D. Ward, *Chem. Eur. J.,* 2014, **20**, 8898.
10. D. Sykes, S. C. Parker, I. V. Sazanovich, A. Stephenson, J. A. Weinstein and M. D. Ward, *Inorg. Chem.,* 2013, **52**, 10500.
11. K. Ziegler, G. Schenk, E. W. Krockow, A. Siebert, A. Wenz and H. Weber, *Liebigs Ann.,* 1942, **551**, 1.
12. K. A. King and R. J. Watts, *J. Am. Chem. Soc.,* 1987, **109**, 1589.
13. B. Schmid, F. O. Garces and R. J. Watts, *Inorg. Chem.,* 1994, **33**, 9.
14. F. Barigelletti and L. Flamigni, *J. Am. Chem. Soc.,* 1999, **121**, 5009.
15. J. Li, P. I. Djurovich, B. D. Alleyne, M. Yousufuddin, N. N. Ho, J. C. Thomas, J. C. Peters, R. Bau and M. E. Thompson, *Inorg. Chem.,* 2005, **44**, 1713.
16. M. Hissler, A. Harriman, A. Khatyr and R. Ziessel, *Chem. Eur. J.,* 1999, **5**, 3366.

17. A. F. Morales, G. Accorsi, N. Armaroli, F. Barigelletti, S. J. A. Pope and M. D. Ward, *Inorg. Chem.,* 2002, **41**, 6711.
18. D. Sykes, I. S. Tidmarsh, A. Barbieri, I. V. Sazanovich, J. A. Wenstein and M. D. Ward, *Inorg. Chem.,* 2011, **50**, 11323.
19. W. E. Ford and M. A. J. Rodgers, *J. Phys. Chem.,* 1992, **96**, 2917.
20. E. B. Priestley and A. Haug, *J. Chem. Phys.,* 1968, **49**, 622.
21. A. P. Marchetti and D. R. Kearns, *J. Am. Chem. Soc.,* 1967, **89**, 768.
22. P. B. Merkel and J. P. Dinnocenzo, *J. Photochem. Photobiol. A: Chem.,* 2008, **193**, 110.
23. A. Dadabhoy, S. Faulkner and P. G. Sammes, *J. Chem. Soc., Perkin Trans. 2,* 2002, 348.
24. W. D. Horrocks and D. R. Sudnick, *J. Am. Chem. Soc.,* 1979, 334.
25. G. Grynkiewicz, M. Poenie and R. Y. Tsien, *J. Biol. Chem.,* 1985, **260**, 3440.

5

Experimental

5.1 Reagents and Equipment

5.1.1 Chemicals

All reagents and solvents, unless otherwise stated, were purchased from commercial sources and used as received.

5.1.2 ^{1}H NMR spectra

^{1}H NMR spectra were recorded using a Bruker AV1-400 MHz spectrometer with tryimethylsilane as the internal standard. Chemical shifts are quoted in ppm.

5.1.3 Mass spectra

All ES mass spectra were recorded with a Micromass LCT ES-TOF mass spectrometer. All spectra were run by either Simon Thorpe or Sharon Spey of the University of Sheffield Mass Spectrometry Service.

5.1.4 Photophysical measurements

The photoluminescence spectra were taken on Horiba Jobin Yvon Fluoromax-4-Spectrofluorometer. Absorption spectra were measured on Varian Cary 50 Bio UV-Visible Spectrophotometer and baseline corrected. Time-resolved luminescence measurements were performed using the Edinburgh Instruments Mini-τ instrument fitted with a 405 nm pulsed laser excitation source.

5.1.5 Elemental analysis

All elemental analyses were measured on a Perkin Elmer 2400 CHNS/O Series II Elemental Analyser. All measurements were run by Mrs Jennifer Louth of the University of Sheffield Elemental Analysis Service.

5.1.6 X-ray crystallography

Single crystal X-ray diffraction measurements were conducted at 100 K for all samples. X-ray data were collected using either a Bruker Smart APEX-II or a Bruker Kappa APEX-II system. Absorption correction was conducted by empirical methods (SADABS),[1] based upon symmetry-equivalent reflections combined with measurements at different azimuthal angles. Structures were solved and refined against all F^2 values using the SHELXTL program suite.[2] Hydrogen atoms were placed in calculated positions, refined using idealised geometries (riding model) and were assigned fixed isotropic displacement parameters.

5.1.7 Cyclic voltammetry

Cyclic voltammetric measurements were performed with an Ecochimie Autolab 100 potentiostat using a conventional three-electrode cell with a Pt disc working electrode; the base electrolyte was 0.1 M Bu_4NPF_6 and the solvent was CH_2Cl_2.

5.1.8 HPLC

HPLC purification was carried out on a Varian Prostar preparative HPLC system using a Model 410 autosampler, Model 320 UV/Vis detector, two Model 210 pumps and a Model 701 fraction collector.

5.1.9 Cell imaging

Cells were imaged in PBS (phosphate buffer solution) using a x40 water-dipping objective (in 6 well plates). Confocal images were carried out on a Zeiss LSM 510 upright confocal microscope using a Ti:Sa multiphoton laser (λ_{ex} = 780 nm). Measurements were carried out by Dr Elizabeth Baggaley at the University of Sheffield.

5.2 General Procedure for Photophysical Measurements

5.2.1 Luminescence, UV/Vis and time-resolved measurements

Approximately 5 mg of the iridium complex was placed into a 50 mL volumetric flask and filled with the aerated solvent for the luminescence and time-resolved luminescence measurements. Approximately 2.5 mg of the iridium complex was placed into a 50 mL volumetric flask and filled with aerated solvent for the UV/Vis measurements. 2 mL of this solution was measured into a quartz luminescence cell (1 cm path length) and the luminescence, time-resolved luminescence measurements and UV/Vis measurements were recorded.

5.2.2 Titration of the iridium complexes with [Ln(hfac)$_3$.2H$_2$O]

Approximately 5 mg of the iridium complex was placed into a 50 mL volumetric flask and filled with CH_2Cl_2 to give a stock solution. Approximately 10 mg of [Ln(hfac)$_3$.2H$_2$O] was placed into a 10 mL volumetric flask and the flask with filled with the iridium stock solution. A quartz luminescence cell (1 cm path length) was filled with 2 mL of the stock solution and measurements were made by adding aliquots of the [Ln(hfac)$_3$.2H$_2$O] (0 μL-500 μL) into the cell. UV/Vis absorption, luminescence and time-resolved measurements were recorded.

5.2.3 Luminescence measurements at 77 K

Approximately 5 mg the iridium complex was dissolved in 50 mL of ethanol/methanol (4:1). An NMR tube was filled with 1.2 mL of the solution. A quartz nitrogen dewar was filled with liquid nitrogen and the NMR tube was placed slowly in this to form a clear solid. This was then placed into the spectrofluorometer and the luminescence measurements were recorded.

5.2.4 Cell culture and staining

MCF7 cells were cultured in a humidified 37°C, 5% CO_2/95% air (v/v) environment in Roswell Park Memorial Institute medium (RPMI, Sigma Aldrich) supplemented with 10% (v/v) FCS (foetal calf serum), L-glutamine (200 mM, 5 mL), penicillin/streptomycin (5mL) and fungizone (1.25 mL). The cells were seeded in to sterile 6 well plates and cultured until 60% confluent.

After removal of growth media, cells were washed with PBS (1 mL/well) before treating with a solution of the appropriate complex at 25 μM (0.125% DMSO, 4h at 37°C, 1 mL/well), 50 μM (0.25% DMSO, 4h and 24h at 37°C, 1 mL/well), and 100 μM (0.5% DMSO, 4h at 37°C, 1 mL /well) in RPMI. All incubation solutions were diluted from a 20 mM stock solution of the complex in DMSO.

5.3 Synthesis of Compounds in Chapter 2

5.3.1 Tetrakis[2-(2,4-difluorophenyl)-pyridine-*C*^{2},*N'*](μ-dichloro)diiridium - [$Ir_2(fppy)_4Cl_2$]

The synthetic procedure for [$Ir_2(fppy)_4Cl_2$] was taken from literature.[3] 2-(2,4-difluorophenyl)pyridine (Sigma Aldrich) (0.58 g, 3.0 mmol) was dissolved in a mixture of 2-ethoxyethanol (30 mL) and water (10 mL). To this iridium trichloride hydrate (Alfa Aesar) (0.2 g, 0.68 mmol) was added. The round bottom flask was covered in foil and heated to reflux for 18 h. The solution was cooled to room temperature and the bright yellow precipitate was collected on a glass filter frit. The precipitate was washed with ethanol (30 mL) and acetone (30 mL) and dried to give [$Ir(fppy)_2Cl]_2$ (0.69 g, 83 %).

^{1}H NMR (400 MHz, $CDCl_3$, 298 K): δ_H 9.14 (d, *J* = 6.7 Hz, 4H), 8.33 (d, *J* = 8.4 Hz, 4H), 7.85 (t, *J* = 8.4 Hz, 4H), 6.85 (t, *J* = 7.3 Hz, 4H), 6.41 – 6.32 (m, 4H), 5.31 (dd, *J* = 9.1, 2.3 Hz, 4H). **ES-MS:** *m/z* = 1217 (MH^+).

5.3.2 L^{pytz}

The synthetic procedure for L^{pytz} was taken from literature.[4] A 250 mL round bottom flask was charged with 4-amino-3,5-di-2-pyridyl-4H-1,2,4-triazole (Sigma Aldrich) (1.0 g, 4.2 mmol), $HNO_{3\ (aq)}$ (10 mL, 5 M) and the mixture was stirred at 40°C for 30 min. The solution was cooled to 0°C and $NaNO_2$ (2.0 g in 10 mL of H_2O) was added drop wise. The mixture was maintained at 0°C and stirred for a further 30 min. NH_3OH (3 M) was then added drop wise until the mixture was alkaline and a white precipitate formed. The precipitate was filtered and dried to give white crystals of L^{pytz} (0.85 g, 91 %).

^{1}H NMR (400 MHz, MeOD, 298 K): δ_H 8.72 (d, *J* = 4.4 Hz, 2H), 8.27 (d, *J* = 7.9 Hz, 2H), 8.00 (td, *J* = 7.8, 1.7 Hz, 2H), 7.51 (ddd, *J* = 7.6, 4.9, 1.1 Hz, 2H). **ES-MS:** *m/z* = 224 (MH^+).

5.3.3 [Ir(fppy)$_2$L^{pytz}]

The synthetic procedure for [Ir(fppy)$_2$L^{pytz}] was taken from literature.[5] A two-neck 250 mL round bottom flask was flushed with N_2 and charged with L^{pytz} (0.05 g, 0.22 mmol), methanol (90 mL) and CH_2Cl_2 (45 mL). To this [Ir$_2$(fppy)$_4$Cl$_2$] (0.09 g, 0.074 mmol) was added. The flask was covered in foil and heated to reflux for 18 h under N_2. The mixture was cooled to room temperature and the solvent was removed under vacuum to give yellow coloured precipitate. The product was then obtained by column chromatography on silica gel (200-300 mesh) using CH_2Cl_2/MeOH (99:1) and then CH_3CN as the eluents, to give a yellow solid of [Ir(fppy)$_2$L^{pytz}] (0.051 g, 87 %).

^{1}H NMR (400 MHz, CDCl$_3$, 298 K): δ_H 8.71 (d, *J* = 4.6 Hz, 1H), 8.47 (d, *J* = 7.2 Hz, 1H), 8.30 (d, *J* = 9.1 Hz, 1H), 8.25 (d, *J* = 8.2 Hz, 1H), 8.19 (d, *J* = 7.9 Hz, 1H), 7.90 (dd, *J* = 13.6, 6.6 Hz, 2H), 7.72 (dt, *J* = 13.6, 6.0 Hz, 4H), 7.52 (d, *J* = 5.6 Hz, 1H), 7.20 (dd, *J* = 12.4, 5.8 Hz, 2H), 6.94 (dt, *J* = 21.6, 6.7 Hz, 2H), 6.58 – 6.42 (m, 2H), 5.82 (dd, *J* = 8.3, 2.1 Hz, 1H), 5.75 (dd, *J* = 8.7, 2.1 Hz, 1H). **ES-MS:** *m/z* = 796 (M$^+$). **Elemental analysis** ($IrC_{34}H_{20}N_7F_4$)**:** found (%): C: 51.2; H: 2.3; N: 12.0; calculated (%): C: 51.4; H 2.5; N: 12.3.

5.3.4 [Ir-pic] (Intermediate B)

The synthetic procedure for [Ir-pic] was modified from literature.[6] [Ir$_2$(fppy)$_4$Cl$_2$] (0.1 g, 0.087 mmol) and sodium carbonate (0.093 g, 0.87 mmol) were added to 2-ethoxyethanol (80 mL). 3-Hydroxypicolinic acid (Sigma Aldrich) (0.03 g, 0.22 mmol) was added to this and the mixture was refluxed under N_2 for 18 h. The precipitate was filtered and the solvent from the filtrate was removed under vacuum to give a yellow solid. The product was then obtained by column chromatography on silica gel (200-300 mesh) using CH_2Cl_2/methanol (95:5) as the eluent to yield a yellow solid of [Ir-pic] (0.042 g, 68%).

^{1}H NMR (400 MHz, CDCl$_3$, 298 K): δ_H 8.69 (dd, *J* = 5.8, 0.9 Hz, 1H), 8.33 (d, *J* = 8.5 Hz, 1H), 8.27 (d, *J* = 8.3 Hz, 1H), 7.83 (t, *J* = 7.8 Hz, 2H), 7.52 – 7.42 (m, 2H), 7.31 – 7.29 (m, 2H), 7.25 (ddd, *J* = 7.3, 4.2, 1.3 Hz, 1H), 7.06 (ddd, *J* = 7.3, 5.8, 1.3

Hz, 1H), 6.56 – 6.38 (m, 2H), 5.80 (dd, *J* = 8.7, 2.3 Hz, 1H), 5.60 (dd, *J* = 8.7, 2.3 Hz, 1H). **ES-MS:** *m/z* = 712 (MH^+).

5.3.5 Intermediate spacer unit (A)

3-(2-pyridyl)pyrazole (0.5 g, 3.46 mmol) (supplied by Dr Andrew Stephenson) was added to a mixture of THF (50 mL) and aqueous NaOH (1 M, 50 mL) and stirred for 10 minutes. To this α,α'-dibromo-*p*-xylene (Sigma Aldrich) (3.6 g, 0.014 mol) was added and the reaction was stirred at room temperature for 48 h. The organic layer was separated and the solvent was removed under vacuum. The precipitate was dissolved in CH_2Cl_2 (50 mL) and washed with H_2O (3 × 50 mL). The organic layer was dried under $MgSO_4$, filtered and the solvent was removed under vacuum. The product was then obtained by column chromatography on silica gel (200-300 mesh) using CH_2Cl_2/MeOH (99:2) as the eluent (0.77 g, 62%).

^{1}H NMR (400 MHz, $CDCl_3$, 298 K): δ_H 8.66 (dd, *J* = 4.1, 0.8 Hz, 1H), 7.97 (d, *J* = 8.0 Hz, 1H), 7.75 (td, *J* = 7.8, 1.8 Hz, 1H), 7.45 (d, *J* = 2.3 Hz, 1H), 7.39 (d, *J* = 8.1 Hz, 2H), 7.24 (dd, *J* = 9.9, 3.6 Hz, 3H), 6.97 (d, *J* = 2.2 Hz, 1H), 5.41 (s, 2H), 4.49 (s, 2H). **ES-MS:** *m/z* = 329 (MH^+).

5.3.6 [Ir(fppy)$_2$L^{pic}]

[Ir-pic] (0.19 g, 0.27 mmol) and potassium carbonate (0.37 g, 2.7 mmol) were added to acetone (60 mL), followed by the intermediate spacer unit (**A**) (0.13 g, 0.041 mmol). The mixture was heated to reflux under $N_{2\ (g)}$ for 48 h. The solvent was removed under vacuum and the solid was dissolved in CH_2Cl_2 (50 mL) and extracted with H_2O (3 × 30 mL). The organic layer was dried over $MgSO_4$, filtered and the solvent was removed under vacuum to give a yellow solid. The product was then obtained by column chromatography on silica gel (200-300 mesh) using CH_2Cl_2/MeOH (90:10) as the eluent to yield a yellow solid (0.051 g, 20%).

^{1}H NMR (400 MHz, $CDCl_3$, 298 K): δ_H 8.82 (dd, *J* = 5.8, 0.9 Hz, 1H), 8.65 (d, *J* = 4.2 Hz, 1H), 8.28 (d, *J* = 8.6 Hz, 1H), 8.23 (d, *J* = 8.4 Hz, 1H), 7.96 (t, *J* = 8.1 Hz, 1H), 7.82 – 7.69 (m, 3H), 7.55 (t, *J* = 10.8 Hz, 2H), 7.48 – 7.39 (m, 4H), 7.28 – 7.18 (m, 5H), 7.00 – 6.91 (m, 2H), 6.46 (ddd, *J* = 11.8, 9.2, 2.3 Hz, 1H), 6.43 – 6.36 (m, 1H), 5.80 (dd, J = 8.7, 2.3 Hz, 1H), 5.61 – 5.50 (m, 1H), 5.40 (s, 2H), 5.33 (d, J = 5.0 Hz, 2H).

ES-MS: m/z = 959 (MH^+). **Elemental analysis** ($IrC_{44}H_{29}N_6O_3F_4$)**:** found (%): C: 54.0; H: 3.0; N: 8.6; calculated with a coordinated H_2O (%): C: 54.2; H 3.2; N: 8.6.

5.4 Synthesis of Compounds in Chapter 3

5.4.1 (Pyridine-2-yl) amidrazone

The synthetic procedure for (pyridine-2-yl) amidrazone was taken from literature.[7] 2-Pyridinecarbonitrile (Sigma Aldrich) (10.3 g, 0.09 mol) was melted and hydrazine monohydrate (5.4 g, 0.09 mol) was added to this and stirred. Ethanol (4 mL) was added to the mixture and then stirred for 16 h at room temperature. The solvent was removed under vacuum and the solid was suspended in petroleum ether (50 mL), cooled in an ice bath, filtered and washed with cold petroleum ether to give a pale yellow solid (8.2 g, 67%).

^{1}H NMR (400 MHz, $CDCl_3$, 298 K): δ_H 8.53 (ddd, *J* = 4.9, 1.7, 1.0 Hz, 1H), 8.03 (dt, *J* = 8.1, 1.1 Hz, 1H), 7.71 (ddd, *J* = 8.0, 7.5, 1.8 Hz, 1H), 7.30 (t, *J* = 1.7 Hz, 1H), 7.27 (dd, *J* = 4.9, 1.2 Hz, 1H), 5.32 (s, 2H). **ES-MS:** *m*/*z* = 137 (MH^+).

5.4.2 L^{tol}

The synthetic procedure for L^{tol} was taken from literature.[7] (Pyridine-2-yl) amidrazone (2.0 g, 0.015 mol) was added to a flame-dried, nitrogen-purged Schlenk tube. To this dry DMAA (15 mL) and THF (5 mL) were added and the suspension was cooled to 0°C. In a separate flask, *p*-toluoyl chloride (Sigma Aldrich) (2.3 g, 0.015 mol) was dissolved in dry DMAA (5 mL). This was then cooled and added drop wise to the other mixture and stirred. The mixture was slowly warmed to room temperature and stirred for an addition 5 h. CH_2Cl_2 (50 mL) was then added resulting in precipitate. This was filtered and the precipitate was heated to 190°C for 25 min in glycerol. Upon cooling H_2O (50 mL) was added, resulting in pale yellow precipitate, which was filtered. The product was then obtained by column chromatography on silica gel (200-300 mesh) using $CHCl_3$/methanol (95:5) as the eluent to yield a white solid (2.6 g, 74 %).

^{1}H NMR (400 MHz, $CDCl_3$, 298 K): δ_H 8.84 (d, *J* = 4.8 Hz, 1H), 8.34 (d, *J* = 7.9 Hz, 1H), 8.13 (d, *J* = 8.2 Hz, 2H), 7.93 (td, *J* = 7.8, 1.7 Hz, 1H), 7.50 (ddd, *J* = 7.6, 4.8, 1.1 Hz, 1H), 7.36 (d, *J* = 8.0 Hz, 2H), 2.46 (s, 3H). **ES-MS:** *m*/*z* = 237 (MH^+).

5.4.3 [Ir(fppy)$_2$L^{tol}].(PF$_6$)

The synthetic procedure for [Ir(fppy)$_2$L^{tol}] was modified from literature.[5] A two-neck 250 mL round bottom flask was flushed with N_2 and charged with L^{tol} (0.062 g, 0.26 mmol), methanol (90 mL) and CH_2Cl_2 (45 mL). To this [Ir$_2$(fppy)$_4$Cl$_2$] (0.1 g, 0.087 mmol) was added. The flask was covered in foil and heated to reflux for 18 h under N_2. The mixture was cooled to room temperature and the solvent was removed under vacuum to give yellow coloured precipitate. The precipitate was dissolved in CH_2Cl_2 (30 mL) and washed with H_2O (3 × 30 mL), followed by saturated aqueous KPF_6 (10 mL), dried ($MgSO_4$) and filtered. The solvent was removed under vacuum to give a yellow precipitate. The product was then obtained by column chromatography on silica gel (200-300 mesh) using CH_2Cl_2/MeOH (99:1) and then with CH_3CN/H_2O (99:1) as the eluents, to yield a yellow solid (0.041 g, 58 %).

^{1}H NMR (400 MHz, CDCl$_3$, 298 K): δ_H 8.78 (d, *J* = 7.9 Hz, 1H), 8.38 (td, *J* = 7.9, 1.4 Hz, 1H), 8.31 (d, *J* = 4.1 Hz, 2H), 8.12 (d, *J* = 5.8 Hz, 1H), 8.07 (d, *J* = 8.2 Hz, 2H), 7.93 (d, *J* = 5.3 Hz, 1H), 7.84 (q, *J* = 7.4 Hz, 2H), 7.66 (t, *J* = 5.9 Hz, 2H), 7.35 (t, *J* = 9.2 Hz, 2H), 7.18 (dt, *J* = 9.0, 6.7 Hz, 2H), 6.68 – 6.50 (m, 2H), 5.71 (ddd, *J* = 14.7, 8.4, 2.2 Hz, 2H), 2.44 (s, *J* = 12.0 Hz, 3H). **ES-MS:** *m/z* = 809 (MH$^+$). **Elemental analysis** ($C_{36}H_{24}N_6F_{10}P$)**:** found (%): C: 45.8; H: 2.8; N: 9.7; calculated with a coordinated CH_3CN and PF_6^- (%): C: 45.9; H 2.7; N: 9.9.

5.4.4 TosylPEG

The synthetic procedure for TosylPEG was taken from literature.[8] Triethylene glycol monomethyl ether (Sigma Aldrich) (3.01g 18 mmol), *p*-toluenesulfonyl chloride (Sigma Aldrich) (3.51g 18 mmol) and 4-dimethylaminopyridine (Sigma Aldrich) (*cat.*) were added to a two-neck round bottom flask and flushed with $N_{2\ (g)}$. To this, CH_2Cl_2 (80 mL) was added, followed by triethylamine (Sigma Aldrich) (2.22 g, 22 mmol) and the reaction was stirred at room temperature for 18 h. The reaction was quenched by the addition of H_2O (75 mL). The organic layer was then washed with H_2O (2 × 75 mL). The organic layer was then dried ($MgSO_4$), filtered and the solvent removed under vacuum to give a colourless oil (5.2 g, 90%).

^{1}H NMR (400 MHz, $CDCl_3$, 298 K): δ_H 7.75 (d, *J* = 8.3 Hz, 2H), 7.31 (d, *J* = 8.1 Hz, 2H), 4.12 (dd, 2H), 3.64 (dd, 2H), 3.59 – 3.53 (m, 6H), 3.49 (dd, *J* = 5.7, 3.3 Hz, 2H), 3.33 (s, 3H), 2.41 (s, 3H). **ES-MS:** *m/z* = 319 (MH^+).

5.4.5 [Ir_2(ppy-Ald)$_4$$Cl_2$]

The synthetic procedure for [Ir_2(ppy-Ald)$_4$$Cl_2$] was modified from literature.[9] 4-(2-pyridyl) benzaldehyde (Sigma Aldrich) (0.84 g, 4.6 mmol) was dissolved in a mixture of 2-ethoxyethanol (30 mL) and water (10 mL). To this iridium trichloride hydrate (Alfa Aesar) (0.3 g, 1.0 mmol) was added. The round bottom flask was covered in foil and heated to reflux for 18 h. The solution was cooled to room temperature and the bright red precipitate was collected on a glass filter frit. The precipitate was washed with ethanol (40 mL) and H_2O (10 mL) and dried to give [Ir(fppy)$_2$Cl]$_2$ (0.58 g, 48%).

^{1}H NMR (400 MHz, DMSO-d_6, 298 K): δ_H 9.88 (d, *J* = 5.1 Hz, 2H), 9.66 (s, 2H), 9.61 – 9.56 (m, *J* = 7.0 Hz, 4H), 8.48 (d, *J* = 8.1 Hz, 2H), 8.40 (d, *J* = 7.9 Hz, 2H), 8.31 – 8.21 (m, 2H), 8.21 – 8.14 (m, 2H), 8.07 (d, *J* = 8.0 Hz, 2H), 8.03 (d, *J* = 8.0 Hz, 2H), 7.74 (dd, *J* = 9.7, 3.6 Hz, 2H), 7.69 – 7.61 (m, 2H), 7.43 (ddd, *J* = 16.3, 7.9, 1.4 Hz, 4H), 6.75 (d, *J* = 1.3 Hz, 2H), 6.14 (d, *J* = 1.3 Hz, 2H). **ES-MS:** *m/z* = 557 (MH^+/2).

5.4.6 [Ir(ppy-Ald)$_2$$L^{pytz}$]

The synthetic procedure for [Ir(ppy-Ald)$_2$$L^{pytz}$] was modified from literature.[5] A two-neck 250 mL round bottom flask was flushed with N_2 and charged with L^{pytz} (0.28 g, 1.3 mmol), MeOH (90 mL) and CH_2Cl_2 (45 mL). To this [Ir(ppy-Ald)$_2$$L^{pytz}$] (0.51 g, 0.42 mmol) was added. The flask was covered in foil and heated to reflux for 18 h under N_2. The mixture was cooled to room temperature and the solvent was removed. The crude was columned twice on alumina gel (Brockmann Grade III), first using CH_2Cl_2/MeOH (99:1) and then using CH_3CN/H_2O (99:1) as the eluents, to give an orange precipitate (0.25 g, 78%).

^{1}H NMR (400 MHz, $CDCl_3$, 298 K): δ_H 9.75 (s, *J* = 4.9 Hz, 2H), 9.70 (s, *J* = 3.9 Hz, 2H), 8.68 (d, *J* = 4.0 Hz, 1H), 8.49 (d, *J* = 7.9 Hz, 1H), 8.13 (d, *J* = 7.9 Hz, 1H), 8.00 (t, *J* = 7.9 Hz, 3H), 7.89 (td, *J* = 7.8, 1.5 Hz, 1H), 7.85 – 7.82 (m, 1H), 7.81 (d, *J* = 3.1 Hz, 1H), 7.71 (d, *J* = 5.5 Hz, 1H), 7.68 – 7.62 (m, 2H), 7.52 (dd, *J* = 8.0, 1.5 Hz, 1H), 7.47 (dd, *J* = 8.0, 1.5 Hz, 1H), 7.21 – 7.12 (m, 2H), 7.11 – 7.01 (m, 2H), 6.86 (d, *J* = 1.4 Hz, 1H), 6.80 (d, *J* = 1.4 Hz, 1H). **ES-MS:** *m*/*z* = 780 (MH^+).

5.4.7 [Ir(ppyOH)$_2$L^{pytz}]

The synthetic procedure of reduction of the aldehyde groups was modified from literature.[10] [Ir(ppy-Ald)$_2$L^{pytz}] (0.25 g, 0.33 mmol) was dissolved in CH_2Cl_2 (15 mL) this was then added to a solution of ethanol (50 mL) followed by sodium borohydride (0.04 g, 1.1 mol). The reaction was stirred at room temperature for 30 min. The solvent was removed under vacuum and the mixture was dissolved in CH_2Cl_2/H_2O (30 mL/ 100 mL). Sodium carbonate (0.17 g, 1.6 mol) was then added and the mixture was stirred at room temperature for 30 min. The organic layer was extracted into CH_2Cl_2 (5 × 30 mL), combined, dried over $MgSO_4$ and the solvent was removed under vacuum. The crude product was columned on alumina gel (Brockmann Grade III) using CH_2Cl_2/MeOH (95:5) to give a yellow precipitate (0.24 g, 92%).

^{1}H NMR (400 MHz, $CDCl_3$, 298 K): δ_H 8.67 (d, *J* = 4.1 Hz, 1H), 8.53 (s, 1H), 8.20 (d, *J* = 8.1 Hz, 1H), 7.94 – 7.82 (m, 4H), 7.79 – 7.61 (m, 6H), 7.55 (d, *J* = 6.0 Hz, 1H), 7.24 – 7.18 (m, 1H), 7.18 – 7.12 (m, 1H), 7.04 (td, *J* = 8.1, 1.6 Hz, 2H), 6.98 – 6.85 (m, 2H), 6.40 (d, *J* = 1.3 Hz, 1H), 6.34 (d, *J* = 1.3 Hz, 1H), 4.48 (s, 2H), 4.43 (s, 2H). **ES-MS:** *m*/*z* = 784 (MH^+).

5.4.8 [Ir(ppy-PEG)$_2$L^{pytz}]

A round bottom flask was flushed with N_2 and to this NaH (0.3 g, 0.013 mol) was added. 100 mL of hexane was added and the mixture was stirred for 5 min. The hexane was then removed and dry THF was added (50 mL). DMF (50 mL) and [Ir(ppy-OH)$_2$L^{pytz}] (0.24 g, 0.3 mmol) was then added and the mixture was stirred under N_2 for 30 min. TosylPEG (1.5 g, 4.7 mmol) and Bu^4NI (Sigma Aldrich) (*cat.*) were then added and the mixture was heated to reflux for 18 h. The reaction was allowed to cool and unreacted NaH was quenched with MeOH (10 mL). The solvent was removed under vacuum and the crude mixture was dissolved in CH_2Cl_2 (50 mL). The organic layer was washed with H_2O (5 × 40 mL), dried over $MgSO_4$ and the solvent was removed under vacuum. The crude was columned on alumina gel (Brockmann Grade III) using CH_2Cl_2/MeOH (99:1). The product was obtained through further purification by analytical HPLC in 60% H_2O (0.1% TFA) and 40% CH_3CN (retention time = 6 min) to give a yellow precipitate (0.078 g, 24%).

^{1}H NMR (400 MHz, $CDCl_3$, 298 K): δ_H 8.76 (d, *J* = 4.8 Hz, 1H), 8.70 (d, *J* = 7.9 Hz, 1H), 8.29 (d, *J* = 8.0 Hz, 1H), 8.12 – 8.01 (m, 1H), 7.97 (td, *J* = 7.9, 1.3 Hz, 1H), 7.90 (dd, *J* = 11.1, 8.0 Hz, 3H), 7.84 (d, *J* = 4.8 Hz, 1H), 7.79 – 7.70 (m, 2H), 7.66 (d, *J* = 8.0 Hz, 2H), 7.48 (t, *J* = 6.7 Hz, 2H), 7.39 – 7.31 (m, 1H), 7.04 (tdd, *J* = 13.0, 8.7, 4.7 Hz, 3H), 6.99 – 6.92 (m, 1H), 6.22 (d, *J* = 16.4 Hz, 2H), 4.44 – 4.27 (m, 4H), 3.69 – 3.46 (m, 24H), 3.40 – 3.31 (m, 6H). **ES-MS:** *m/z* = 1076 (MH^+). **Elemental analysis** ($IrC_{49}H_{36}N_7O_8$)**:** found (%): C: 53.7; H: 5.9; N: 8.7; calculated with two coordinated H_2O molecules (%): C: 54.0; H 5.5; N: 8.8.

5.4.9 [Ir(ppy-Ald)$_2$L^{tol}]

The synthetic procedure for [Ir(ppy-Ald)$_2$L^{tol}] was modified from literature.[5] A two-neck 250 mL round bottom flask was flushed with N_2 and charged with L^{tol} (0.22 g, 0.93 mmol), MeOH (90 mL) and CH_2Cl_2 (45 mL). To this [Ir(ppy-Ald)$_2$L^{pytz}] (0.51 g, 0.42 mmol) was added. The flask was covered in foil and heated to reflux for 18 h under N_2. The mixture was cooled to room temperature and the solvent was removed. The crude was columned twice, first on silica gel (200-300 gel mesh) using CH_2Cl_2/MeOH (98:2) as the eluent, and then on alumina gel (Brockmann Grade III), using CH_2Cl_2 as the eluent to give an orange precipitate (0.2 g, 60%).

^{1}H NMR (400 MHz, $CDCl_3$, 298 K): δ_H 9.73 (d, *J* = 16.2 Hz, 2H), 8.35 (d, *J* = 8.0 Hz, 1H), 7.98 (dd, *J* = 19.4, 11.4 Hz, 5H), 7.93 – 7.59 (m, 8H), 7.60 – 7.42 (m, 2H), 7.25 – 6.93 (m, 4H), 6.84 (d, *J* = 17.4 Hz, 2H), 2.33 (s, 3H). **ES-MS:** *m/z* = 792 (MH^+).

5.4.10 [Ir(ppy-OH)$_2$L^{tol}]

The synthetic procedure of reduction of the aldehyde groups was modified from literature.[10] [Ir(ppy-Ald)$_2$L^{ptol}] (0.2 g, 0.25 mmol) was dissolved in CH_2Cl_2 (15 mL) this was then added to a solution of ethanol (50 mL) followed by sodium borohydride (0.038 g, 1.0 mmol). The reaction was stirred at room temperature for 30 min. The solvent was removed under vacuum and the mixture was dissolved in CH_2Cl_2/H_2O (30 mL/ 100 mL). Sodium carbonate (0.13 g, 1.3 mmol) was then added and the mixture was stirred at room temperature for 30 min. The organic layer was extracted into CH_2Cl_2 (5 × 30 mL), combined, dried over $MgSO_4$ and the solvent was removed under vacuum. The crude product was columned on alumina gel (Brockmann Grade III) using CH_2Cl_2/MeOH (98:2) to give a yellow precipitate (0.22 g, 62%).

^{1}H NMR (400 MHz, $CDCl_3$, 298 K): δ_H 8.29 (d, *J* = 7.9 Hz, 1H), 8.01 (d, *J* = 8.1 Hz, 2H), 7.91 (d, *J* = 5.7 Hz, 1H), 7.82 (dt, *J* = 7.9, 4.0 Hz, 3H), 7.71 (d, *J* = 5.0 Hz, 1H), 7.69 – 7.57 (m, 4H), 7.52 (d, *J* = 5.8 Hz, 1H), 7.15 (d, *J* = 8.0 Hz, 2H), 7.12 – 7.04 (m, 1H), 6.99 (dd, *J* = 19.7, 7.9 Hz, 2H), 6.92 – 6.81 (m, 2H), 6.35 (d, *J* = 20.7 Hz, 2H), 4.41 (d, *J* = 16.9 Hz, 4H), 2.33 (s, 3H). **ES-MS:** *m/z* = 796 (MH^+).

5.4.11 [Ir(ppy-PEG)$_2$L^{tol}]

A round bottom flask was flushed with N_2 and to this NaH (0.3 g, 0.013 mol) was added. 100 mL of hexane was added and the mixture was stirred for 5 min. The hexane was then removed and dry THF was added (50 mL). DMF (50 mL) and [Ir(ppy-OH)$_2$L^{tol}] (0.22 g, 0.28 mmol) was then added and the mixture was stirred under N_2 for 30 min. TosylPEG (1.3 g, 4.2 mmol) and Bu^{4}NI (Sigma Aldrich) (*cat.*) were then added and the mixture was heated to reflux for 18 h. The reaction was allowed to cool and unreacted NaH was quenched with MeOH (10 mL). The solvent was removed under vacuum and the crude mixture was dissolved in CH_2Cl_2 (50 mL). The organic layer was washed with H_2O (5 × 40 mL), dried over $MgSO_4$ and the solvent was removed under vacuum. The crude was columned on silica gel (200-300 mesh) using CH_2Cl_2/MeOH (98:2). The product was obtained through further purification by analytical HPLC in 60% H_2O and 40% CH_3CN (retention time = 6 min) to give a yellow precipitate (0.062 g, 21%).

^{1}H NMR (400 MHz, $CDCl_3$, 298 K): δ_H 8.29 (d, *J* = 8.0 Hz, 1H), 8.02 (d, *J* = 8.1 Hz, 2H), 7.85 (ddd, *J* = 15.5, 10.2, 3.6 Hz, 4H), 7.73 (d, *J* = 5.4 Hz, 1H), 7.71 – 7.60 (m, 4H), 7.54 (d, *J* = 5.5 Hz, 1H), 7.23 – 7.13 (m, 2H), 7.13 – 7.05 (m, 1H), 6.99 (dd, *J* = 15.6, 8.5 Hz, 2H), 6.89 (dt, *J* = 25.9, 6.6 Hz, 2H), 6.28 (d, *J* = 5.2 Hz, 2H), 4.35 (dt, *J* = 12.4, 9.0 Hz, 4H), 3.78 – 3.46 (m, *J* = 21.7, 15.3, 9.5, 4.8 Hz, 24H), 3.39 (t, *J* = 4.3 Hz, 6H), 2.34 (s, 3H). **ES-MS:** *m/z* = 1090 (MH^+). **HRMS ES^+:** Calculated for $IrC_{52}H_{60}N_6O_8$: 1089.4102; Found: 1089.4102.

5.5 Synthesis of Compounds in Chapter 4

5.5.1 1,4-di(bromomethyl)naphthalene

The synthetic for 1,4-di(bromomethyl)naphthalene procedure was taken from literature.[11] 1,4-dimethylnaphthalene (Sigma Aldrich) (2.0 g, 0.013 mol) was added to a round bottom flask containing CCl_4 (50 mL). To this NBS (5.010 g, 0.028 mol) was added followed by AIBN (0.1 g, 0.61 mmol). The mixture was heated to reflux for 2 h under a 240 V tungsten lamp. The solvent was removed under vacuum and the crude was dissolved in CH_2Cl_2 (50 mL) and washed with H_2O (3 × 30 mL), dried over $MgSO_4$, filtered and the solvent was removed under vacuum. The product was obtained by recrystallisation in boiling toluene (15 mL) to give white precipitate (2.1 g, 52%).

^{1}H NMR (400 MHz, $CDCl_3$, 298 K): δ_H 8.29 – 8.18 (m, 2H), 7.76 – 7.63 (m, 2H), 7.51 (s, 2H), 4.96 (s, 4H). **EI-MS:** *m*/*z* = 314 (M).

5.5.2 Nap^{pypz}

The synthetic procedure for nap^{pypz} was modified from literature.[11] 1,4-di(bromomethyl)naphthalene (1.5 g, 4.8 mmol) was added to THF (50 mL) and stirred. To this, NaOH (2M, 50 mL) was added and stirred for 10 min. Pyridyl pyrazole (0.23 g, 1.6 mmol) was dissolved in THF (10 mL) and added drop-wise to the reaction mixture over 10 min. The reaction was allowed to proceed at room temperature for 3 days. The THF was separated and removed under vacuum. The residue was dissolved in CH_2Cl_2 (200 mL) and extracted with H_2O (3 × 50 mL). The organic layer was dried over $MgSO_4$, filtered and the solvent was removed under vacuum. The product was obtained by column chromatography on silica gel (200-300 mesh) using CH_2Cl_2/MeOH (98:2) as the eluent, to yield a white solid (0.38 g, 63%).

^{1}H NMR (400 MHz, $CDCl_3$, 298 K): δ_H 8.66 (ddd, *J* = 4.9, 1.7, 0.9 Hz, 1H), 8.22 (d, *J* = 8.4 Hz, 1H), 8.07 (d, *J* = 7.8 Hz, 1H), 7.98 (d, *J* = 8.0 Hz, 1H), 7.73 (td, *J* = 7.7, 1.8 Hz, 1H), 7.66 (ddd, *J* = 8.3, 6.9, 1.2 Hz, 1H), 7.60 – 7.49 (m, 2H), 7.31 (t, *J*

= 1.8 Hz, 1H), 7.25 – 7.16 (m, 2H), 6.89 (d, *J* = 2.4 Hz, 1H), 5.85 (d, *J* = 7.0 Hz, 2H), 4.95 (s, 2H). **ES-MS:** *m/z* = 380 (MH^+).

5.5.3 [Ir(fppy)$_2$Lnap^{pic}]

[Ir-pic] (0.46 g, 0.64 mmol) and potassium carbonate (0.89 g, 6.4 mmol) were added to acetone (60 mL), followed by nap^{pypz} (0.61 g, 1.6 mmol). The mixture was heated to reflux for 48 h. The solvent was removed under vacuum and the solid was dissolved in CH_2Cl_2 (50 mL) and extracted with H_2O (3 × 30 mL). The organic layer was dried over $MgSO_4$, filtered and the solvent was removed under vacuum to give a yellow solid. The product was then obtained by column chromatography twice, first on alumina gel (Brockmann Grade III) using CH_2Cl_2/MeOH (99:0.1) as the eluent, followed by silica gel (200-300 mesh) using CH_3CN as the eluent, to yield a yellow solid (0.16 g, 25%).

^{1}H NMR (400 MHz, acetone-d$_6$, 298 K): δ_H 8.85 – 8.77 (m, 1H), 8.63 – 8.52 (m, 1H), 8.39 – 8.28 (m, 4H), 8.26 (d, *J* = 7.3 Hz, 1H), 8.09 (dd, *J* = 7.2, 2.7 Hz, 1H), 8.07 – 7.99 (m, 3H), 7.87 – 7.75 (m, 2H), 7.73 (d, *J* = 2.3 Hz, 1H), 7.66 – 7.57 (m, 2H), 7.57 – 7.45 (m, 3H), 7.43 (d, *J* = 7.3 Hz, 1H), 7.26 (ddd, *J* = 7.4, 4.9, 1.2 Hz, 2H), 6.91 (d, *J* = 2.3 Hz, 1H), 6.68 – 6.49 (m, 2H), 5.95 (s, 2H), 5.89 – 5.82 (m, 3H), 5.61 (dd, *J* = 8.8, 2.3 Hz, 1H). **ES-MS:** *m/z* = 1009 (MH^+).

5.5.4 Triester

The synthetic procedure for triester was taken from literature.[12] CH_3CN (60 mL) was cooled to 0°C in an ice bath. To this, cyclen (Sigma Aldrich) (1.8 g, 10 mmol) and $NaHCO_3$ (2.8 g, 33 mmol) was added. *Tert*-butyl bromoacetate (Sigma Aldrich) (6.4 g, 33 mmol) was then added dropwise over 30 min. The reaction was allowed to stir at room temperature for 48 h. The precipitate was filtered and the solvent from the filtrate was removed under vacuum. The remaining precipitate was recrystallized with toluene to give a white precipitate (1.9 g, 38%).

^{1}H NMR (400 MHz, CDCl$_3$, 298 K): δ_H 10.07 (s, 1H), 3.43 – 2.83 (m, 22H), 1.48 (d, *J* = 2.7 Hz, 27H). **ES-MS:** *m/z* = 515 (MH^+).

5.5.5 Pypz-nap-triester

Nap^{pypz} (0.26 g, 0.68 mmol) was added to a CH_3CN (50 mL), followed by trimester (1.1 g, 2.1 mmol), Cs_2CO_3 (2.2 g, 6.8 mmol) and KI (*cat.*). The reaction was stirred at 45 °C under $N_{2\ (g)}$ for 18 h. The solvent was removed under vacuum and the precipitate was dissolved in CH_2Cl_2 (50 mL). This was washed with H_2O (3 × 30 mL) and the organic layer was dried over $MgSO_4$, filtered and the solvent was removed under vacuum. Most impurities were removed by size exclusion column chromatography on Sephadex LH-20 using CH_2Cl_2 as the eluent to give an orange oil (0.22 g, 39%).

^{1}H NMR (400 MHz, $CDCl_3$, 298 K): δ_H 8.66 (ddd, *J* = 4.9, 1.7, 0.9 Hz, 1H), 8.55 (d, *J* = 7.5 Hz, 1H), 8.03 – 7.95 (m, 2H), 7.75 (td, *J* = 7.7, 1.8 Hz, 1H), 7.59 – 7.47 (m, 3H), 7.28 – 7.19 (m, 3H), 6.84 (d, *J* = 2.3 Hz, 1H), 5.85 (s, 2H), 3.96 (s, 2H), 3.80 – 1.80 (m, 32H), 1.44 (d, *J* = 24.9 Hz, 37H). **ES-MS:** *m/z* = 812 (MH^+), 515 (MH^+ from free triester).

5.5.6 Protected $[Ir(fppy)_2L^2].(PF_6)$

The synthetic procedure for $[Ir(fppy)_2L^2]$ was modified from literature.[5] A round bottom flask was flushed with N_2 and charged with pypz-nap-triester (0.22 g, 0.27 mmol), methanol (90 mL) and CH_2Cl_2 (45 mL). To this $[Ir_2(fppy)_4Cl_2]$ (0.16 g, 0.13 mmol) was added. The flask was covered in foil and heated to reflux for 48 h under N_2. The mixture was cooled to room temperature and the solvent was removed under vacuum. The precipitate was dissolved in CH_2Cl_2 (30 mL) and washed with H_2O (3 × 30 mL). The organic layer was then washed with saturated $KPF_{6\ (aq)}$ (10 mL), dried ($MgSO_4$) and filtered. The solvent was removed under vacuum to give a yellow precipitate. The product was then obtained by column chromatography on silica gel (200-300 mesh) using CH_2Cl_2/MeOH (99:1) as the eluent to yield a yellow solid (0.17 g, 45 %).

^{1}H NMR (400 MHz, $CDCl_3$, 298 K): δ_H 8.47 (s, 1H), 8.25 (t, *J* = 10.2 Hz, 3H), 8.11 (td, *J* = 7.9, 1.5 Hz, 1H), 7.96 (dd, *J* = 11.7, 6.4 Hz, 2H), 7.89 – 7.75 (m, 3H), 7.70 (d, *J* = 5.1 Hz, 1H), 7.60 – 7.39 (m, 6H), 7.35 (ddd, *J* = 13.5, 7.4, 4.6 Hz, 2H), 7.30 (d, *J* = 1.5 Hz, 2H), 7.15 (t, *J* = 6.7 Hz, 1H), 6.49 (t, *J* = 9.6 Hz, 1H), 5.89 (d, *J* =

14.9 Hz, 1H), 5.68 (d, *J* = 17.0 Hz, 1H), 5.59 (d, *J* = 8.1 Hz, 2H), 5.51 (s, 2H), 3.11 – 2.21 (m, 22H), 1.52 (s, *J* = 4.8 Hz, 18H), 1.39 (s, 9H). **ES-MS:** *m*/*z* = 1384 (MH^+).

5.5.7 [Ir(fppy)$_2$L^2].(PF$_6$)

This synthetic procedure was modified from literature.[12] Protected [Ir(fppy)$_2$L^2] (0.17 g, 0.12 mmol) dissolved in CH_2Cl_2 (10 mL). To this TFA (10 mL) was added and the mixture was stirred at room temperature for 48 h. The solvent was then removed, and the residue was dissolved in CH_2Cl_2 (15 mL) and removed under vacuum. This step was repeated 10 times. MeOH (15 mL) was then added and this was removed under vacuum. This step was also repeated 10 times. The precipitate was then dissolved in the minimum volume of EtOH and triturated in diethyl ether. The yellow precipitate was filtered (0.11 g, 72%).

^{1}H NMR (400 MHz, MeOD, 298 K): δ_H 8.49 (d, *J* = 8.0 Hz, 1H), 8.40 (s, 1H), 8.33 (t, *J* = 7.9 Hz, 2H), 8.20 (dd, *J* = 11.1, 4.7 Hz, 1H), 8.02 (t, *J* = 7.9 Hz, 1H), 7.98 – 7.87 (m, 2H), 7.81 (d, *J* = 4.9 Hz, 1H), 7.78 – 7.71 (m, 1H), 7.59 (dd, *J* = 9.0, 4.1 Hz, 2H), 7.49 (t, *J* = 6.6 Hz, 2H), 7.41 (d, *J* = 7.7 Hz, 1H), 7.37 – 7.18 (m, *J* = 22.5, 12.7, 6.0 Hz, 4H), 6.66 (ddd, *J* = 11.7, 9.2, 2.3 Hz, 1H), 5.92 – 5.79 (m, 2H), 5.73 (s, 1H), 5.70 – 5.61 (m, 1H), 5.54 (d, *J* = 6.4 Hz, 1H), 5.41 (dd, *J* = 8.5, 2.2 Hz, 1H), 3.94 (d, *J* = 16.7 Hz, 2H). **ES-MS:** *m*/*z* = 1216 (MH^+). **HRMS ES$^+$:** Calculated for $IrC_{56}H_{53}N_9O_6F_4$: 1216.3684; Found: 1216.3694.

5.5.8 [IrL^2•Eu].(PF$_6$)

[Ir(fppy)$_2$L^2] (0.054 g, 0.044 mmol) was dissolved in MeOH (20 mL). To this Eu(OTf)$_3$ (Sigma Aldrich) (0.029 g, 0.048 mmol) was added. To reaction was heated to 50°C and stirred for 48 h. The solvent was removed under vacuum and the precipitate was dissolved in H_2O (10 mL). The pH was adjusted to 10 using aqueous NaOH. From this the solids were filtered and the pH of the solution was readjusted to 7. The solvent was removed under vacuum. The precipitate was dissolved in the minimum volume of EtOH and the product was triturated in diethyl ether. The precipitate was filtered (0.045 g, 74%). **ES-MS:** *m*/*z* = 1366 (MH^+). **TOF:** 3.2 min. **HRMS ES$^+$:** Calculated for $IrC_{56}H_{50}N_9O_6F_4Eu$: 1365.267; Found: 1365.2636.

5.5.9 [IrL^2•Gd].(PF$_6$)

[Ir(fppy)$_2$L^2] (0.054 g, 0.044 mmol) was dissolved in MeOH (20 mL). To this Gd(OTf)$_3$ (Sigma Aldrich) (0.03 g, 0.048 mmol) was added. To reaction was heated to 50°C and stirred for 48 h. The solvent was removed under vacuum and the precipitate was dissolved in H_2O (10 mL). The pH was adjusted to 10 using aqueous NaOH. From this the solids were filtered and the pH of the solution was readjusted to 7. The solvent was removed under vacuum. The precipitate was dissolved in the minimum volume of EtOH and the product was triturated in diethyl ether. The precipitate was filtered (0.047 g, 77%). **ES-MS:** *m/z* = 1371 (MH$^+$). **TOF:** 3.2 min. **HRMS ES$^+$:** Calculated for $IrC_{56}H_{50}N_9O_6F_4Gd$: 1371.2683; Found: 1371.2683.

5.5.10 Intermediate A

[Ir-pic] (0.51 g, 0.70 mmol) and potassium carbonate (0.96 g, 0.71 mol) were added to acetone (60 mL), followed by α-α'-dibromo-*p*-xylene (Sigma Aldrich) (0.94 g, 0.36 mol). The mixture was heated to reflux for 48 h under $N_{2\,(g)}$. The solvent was removed under vacuum and the solid was dissolved in CH_2Cl_2 (50 mL) and extracted with H_2O (3 × 30 mL). The organic layers were combined, dried over $MgSO_4$, filtered and the solvent was removed under vacuum to give a yellow solid. The product was then obtained by column chromatography on silica gel (200-300 mesh) using CH_2Cl_2/MeOH (98:2) as the eluent to yield a yellow solid (0.22 g, 36%).
^{1}H NMR (400 MHz, CDCl$_3$, 298 K): δ_H 8.84 (dd, *J* = 5.8, 0.9 Hz, 1H), 8.31 (d, *J* = 8.6 Hz, 1H), 8.25 (d, *J* = 8.3 Hz, 1H), 7.80 (t, *J* = 7.8 Hz, 2H), 7.55 (d, *J* = 8.1 Hz, 2H), 7.48 – 7.38 (m, 5H), 7.26 – 7.20 (m, 2H), 7.01 (ddd, *J* = 7.3, 5.9, 1.3 Hz, 1H), 6.52 – 6.34 (m, 2H), 5.82 (dd, *J* = 8.7, 2.4 Hz, 1H), 5.55 (dd, *J* = 8.7, 2.3 Hz, 1H), 5.35 (s, 2H), 4.51 (s, 2H). **ES-MS:** *m/z* = 894 (MH$^+$).

5.5.11 Protected [Ir(fppy)$_2$L^3]

Complex **A** (0.22 g, 0.24 mmol) and caesium carbonate (0.86 g, 0.24 mol) were added to CH_3CN (60 mL), followed by triester (0.15 g, 0.30 mol). The mixture was heated to reflux under $N_{2\,(g)}$ for 24 h. The solvent was removed under vacuum and the solid was dissolved in CH_2Cl_2 (50 mL) and extracted with H_2O (3 × 30 mL). The organic layer was dried over $MgSO_4$, filtered and the solvent was removed under vacuum to give a yellow solid. The product was then obtained by column chromatography on silica gel (200-300 mesh) using CH_2Cl_2/MeOH (95:5) as the eluent to yield a yellow solid (0.088 g, 27%).

^{1}H NMR (400 MHz, $CDCl_3$, 298 K): δ_H 8.82 (d, *J* = 4.9 Hz, 1H), 8.28 (dd, *J* = 14.8, 8.7 Hz, 2H), 7.79 (dd, *J* = 10.9, 4.9 Hz, 2H), 7.69 (d, *J* = 8.5 Hz, 1H), 7.62 (d, *J* = 8.0 Hz, 2H), 7.51 – 7.36 (m, 5H), 7.19 (t, *J* = 6.0 Hz, 1H), 7.02 (t, *J* = 6.0 Hz, 1H), 6.54 – 6.35 (m, *J* = 14.8, 11.7, 9.2, 2.3 Hz, 2H), 5.81 (dd, *J* = 8.6, 2.3 Hz, 1H), 5.61 – 5.51 (m, 1H), 1.47 (d, *J* = 8.6 Hz, 27H). **ES-MS:** *m/z* = 1328 (MH^+).

5.5.12 [Ir(fppy)$_2$L^3]

This synthetic procedure was modified from literature.[12] Protected [Ir(fppy)$_2$L^3] (0.088 g, 0.066 mmol) dissolved in CH_2Cl_2 (10 mL). To this TFA (10 mL) was added and the mixture was stirred at room temperature for 48 h. The solvent was then removed, and the residue was dissolved in CH_2Cl_2 (15 mL) and removed under vacuum. This step was repeated 10 times. MeOH (15 mL) was then added and this was removed under vacuum. This step was also repeated 10 times. The crude product was purified by size exclusion chromatography on Sephadex LH-20 in MeOH (0.0172 g, 23%).

^{1}H NMR (400 MHz, MeOD, 298 K): δ_H 8.66 (d, *J* = 5.4 Hz, 1H), 8.34 (dd, *J* = 14.9, 8.7 Hz, 2H), 7.98 (dd, *J* = 19.3, 7.8 Hz, 2H), 7.85 (d, *J* = 6.7 Hz, 1H), 7.73 (d, *J* = 5.4 Hz, 1H), 7.63 (s, 4H), 7.49 (d, *J* = 2.7 Hz, 2H), 7.39 (t, *J* = 6.4 Hz, 1H), 7.24 (t, *J* = 6.4 Hz, 1H), 6.66 – 6.46 (m, *J* = 14.7, 11.7, 9.3, 2.2 Hz, 2H), 5.75 (dd, *J* = 8.7, 2.2 Hz, 1H), 5.55 (dd, *J* = 8.6, 2.2 Hz, 1H), 5.37 (s, *J* = 14.0 Hz, 2H), 3.78 (s, *J* = 41.2 Hz, 2H). **ES-MS:** *m/z* = 1160 (MH^+). **HRMS ES$^+$:** Calculated for $IrC_{50}H_{48}N_7O_9F_4$: 1160.3157; Found: 1160.3124.

5.5.13 [IrL^3•Eu]

[Ir(fppy)$_2$L^3] (0.0017 g, 0.015 mmol) was dissolved in MeOH (20 mL). To this $Eu(OTf)_3$ (Sigma Aldrich) (0.0098 g, 0.016 mmol) was added. To reaction was heated to 50°C and stirred for 48 h. The solvent was removed under vacuum and the crude product was purified by size exclusion chromatography on Sephadex LH-20 in MeOH (5.0 mg, 26%).

ES-MS: *m/z* = 1308 (MH^+). **HRMS ES$^+$:** Calculated for $IrC_{50}H_{45}N_7O_9F_4Eu.Na^+$: 1330.1941; Found: 1330.1957.

5.6 References

1. G. M. Sheldrick, *SADABS: A program for absorption correction with the Siemens SMART system,* University of Göttingen, Germany, 1996.
2. G. M. Sheldrick, *Acta. Crystallogr. Sect. A,* 2008, **64**, 112.
3. S. Sprouse, K. A. King, P. J. Spellane and R. J. Watts, *J. Am. Chem. Soc.,* 1984, **106**, 6647.
4. J. F. Gerdard and F. J. Lion, *Org. Chem.,* 1965, **30**, 318.
5. P. Coppo, E. Plummer and L. De Cola, *Chem. Commun.,* 2004, 1774.
6. T. Fei, G. Cheng, D. Hu, W. Dong, P. Lu and Y. Ma, *J. Polym. Sci. A Polym. Chem.,* 2010, **48**, 1859.
7. E. Orselli, G. S. Kottas, A. E. Konradsson, P. Coppo, R. Fröhlich, L. De Cola, A. van Dijken and H. Börner, *Inorg. Chem.,* 2007, **46**, 11082.
8. P. S. Shirude, V. A. Kumar and K. N. Ganesh, *Eur. J. Org. Chem.,* 2005, 5207.
9. K. K-W. Lo, C-K. Chung and N. Zhu, *Chem. Eur. J.,* 2003, **9**, 475.
10. X. Zeng, A. S. Batsanov and M. R. Bryce, *J. Org. Chem.,* 2006, **71**, 9589.
11. S. P. Argent, H. Adams, L. P. Hardin, T. Riis-Johannessen, J. C. Jeffery and M. D. Ward, *New J. Chem.,* 2005, **29**, 904.
12. A. Dadabhoy, S. Faulkner and P. G. Sammes, *J. Chem. Soc., Perkin Trans. 2,* 2002, 348.

Appendix

X-Ray Crystallography Data

A.1 Crystal data and structure refinement for [Ir(fppy)$_2$L^{pytz}]

Identification code	imw1685p21c	
Empirical formula	$C_{34} H_{20} F_4 Ir N_7$	
Formula weight	794.77	
Temperature	100(2) K	
Wavelength	0.71073 Å	
Crystal system	Monoclinic	
Space group	P2(1)/c	
Unit cell dimensions	a = 17.1044(6) Å	a= 90°.
	b = 9.5727(3) Å	b= 102.776(2)°.
	c = 17.7156(6) Å	g = 90°.
Volume	2828.85(16) Å^3	
Z	4	
Density (calculated)	1.866 Mg/m^3	
Absorption coefficient	4.786 mm^{-1}	
F(000)	1544	
Crystal size	0.30 x 0.30 x 0.25 mm^3	
Theta range for data collection	1.22 to 27.57°.	
Index ranges	-22<=h<=21, -12<=k<=11, -23<=l<=22	
Reflections collected	45693	
Independent reflections	6460 [R(int) = 0.0614]	
Completeness to theta = 27.57°	98.7 %	
Absorption correction	Semi-empirical from equivalents	
Max. and min. transmission	0.3808 and 0.3278	
Refinement method	Full-matrix least-squares on F^2	
Data / restraints / parameters	6460 / 372 / 415	
Goodness-of-fit on F^2	1.086	
Final R indices [I>2sigma(I)]	R1 = 0.0393, wR2 = 0.0854	
R indices (all data)	R1 = 0.0685, wR2 = 0.1002	
Largest diff. peak and hole	2.754 and -1.928 e.Å^{-3}	

Table 2. Bond lengths [Å] and angles [°] for imw1685p21c.

Ir(1)-C(221)	2.004(6)
Ir(1)-C(321)	2.011(6)
Ir(1)-N(311)	2.024(5)
Ir(1)-N(211)	2.034(6)
Ir(1)-N(121)	2.124(5)
Ir(1)-N(111)	2.156(5)

C(221)-Ir(1)-C(321)	89.8(2)
C(221)-Ir(1)-N(311)	94.2(2)
C(321)-Ir(1)-N(311)	80.6(2)
C(221)-Ir(1)-N(211)	80.7(2)
C(321)-Ir(1)-N(211)	94.2(2)
N(311)-Ir(1)-N(211)	172.81(19)
C(221)-Ir(1)-N(121)	98.9(2)
C(321)-Ir(1)-N(121)	171.2(2)
N(311)-Ir(1)-N(121)	97.20(19)
N(211)-Ir(1)-N(121)	88.63(19)
C(221)-Ir(1)-N(111)	173.2(2)
C(321)-Ir(1)-N(111)	94.6(2)
N(311)-Ir(1)-N(111)	91.7(2)
N(211)-Ir(1)-N(111)	93.7(2)
N(121)-Ir(1)-N(111)	76.88(19)
C(116)-N(111)-Ir(1)	126.6(4)
C(112)-N(111)-Ir(1)	114.9(4)
C(122)-N(121)-Ir(1)	115.1(4)
N(125)-N(121)-Ir(1)	136.6(4)
C(216)-N(211)-Ir(1)	124.6(5)
C(212)-N(211)-Ir(1)	116.7(5)
C(226)-C(221)-Ir(1)	127.3(5)
C(222)-C(221)-Ir(1)	114.3(5)
C(316)-N(311)-Ir(1)	124.9(4)
C(312)-N(311)-Ir(1)	116.9(4)

C(322)-C(321)-Ir(1)	114.5(4)
C(326)-C(321)-Ir(1)	126.3(5)

Symmetry transformations used to generate equivalent atoms:

Table 3. Torsion angles [°] for imw1685p21c.

C(221)-Ir(1)-N(111)-C(116)	127.2(17)
C(321)-Ir(1)-N(111)-C(116)	-2.4(6)
N(311)-Ir(1)-N(111)-C(116)	-83.2(6)
N(211)-Ir(1)-N(111)-C(116)	92.1(6)
N(121)-Ir(1)-N(111)-C(116)	179.8(6)
C(221)-Ir(1)-N(111)-C(112)	-44.0(19)
C(321)-Ir(1)-N(111)-C(112)	-173.7(4)
N(311)-Ir(1)-N(111)-C(112)	105.6(4)
N(211)-Ir(1)-N(111)-C(112)	-79.1(4)
N(121)-Ir(1)-N(111)-C(112)	8.6(4)
Ir(1)-N(111)-C(112)-C(113)	169.6(5)
Ir(1)-N(111)-C(112)-C(122)	-7.9(7)
Ir(1)-N(111)-C(116)-C(115)	-168.1(5)
C(221)-Ir(1)-N(121)-C(122)	166.5(5)
C(321)-Ir(1)-N(121)-C(122)	-22.9(17)
N(311)-Ir(1)-N(121)-C(122)	-98.0(4)
N(211)-Ir(1)-N(121)-C(122)	86.2(4)
N(111)-Ir(1)-N(121)-C(122)	-8.0(4)
C(221)-Ir(1)-N(121)-N(125)	-2.0(6)
C(321)-Ir(1)-N(121)-N(125)	168.6(13)
N(311)-Ir(1)-N(121)-N(125)	93.4(6)
N(211)-Ir(1)-N(121)-N(125)	-82.3(6)
N(111)-Ir(1)-N(121)-N(125)	-176.5(6)
Ir(1)-N(121)-C(122)-N(123)	-172.0(4)
Ir(1)-N(121)-C(122)-C(112)	6.5(7)
Ir(1)-N(121)-N(125)-C(124)	169.1(5)
C(221)-Ir(1)-N(211)-C(216)	179.4(5)
C(321)-Ir(1)-N(211)-C(216)	90.3(5)
N(311)-Ir(1)-N(211)-C(216)	134.3(15)
N(121)-Ir(1)-N(211)-C(216)	-81.3(5)
N(111)-Ir(1)-N(211)-C(216)	-4.6(5)
C(221)-Ir(1)-N(211)-C(212)	2.3(4)

C(321)-Ir(1)-N(211)-C(212)	-86.8(4)
N(311)-Ir(1)-N(211)-C(212)	-42.9(17)
N(121)-Ir(1)-N(211)-C(212)	101.5(4)
N(111)-Ir(1)-N(211)-C(212)	178.3(4)
Ir(1)-N(211)-C(212)-C(213)	177.8(5)
Ir(1)-N(211)-C(212)-C(222)	-2.8(7)
Ir(1)-N(211)-C(216)-C(215)	-177.8(5)
C(321)-Ir(1)-C(221)-C(226)	-84.8(5)
N(311)-Ir(1)-C(221)-C(226)	-4.2(5)
N(211)-Ir(1)-C(221)-C(226)	-179.1(6)
N(121)-Ir(1)-C(221)-C(226)	93.7(5)
N(111)-Ir(1)-C(221)-C(226)	145.3(16)
C(321)-Ir(1)-C(221)-C(222)	93.1(5)
N(311)-Ir(1)-C(221)-C(222)	173.7(4)
N(211)-Ir(1)-C(221)-C(222)	-1.2(4)
N(121)-Ir(1)-C(221)-C(222)	-88.3(4)
N(111)-Ir(1)-C(221)-C(222)	-37(2)
Ir(1)-C(221)-C(222)-C(223)	-177.8(5)
Ir(1)-C(221)-C(222)-C(212)	0.1(7)
Ir(1)-C(221)-C(226)-C(225)	179.1(4)
C(221)-Ir(1)-N(311)-C(316)	89.1(5)
C(321)-Ir(1)-N(311)-C(316)	178.2(5)
N(211)-Ir(1)-N(311)-C(316)	133.6(14)
N(121)-Ir(1)-N(311)-C(316)	-10.4(5)
N(111)-Ir(1)-N(311)-C(316)	-87.4(5)
C(221)-Ir(1)-N(311)-C(312)	-85.0(4)
C(321)-Ir(1)-N(311)-C(312)	4.1(4)
N(211)-Ir(1)-N(311)-C(312)	-40.5(18)
N(121)-Ir(1)-N(311)-C(312)	175.4(4)
N(111)-Ir(1)-N(311)-C(312)	98.4(4)
Ir(1)-N(311)-C(312)-C(313)	176.6(5)
Ir(1)-N(311)-C(312)-C(322)	-5.5(7)
Ir(1)-N(311)-C(316)-C(315)	-176.1(5)
C(221)-Ir(1)-C(321)-C(322)	92.8(5)

N(311)-Ir(1)-C(321)-C(322)	-1.5(4)
N(211)-Ir(1)-C(321)-C(322)	173.4(4)
N(121)-Ir(1)-C(321)-C(322)	-77.9(15)
N(111)-Ir(1)-C(321)-C(322)	-92.5(4)
C(221)-Ir(1)-C(321)-C(326)	-90.1(5)
N(311)-Ir(1)-C(321)-C(326)	175.6(5)
N(211)-Ir(1)-C(321)-C(326)	-9.5(5)
N(121)-Ir(1)-C(321)-C(326)	99.2(15)
N(111)-Ir(1)-C(321)-C(326)	84.6(5)
Ir(1)-C(321)-C(322)-C(323)	178.8(4)
Ir(1)-C(321)-C(322)-C(312)	-1.1(7)
Ir(1)-C(321)-C(326)-C(325)	-177.0(4)

Symmetry transformations used to generate equivalent atoms:

A.2 Crystal data and structure refinement for [Ir(fppy)$_2$L^{tol}].(PF$_6$)

Identification code	imw1705p21n	
Empirical formula	$C_{39} H_{30} F_{10} Ir N_6 O P$	
Formula weight	1011.86	
Temperature	100(2) K	
Wavelength	0.71073 Å	
Crystal system	Monoclinic	
Space group	P 21/c	
Unit cell dimensions	a = 17.1469(16) Å	a= 90°.
	b = 26.065(2) Å	b= 129.142(5)°.
	c = 21.6564(16) Å	g = 90°.
Volume	7506.9(11) Å^3	
Z	8	
Density (calculated)	1.789 Mg/m^3	
Absorption coefficient	3.692 mm^{-1}	
F(000)	3960	
Crystal size	0.1 x 0.1 x 0.1 mm^3	
Theta range for data collection	1.442 to 27.783°.	
Index ranges	-22<=h<=22, -34<=k<=34, -28<=l<=28	
Reflections collected	127408	
Independent reflections	17421 [R(int) = 0.1991]	
Completeness to theta = 25.242°	100.0 %	
Absorption correction	Semi-empirical from equivalents	
Max. and min. transmission	0.7456 and 0.5030	
Refinement method	Full-matrix least-squares on F^2	
Data / restraints / parameters	17421 / 792 / 1051	
Goodness-of-fit on F^2	1.129	
Final R indices [I>2sigma(I)]	R1 = 0.0634, wR2 = 0.1006	
R indices (all data)	R1 = 0.1372, wR2 = 0.1194	
Extinction coefficient	n/a	
Largest diff. peak and hole	1.790 and -2.043 e.Å^{-3}	

Table 2. Bond lengths [Å] and angles [°] for imw1705p21n.

Ir(1)-C(151)	1.996(8)
Ir(1)-C(171)	2.007(8)
Ir(1)-N(161)	2.036(6)
Ir(1)-N(141)	2.048(6)
Ir(1)-N(121)	2.149(6)
Ir(1)-N(111)	2.168(6)
Ir(2)-C(271)	1.996(7)
Ir(2)-C(251)	1.999(8)
Ir(2)-N(261)	2.040(7)
Ir(2)-N(241)	2.047(6)
Ir(2)-N(221)	2.141(6)
Ir(2)-N(211)	2.184(6)

C(151)-Ir(1)-C(171)	87.3(3)
C(151)-Ir(1)-N(161)	92.5(3)
C(171)-Ir(1)-N(161)	80.0(3)
C(151)-Ir(1)-N(141)	80.8(3)
C(171)-Ir(1)-N(141)	94.8(3)
N(161)-Ir(1)-N(141)	171.7(3)
C(151)-Ir(1)-N(121)	100.9(3)
C(171)-Ir(1)-N(121)	171.4(3)
N(161)-Ir(1)-N(121)	101.9(2)
N(141)-Ir(1)-N(121)	84.2(2)
C(151)-Ir(1)-N(111)	176.1(3)
C(171)-Ir(1)-N(111)	95.9(3)
N(161)-Ir(1)-N(111)	86.0(2)
N(141)-Ir(1)-N(111)	101.1(2)
N(121)-Ir(1)-N(111)	75.9(2)
C(271)-Ir(2)-C(251)	87.9(3)
C(271)-Ir(2)-N(261)	80.8(3)
C(251)-Ir(2)-N(261)	92.5(3)
C(271)-Ir(2)-N(241)	94.9(3)

C(251)-Ir(2)-N(241)	79.7(3)
N(261)-Ir(2)-N(241)	171.2(2)
C(271)-Ir(2)-N(221)	171.3(3)
C(251)-Ir(2)-N(221)	100.8(3)
N(261)-Ir(2)-N(221)	98.7(2)
N(241)-Ir(2)-N(221)	86.8(2)
C(271)-Ir(2)-N(211)	95.5(3)
C(251)-Ir(2)-N(211)	176.4(3)
N(261)-Ir(2)-N(211)	86.9(2)
N(241)-Ir(2)-N(211)	101.2(2)
N(221)-Ir(2)-N(211)	75.8(2)
C(116)-N(111)-Ir(1)	125.3(5)
C(112)-N(111)-Ir(1)	116.7(5)
C(122)-N(121)-Ir(1)	112.1(5)
N(125)-N(121)-Ir(1)	137.0(5)
C(146)-N(141)-Ir(1)	125.0(5)
C(142)-N(141)-Ir(1)	115.5(5)
C(156)-C(151)-Ir(1)	126.9(6)
C(152)-C(151)-Ir(1)	114.6(6)
C(153)-C(152)-C(151)	117.5(8)
C(162)-N(161)-Ir(1)	117.5(6)
C(166)-N(161)-Ir(1)	123.1(5)
C(176)-C(171)-Ir(1)	125.8(6)
C(172)-C(171)-Ir(1)	113.9(6)
C(216)-N(211)-Ir(2)	126.8(5)
C(212)-N(211)-Ir(2)	116.5(5)
C(222)-N(221)-Ir(2)	113.2(5)
N(225)-N(221)-Ir(2)	138.1(5)
C(246)-N(241)-Ir(2)	124.5(5)
C(242)-N(241)-Ir(2)	116.2(5)
C(252)-C(251)-Ir(2)	115.8(6)
C(256)-C(251)-Ir(2)	126.2(6)
C(266)-N(261)-Ir(2)	123.9(5)
C(262)-N(261)-Ir(2)	115.0(6)

C(276)-C(271)-Ir(2)	126.2(6)
C(272)-C(271)-Ir(2)	114.0(6)

Symmetry transformations used to generate equivalent atoms:

Table 3. Torsion angles [°] for imw1705p21n.

Ir(1)-N(111)-C(112)-C(113)	174.5(6)
Ir(1)-N(111)-C(112)-C(122)	-4.5(9)
Ir(1)-N(111)-C(116)-C(115)	-171.3(6)
Ir(1)-N(121)-C(122)-N(123)	167.3(5)
Ir(1)-N(121)-C(122)-C(112)	-13.2(10)
Ir(1)-N(121)-N(125)-C(124)	-159.6(6)
Ir(1)-N(141)-C(142)-C(143)	-179.0(6)
Ir(1)-N(141)-C(142)-C(152)	-0.3(8)
Ir(1)-N(141)-C(146)-C(145)	-179.6(6)
Ir(1)-C(151)-C(152)-C(153)	178.5(5)
Ir(1)-C(151)-C(152)-C(142)	-3.0(9)
Ir(1)-C(151)-C(156)-C(155)	-177.4(6)
Ir(1)-N(161)-C(162)-C(163)	-173.3(6)
Ir(1)-N(161)-C(162)-C(172)	6.5(9)
Ir(1)-N(161)-C(166)-C(165)	173.2(6)
Ir(1)-C(171)-C(172)-C(173)	-179.2(6)
Ir(1)-C(171)-C(172)-C(162)	-0.9(9)
Ir(1)-C(171)-C(176)-C(175)	177.9(6)
Ir(2)-N(211)-C(212)-C(222)	4.4(8)
Ir(2)-N(211)-C(216)-C(215)	172.7(6)
Ir(2)-N(221)-C(222)-N(223)	-171.2(5)
Ir(2)-N(221)-C(222)-C(212)	8.2(10)
Ir(2)-N(221)-N(225)-C(224)	166.1(6)
Ir(2)-N(241)-C(242)-C(243)	179.3(5)
Ir(2)-N(241)-C(242)-C(252)	-0.7(8)
Ir(2)-N(241)-C(246)-C(245)	-178.2(6)
Ir(2)-C(251)-C(252)-C(253)	-179.9(6)
Ir(2)-C(251)-C(252)-C(242)	-0.2(9)
Ir(2)-C(251)-C(256)-C(255)	178.3(6)
Ir(2)-N(261)-C(262)-C(263)	174.0(6)
Ir(2)-N(261)-C(262)-C(272)	-5.7(9)
Ir(2)-N(261)-C(266)-C(265)	-173.1(6)

Ir(2)-C(271)-C(272)-C(273)	179.5(6)
Ir(2)-C(271)-C(272)-C(262)	-1.7(10)
Ir(2)-C(271)-C(276)-C(275)	-177.9(6)

Symmetry transformations used to generate equivalent atoms: